# TWO-PHASE MODELLING OF HOT TEARING IN ALUMINIUM ALLOYS USING A SEMI-COUPLED METHOD

THÈSE N$^{O}$ 3859 (2007)

PRÉSENTÉE LE 7 SEPTEMBRE 2007

À LA FACULTÉ DES SCIENCES ET TECHNIQUES DE L'INGÉNIEUR
LABORATOIRE DE SIMULATION DES MATÉRIAUX
PROGRAMME DOCTORAL EN SCIENCE ET GÉNIE DES MATÉRIAUX

ÉCOLE POLYTECHNIQUE FÉDÉRALE DE LAUSANNE

POUR L'OBTENTION DU GRADE DE DOCTEUR ÈS SCIENCES

PAR

Vincent MATHIER

ingénieur en science des matériaux diplômé EPF
de nationalité suisse et originaire de Salquenen (VS)

acceptée sur proposition du jury:

Prof. H. J. Mathieu, président du jury
Prof. M. Rappaz, directeur de thèse
Dr Ph. Gilgien, rapporteur
Prof. T. Gmür, rapporteur
Prof. A. Mo, rapporteur

ÉCOLE POLYTECHNIQUE
FÉDÉRALE DE LAUSANNE

Suisse
2007

Il n'est point de secrets que le temps ne révèle

J. Racine
*Britannicus*, 1669

# Remerciements

Tout d'abord, je souhaite remercier le Professeur Michel Rappaz de m'avoir accepté dans son laboratoire pour faire mon travail de diplôme et de m'avoir engagé pour faire cette thèse. J'ai beaucoup apprécié sa façon de diriger mon travail, en étant toujours disponible quand j'avais besoin d'aide et de conseils tout en me laissant également l'opportunité de travailler de manière indépendante. De plus, je le remercie d'avoir su insuffler un excellent esprit au sein de son laboratoire.

Je remercie également les membres du jury qui ont examiné ce travail : le Pr. A. Mo pour son examen approfondi des aspects théoriques et les discussions très intéressantes que nous avons pu avoir sur ces questions ; le Dr. P. Gilgien (qui est la première personne à m'avoir mis en contact avec le monde de l'industrie de l'aluminium) pour m'avoir permis de mettre en perspective mon travail par rapport au monde réel ; le Pr. T. Gmür pour l'apport de son point de vue sur les aspects numériques et finalement le Pr. H.-J. Mathieu pour avoir présidé le jury et dirigé les débats lors de l'examen.

Ce projet n'aurait pas pu être mené à bien sans le soutien de la commission pour la technologie et l'innovation (CTI, Bourse 6167.1) ainsi que la participation, aussi bien financière que scientifique, des différents partenaires industriels du projet POST : Calcom-ESI, Alcan (FR and CH), Hydro Aluminum, Umicore et General Motors.

J'ai beaucoup aimé collaborer avec le Dr. Stéphane Vernède et pouvoir apprendre à le connaître en tant qu'ami. Il m'a beaucoup aidé sur les aspects aussi bien théoriques que pratiques concernant la fissuration à chaud et c'est avec grand plaisir que j'ai vu nos différentes approches se développer tout en se rapprochant.

Je remercie également le Dr. Gaël Couturier, avec qui j'ai et je vais partager un bureau, pour m'avoir aidé à me débattre dans le module de porosité (aussi bien en tant que développeur qu'en tant qu'utilisateur), pour m'avoir fait profiter de son expérience et pour tous les autres moments partagés loin des problèmes de fonderie.

Toujours dans la catégorie de mes anciens et néanmoins futurs collègues, le Dr. Olivier "qu'est-ce que je prends ?" Ludwig, m'a beaucoup apporté pour la compréhension des lois rhéologiques et je lui en suis très reconnaissant. J'ai aussi beaucoup apprécié son soutien dans la lutte pour la convergence des calculs mécaniques. Je tiens également à le remercier pour les bons moments passés autour d'un verre plutôt que devant un écran.

Lors de ce travail, j'ai utilisé des techniques numériques pour la résolution de problèmes physiques. Je me suis donc trouvé confronté à de multiples interrogations concernant divers aspects et je suis très reconnaissant à Jean-Luc Desbiolles d'avoir pris le temps de répondre à mes nombreuses questions. J'ai été très impressionné par sa capacité à toujours avoir une réponse intelligente et constructive à me donner.

Je remercie également le Dr. Jean-Marie Drezet pour m'avoir donné de multiples conseils

lors de ma prise en main d'Abaqus, pour m'avoir transmis son travail sur l'implémentation du modèle rhéologique et pour toutes les autres collaborations intéressantes que nous avons eues durant mon travail.

Je tiens aussi à exprimer ma gratitude au Dr. Pierre-Daniel Grasso pour m'avoir assisté durant mon travail de diplôme et pour avoir pris le temps de retrouver les données expérimentales brutes de son test de traction. Je remercie également Benoît Commet de chez Alcan (Pechiney) pour m'avoir fait profiter de sa grande expérience et de sa curiosité ainsi que pour m'avoir fourni les données concernant le rig test.

Je tiens à dire un chaleureux merci à tous les gens que j'ai pu côtoyer au laboratoire pour avoir toujours maintenu une excellente ambiance. En particulier, je suis très reconnaissant à Arlette Blatti et Anne Roy pour m'avoir toujours aidé, avec le sourire, à résoudre les multiples tracas pratiques et administratifs du quotidien.

Mon séjour à l'EPFL aura été une période très heureuse dans ma vie, de par les bonnes conditions de travail mais surtout grace aux amis que je me suis fait durant ces années. Je les remercie tous pour les repas, parties de cartes, bières et sorties que nous avons pu partager : Sam, Maf, Fred K, Gonzo, Stéphane, Milan, Christoph, Aurèle, Jonathan, James Bond, Lou Bega, Aurélie, Olivier, Gaël, ...

Je remercie également les piliers de l'équipe de volley de l'IMX pour m'avoir permis de maintenir une activité physique et relaxante pendant mes années de thèse, ce qui aura été particulièrement précieux durant la période de rédaction : Markus, Ludger, Alvaro, Sam et Christian.

Je tiens à exprimer ma profonde gratitude à ma famille pour leur support constant : mes oncles et tantes, mes grands-parents (notamment mon grand-père chez qui j'ai vécu pendant la majeure partie de mes études) et ma soeur (qui m'aura notamment apporté son aide précieuse quand j'ai dû me préoccuper des aspects esthétiques de la présentation de mes travaux). Plus particulièrement, je remercie mes parents pour tout leur amour et pour m'avoir donné la meilleure education qui soit.

Finalement, je remercie Anna de tout mon coeur pour son soutien et son amour. Elle rend ma vie meilleure chaque jour et elle est sans aucun doute le plus beau cadeau que j'ai reçu au cours de ces années de thèse.

# Abstract

Hot tearing is one of the most severe defects observed in castings, e.g. in billets or sheet ingots of aluminum alloys produced by DC casting. It is due to both tensile strains and a lack of interdendritic feeding in the mushy zone. In order to predict this phenomenon at the scale of an entire casting, the two-phase averaged conservation equations for mass and momentum must be solved in the mushy (i.e. mixed solid and liquid) region of the material. In recent contributions, M'Hamdi *et al* [1] proposed a strongly coupled resolution scheme for this set of equations. The solution of the problem was obtained using a rheological model established by Ludwig *et al* [2] and that captures the partially cohesive nature of the mushy alloy.

In the present contribution, the problem is addressed using a slightly different approach. The same rheological model (i.e. saturated porous media treatment) is used, but the influence of the liquid pressure is neglected at this stage. This assumption allows for a weakly coupled resolution scheme in which the mechanical problem is first solved alone using ABAQUS$^{TM}$ and user subroutines. Then the pressure in the liquid phase is calculated separately accounting for the viscoplastic deformation of the porous solid skeleton and solidification shrinkage. This is done with a code previously developed for porosity calculations, and that uses a refined mesh in the mushy zone [3].

This semi-coupled method was implemented and its numerical convergence studied from the point of view of both time step and mesh size. Guidelines for selecting these numerical parameters as well as the conditions under which the semi-coupled method may be applied are provided.

The model was then applied to three cases, i.e. two tensile tests conducted on mushy alloys [4, 5] and the casting of an entire billet [6]. Experimental data was indeed available concerning these problems prior to the present work. This information was used for the validation of the thermal and mechanical models that were setup to describe these different cases.

The results of the semi-coupled approach were also used to describe in more details these different castings. First of all, the numerical study of the mushy zone tearing test [5] proved helpful for distinguishing different fracture modes. The role of the high strain rate applied to the mushy alloy in this case was also outlined.

Another tensile test, referred to as the rig test [4], was successfully modeled in the present framework. The numerical results could be used to quantify the redistribution of strain in the mushy sample. As a consequence, intrinsic properties of the material, such as its ductility, could be extracted from the results. This study also gave further insight about the conditions under which tearing occurs in the samples.

Finally, the semi-coupled method was used to study the DC casting process. In this case, a real process performed under realistic conditions for the production of an industrial scale billet was modeled. As it is more complex and difficult to characterize experimentally, the conditions for hot tearing formation are less accessible. However, the isotherm velocity, the strain, the

strain rate and the liquid pressure could be described reasonably accurately. It was thus possible to correlate experimental observations of the hot tear with various calculated indicators of hot tearing susceptibility. Even with this information, it remains difficult to formulate new hot tearing criteria because all the indicators follow a similar trend during the casting and their respective contributions can thus not be distinguished.

The present work showed that the level of accuracy and detail that can be reached using two-phase models with appropriate materials properties and boundary conditions is satisfactory. It is indeed possible to model the relevant phenomena (heat flow, solid deformation and liquid feeding) at the scale of an entire casting. The variation of the different simulated fields can be described down to a scale of the order of a few millimeters. In that sense, this approach is one important aspect required to build a multiscale model for the problem of hot tearing.

It is expected that coupling such a method with granular models (which cover length scales from a few microns to a few centimeters [7]) will allow for a more complete description of the phenomena at hand. In the future, the development of such a multiscale numerical tool may prove to be the most efficient way towards quantitative predictions of hot tearing formation in real solidification processes.

**Keywords :** Hot tearing, mushy zone, solidification processing, two-phase modeling, semi-coupled method.

# Résumé

La fissuration (ou crique) à chaud est l'un des plus graves défauts observés dans les pièces coulées, notamment dans les lingots et billettes d'alliages d'aluminium produits par coulée DC. Ce défaut est dû à l'effet combiné de déformations (en traction) et du manque d'alimentation en liquide dans la zone pâteuse. Afin de prédire ce phénomène à l'échelle de la pièce, les équations à deux phases de conservation de la masse et de la quantité de mouvement doivent être résolues dans la région où l'alliage est pâteux (i.e. mélange solide et liquide). Récemment, M'Hamdi *et al* [1] ont proposé un schéma de résolution en couplage fort pour ce système d'équations. La solution du problème est obtenue en utilisant un modèle rhéologique, développé par Ludwig *et al* [2], qui décrit la nature partiellement cohésive de l'alliage à l'état pâteux.

Dans ce travail, l'approche du problème est légèrement différente. Le même modèle rhéologique (i.e. théorie des milieux poreux saturés) est utilisé mais l'influence de la pression dans la phase liquide sur la déformation du solide est négligée à ce stade. Cette hypothèse permet d'utiliser un schéma de résolution faiblement couplé dans lequel le problème mécanique est d'abord résolu seul en utilisant ABAQUS$^{TM}$ et ses fonctions utilisateur. Ensuite, la pression dans le liquide est calculée séparément en prenant en compte la déformation viscopastique du squelette solide et le retrait de solidification. Cette étape est effectuée par un code développé précédemment pour le calcul de porosité et qui utilise un maillage raffiné dans la zone pâteuse [3].

Cette méthode semi-couplée a été implémentée et sa convergence numérique a été étudiée, en fonction de la taille du maillage et du pas de temps. Des règles pour la sélection de ces paramètres numériques, ainsi que les conditions sous lesquelles l'approche semi-couplée est valable, ont pu être déterminées.

Le modèle a ensuite été appliqué à trois cas, à savoir deux essais de traction conduits sur des alliages à l'état pâteux [4, 5] ainsi que la coulée d'une billette complète. Des données expérimentales concernant ces problèmes étaient en effet disponibles avant le début de ce travail. Ces informations ont pu être utilisées pour valider les modèles thermiques et mécaniques mis en place pour décrire ces différentes expériences.

Les résultats des calculs semi-couplés ont aussi été utilisés pour décrire plus en détails ces différentes coulées. Tout d'abord, la modélisation numérique du test de déchirement [5] s'est révélée utile pour distinguer différents modes de rupture. Le rôle de la vitesse de déformation élevée imposée à l'alliage dans ce cas a aussi pu être mis en évidence.

Le test de traction à l'état pâteux (de Alcan-Pechiney) [4] a également été modélisé avec succès dans le cadre de l'approche développée ici. Les résultats numériques ont permis de quantifier la redistribution des déformations dans l'éprouvette pâteuse. En conséquence, des propriétés intrinsèques du matériau, telles que sa ductilité, ont pu être extraites des résultats. Cette étude a aussi permis de donner une description plus précise des conditions dans lesquelles la fissuration à chaud se développe dans ces échantillons.

Finalement, l'approche semi-couplée a été utilisée pour étudier le procédé de coulée DC.

Dans ce cas, un procédé réel, conduit dans des conditions réalistes pour l'obtention d'une billette aux caractéristiques industrielles, a dû être modélisé. Ce procédé étant plus complexe et difficile à caractériser expérimentalement, les conditions de fissuration à chaud sont moins accessibles. Cependant, la vitesse des isothermes, la déformation, la vitesse de déformation et la pression dans le liquide ont pu être décrites avec une précision satisfaisante. Il a donc été possible de corréler des observations expérimentales des criques avec les valeurs simulées de différents indicateurs de la tendance à la fissuration à chaud. Même avec cette information, il reste difficile de formuler un nouveau critère de fissuration car tous les indicateurs suivent la même tendance au cours de la coulée et leurs contributions respectives ne peuvent de ce fait pas être distinguées.

Ce travail a montré que le niveau de précision et de détail qui peut être obtenu dans le cadre de modèles à deux phases utilisant une description appropriée des propriétés du matériau et des conditions aux limites est très satisfaisant. Il est en effet possible de simuler les phénomènes importants (échanges de chaleur, conservation de la quantité de mouvement et alimentation en liquide) à l'échelle de la pièce coulée. Les variations des différents champs peuvent être décrites avec précision allant jusqu'à l'échelle du mm. En ce sens, cette approche constitue un des importants aspects nécessaires à la construction d'un modèle multi-échelles pour le problème de la fissuration à chaud.

Il est probable que le couplage entre une méthode telle que celle présentée ici avec une approche granulaire (couvrant des échelles allant de quelques microns à quelques centimètres [7]) permettra une description plus complète des différents phénomènes en jeu. Dans le futur, le développement de tels outils numériques multi-échelles sera peut-être l'approche la plus efficace pour aller vers la prediction quantitative de la fissuration à chaud dans les procédés industriels de solidification.

**Mots-clés :** Fissuration à chaud, zone pâteuse, procédés de solidification, modélisation à deux phases, approche semi-couplée.

# Contents

# Chapter 1

# Introduction

## 1.1 Aluminum Alloys

### 1.1.1 Properties and Applications

Aluminum is the third most abundant element in the earth's crust after silicon and oxygen. In spite of this apparent availability, aluminum is by far not the first metal to have been used in the history of metallurgy. In nature, this element is indeed always combined with others in minerals. Moreover, it turns out that the extraction of metallic aluminum from the ore (bauxite) is extremely energy intensive. As a consequence, it is only late in the $19^{\text{th}}$ century that aluminum (and its alloys) became industrially available thanks to progress made in extractive metallurgy (the Bayer process is used to obtain pure alumina, which is transformed into metallic aluminum by the Hall-Héroult process) [8]. As it involves an electrolytic step, this process is still very demanding from an energetic point of view. For one ton of aluminum produced, the following are necessary [8] :

- 430 kg of pure carbon (anodes), transformed into more than one ton of $CO_2$
- 30 kg of $Na_3AlF_6$ (cryolite added to lower the melting point of alumina)
- 13 000 kWh of electrical power
- 1900 kg of alumina $Al_2O_3$, which are obtained from :
  - 5000 kg of bauxite ore (mixture of $Al_2O_3$, $Fe_2O_3$ and $SiO_2$)
  - 210 kg of NaOH
  - 13 500 kg of water
  - 600 kg of fuel

Aluminum and its alloys exhibit various interesting properties such as good thermal and electrical conductivity. Its most important advantage however is that it is light (with a density about three time less than steel). This low density, combined with fairly interesting mechanical properties such as tensile strength (which can be tuned by controlled precipitation hardening) or elastic modulus, is the reason why aluminum alloys are useful structural materials. Moreover,

good resistance to corrosion under atmospheric conditions (due to the formation of a passive oxide layer) is another significant reason why aluminum is used widely in daily life applications [8].

Nowadays, aluminum alloys are the second mostly used (by volume) metallic material after iron alloys (steel and cast iron). Examples of their main applications are :

- Transport (36% of aluminum use in Western Europe for 2005 [9]) : aluminum alloys are used in automotive, rail, aerospace and marine transport applications. They are appreciated for their low density, low corrosion tendency and good shock absorption capability.
- Construction (27% of aluminum use in Western Europe for 2005 [9]) : the resistance to corrosion of aluminum alloys makes them very desirable for various parts of buildings. Moreover, well selected alloys can be joined fairly easily.
- Packaging (16% of aluminum use in Western Europe for 2005 [9]) : aluminum foil and cans are famous examples. In such applications, the advantages of aluminum alloys are numerous : good heat conductivity, impermeability, non-toxicity, ...
- Engineering (14% of aluminum use in Western Europe for 2005 [9]) : due to their good formability and joining capabilities, aluminum alloys are quite often used in engineering applications such as industrial machines or technical equipment.
- Electricity : aluminum is a very interesting material for electrical energy distribution cables. It exhibits indeed a low electrical resistivity and is much lighter than any metal with better conductivity (e.g. silver, gold or copper).

Because of their broad range of possible applications, aluminum alloys are more and more in demand. In 2005, the annual use of primary aluminum in the world increased by 5.3% to reach 31.7 million tons (Mtons). The total production was 31.86 Mtons with 4.8 Mtons coming from Western Europe. The use and production of aluminum is quite steady in Western Europe and North America (less than 3% increase). On the other hand, China is progressing extremely fast with a growth rate of 18.5% in production and 15.1% in use for 2005 [9]. As a consequence, there are now three main actors in the world aluminum consumption, i.e. Western Europe (24%, 7.71 Mtons), North America (23%) and China (22%). Western Europe is actually consuming much more than its own production and had to import 2.9 Mtons of primary aluminum in 2005 [9]. In this context, the ton of primary aluminum reached its highest value since 2000 at €2400 in April 2006.

Due to the high costs associated with the extraction of primary aluminum from the bauxite, aluminum alloys are very often recycled. Moreover, as metals, they can be processed numerous times without significant decrease of their intrinsic properties. Aluminum alloys are thus very relevant to today's industrial developments, which include more and more sustainable growth considerations. In Western Europe, the amount of recycled aluminum available went from 2 Mtons in 1988 to 4.7 Mtons in 2004 [9].

### 1.1.2 Identification

The present study focuses on wrought alloys to be used for rolling or extrusion. In industry, such alloys are classified using a four digit numbering scheme [8]. The first digit indicates the principal alloying element, while the following three are indicators of the exact composition :

- 1xxx : Pure aluminum above 99% purity with Fe and Si as most common impurities.

- 2xxx : Al-Cu series that can be heat treated for precipitation hardening. One common example is the 2024 alloy used in structural applications.
- 3xxx : Al-Mn alloys, e.g. 3004 used for the body of beverage cans.
- 4xxx : Al-Si. Note that silicon is more often used as a primary alloying element in cast alloys.
- 5xxx : Al-Mg alloys used in transport and structural applications. The 5182 alloy (used in beverage can tops) is often used as a model system to study hot tearing.
- 6xxx : Al-Mg-Si. These heat-treatable alloys, e.g. 6056, are to be used in novel aircrafts such as the Airbus A380.
- 7xxx : Al-Zn. Often used in coatings. Their good mechanical properties make them desirable in aeronautical applications (e.g. 7075).
- 8xxx : other alloys, e.g. Al-Li, which are light alloys with high bending stiffness.

Similarly, there exists a three digit scheme for the designation of cast alloys. Unlike wrought alloys, which are rolled or extruded, cast alloys are subsequently remelted, directly cast in complex final shapes and used in service without any prior deformation processing step.

## 1.2 Processing

### 1.2.1 Fabrication of Aluminum Products

When developing the production of an aluminum part, there are several processing methods to choose from. Quite a lot of them involve solidification at some stage. The first possible processing route is shape casting (high or low pressure die casting, sand casting, investment casting, ...) In this case, the liquid alloy is poured in a mold and solidified to obtain a product with definitive (or near definitive) shape. With such a method, it is possible to obtain complex geometries. This process can be made economically viable for both small and large numbers of parts.

In the automotive or aircraft industry for example, rather simple aluminum parts have to be joined together to form large and complex structures. Nowadays, welding (laser, friction, ...) is being more and more used as a joining technique. In this case, the alloys are heated very locally and a small liquid pool is obtained at the interface between two parts. Joining is achieved upon resolidification.

Finally, quite a large amount of applications for aluminum alloys involve parts with a fairly simple geometry (at least in one direction). In this case, deformation processing, such as rolling or extrusion is very adapted. Large amounts of finished or semi-finished products can be obtained at high rates. In general, sheet ingots (rectangular cross section of typically 1.5 m x 0.5 m, typical length of 8 m, also known as slabs) are rolled and billets (cylindrical shape, typically 25 cm in diameter and 3.5 m in length) are used for extrusion. The quality of the final product depends on both the control over the deformation process and the quality of the starting ingot or billet. The next section will present in more details the direct-chill (DC) casting method, which is standard for production of both slabs and billets (see Figure 1.1).

### 1.2.2 DC Casting

In order to be used for extrusion or rolling, ingots and billets must have a relatively constant cross section, a good surface quality and be defect-free. Nowadays, the most standard technique to achieve these goals is a semi-continuous process known as direct-chill (DC) casting [10, 11].

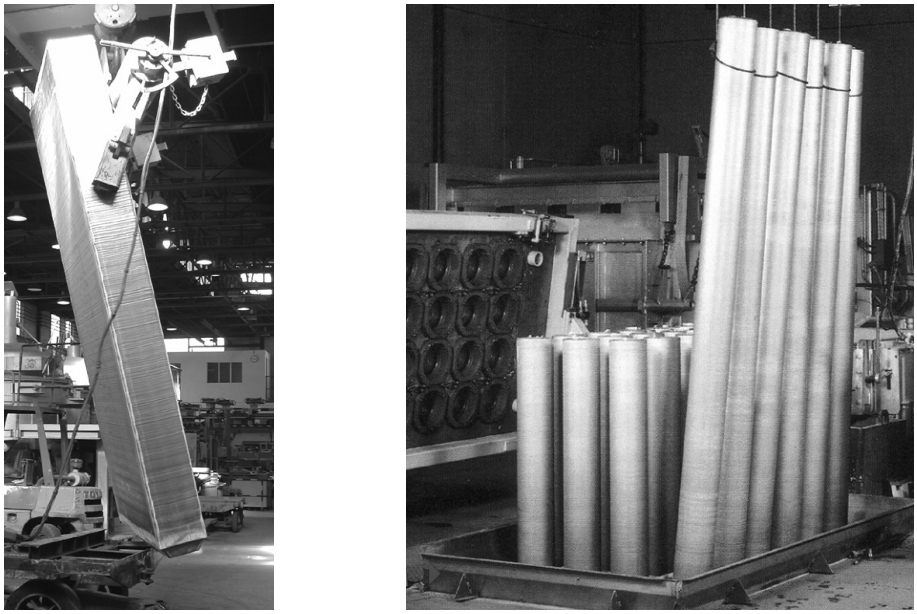

**(a)** **(b)**

**Figure 1.1:** (a) Slab (b) 24 billets cast using the DC casting process with Wagstaff technology [5].

In this process (see Figure 1.2), a mold defining the desired cross-section is closed initially by a movable bottom block. In some cases, the mold is covered with a system designed to control the cooling conditions (hot top). The alloy melted in a furnace is poured inside the mold from the top through a distribution bag. Grain refiner (Al-Ti-B alloy containing Ti-$B_2$ particles that will act as grain nucleation centers) is added to the liquid alloy in a proportion of typically 1 kg of refiner per ton of alloy. The role of the distribution bag, which consists of a fiber glass cloth of a relevant shape with variable permeability, is twofold. Firstly, this system can filter oxide inclusions coming from the liquid feed. In addition, this bag is designed in order to control the flow of the liquid alloy. In general, it is desired to direct the flow of liquid towards the sides of the ingot or billet so as to minimize the depth of the liquid pool. Cooling is achieved from the sides and bottom of the cast. As a consequence, a solid crust is formed in contact with the mold and the solidified alloy can thus hold the liquid inside. Once this condition is satisfied, the continuous casting may begin. Liquid alloy will be continuously fed into the system while the bottom block is pulled downwards at some velocity $v_{cast}$, referred to as the casting speed.

The beginning of this casting process (i.e. the start-up phase) corresponds to a transient behavior of the thermal field. After about typically 1 m of ingot has been cast, a steady state regime is reached (the thermal field close to the mold no longer evolves with time). The ingot or billet can then be grown to be several meters high with good control. When the desired height is achieved, feeding is cut off and the bottom block is stopped. After solidification is completed, one ingot (or possibly several billets) is obtained, which means that DC casting is indeed a semi-continuous process. Please note that a similar method, in which the bottom block is pulled away horizontally, is also used sometimes in the industry. This is known as horizontal casting [10].

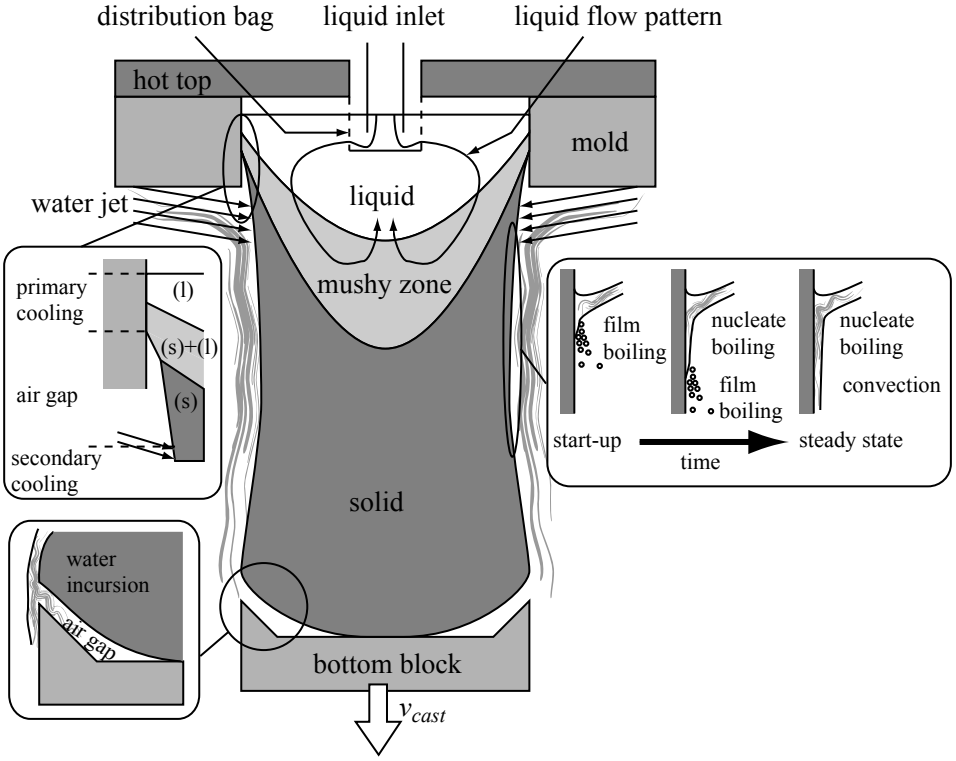


**Figure 1.2:** Schematic (vertical cut) representation of the DC casting process (N.B. some of this picture was reproduced from [12]).

DC casting has been optimized very thoroughly over the years and involves many technical refinements [10]. Among other specific features, it is important to focus on one of them at this stage, namely the cooling history at the surface of the ingot [13]. Firstly, the alloy is in contact with the mold, and this is referred to as primary cooling. At this stage, it is worth noting that there are different types of mold. On the one hand, in standard DC casting, the melt is in direct contact with the mold. On the other hand, a variation of this method, known as EMC (electromagnetic casting), is obtained with a mold that uses magnetic forces to confine the melt. In this technique, there is no contact between the mold and the liquid alloy.

After some cooling, the ingot will usually deform due to thermal gradients and contact with mold is lost (air gap formation). The heat transfer at the surface thus becomes very inefficient and the presence of the hot alloy at the center of the ingot may lead to reheating and possibly partial remelting of the ingot surface and to exudations. Below the mold, water is sprayed on the surface of the cast and the heat transfer efficiency increases strongly. The cooling obtained from the water jets is referred to as secondary cooling (see Figure 1.2) and can itself be divided in different regimes depending on the turbulence of the water jet and on the temperature, $T_{surf}$, of the surface on which the water impinges [12–15]. As a consequence, the convective heat transfer coefficient, $h$, will vary with time and position

The preceding description shows that the heat transfer along the sides of the ingot is quite complex. This is also valid for the thermal contact between the butt of the ingot and the bottom block [13, 16]. Again, due to thermally-induced strains, contact between the block and the ingot is usually lost on most of the surface. The efficiency of the cooling in this case depends on the width of the air gap and is also strongly affected when water from the side of the ingot flows inside the gap (water incursion) [13, 17, 18].

The DC casting process is well optimized and mastered. The beginning of the casting remains however quite critical. There are several parameters that can be altered to try and reduce the formation of defects during the start-up phase. The most important ones are the following :

- Casting recipe : the casting speed (downwards velocity of the bottom block $v_{cast}$) varies during the cast. It is usually slower during the start-up phase to reduce the amount of defects and increased slowly to reach steady state and minimize the casting time. If the casting speed is too high, the solid shell supporting the liquid alloy outside the mold may become too thin, leading to surface defects.
- Secondary cooling : in order to reduce thermal gradients at start-up, the intensity of the secondary cooling may be decreased. This can be achieved using several methods such as adding gas bubbles into the cooling water, pulsing the water jets and varying the impingement angle or water flow rate.
- Setup geometry : the shape of both the mold and bottom block will play an important role throughout the process. Their optimization is often a complex problem because many goals are to be achieved simultaneously (thermal field control, shape of the final product, durability of the mold [19]).

## 1.3 Casting Defects

### 1.3.1 Defects in DC Casting

There are numerous defects which may form during solidification in casting processes. Some of the industrially relevant types of defects are summarized in this section.

**Macrosegregation** The flow of solute-rich liquid within the liquid pool and the mushy zone, together with the motion of solute-deprived solid grains lead to an inhomogeneous solute content in the final product [20]. Some regions of the solidified alloy may contain significantly more solute than others. This will also cause mechanical properties to be inhomogeneous within the part.

**Surface quality** For rolling, the surface of the ingot has to be flat and smooth enough. If the surface is too rough, it will have to be scraped off. The general surface quality is determined, among other factors, by the contact between the solid shell and the mold. From that point of view, electromagnetic casting is interesting because a better surface quality may be achieved. The surface may also be significantly altered by defects such as exudations (segregation close to the mold) [21, 22] or bleed-outs. The latter form in the region where the air gap is found below the primary cooling region. If the solid crust is reheated too much by the hot liquid, the shell becomes mushy and liquid will leak out. Such a defect is typically found when the casting speed is too high.

**Distortions and residual stress** The thermal gradients in a solidifying part can be large. Due to thermal expansion, this will result in inhomogeneous straining of the solid shell. As a consequence, both residual stresses and part distortions are found in the product. As was already mentioned, the distortions are important because they alter the thermal conditions experienced by the metal. Moreover, the final cross section of the product will depend on the position along the casting direction (and be different from the shape of the mold). The

most famous distortions in DC casting are known as butt-curl, butt-swell or lateral faces pull-in [18, 23–26]. These must be corrected by sawing before rolling. Together with these distortions, residual stresses also give rise to difficulties, e.g. when sawing the ingots [27]. The heat treatment necessary to relieve such stresses can also be quite long and costly.

**Porosity** In the mushy zone, voids may appear for several reasons. First of all, if a mushy region (pocket) becomes isolated from a source of liquid, solidification shrinkage will have to be compensated by voids appearing at the end of solidification. These voids are typically quite large (a few mm or even cm) and are referred to as macroporosity [28]. This type of defect is encountered mostly in shape casting. It can be prevented by controlling the cooling conditions to prevent the formation of isolated liquid pockets in the part and by using adapted risers. Moreover, there is usually some gas dissolved in the liquid alloy that is cast. This gas may precipitate out as bubbles and lead to what is known as microporosity [3]. In general, porosity decreases the mechanical properties of the product, especially in fatigue. To some extent, it may be closed by hot isostatic pressing or during rolling.

**Inclusions** If the liquid feeding system is not carefully designed, parts of the oxide skin[1] may be entrained in the casting [29]. Any entrapped oxide may serve as a very efficient starting point for more severe defects, such as cracking or formation of large holes in the part. As far as DC casting is concerned, the feeding system has been optimized to prevent that problem to a great extent.

**Hot tearing** This defect is the main focus of this thesis and a more extended description of its features shall be given in the following section.

### 1.3.2 Hot Tearing

Hot tearing is a very important defect that is observed in various solidification processes. During solidification, thermal stresses arise because of the inhomogeneous temperature distribution, which causes gradients of thermal strain. These stresses may become large enough to induce cracks in the alloy. These may be encountered in shape casting as well as welding. In those cases, the apparition of this defect will cause the part to be rejected. In DC casting, such cracks are also found and may be very extended as shown on Figure 1.3. The cracked parts of the ingots or billets will have to be sawn off before rolling or extrusion can be performed. This leads to significant losses of productivity (in the worst cases, the casting process must be stopped).

This defect has been known in the casting practice for a long time. As identified by Campbell [29], hot tears can be recognized from a few common features :

1. Tears are ragged and branching cracks.
2. Hot tears propagate mainly between solid grains (intergranular failure).
3. The fracture surface reveals the dendritic pattern that existed at the time of fracture. This surface also appears to have been heavily oxidized, suggesting that fracture occurs at high temperature (see e.g. Figure 1.4).
4. The cracks are often found in hot spots or at locations where strains tend to be concentrated.

[1] Formed almost instantaneously where the melt is in contact with ambient air.

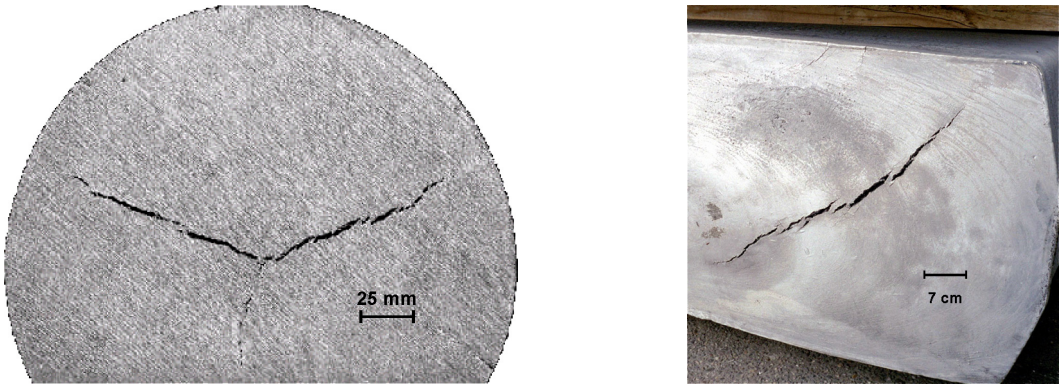


(a) (b)

**Figure 1.3:** (a) Star crack in a billet and (b) butt crack in a sheet ingot.

5. The tendency of this defect to appear will vary a lot depending upon which alloy is being cast.

6. The onset and extent of tearing may vary significantly even if the processing conditions are kept constant. This variation appears to be quite random.

These features suggest that hot tears are formed due to thermal strains experienced by the mushy zone. Is thus different from cold cracking or crack propagation through a fully solidified material.

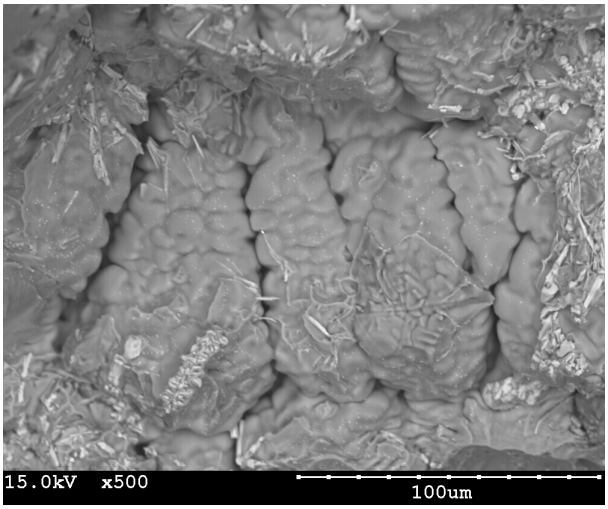


**Figure 1.4:** SEM image of a hot tear found in an AA5182 billet cast within the framework of the VIRCAST project [30]. This fractography reveals the intergranular nature of hot tearing.

As a conclusion to this section, it is interesting to review a few features of hot tearing in DC casting. This will outline how complex this problem may become and why it is difficult to solve at the industrial scale :

1. The casting speed is an important parameter. If the billet is cast slower, hot tearing may be prevented. Furthermore, once a hot tear has formed, the casting speed should be decreased significantly in order to get rid of it. It is also found that if the melt is poured at a higher

temperature, the hot tearing tendency will decrease. However, a hotter melt may also give rise to more surface defects as already explained [31].

2. The composition of the alloy is very important. In some alloys, tears are very difficult to avoid while other compositions are virtually free of this problem. In binary alloys, there is usually one composition below the maximum solubility for which the hot tearing susceptibility (HCS) is at a maximum [32]. As a consequence, some alloys series (e.g. 5xxx) and some specific compositions (e.g. 5182) are known to be difficult to cast [33].

3. The grain size and morphology is also an important parameter. Globular grains are less prone to hot tearing than dendritic mushy zones. As a consequence, the amount of grain refiner added to the alloy is selected in order to obtain globular grains with a reasonable size (typically 100 $\mu$m) [34–36].

Each one of these factors plays a role of its own in the hot tearing susceptibility. Moreover, they will obviously influence each other (e.g. the grain size will depend on the casting speed and alloy composition), which increases even further the complexity of the phenomenon. As a final remark, it should be mentioned that hot tearing is not specifically related to an alloy. It is indeed the processing conditions, together with the alloy composition, that will determine whether hot tearing occurs or not [33].

## 1.4 Objectives and Outline

For the past few decades, hot tearing has been an active field of research among the casting community. Both experimental and theoretical efforts led to significant advances in the understanding of this complex phenomenon. However, quantitative prediction of the apparition and extent of this defect remains very difficult, due to the great complexity of the problem. Several physical phenomena such as heat flow, liquid flow and deformation are occurring simultaneously. In addition, hot tearing is typically a multi-scale problem in which solid grains of typically 100 $\mu$m are grouped in mushy zones that are a few cm thick and experience constraints imposed by an industrial process at the meter scale. Moreover, mushy alloys have properties that are neither easy to measure, nor straightforward to model.

Due to the years of active research, various elements were available prior to the present thesis : experimental data [4–6], theoretical descriptions of hot tearing [37], rheological models for the mushy zone [2] and solution procedure to the coupled thermomechanical and feeding problem [1].

The objectives of this thesis were defined in this context :

- The first one was to develop and assess the accuracy of a semi-coupled method for solving the problems of momentum conservation in the mushy zone and liquid flow through the solid skeleton at the macroscopic scale. This method is based on a decoupling assumption, which means that some inaccuracy may arise due to a simplification of the problem. However, in cases where this assumption is relevant, a greater efficiency and flexibility can be obtained because more specialized modeling softwares can be used to solve each problem.

- Using this method, the goal of the present study is to model hot tearing tests at the laboratory or casthouse scale. Using the available experimental data to validate the numerical model, further quantitative information can be obtained from the computations. These results can be used to gain a better understanding of what happens in those tests. By extension, it is desired to extract information about hot tearing in these systems.

– Finally, it is desired to give a few elements about how process-scale modeling could be developed towards more quantitative hot tearing predictions.

The outline of this document follows these goals. In the first chapter, a brief introduction about aluminum alloys, hot tearing and DC casting has been provided. In Chapter 2, the morphology of the mushy zone is described in the context of hot tearing. This means that what happens at the end of solidification (coalescence, aggregation of solid grains, disappearance of intergranular liquid films) is focused on. The two-phase approach to mass and momentum conservation is then presented as well as the rheological model that will be used for mushy alloys.

In Chapter 3, the semi-coupled method is described. The decoupling assumption is formulated and details are given about the implementation of the method using three different solvers : thermal (CalcoSoft$^{TM}$), mechanical (Abaqus$^{TM}$) and liquid pressure (ProCast$^{TM}$ porosity module). Moreover, the accuracy of these solvers as well as suitable numerical parameters are determined. Finally, the validity of the decoupling assumption is assessed.

Chapter 4 is dedicated to describing the methods that were used to obtain the experimental data available prior to this work. In parallel, Chapter 5 describes all the parameters of the numerical models built during the present thesis. These models were setup to describe as accurately as possible the actual experiments.

In Chapter 6, the results of the numerical models are compared to experimental data. After assessing their validity, these results are used further in order to describe in more details what happens when the mushy alloys fails under strain. Finally, conclusions and perspectives of future work are found in Chapter 7.

# Chapter 2

# Theory

## 2.1 Mushy Zone Morphology

### 2.1.1 Basic Aspects of Solidification

In castings, a liquid alloy containing a nominal concentration $c_0$ of alloying element is poured into a mold, cooled down and solidified. Once the temperature has dropped below the liquidus temperature of the alloy, $T_{liq}$, it is thermodynamically favorable for a solid phase to start growing as indicated by the phase diagram. The solid phase will grow and occupy a volume fraction $g_s$ that increases as solidification progresses. At equilibrium, solidification is completed ($g_s = 1$) at the solidus temperature $T_{sol}$.

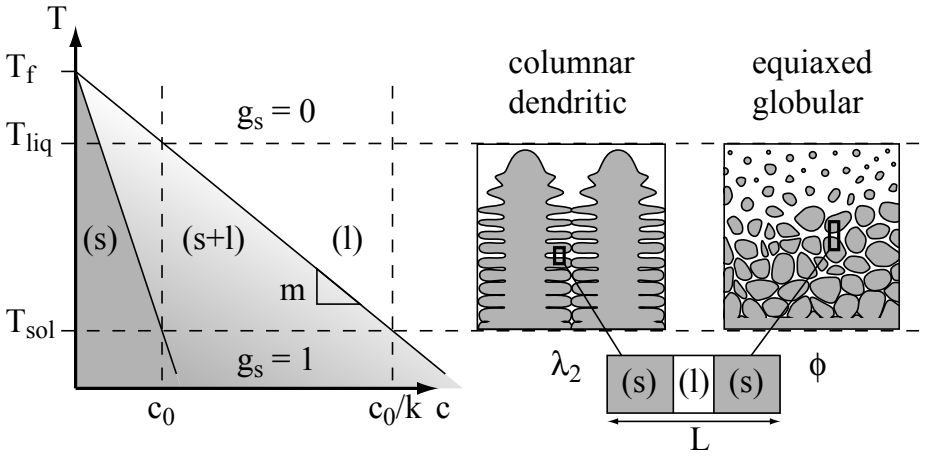


**Figure 2.1:** Solidification of a binary alloy. The amount of solid (grey phase) goes from $g_s = 0$ to 1 over a range of temperature (among other factors, this freezing range depends on the phase diagram shown on the left). The characteristic microstructural length is also indicated for two classical microstructures.

As suggested on Figure 2.1, solidification thus occurs over a temperature range (known as the freezing range) in which the volume fraction of solid $g_s$ goes from 0 to 1. At equilibrium, this range depends on the alloy (concentration $c_0$) and on the phase diagram (slope of the liquidus line $m$, partition coefficient $k$ and melting point of the pure solvent $T_f$). In general, this freezing range will also depend upon non-equilibrium factors related to the finite speed at which solidification

occurs. In particular, diffusion in the liquid close to the liquidus and diffusion in the solid over the entire freezing range will be of importance.

It is not our purpose to discuss kinetic effects and microstructure formation, which have been detailed elsewhere [38]. However, it is important to note that there exists a representative volume element (RVE), in which solidification can be modeled. This volume element has a size $\lambda_2$ (secondary dendrite arm spacing) in dendritic microstructures and a size $\phi$ (grain size) in the case of a globular morphology, which is most often encountered in DC cast ingots. The consideration of the RVE is used to describe how the solid fraction increases with temperature.

At equilibrium, the solidification path $g_s(T)$ is described by the lever rule:

$$g_s = \frac{1}{1-k}\left(\frac{T-T_{liq}}{T-T_f}\right) \tag{2.1}$$

If solidification is relatively fast, the solute has no time to diffuse in the solid phase and Scheil-Gulliver's model applies. Please note that, in such a case, solidification has to be terminated by a eutectic reaction occurring at the eutectic temperature $T_{eut}$:

$$g_s = 1 - \left(\frac{T_f - T_{liq}}{T_f - T}\right)^{\frac{1}{1-k}} \quad \text{and} \quad g_s = 1 \quad \text{for} \quad T \leq T_{eut} \tag{2.2}$$

In real cases, diffusion is possible in both the solid and liquid phase. However, the consideration of appropriate Fourier numbers indicates that diffusion in the liquid plays a role only close to $g_s = 0$. As we are interested mainly in the last stage of solidification, it is necessary to consider only diffusion in the solid phase, i.e. back-diffusion (while diffusion in the liquid can be regarded as infinitely fast). The model formulated by Brody and Flemings [39] and improved by Clyne and Kurz [40] describes this situation. The latter authors introduced a modified Fourier number $\alpha'$ relating the diffusion coefficient in the solid $D_s$, the local solidification time $t_f$ and the RVE size $L$: $\alpha' = Fo\left(1-\exp\left(-\frac{1}{Fo}\right)\right) - \frac{1}{2}\exp\left(-\frac{1}{2Fo}\right)$ where $Fo = \frac{D_s t_f}{L^2}$. This analysis results in the following expression [39, 40]:

$$g_s = \left(\frac{1}{1-2\alpha' k}\right)\left[1 - \left(\frac{T_f - T_{liq}}{T_f - T}\right)^{\frac{1-2\alpha' k}{1-k}}\right] \tag{2.3}$$

Please note that the lever rule and Scheil's model are recovered for $\alpha' = 0.5$ and $\alpha' = 0$ respectively, i.e. $Fo = \infty$ and $Fo = 0$.

There are many other models that have been developed since then, taking into account various factors such as dendritic grains, columnar and equiaxed growth, coarsening, ... [41, 42]. Moreover, advanced computer models can be built to take into account even more complex factors such as macrosegregation [43] and also become applicable to complex multicomponent systems. All these advances are important because the solid fraction is the primary factor that controls the behavior of the mushy zone.

### 2.1.2 Coalescence

In the context of hot tearing, the high solid fraction region of the mushy zone is the most important. In this region, the mushy alloy consists of solid grains separated from each other by the liquid phase. At the scale of the RVE shown on Figure 2.1, this means that two solid-liquid (s/l) interfaces are moving towards each other and that the intergranular liquid film becomes thinner and thinner as solidification progresses.

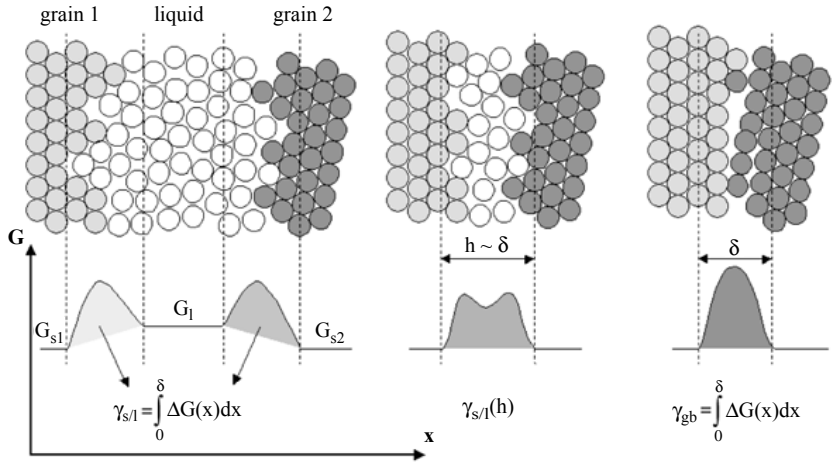


**Figure 2.2:** Coalescence of two solid-liquid interfaces merging into a grain boundary and schematic representation of the excess free energy (G) associated with the interfaces [44].

At the very last stage of solidification, s/l interfaces are getting very close to each other. However, solidification is complete only when all the liquid films between two neighboring grains have disappeared and grain boundaries have been formed instead. The process of merging two s/l interfaces into a solid grain boundary is known as coalescence or bridging (see Figure 2.2). This process was described recently by Rappaz *et al* from a thermodynamic point of view [44]. These authors have taken into account the fact that, upon coalescence, the excess energy associated with two s/l interfaces disappears. On the other hand, the excess energy associated with the formation of a grain boundary has to be introduced. In most cases, the grain boundary energy $\gamma_{gb}$, which is a function of the crystal lattice misorientation between both grains, is larger than twice the s/l interface energy, $2\gamma_{s/l}$.

As a consequence it takes an additional driving force for coalescence to occur[1]. The corresponding temperature drop required for coalescence to be complete can be expressed, introducing the entropy of fusion $\Delta s_f$ and the interface thickness $\delta$:

$$\Delta T_b = \frac{\gamma_{gb} - 2\gamma_{s/l}}{\delta \Delta s_f} \tag{2.4}$$

This expression describes when two solid grains will become linked by a grain boundary locally. It has been used by Mathier *et al* [45] and then by Vernède *et al* [46] to predict the evolution of the liquid films network in a globular mushy zone in which grains are randomly oriented. As shown on Figure 2.3, liquid films gradually disappear as the temperature decreases, depending on crystallographic orientation and local grain size. As a consequence, the solid skeleton is composed of grains that become more and more linked together, i.e. percolation of the solid phase occurs.

Please note that this gradual percolation of the solid phase starts only when the fraction of solid is already very high (above 90%) [46]. Moreover, such models indicate that coalescence may not be completed immediately below the eutectic temperature.

[1]this is in fact true for intergranular coalescence. If two dendrite arms from the same grain grow close to each other, they will bridge immediately, because their crystal orientation is the same and thus their grain boundary energy is zero.

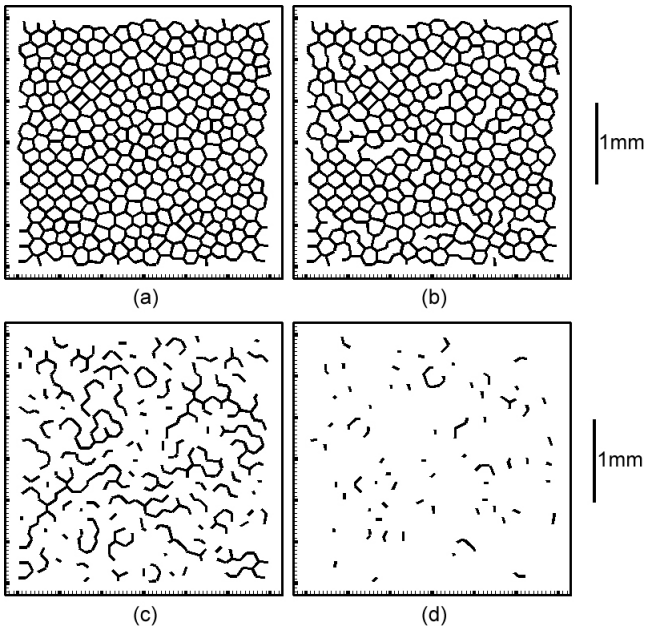


**Figure 2.3:** Intergranular liquid films in a mushy Al-1wt%Cu grain-refined alloy at (a) 600 °C (b) 550 °C (c) 500 °C and (d) 490 °C [45].

### 2.1.3 Morphological Features of the Mushy Zone

Having exposed briefly the key phenomena that come into play during the solidification of a population of globular grains, it is possible to give a description of the typical morphology of the mushy zone in the context of DC-cast, grain-refined aluminum alloys. In this section, we will thus focus on the morphological changes in a mushy alloy as the solid fraction increases, as suggested by Figure 2.4.

First of all, when there is only a relatively small amount of solid, the solid grains float freely in the liquid. The mushy alloy is then basically a slurry with a viscosity that increases with $g_s$ [47]. This liquid-like behavior is lost when the solid fraction becomes larger than $g_s^{coh}$. Above this limit, solid grains start to form a network and the materials can no longer be considered as liquid. The mush is then said to be coherent and $g_s^{coh}$ is known as the coherency point[2]. In shear, this value can be as low as $g_s^{coh} = 0.2 - 0.3$ for dendritic grains while it is closer to 0.5 for globular grains (packing of spheres) [48]. For globular grains in tension it will be around $g_s^{coh} = 0.6 - 0.7$ [2]. In a coherent mushy zone, the resistance to shear and compression are significant while the resistance to tensile stresses remains small.

As the solid fraction increases, solid grains fill more and more space, leading to an increase in the strength of the material. For dendritic grains, intragranular coalescence between dendrite arms has already started. However, these grains remain isolated until intergranular coalescence starts, i.e. solid grains start bridging together. This process corresponds to the point where most of the tensile strength of the material develops. As a consequence, it is customary to introduce a coalescence fraction $g_s^{coal}$ above which the mushy material can withstand significant tensile stresses. The coalescence point is typically reached around 95% of solid [2, 37]. Recently, Vernède *et al* [49] gave a more precise description of the steps leading to the formation of a fully coalesced solid skeleton.

[2]please note that the temperature corresponding to the solid fraction $g_s^{coh}$ will be referred to as the coherency temperature $T^{coh}$.

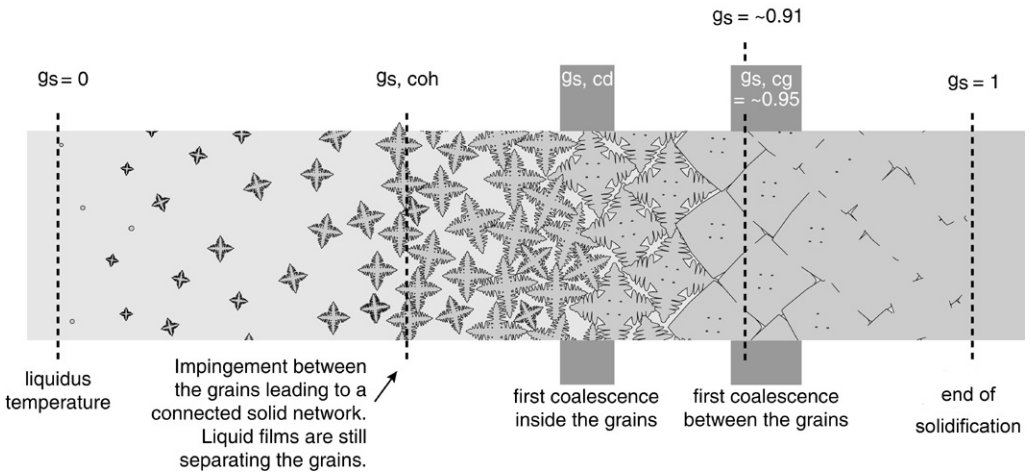


**Figure 2.4:** Morphology of the mushy zone for different solid fractions [5]. Please note that $g_s^{coh}$ is noted $g_{s,coh}$ on this figure and that a distinction is made between intra and intergranular coalescence. In general $g_s^{coal}$ corresponds to intergranular coalescence, i.e. to $g_{s,cg}$. Please note that the evolution of $g_s$ close to the liquidus is usually much faster in low concentration alloys than what is suggested on this figure.

These are illustrated on Figure 2.5. Typically, below 90% of solid, all grains are isolated from each other. Between $g_s = 90\%$ and $g_s^{coal}$, coalescence occurs at some grains boundaries. Only a few intergranular liquid films disappear and small clusters (involving a few grains) are formed. Once the solid fraction exceeds $g_s^{coal}$, large clusters of grains exist and the solid phase becomes continuous, which is why tensile strength develops in the mushy alloy at this point. At this stage, the alloy will exhibit a solid-like behavior. Finally (i.e. for $g_s > 99\%$), the last remaining intergranular liquid films are isolated and solidification is completed when they disappear.

## 2.2 Mass Conservation

### 2.2.1 Two-Phase Approach

In this work, mushy alloys and their behavior in real processes are considered. In this context, it is desired to use conservation equations that can be solved at the scale of the entire casting. Such macroscopic (or averaged) conservation equations were derived by Ni and Beckermann considering both the solid and liquid phases present in the mushy alloy. In that sense, using these equations is a two-phase approach to the problem at hand [50].

The homogenization procedure is defined considering an averaging volume $\Omega_0$. The latter must be smaller than the size of the entire system but large when compared to the microstructural features of the mushy zone (e.g. the grain size). The average of some quantity $\Psi$ in phase $\nu$ ($\nu = s$ for the solid and $\nu = l$ for the liquid) is defined as :

$$\langle \Psi_\nu \rangle = \frac{1}{\Omega_0} \int_{\Omega_0} X_\nu \Psi \mathrm{d}V \tag{2.5}$$

where $\mathrm{d}V$ is the volume increment and $X_\nu$ is a phase function, which is equal to 1 in phase $\nu$ and to 0 elsewhere. Moreover, introducing the volume fraction of phase $\nu$, $g_\nu$ (i.e. the ratio $\Omega_\nu/\Omega_0$

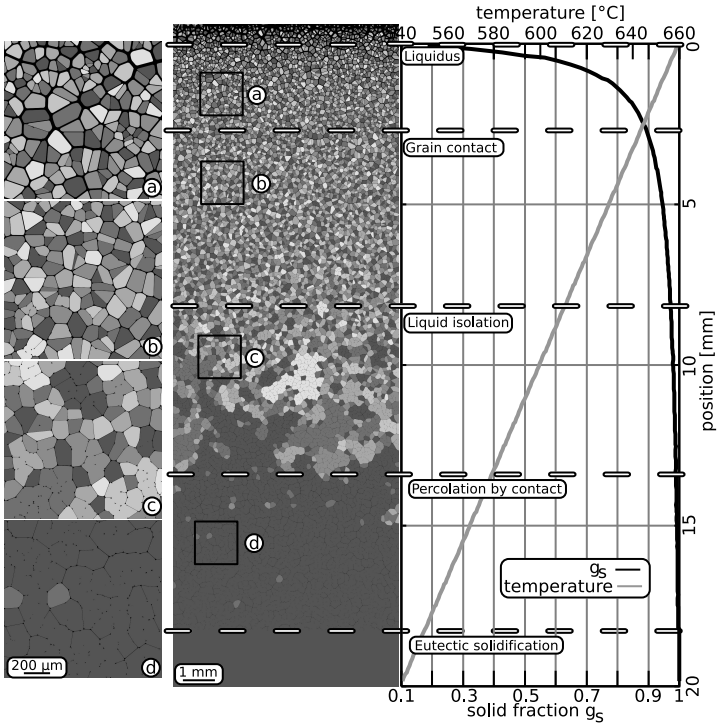


**Figure 2.5:** Simulated mushy zone morphology for globular grains in Al-1wt%Cu [49]. Grains that are linked to each other by a solid bridge are colored with the same shade of grey. Different regions are outlined : (a) isolated grains growing in the liquid (b) small clusters are formed (c) large clusters of solid grains are formed and the solid phase becomes continuous (d) solidification of the remaining liquid pockets is completed.

where $\Omega_\nu$ is the volume occupied by phase $\nu$), the intrinsic average is defined as :

$$\langle \Psi_\nu \rangle^\nu = \frac{1}{\Omega_\nu} \int_{\Omega_0} X_\nu \Psi \mathrm{d}V = \frac{\langle \Psi_\nu \rangle}{g_\nu} \tag{2.6}$$

The exact (microscopic) mass conservation equation for phase $\nu$ can be averaged according to Equation (2.5). In the following expression, $\rho$ is the density and $\mathbf{v}$ is the velocity field in the considered phase.

$$\frac{1}{\Omega_0} \int_{\Omega_0} X_\nu \left[ \frac{\partial \rho}{\partial t} + \nabla \cdot (\rho \mathbf{v}) \right] \mathrm{d}V = 0 \tag{2.7}$$

Mathematical properties of the average can be derived as shown in [50]. They may be used to rewrite Equation (2.7) in terms of the average density and velocity of the phase. Please note that this introduces an interfacial balance term $\Gamma_\nu$, which represents the mass transferred from other phases to phase $\nu$ across the corresponding interface. In our case, it describes the fact that liquid is transformed into solid at the s/l interface upon solidification. This leads to :

$$\frac{\partial \left( g_\nu \langle \rho_\nu \rangle^\nu \right)}{\partial t} + \nabla \cdot \left( g_\nu \langle \rho_\nu \rangle^\nu \langle \mathbf{v}_\nu \rangle^\nu \right) = \Gamma_\nu \tag{2.8}$$

From now on, the notation will be simplified by writing $\langle \rho_\nu \rangle^\nu \equiv \rho_\nu$ and $\langle \mathbf{v}_\nu \rangle^\nu \equiv \mathbf{v}_\nu$. In most cases (excepted for solute conservation), the intrinsic values are indeed considered to be uniform

at the scale of $\Omega_0$. Rewriting the averaged conservation equations for both phases thus yields :

$$\begin{aligned} \frac{\partial}{\partial t}\left(g_s\rho_s\right) + \nabla\cdot\left(g_s\rho_s\mathbf{v}_s\right) &= \Gamma_s \\ \frac{\partial}{\partial t}\left(g_l\rho_l\right) + \nabla\cdot\left(g_l\rho_l\mathbf{v}_l\right) &= \Gamma_l \end{aligned} \tag{2.9}$$

Considering only two phases, it is found that the interfacial balance terms compensate exactly : $\Gamma_s = -\Gamma_l$. Equations (2.9) can thus be added together to obtain :

$$\frac{\partial}{\partial t}\left(g_s\rho_s + g_l\rho_l\right) + \nabla\cdot\left(g_s\rho_s\mathbf{v}_s + g_l\rho_l\mathbf{v}_l\right) = 0 \tag{2.10}$$

At this stage, it is relevant to define the average density of the mixture of phases : $\overline{\rho} = g_s\rho_s + g_l\rho_l$. This can be introduced into Equation (2.10) to obtain the following expression [1] :

$$\frac{\partial}{\partial t}\overline{\rho} + \nabla\cdot\left(\overline{\rho}\mathbf{v}_s\right) + \nabla\cdot\left(g_l\rho_l\left(\mathbf{v}_l - \mathbf{v}_s\right)\right) = 0 \tag{2.11}$$

The next step towards obtaining a useful equation for the problem at hand is to describe how the liquid phase may flow through the solid skeleton.

### 2.2.2 Liquid Flow in the Mushy Zone

In this two-phase problem, liquid may flow through the solid phase network. It is thus customary to consider that the liquid alloy is flowing within a porous solid (matrix formed by the solidified grains). In such a case, it is well known that the pressure in the liquid phase, $p_l$, follows Darcy's law [51] :

$$g_l\left(\mathbf{v}_l - \mathbf{v}_s\right) = -\frac{K}{\mu}\left(\nabla p_l - \rho_l\mathbf{g}\right) \tag{2.12}$$

where, $\mathbf{g}$ is the gravity vector, $\mu$ is the viscosity of the liquid phase and $K$ is the permeability of the solid skeleton. The latter quantifies how the porous solid resists to the flow of liquid. As indicated by experimental data, the permeability of the mushy zone is well described by the Carman-Kozeny relation [52] :

$$K = \frac{\left(1-g_s\right)^3}{g_s^2}\frac{\lambda^2}{180} \tag{2.13}$$

To obtain this expression, the solid-liquid interfacial area was related to a unique characteristic length of the microstructure, $\lambda$. If the solid grains are dendritic, $\lambda$ should be equal to the secondary dendrite arm spacing $\lambda_2$, which varies strongly with time due to coarsening. On the other hand, if the solid grains are globular, $\lambda$ will be equal to the grain size $\phi$ and will remain nearly constant over time (since it is related mostly to the nucleation density). In both cases however, the value of $\lambda$ may vary very significantly in space.

Please note that a recent granular model from Vernède *et al* [46] indicates that Equation (2.13) is indeed valid over a very broad range of solid fractions. It is only above typically $g_s = 0.98$ that $K$ is expected to decrease more rapidly than predicted by Equation (2.13), at least in two dimensions. This deviation is due to clustering and percolation in the mushy zone (leading to a decrease in the solid-liquid interfacial area) at such solid fraction.

Having described the permeability of the solid phase, it is of interest to substitute Equation (2.12) into the mass conservation expression (Equation (2.11)). This leads to the two-phase mass conservation expression that shall be used in this work :

$$\frac{\partial}{\partial t}\overline{\rho} + \nabla\cdot\left(\overline{\rho}\mathbf{v}_s\right) - \nabla\cdot\left(\frac{\rho_l K}{\mu}\left(\nabla p_l - \rho_l\mathbf{g}\right)\right) = 0 \tag{2.14}$$

In Equation (2.14), the first term represents the local change of density (due to solidification and cooling). This change can be compensated by two contributions. On one hand, the solid may deform (second term in Equation (2.14)). On the other, liquid may flow through the solid skeleton and alter the local density (third term in Equation (2.14)).

### 2.2.3 Porosity

In most solidifying systems, the average density $\overline{\rho}$ increases when the temperature decreases, and will thus increase with time during solidification. This is a consequence of the fact that, most often, $\rho_s > \rho_l$. If strain in the solid and gravity are neglected, Equation (2.14) indicates that a liquid pressure gradient is established across the mushy zone due to this change in density (i.e. suction of liquid towards high solid fraction regions). As illustrated on Figure 2.6, not only does $p_l$ decrease for an increasing $g_s$ but $|\nabla p_l|$ also increases as solidification proceeds due to the strong dependence of the permeability $K$ upon $g_s$.

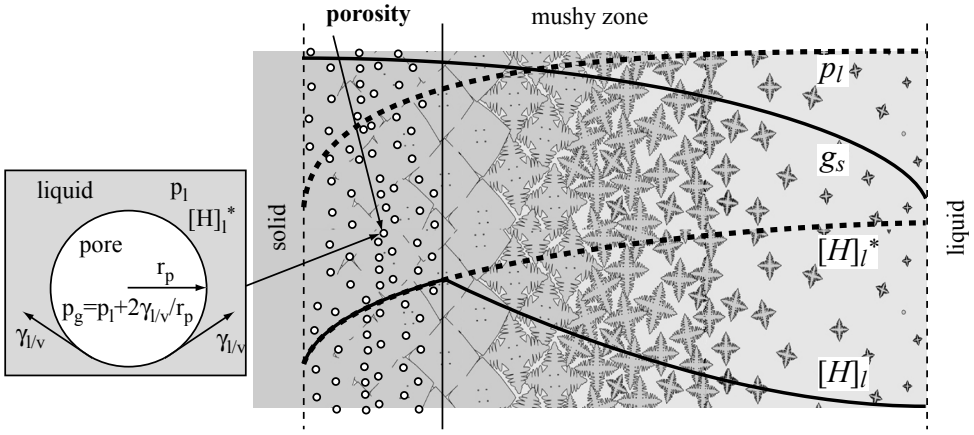


**Figure 2.6:** Schematic representation of the mechanism for pore nucleation in the mushy zone, inspired from [53].

From a physics standpoint, this pressure gradient is due to the fact that the density of the mushy material increases with solid fraction. As a consequence, the specific volume is smaller deep in the mushy zone, where most of the alloy is solidified. In general, this volume change cannot be compensated by strains in the solid. As a consequence, liquid has to flow towards the bottom of the mushy zone is order to fill the volume. This phenomenon, referred to as feeding [29], can only occur if a pressure gradient is present in the liquid phase.

The fact that the pressure in the liquid, $p_l$, decreases as $g_s$ increases has several consequences, one of them being the formation of microporosity in the mushy zone. As mentioned in the introduction, microporosity [29] is a casting defect that must not be mistaken for shrinkage porosity (large holes appearing in the part of the casting that solidifies last because shrinkage of the last liquid pocket cannot be compensated by feeding). Microporosity is a phenomenon that is due to the liquid pressure drop across the mushy zone [54]. This defect may form even when liquid is still potentially available for feeding.

In liquid aluminum, some dissolved hydrogen is practically always found (nominal concentration $[H]_0$) due to ambient humidity. Moreover, hydrogen is less soluble in the solid phase than in the liquid (partition coefficient $k_H < 1$). As a consequence, upon solidification, the concentration of hydrogen in the liquid $[H]_l$ will increase with $g_s$ due to microsegregation [3, 53] (see Figure 2.6).

Moreover, the solubility limit of hydrogen in the liquid, $[H]_l^*$, i.e. the maximum amount of hydrogen that can be dissolved into the liquid before the gas phase (hydrogen bubbles) precipitates out, is determined by Sieverts' law [3]:

$$[H]_l^* = S\left(T, c_l\right)\sqrt{\frac{p_g}{p_0}} \tag{2.15}$$

The solubility limit of hydrogen in the melt thus depends on the alloy (alloying elements and their concentration $c_l$ [53]) and on the temperature through the Sieverts' coefficient $S$. Moreover, $[H]_l^*$ also depends on the pressure in the liquid and on the radius, $r_p$ of the hydrogen bubbles[3] formed. This is due to the fact that $p_g$ is the pressure in the pore, which includes both the liquid pressure contribution and a curvature term (capillarity):

$$p_g = p_l + \kappa\gamma_{l/v} \tag{2.16}$$

where $\kappa$ is the curvature of the pore ($\kappa = \frac{2}{r_p}$ for a spherical pore of radius $r_p$) and $\gamma_{l/v}$ is the interfacial energy between the melt and the vapor phase in the pore (pores can only evolve when in contact with the liquid phase).

As suggested on Figure 2.6, a pore of radius $r_p$ will thus nucleate when the local concentration of hydrogen in the melt $[H]_l\left(g_s\right)$ exceeds the solubility limit $[H]_l^*$. The dependence of $[H]_l$ upon $g_s$ is described by a microsegregation model of hydrogen (the highest value of $[H]_l$ is found at the end of solidification). Since this is a rapidly diffusing species, a lever rule is typically introduced [3] but more advanced models also exist (e.g. finite hydrogen diffusion [55]). On the other hand, $[H]_l^*\left(T, c_l, p_l, r_p\right)$ is typically low deep in the mushy zone (due to the low value of $p_l$ and $T$). As a consequence, microporosity appears at fairly high solid fractions (typically 80% and above).

Choosing a nucleation criterion for porosity by setting the value of the pore radius at nucleation $r_{p,n}$, pores form when:

$$[H]_l\left(g_s\right) \geq [H]_l^*\left(T, c_l, p_l, r_p = r_{p,n}\right) \tag{2.17}$$

At this stage, it is possible to make a distinction between two different types of microporosity. On one hand, gas microporosity is due to the fact that the hydrogen accumulated in the liquid by segregation $[H]_l$ satisfies the nucleation criterion (2.17) at low $g_s$, when the pressure drop induced by shrinkage is negligible. On the other hand, shrinkage microporosity is due to the fact that the pressure in the liquid decreases dramatically, leading to a very low value of $[H]_l^*$. In this case, pores are formed even if the melt was well degassed and the hydrogen is not strongly segregated in the liquid. Obviously, there is not a clear-cut limit between these two regimes and, most often, both the pressure drop and the gas segregation will significantly contribute to the formation of porosity.

As a conclusion to this section, it is worth introducing the most important concepts for modeling microporosity development. The framework for describing the nucleation of pores has indeed been given above. However, in order to obtain quantitative predictions of the porosity fraction obtained in a casting, it is necessary to be able to describe the growth of pores. Typically, the growth model is based on the expression of hydrogen conservation. The formation of pores (apparition of a third phase) influences significantly this balance since a significant amount is no longer dissolved in the liquid but found as a vapor phase inside the pores [3].

Moreover, the amount of hydrogen that is found as vapor will depend of the hydrogen concentration in the pores, which is equal to $[H]_l^*$ and thus depends upon $p_g$. The latter quantity

[3] please note that such hydrogen bubbles are in fact micropores

depends strongly on the pore radius $r_p$ (through the curvature $\kappa$). As a consequence, one of the great challenge for modeling growth of micropores at the casting scale is to express how $r_p$ depends on the solid fraction $g_s$. This means that some model for the geometry of a growing pore constrained by a network of solid grains must be found [53].

## 2.3 Momentum Conservation

### 2.3.1 Thermomechanics

The aim of this section is to remind a few concepts of continuum mechanics that are used when developing an approach to momentum conservation in two-phase media. Let us start by reminding how momentum conservation is expressed in a single phase material for a quasi-static situation :

$$\nabla \cdot \boldsymbol{\sigma} + \mathbf{f}_v = 0 \tag{2.18}$$

In this expression, $\boldsymbol{\sigma}$ is the stress tensor[4] (of components $\sigma_{ij}$ with $i, j = 1, 2, 3$ in 3D) and $\mathbf{f}_v$ is the body force vector. Often, the body forces are simply due to gravity ($\mathbf{f}_v = \rho \mathbf{g}$) and this contribution may often be neglected [56].

In real materials, stresses always arise together with strains. The definition of the strain tensor is based on the displacement field $\mathbf{u}(\mathbf{x}, t)$ where $\mathbf{x} = (x_1, x_2, x_3)$ is the position in space and $t$ is time. For small strains, the strain tensor is defined as :

$$\boldsymbol{\epsilon} = \frac{1}{2}\left(\nabla \mathbf{u} + \nabla \mathbf{u}^T\right) \Leftrightarrow \epsilon_{ij} = \frac{1}{2}\left(\frac{\partial u_i}{\partial x_j} + \frac{\partial u_j}{\partial x_i}\right) \tag{2.19}$$

Similarly, the strain rate will be defined based on the velocity field $\mathbf{v}(\mathbf{x}, t) = \frac{\partial \mathbf{u}}{\partial t} \equiv \dot{\mathbf{u}}$ :

$$\frac{\partial \boldsymbol{\epsilon}}{\partial t} \equiv \dot{\boldsymbol{\epsilon}} = \frac{1}{2}\left(\nabla \mathbf{v} + \nabla \mathbf{v}^T\right) \Leftrightarrow \dot{\epsilon}_{ij} = \frac{1}{2}\left(\frac{\partial v_i}{\partial x_j} + \frac{\partial v_j}{\partial x_i}\right) \tag{2.20}$$

There are different types of strain (or strain rate) that should be distinguished. The total strain (or strain rate) will be decomposed according to the following relations :

$$\begin{aligned} \boldsymbol{\epsilon} &= \boldsymbol{\epsilon}^{el} + \boldsymbol{\epsilon}^{th} + \boldsymbol{\epsilon}^{ie} = \boldsymbol{\epsilon}^{el} + \boldsymbol{\epsilon}^{th} + \boldsymbol{\epsilon}^{pl} + \boldsymbol{\epsilon}^{vp} \\ \dot{\boldsymbol{\epsilon}} &= \dot{\boldsymbol{\epsilon}}^{el} + \dot{\boldsymbol{\epsilon}}^{th} + \dot{\boldsymbol{\epsilon}}^{ie} = \dot{\boldsymbol{\epsilon}}^{el} + \dot{\boldsymbol{\epsilon}}^{th} + \dot{\boldsymbol{\epsilon}}^{pl} + \dot{\boldsymbol{\epsilon}}^{vp} \end{aligned} \tag{2.21}$$

This indicates that the different contributions to the total strain are elastic (superscript $el$), thermal (superscript $th$) and inelastic (superscript $ie$). The latter can be subdivided into plastic (superscript $pl$) and viscoplastic (superscript $vp$) components. Each one of these different strains shall now be considered.

First of all, the elastic contribution $\boldsymbol{\epsilon}^{el}$ is directly related to the stress by the stiffness tensor $\mathbf{C}$ via Hooke's law $\boldsymbol{\sigma} = \mathbf{C} : \boldsymbol{\epsilon}^{el}$. In an isotropic material, only two parameters are required to describe the elastic behavior, i.e. Young's modulus $E$ and Poisson's ratio $\nu$. Both of them can be determined from a standard tensile test. For isotropic linear elasticity (which is applicable to polycristalline metals), when introducing Einstein's convention of summing over repeated indices

[4] the stress tensor is defined by the fact that the force density $\mathbf{f}$ acting on a plane of normal $\mathbf{n}$ in the material is given by $\mathbf{f} = \boldsymbol{\sigma} \cdot \mathbf{n}$

(e.g. $\sigma_{kk} \equiv \sum_{k=1}^{3} \sigma_{kk} \equiv \mathrm{tr}\,(\boldsymbol{\sigma})$) and Kronecker's symbol ($\delta_{ij} = 1$ if $i = j$, $\delta_{ij} = 0$ if $i \neq j$), the following is obtained :

$$\epsilon_{ij}^{el} = \frac{1+\nu}{E}\sigma_{ij} - \frac{\nu}{E}\sigma_{kk}\delta_{ij} \tag{2.22}$$

Let us now consider the thermal contribution $\boldsymbol{\epsilon}^{th}$. For a material in an unstrained state at temperature $T_{ref}$, changing the temperature to a value $T$ will cause straining due to thermal expansion. The linear thermal expansion coefficient $\alpha^{th}$ is a measure of this phenomenon and usually depends on temperature. Most often, thermal strain is isotropic and may be simply expressed when the unit tensor $\mathbf{I}$ is introduced ($I_{ij} = \delta_{ij}$) :

$$\boldsymbol{\epsilon}^{th} = \alpha^{th}\,(T - T_{ref})\,\mathbf{I} \tag{2.23}$$

This strain contribution is very important when dealing with castings. During a solidification process temperature gradients are introduced in the part and the mold may prevent free contraction of the casting. In any case, $\boldsymbol{\epsilon}^{th}$ will be inhomogeneous and it is the reason why stresses arise in cooling materials. During solidification, the rate of thermal contraction is thus very important and may be expressed as a function of the local cooling rate $\dot{T}$ :

$$\dot{\boldsymbol{\epsilon}}^{th} = \alpha^{th}\dot{T}\mathbf{I} \tag{2.24}$$

The remaining strain contribution $\boldsymbol{\epsilon}^{ie}$ is made up of all the permanent deformation (i.e. plasticity at low temperature) [56]. In general, there exists a function $\mathcal{F}$ of the stress state that will determine whether some plastic deformation occurs or not. When $\mathcal{F}\,(\boldsymbol{\sigma}) < 0$ the strain will remain elastic. Plastic straining is occurring locally in the material when :

$$\mathcal{F}\,(\boldsymbol{\sigma}) = 0 \tag{2.25}$$

As a consequence, the surface defined by Equation (2.25) is known as the yield surface. Please note that the condition, $\mathcal{F}\,(\boldsymbol{\sigma}) > 0$ is not physical. As a consequence, when loading continues after yielding, the yield surface changes in order to keep up with condition (2.25). This is known as hardening and can be accounted for by describing how $\mathcal{F}$ depends on hardening parameters (typically the plastic strain).

The most classical expression of $\mathcal{F}$ is given by the von Mises yield criterion. Since it is known experimentally that hydrostatic pressure neither influences nor causes plastic deformation, it is more relevant to consider the deviatoric stress tensor $\mathbf{S}$. The latter is obtained by removing the hydrostatic pressure $P_s$ from the stress tensor $\boldsymbol{\sigma}$ (please note that this pressure is positive in compression while stresses are taken to be positive in tension). This pressure is an invariant (does not depend on the coordinates system) and is defined as :

$$P_s = -\frac{1}{3}\mathrm{tr}\,(\boldsymbol{\sigma}) \tag{2.26}$$

The deviatoric stress tensor contains only the non-isostatic stress components and is defined as :

$$\mathbf{S} = \boldsymbol{\sigma} + P_s\mathbf{I} \tag{2.27}$$

The second invariant of $\mathbf{S}$ is known as the (von) Mises stress and is given by :

$$\sigma_M = \sqrt{\frac{3}{2}\mathbf{S} : \mathbf{S}} = \sqrt{\frac{3}{2}S_{ij}S_{ij}} \tag{2.28}$$

Having given those definitions, the von Mises criterion can be expressed in its simplest form by introducing $\sigma_y$, which is the yield stress in tension. Please note that $\sigma_y$ can be measured in a tensile test and depends on the plastic strain undergone by the material (work hardening) [56]:

$$\mathcal{F} = \sigma_M - \sigma_y \tag{2.29}$$

Let us now consider the maximum work principle, which basically states that, for a given plastic strain rate $\dot{\boldsymbol{\epsilon}}^{pl}$, the resulting stress state corresponds to a maximum in the energy dissipated by plastic deformation [56]. Two important properties of the yield surface can be derived based on this principle. Firstly, the yield surface given by $\mathcal{F}(\boldsymbol{\sigma}) = 0$ must be convex. Secondly, the inelastic strain rate must be normal to the yield surface. This is known as the normality rule and can be expressed under the following form:

$$\dot{\boldsymbol{\epsilon}}^{pl} = \lambda^{pl} \frac{\partial \mathcal{F}}{\partial \boldsymbol{\sigma}} \tag{2.30}$$

where $\frac{\partial \mathcal{F}}{\partial \boldsymbol{\sigma}}$ is the normal to the yield surface in stress space and $\lambda^{pl}$ is the proportionality constant. Please note that, in general, it is possible to define an inelastic potential $\mathcal{G}$ by the normality property given by Equation (2.30). For plasticity of metals, the yield function $\mathcal{F}$ is the same as the inelastic potential $\mathcal{G}$ [5].

It is very customary to use the von Mises yield criterion to describe the plastic behavior of alloys. When this expression of $\mathcal{F}$ is used, the normality rule may be rewritten to obtain [56]:

$$\dot{\boldsymbol{\epsilon}}^{pl} = \frac{3}{2} \frac{\dot{\epsilon}_e^{pl}}{\sigma_M} \mathbf{S} \tag{2.31}$$

where $\dot{\epsilon}_e^{pl} = \sqrt{\frac{2}{3} \dot{\boldsymbol{\epsilon}}^{pl} : \dot{\boldsymbol{\epsilon}}^{pl}}$ is the effective plastic strain rate. Please note that the plastic strain rate is directly proportional to the deviatoric stress tensor $\mathbf{S}$. Since $\mathrm{tr}(\mathbf{S}) = 0$, $\mathrm{tr}\left(\dot{\boldsymbol{\epsilon}}^{ie}\right) = 0$ is also true, which means that the plastic strain proceeds without altering the volume of the material. This is a well established experimental fact in solid alloys.

Up to this point, plastic strain was considered. Two different broad types of inelastic strain, i.e. permanent deformation, may be distinguished. On one hand, the classical view of plasticity is based on dislocations gliding or twinning under stress without much assistance from thermal activation. This kind of strain is referred to as plastic and noted $\boldsymbol{\epsilon}^{pl}$. The important features of this kind of strain is that it is caused by stress only, i.e. only an increase in $\boldsymbol{\sigma}$ will cause $\boldsymbol{\epsilon}^{pl}$ to increase as indicated by Equation (2.31). Plasticity is clearly the inelastic deformation mechanism that is active at rather low temperature (e.g. room temperature for aluminum alloys). The stress is thus a function of plastic strain.

On the other hand, when the temperature exceeds typically half the melting point (expressed in Kelvin [58]), thermal activation effects become noticeable. The motion of dislocations becomes thermally assisted (dislocation creep) and strain may also be achieved by diffusion of atoms, either in the bulk (Nabarro-Herring creep) or through grain boundaries (Coble creep). All of these mechanisms lead to a strain that depends not only on stress but also on time (at constant stress, strain may still change). These time-dependent deformation mechanisms will be referred to as viscoplastic and the viscoplastic strain will be noted $\boldsymbol{\epsilon}^{vp}$. When the temperature is high enough, dynamic recovery effects may also prevent work hardening. As a consequence, in such a regime, the stress becomes a function of the viscoplastic strain rate $\dot{\boldsymbol{\epsilon}}^{vp}$ alone. This aspect is discussed in details in Section 2.3.3.

[5] please note that this may not be true for some other problems, e.g. in soil mechanics [57].

At intermediate temperature, the distinction between plastic and viscoplastic deformation is not very clear. The stress will thus depend on both strain and strain rate. Please note that the description of the mechanical behavior of the alloy at different temperature shall be addressed in further sections.

In conclusion, let us summarize how castings should be considered from a thermomechanical point of view. In general, the solidification process induces thermal gradients in the part. Moreover, the process sometimes constrains the displacement of the boundaries of the cast (mold). This leads to thermal strain gradients which must be accommodated by inhomogeneous inelastic and elastic strains. The elastic strains can be used to calculated the stress (using Hooke's law). This is possible only when the inelastic strains are described as a function of stress. Such problems are thus non-linear and may involve complex geometries. As a consequence, their resolution can only be carried out using appropriate numerical methods.

### 2.3.2 Two-Phase Approach

The framework described in the preceding section has to be adapted when dealing with alloys in the mushy state. Let us first remind that the mushy zone is considered to be a two-phase mixture consisting of both solid and liquid. If any vapor phase (e.g. pores) is formed, it will be neglected from the point of view of momentum conservation. This is a satisfactory assumption for the problems of interest in the present work.

Similarly to what was done in Section 2.2.1, averaging concepts will be applied to momentum conservation. In a quasi-static case, the momentum conservation expressed in Equation (2.18) can be averaged in each phase :

$$\frac{1}{\Omega_0}\int_{\Omega_0} X_\nu \left[\nabla\cdot\boldsymbol{\sigma}+\rho\mathbf{g}\right]\mathrm{d}V = 0 \tag{2.32}$$

After using the mathematical properties of averages and introducing again simplified notations $\langle\boldsymbol{\sigma}_\nu\rangle^\nu \equiv \boldsymbol{\sigma}_\nu$, the following is obtained [50] :

$$\nabla\cdot(g_s\boldsymbol{\sigma}_s)+g_s\rho_s\mathbf{g} = \mathbf{M}_s \tag{2.33}$$

$$\nabla\cdot(g_l\boldsymbol{\sigma}_l)+g_l\rho_l\mathbf{g} = \mathbf{M}_l \tag{2.34}$$

In these expressions, $\mathbf{M}$ represents the momentum transfer at the solid-liquid interface. Please note that the momentum transfer due to phase change is neglected in this case. For the liquid phase, Equation (2.34) may be rewritten using $\boldsymbol{\sigma}_l = -p_l\mathbf{I}$ where $p_l$ is the pressure experienced by the liquid phase.

$$-g_l\nabla p_l + g_l\rho_l\mathbf{g} = \mathbf{M}_l + p_l\nabla g_l \tag{2.35}$$

By introducing Darcy's law (Equation (2.12), where $\mu$ is the viscosity of the liquid) and thus taking into account viscous forces at the solid-liquid interface, the momentum transfer term can be expressed :

$$\frac{\mu g_l^2}{K}\left(\mathbf{v}_l-\mathbf{v}_s\right) = \mathbf{M}_l + p_l\nabla g_l \tag{2.36}$$

As a consequence, for the liquid (assuming mechanical equilibrium at the solid-liquid interface), momentum conservation will be given by :

$$-g_l\nabla p_l + g_l\rho_l\mathbf{g} = \frac{\mu g_l^2}{K}\left(\mathbf{v}_l-\mathbf{v}_s\right) \tag{2.37}$$

Moreover, in the two-phase medium, any momentum transferred to the solid at the solid-liquid interface must come from the liquid. As a consequence, $\mathbf{M}_s = -\mathbf{M}_l$ and the solid momentum conservation (Equation (2.33)) may take this fact into account :

$$\nabla \cdot (g_s \boldsymbol{\sigma}_s) + g_s \rho_s \mathbf{g} = -\frac{\mu g_l^2}{K} (\mathbf{v}_l - \mathbf{v}_s) + p_l \nabla g_l \tag{2.38}$$

Please note that that the properties of the solid-liquid interface are neglected in this expression.

Equations (2.37) and (2.38) can now be added. After simplification, the expression of this sum becomes :

$$\nabla \cdot (g_s \boldsymbol{\sigma}_s - g_l p_l \mathbf{I}) + \overline{\rho} \mathbf{g} = 0 \tag{2.39}$$

where $\boldsymbol{\sigma} = g_s \boldsymbol{\sigma}_s - g_l p_l \mathbf{I}$ is the mixture stress, which is the quantity that can be measured experimentally.

A coherent mushy zone consists of a solid skeleton filled with liquid. From that point of view it is similar to a saturated porous medium. In dense metals, the von Mises criterion takes into account the fact that plastic deformation is not due to the isostatic stress contribution. Similarly, in porous media, it is well known that the pressure in the liquid phase $p_l$ does not alter the inelastic behavior of the two-phase material. As a consequence, it is usually more relevant to consider the effective stress $\hat{\boldsymbol{\sigma}}$ instead of the total stress $\boldsymbol{\sigma}$. The contribution of liquid pressure is basically removed from the total stress in theoretical considerations (while $\boldsymbol{\sigma}$ remains the value measured in experiments). If the matrix consists of an incompressible solid (as is the case in mushy alloys), the effective stress[6] may be defined as [57] :

$$\hat{\boldsymbol{\sigma}} = \boldsymbol{\sigma} + p_l \mathbf{I} \tag{2.40}$$

Having introduced this concept, it is relevant to rewrite the momentum conservation (Equation (2.39)) as a function of the effective stress [1] :

$$\nabla \cdot \hat{\boldsymbol{\sigma}} + \overline{\rho} \mathbf{g} = \nabla p_l \tag{2.41}$$

### 2.3.3 Strains in the Mushy Zone

In Section 2.3.2, the way to treat correctly momentum conservation in a mushy zone was established. It is thus now necessary to consider other specificities of mushy alloys, i.e. how strains $\boldsymbol{\epsilon}^{el}$, $\boldsymbol{\epsilon}^{th}$ and $\boldsymbol{\epsilon}^{ie}$ are described for solidifying alloys.

#### Elastic and Thermal Contributions

First of all, let us consider the elastic behavior of the mushy zone. Above the coherency temperature $T^{coh}$, the behavior is essentially liquid-like and very little elasticity is found in the mushy alloy. The coherent mushy zone (below $T^{coh}$) will bear elastic stresses and related strains as given by Equation (2.22). The elastic modulus $E$ will typically be rather low in a mushy system and vary strongly with $g_s$. The value of $\boldsymbol{\epsilon}^{el}$ is thus quite straightforward to consider in theoretical developments. However, it is necessary to keep in mind the fact that it is not trivial to measure $E$ experimentally at such high temperatures.

[6] please note that the pressure in the liquid phase $p_l$ is different from the pressure in the solid phase $P_s$ due to capillarity, liquid flow and deviatoric stress components normal to the solid-liquid interface.

The thermal contraction behavior of mushy alloys must also be examined carefully. As was already mentioned, the inhomogeneous thermal strain $\boldsymbol{\epsilon}^{th}$ (or strain rate $\dot{\boldsymbol{\epsilon}}^{th}$) is responsible for the stress build-up in castings. If a sufficiently large amount of liquid is present in a mushy alloy, the thermal contraction may be accommodated by liquid flow around the solid grains, which can contract without changing the position of their center of mass [59]. In other words, the local volume change due to cooling can be compensated by feeding. In such a case, no significant stress will arise in the material. On the other hand, when the network of solid grains becomes entangled enough, the inhomogeneous thermal strain cannot be compensated by mass feeding and stresses will be found in the material.

This is important for modeling solidification processes because it means that $\boldsymbol{\epsilon}^{th}$ should be neglected if the temperature is high enough. Moreover, experimental studies of this problem have been conducted by Stangeland *et al* [59, 60]. These authors have solidified alloys in a mold designed such that one side of the sample is fixed and the other is attached to a moving block. This block will start moving only when both ends of the sample are connected by a ligament with a high enough solid fraction (this ligament contracts upon cooling and is resistent enough to cause motion of the block). This experiment allows determining the critical solid fraction $g_s^{th}$ above which thermal strains will indeed cause stress. In order to account for this, it is necessary to express the thermal strain rate $\dot{\boldsymbol{\epsilon}}^{th}$ as:

$$\dot{\boldsymbol{\epsilon}}^{th} = \Psi\left(g_s\right)\alpha^{th}\dot{T}\mathbf{I} \tag{2.42}$$

The $\Psi$ function describes the onset of thermal strain in the material. In general, the following expression was proposed for $\Psi$ [60]:

$$\Psi\left(g_s\right) = \begin{cases} 0 & \text{for} \quad g_s \leq g_s^{th} \\ \left(\frac{g_s - g_s^{th}}{1 - g_s^{th}}\right)^{\eta} & \text{for} \quad g_s > g_s^{th} \end{cases} \tag{2.43}$$

Experimental results show that, for most of the tested alloys, $\eta = 0$. As a consequence, it is simpler to use $\Psi = 1$ for $g_s > g_s^{th}$ and 0 if $g_s \leq g_s^{th}$, as will be done in the present work. The value of $g_s^{th}$ depends on various factors such a cooling rate, grain refining and alloy composition [61]. Experimental values are in the range $0.63 \leq g_s^{th} \leq 0.94$ [60] and a value of $g_s^{th} = 0.8$ is quite often found.

### Rheology

The most difficult problem is describing the inelastic strain. First of all, as was defined in Section 2.1.3, above the coherency temperature (i.e. for $g_s < g_s^{coh}$) the mushy alloy has a liquid-like behavior. In this regime, the material deforms extremely easily without bearing any significant tensile stress. Experimental evidence [2] suggests that $g_s^{coh}$ is typically of the order of 65%.

The coherent mushy zone ($g_s \geq g_s^{coh}$) is much more interesting. By definition, the homologous temperature ($T_{[\mathrm{K}]}/T_{[\mathrm{K}]}^{melting}$) is very high in this region. As a consequence, pure plasticity is not active and only viscoplastic deformation must be considered: $\dot{\boldsymbol{\epsilon}}^{ie} = \dot{\boldsymbol{\epsilon}}^{vp}$. In this regime, the stress is related to the strain rate. Ludwig and coworkers [2] have proposed a model to describe the rheology of the coherent mushy zone. This model is derived under the assumption of small strain and strain rate and considers the mushy zone as a two-phase medium continuous and isotropic. It is thus suitable for applications at the scale of an entire solidification process.

This model is built considering the viscoplastic potential $\mathcal{G}$ as a function of the effective stress $\hat{\boldsymbol{\sigma}}$. The deviatoric effective stress $\hat{\mathbf{S}}$ and the invariants $\hat{P}_s$ and $\hat{\sigma}_M$ are straightforward to obtain.

Please note that $\hat{\boldsymbol{\sigma}} = \boldsymbol{\sigma}$ in a fully solidified material. The viscoplastic potential $\mathcal{G}$ is defined by its normality property :

$$\dot{\boldsymbol{\epsilon}}^{vp} = \frac{\partial \mathcal{G}}{\partial \hat{\boldsymbol{\sigma}}} \tag{2.44}$$

Moreover, it is known that, for a fully solidified material, creep can be described using a power law :

$$\dot{\boldsymbol{\epsilon}}^{vp} = \frac{3}{2}\dot{\epsilon}_0 \frac{\hat{\sigma}_M^{n-1}}{s_0}\hat{\mathbf{S}} \tag{2.45}$$

where $\dot{\epsilon}_0 = A\exp\left(-\frac{Q}{RT}\right)$ is the thermally activated coefficient. This means that the material parameters $A$, $Q$, $s_0$[7] and $n$ describe the rheology of the fully solid phase. This expression can be rewritten in terms of the solid phase viscoplastic potential $\mathcal{G}^0$ [2] :

$$\mathcal{G}^0 = \frac{\dot{\epsilon}_0 s_0}{n+1}\left(\frac{\hat{\sigma}_M}{s_0}\right)^{n+1} \tag{2.46}$$

The next step is to assess the first effect of the presence of a liquid phase. If the liquid were to be found in isolated pockets, the properties of the material would change because the reduced solid fraction leads to a decrease in load bearing capacity. This is taken into account by multiplying $\mathcal{G}^0$ by a softening function $\mathcal{S}$. A relatively simple expression for $\mathcal{S}$ was taken in [2] :

$$\mathcal{S}\left(X, g_s\right) = \left(A_2\left(g_s\right)X^2 + A_3\left(g_s\right)\right)^{\frac{n+1}{2}} \quad \text{with} \quad X = \frac{\hat{P}_s}{\hat{\sigma}_M} \tag{2.47}$$

In this expression, the stress triaxiality $X$ is introduced and closing relations for $A_2$ and $A_3$ are :

$$\begin{aligned} A_2 &= \tfrac{9}{4}\left\{n\left(\left(1-g_s\right)^{-\frac{1}{n}} - 1\right)\right\}^{-\frac{2n}{n+1}} \\ A_3 &= \left(1 + \tfrac{2}{3}\left(1-g_s\right)\right)\cdot g_s^{-\frac{2n}{n+1}} \end{aligned} \tag{2.48}$$

In real mushy alloys however, the liquid is distributed between the grains. Even at a low liquid fraction ($g_l = 1 - g_s$) the liquid phase is indeed not found in isolated pockets but in a network of intergranular liquid films. As a consequence, the other effect of the liquid phase is that, in addition to decreasing the load bearing area, it disturbs the cohesion of the material. This means that macroscopic strains imposed to the casting are not going to be fully transmitted among the grains (at the microscopic level) [62]. To take this into account, an internal variable $C$, referred to as the cohesion, is introduced in the model. For grains floating freely in liquid (mushy zone above the coherency temperature), there is no cohesion : $C = 0$. On the other hand, in a fully coalesced solid skeleton (liquid is only found in isolated pockets), the cohesion is complete and $C = 1$ [2].

At this stage, the viscoplastic potential $\mathcal{G}$ may be expressed taking into account both the effects detailed above :

$$\mathcal{G} = \mathcal{G}^0\frac{\mathcal{S}}{C^n} \Leftrightarrow \mathcal{G} = \frac{\dot{\epsilon}_0}{\left(n+1\right)\left(Cs_0\right)^n}\left(A_2\hat{P}_s^2 + A_3\hat{\sigma}_M^2\right)^{\frac{n+1}{2}} \tag{2.49}$$

The normality rule given in Equation (2.44) can be applied using this expression to obtain the constitutive law for viscoplastic strain in a coherent mushy zone [2] :

$$\dot{\boldsymbol{\epsilon}}^{vp} = \frac{\dot{\epsilon}_0}{\left(Cs_0\right)^n}\left(-\frac{A_2}{3}\hat{P}_s\mathbf{I} + \frac{3A_3}{2}\hat{\mathbf{S}}\right)\left(A_2\hat{P}_s^2 + A_3\hat{\sigma}_M^2\right)^{\frac{n-1}{2}} \tag{2.50}$$

[7] $s_0$ is constant, which takes into account the experimentally verified fact that strain hardening is negligible at high temperature

The shape of the iso-$\mathcal{G}$ values in the $\hat{\sigma}_M$-$\hat{P}_s$ plane for a constant value of $C$ corresponding to different $g_s$ is illustrated on the left of Figure 2.7. As these iso-lines are elliptic and symmetrical with respect to $\hat{P}_s$, they are similar to those obtained for the plastic potential proposed by Gurson and Tvergaard to describe yielding of porous metals [63]. On the other hand, their symmetry predicts the same behavior in tension and compression. This is different from the plastic potential defined in the Cam clay model [64], which is very classical in soil mechanics.

In order to describe the partial cohesion of the mushy zone, the internal variable $C$ was introduced. The model is thus only complete if an evolution equation is provided for this variable. Ludwig *et al* [2] proposed to describe the variation of $C$ by modeling the fact that cohesion can be created or lost through straining of the material (pulling the solid skeleton together or apart). For this, they introduced a function $\alpha\left(g_s, X\right)$ that describes how $C$ varies at small strain and a function $C^*\left(g_s, X\right)$, which is a saturation value towards which the cohesion will tend for larger strains. These variations can only occur under macroscopic strain[8] [2], which is quantified by the equivalent viscoplastic strain $\dot{\epsilon}_e = \sqrt{\frac{2}{3}\dot{\boldsymbol{\epsilon}}^{vp} : \dot{\boldsymbol{\epsilon}}^{vp}}$:

$$\frac{\mathrm{d}C}{\mathrm{d}t} = \alpha\left(g_s, X\right)\left(1 - \frac{C}{C^*\left(g_s, X\right)}\right)\dot{\epsilon}_e \tag{2.51}$$

If the cohesion $C$ is assumed to be equal to $C^*\left(g_s, X\right)$, the iso-$\mathcal{G}$ values can be plotted again, as shown on the right of Figure 2.7. In this case, the model is no longer symmetrical in tension and in compression. In real situations, the value of $C$ will evolve towards $C^*$ at a finite rate. As a consequence, an iso-$\mathcal{G}$ line will have no sharp corner but its exact shape will depend upon the loading history.

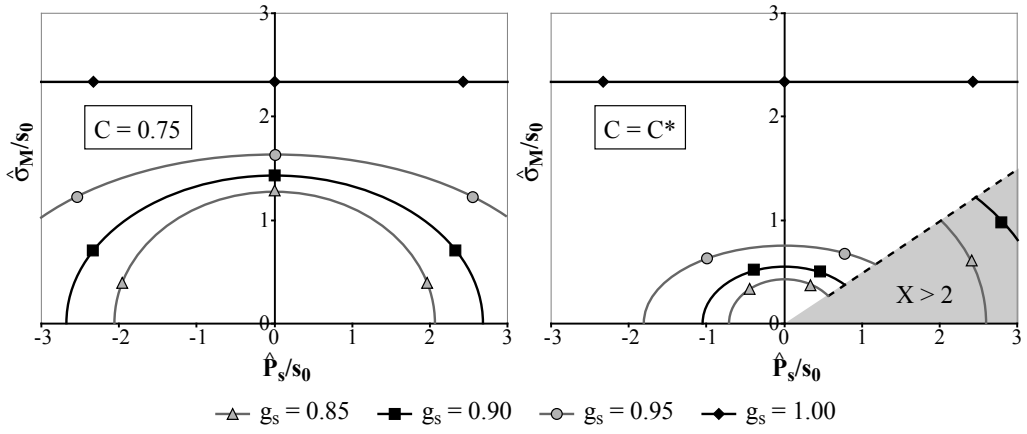


**Figure 2.7:** Adapted from [65]. Isovalues corresponding to $\mathcal{G} = 0.042 s_0$ at different solid fractions, for $C = 0.75$ on the left and when $C$ tends rapidly towards $C^*$ on the right.

Using tensile, compression and shear tests, these authors could identify experimentally these rheological parameters as a function of solid fraction and stress state (characterized by $X$). In compression ($X > 2$), the cohesion will always tend to 1 due to compaction of the solid skeleton. On the other hand, to describe the sharp increase of tensile ($X < 0$) strength at the last stage

[8] the cohesion depends on the loading history and causes the strength of the material to depend not only on strain rate but also on some fraction of the strain ($C$ dictates the mechanical properties of the mushy alloy and is the integral over time of a strain rate-related quantity).

of solidification, the coalescence point $g_s^{coal}$ was introduced [2]:

$$\left.\begin{array}{rcl} C^*\left(g_s, X \leq 2\right) & = & 1-\left(1-g_s\right)^p \\ C^*\left(g_s, X > 2\right) & = & 1 \\ C^*\left(g_s \leq g_s^{coh}, X\right) & = & 0 \end{array}\right\} \tag{2.52}$$

$$\left.\begin{array}{rcl} \alpha\left(g_s, X < 0\right) & = & \alpha_0 + \alpha_1 \frac{g_s^{\frac{1}{3}}}{1-g_s^{\frac{1}{3}}} \exp\left(k\left(g_s - g_s^{coal}\right)\right) \\ \alpha\left(g_s, X \geq 0\right) & = & \alpha_0 + \alpha_1 \frac{g_s^{\frac{1}{3}}}{1-g_s^{\frac{1}{3}}} \\ \alpha\left(g_s \leq g_s^{coh}, X\right) & = & 0 \end{array}\right\} \tag{2.53}$$

All the parameters that appear in these equations have been determined experimentally and the model was validated on separate experimental data [2, 66]. The agreement obtained between the prediction of the model and tensile experiments is illustrated on Figure 2.8 from [2].

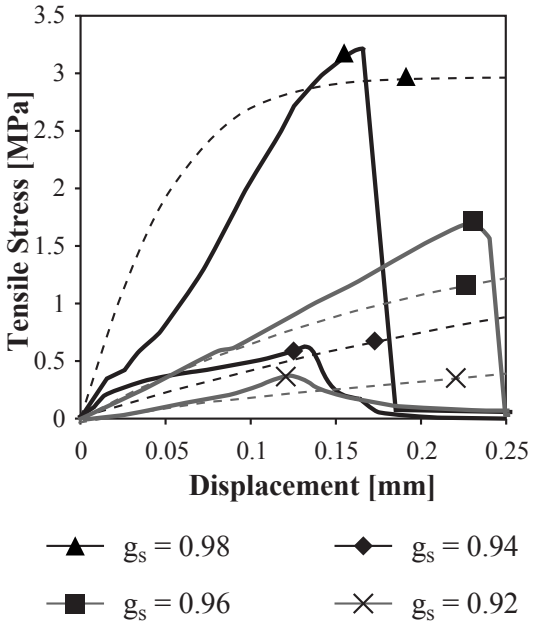


**Figure 2.8:** Redrawn from [2]. Load displacements curves measured in tension as a function of the minimum solid fraction in the Al-Cu sample. The validity of the model (thin dashed lines) is verified against experimental measurements (thicker lines).

The model presented in this section describes the mechanical behavior of a mushy alloy. It captures very important features of the mushy zone:

- The partial cohesion, i.e. the incomplete transmission of strain, in the mushy zone is accounted for. This is introduced through an internal variable and the description of its evolution.
- The behavior of the mushy zone depends on the stress state (the onset of viscoplastic deformation is different in tension and in compression). Even though the expression of the viscoplastic potential $\mathcal{G}$ (Equation (2.49)) is symmetrical with respect to solid pressure $\hat{P}_s$,

this fact is captured in Equation (2.52). The cohesion will indeed vary as a function of the stress state. This represents the dependence of the properties upon the stress state and has the advantage of keeping a relatively simple expression[9] for $\mathcal{G}$.

– The mushy zone is a compressible medium, as it may undergo permanent deformation under isostatic loading. Even though the solid and liquid phase are incompressible, their mixture will become compressible. This is due to the fact that these phases have very different mechanical behaviors. Isostatic stress may then squeeze liquid in or out of the solid skeleton, which behaves like a sponge. This effect leads to a local variation of the solid fraction. This compressibility is specific to the mushy zone since the fully solidified alloy is incompressible (i.e. $\dot{\boldsymbol{\epsilon}}^{vp}\,(g_s = 1)$ has no isostatic component).

Please note however that the effect of the mushy zone morphology (columnar, equiaxed or globular solid grains) is not very detailed (beyond the solid fraction dependence) in this model. It is expected that the shape of the solid network will have an effect. For example, a recent study [68] indicates that adding barium to aluminum-copper alloys delays coalescence and alters the development of tensile strength.

In Equation (2.50), the compressibility of the mushy zone appears since the viscoplastic strain $\dot{\boldsymbol{\epsilon}}^{vp}$ is dependent not only on the deviatoric effective stress $\hat{\mathbf{S}}$ but also on the effective pressure $\hat{P}_s$, which appears in an hydrostatic term (proportional to $\mathbf{I}$). In further considerations, we shall distinguish between two inelastic strain components. On the one hand, $\dot{\epsilon}_{sw} = \frac{1}{3}\mathrm{tr}\,(\dot{\boldsymbol{\epsilon}}^{vp})$ denotes the volumetric strain (the *sw* subscript stands for *swelling*). On the other hand, $\dot{\epsilon}_{cr}$ refers to standard viscoplastic deformation (known in solids, the *cr* subscript stands for *creep*), which progresses at constant volume. This may be taken into account by rewriting Equation (2.50) under the following form.

$$\begin{aligned}
\dot{\epsilon}_{sw} &\equiv -\tfrac{A_2\hat{P}_s}{3}\tfrac{\dot{\epsilon}_0}{(Cs_0)^n}\left(A_2\hat{P}_s^2 + A_3\hat{\sigma}_M^2\right)^{\frac{n-1}{2}} \\
\dot{\epsilon}_{cr} &\equiv \hat{\sigma}_M A_3\tfrac{\dot{\epsilon}_0}{(Cs_0)^n}\left(A_2\hat{P}_s^2 + A_3\hat{\sigma}_M^2\right)^{\frac{n-1}{2}} \\
\dot{\boldsymbol{\epsilon}}^{vp} &= \dot{\epsilon}_{sw}\mathbf{I} + \tfrac{3}{2}\tfrac{\dot{\epsilon}_{cr}}{\hat{\sigma}_M}\hat{\mathbf{S}}
\end{aligned} \tag{2.54}$$

In order to be thorough on alloys rheology, it is still necessary to consider how fully solidified alloys may be described. In casting processes, stresses are indeed mainly built-up in the solid phase and transmitted partially to the coherent mushy zone. Since the model of the mushy zone is built starting from the fully solid viscoplastic potential, it can actually model the behavior of a solid (i.e. $g_s = 1$, $p_l = 0$ and $C = 1$). In such a case, this model reduces to :

$$\dot{\boldsymbol{\epsilon}}^{vp} = \frac{3}{2}\frac{\dot{\epsilon}_{cr}}{\sigma_M}\mathbf{S} \quad \text{with} \quad \dot{\epsilon}_{cr} = \frac{\dot{\epsilon}_0}{s_0^n}\sigma_M^n \quad (\dot{\epsilon}_{sw} = 0) \tag{2.55}$$

This equation is well adapted to modeling the solid phase behavior above typically 400 °C at low strain rates [69]. At lower temperatures, dynamic recovery is no longer fast enough to prevent work hardening. As a consequence, the stress response of the material should depend on both the inelastic strain rate and accumulated inelastic strain. In that case, it is more customary to introduce a generalized Ludwik's model [69–71] :

$$\sigma_M = \kappa\,(T)\,\epsilon_{cr}^{\eta(T)}\left(\frac{\dot{\epsilon}_{cr}}{\dot{\epsilon}_u}\right)^{\lambda(T)} \quad \text{with} \quad \epsilon_{cr} = \int_{t(T\leq T_\epsilon)}^{t}\dot{\epsilon}_{cr}\mathrm{d}t \quad \text{and} \quad \dot{\epsilon}_u = 1\ \mathrm{s}^{-1} \tag{2.56}$$

[9] the difference between tensile and compressive stress states may also be incorporated in the expression of $\mathcal{G}$. See e.g. [65, 67] for details.

where the cumulated strain $\epsilon_{cr}$ can increase only below the temperature $T_\epsilon$, i.e. when strain hardening effects become significant. Moreover, $\kappa(T)$, $\eta(T)$ and $\lambda(T)$ are alloy dependent parameters to be determined experimentally.

## 2.4 Hot Tearing : Mechanisms, Observations and Models

### 2.4.1 Hot Tearing Mechanisms

When an alloy is torn in the mushy state, the fracture surface has a smooth appearance that reveals the dendritic or globular features of the solid grains, as illustrated on Figures 1.4 (page 8) and 4.3 (page 65). When studied more closely, the failure surface exhibits specific features that were observed by Farup *et al* [72], as can be seen on Figure 2.9.

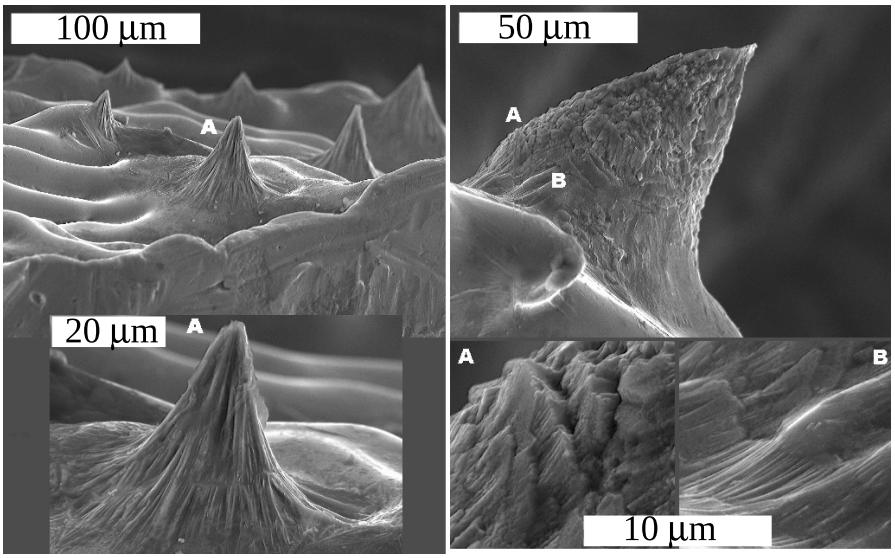


**Figure 2.9:** Details of a torn surface [72]. Spikes (left) are liquid menisci that were broken before solidifying and bridges (right) are solid intergranular bonds that were deformed and broken during hot tearing.

For this purpose, these authors used in-situ observation of transparent alloys. There exists indeed some organic alloys that behave like metals from the microstructure formation point of view (e.g. the succinonitrile-acetone system). However, these systems are transparent and the solidification of thin samples under strain may thus be observed in an optical microscope [72, 73].

When the strain is applied to the mushy zone at relatively low solid fraction, liquid flows from the fully liquid region into the intergranular opening (which is due to strain). This situation corresponds to what is known as a healed hot tear. Nucleation of new grains and bubbles is possible but hot tearing does not occur in such conditions (see Figure 2.10).

If strain is applied to a region with a higher value of $g_s$, the separation between the grains that are pulled apart cannot be compensated by liquid feeding (due to the low permeability). A void is thus created between the grains and this situation corresponds to hot tearing (see Figure 2.11).

During hot tearing the propagation of a hot tear between two grains, two phenomena should be distinguished. On one hand, if solid bridges exist due to local coalescence of the two grains,

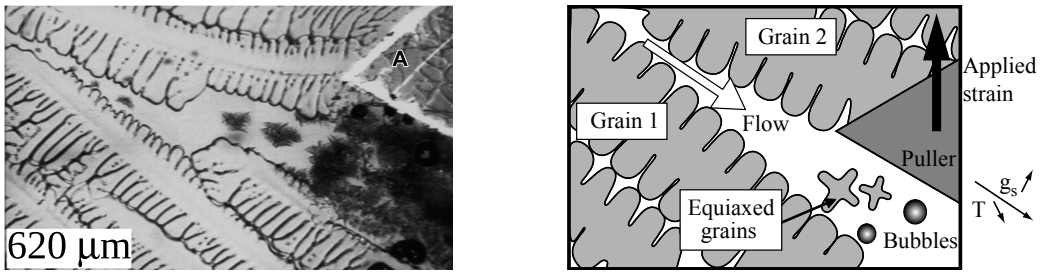


**Figure 2.10:** Healed hot tear : (a) observation in a transparent alloy (b) schematic representation of liquid flow in the intergranular opening [72].

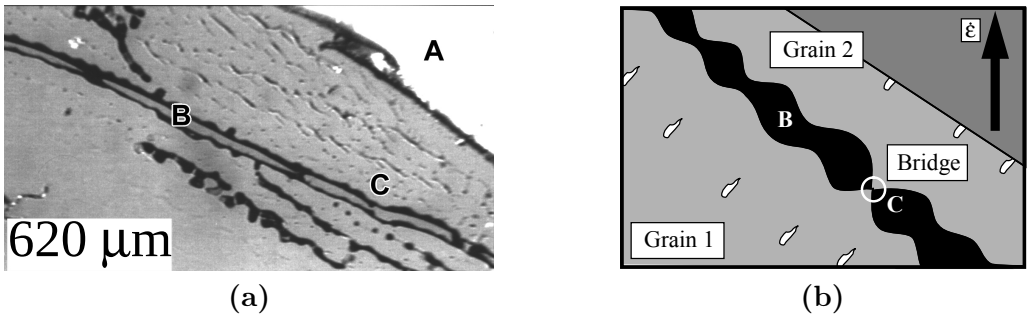


**Figure 2.11:** Bridging : (a) observation in a transparent alloy (b) schematic representation of a solid bridge being broken during propagation of the hot tear (in black) between the solid grains, due to the applied strain [72].

they may be deformed and broken during tear growth. These broken bridges, will be left behind on the fracture surface. Such a mechanism is observed on Figure 2.11 from [72]. It corresponds to what is observed on a real fracture surface as shown on the right on Figure 2.9. Such a bridge indeed exhibits a surface structure that is characteristic of deformation in the solid state.

On the other hand, when a hot tear advances, the remaining intergranular liquid tends to be concentrated in liquid menisci between the two grains. Under strain, such a meniscus may be broken before being solidified. In that case, we shall say that a spike is left behind on the fracture surface. This mechanism is illustrated on Figure 2.12 from [72]. It is what is observed on real fracture surfaces as illustrated on the left on Figure 2.9. A spike has a draped appearance indicating that it was broken in the liquid state before being solidified.

It is important to distinguish between bridges and spikes because bridges are indicators of local intergranular coalescence. On the other hand, spikes will exist also between grains that are not yet linked together by any solid phase.

Please note that direct observations techniques were also designed to observe metallic alloys subjected to tensile loads. In such a case, the specimen is not transparent to visible light. As a consequence, X-rays are more suitable to study what happens within a metallic sample. Radiography is the classical method in which X-rays are used. Recently, Davidson *et al* [74] used this technique to observe the onset and development of hot tears in their experimental setup . Theses authors came to the conclusion that hot tears were initiated for $g_s = 93\%$ in Al-0.5wt%Cu alloys.

More recently, X-ray tomography (by taking several X-ray images of a rotating sample, a 3D reconstruction can be obtained [75]) was also applied to study hot tearing. For example,

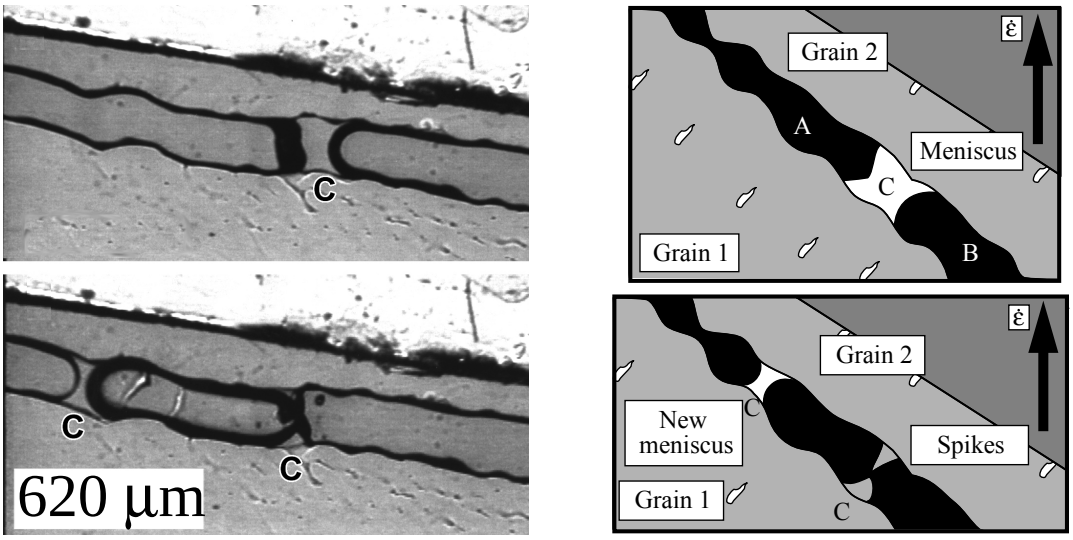


**Figure 2.12:** Spikes : (a) observation in a transparent alloy (b) schematic representation of a liquid meniscus being broken during propagation of the hot tear (in black) between the solid grains, due to the applied strain [72].

Phillion *et al* [76] could study damage accumulation in a tensile sample of an AA5182 alloy at high solid fraction ($g_s \sim 98\%$). They showed that strain is initially mainly accommodated by cross-sectional area reduction. At higher strain the amount of damage increased both by growth of pre-existing microporosity and by nucleation of new voids. If the strain becomes high enough, voids will start to merge, leading to failure of the sample.

All of this experimental evidence indicates that hot tearing is a phenomenon that occurs in the mushy zone, for high solid fractions and under strain. At this stage, it is possible to provide a qualitative explanation of what is expected to happen when a hot tear forms. The physical mechanisms proposed to explain hot tearing are generally well accepted [1, 29, 37, 77].

As suggested by Figure 2.13, hot tearing occurs in the mushy zone, at a rather high solid fraction. At this stage, the solid grains are surrounded by thin liquid films, which form a continuous network. Moreover, the mushy alloy has already developed a significant cohesion, which means that strains from the solid shell underneath are transmitted to this region of the material.

As was already mentioned, the pressure in the liquid $p_l$ is low deep in the mushy zone. The conjunction of this low pressure with strain may lead to the nucleation of a void in the liquid phase. This process is not trivial and may not occur, in which case a tear-free casting is obtained. Understanding the conditions for tear nucleation is thus the first challenge for predicting hot tearing.

If a void has nucleated in the liquid, this void may grow under the strain still transmitted to that specific location in the mushy zone. The second challenge in hot tearing modeling is to understand the conditions for the growth of a small void into an extended hot tear. There are indeed two possibilities for the void to evolve. On one hand, if the permeability of the mushy zone is sufficient, liquid alloy may flow into this void and fill it. The tear is then said to be healed (i.e. filled with liquid). This can be experimentally observed because the healing liquid is often more solute-rich than the surroundings, which lead to a measurable local segregation.

On the other hand, if healing cannot occur (because $K$ is too small) the tear is likely to grow.

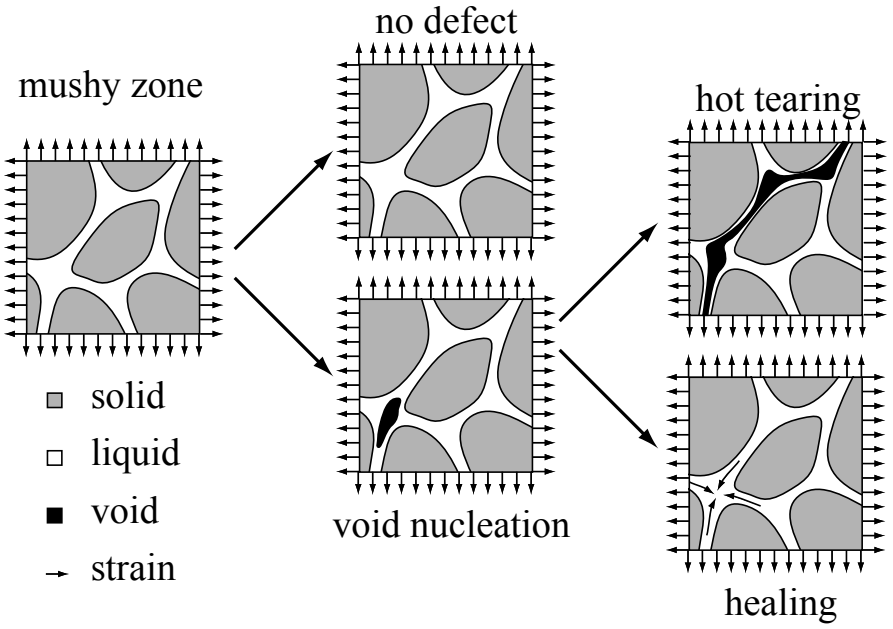


**Figure 2.13:** Schematic representation of the conditions required for hot tearing to occur : applied strain on a mushy alloy at a high solid fraction (i.e. with low permeability) may lead to nucleation and growth of a hot tear. If feeding is sufficient, the strain-induced opening of the solid skeleton can be compensated by liquid flow, leading to what is known as a "healed" hot tear.

The strain rate imposed by the solid shell will indeed tend to be concentrated in the intergranular liquid films and at the tip of the tear. Locally, the strain rate will thus become very large and promote tear growth. The growth of the tear cannot occur in a coalesced materials, i.e. in the absence of a continuous liquid film network (because solid bonds between grains are much more difficult to break). Moreover, the tear cannot propagate into a relatively high permeability region (healing will occur at the tip). Despite these limitations, tear growth can easily lead to fracture of a tensile sample or to meter-long tears in DC cast ingot (where the tip of the crack may follow the traveling mushy zone on a long distance). Having considered these mechanisms, it seems that strain (or strain rate) is more likely to drive the hot tearing process while stresses would be of secondary importance.

At this stage, it is relevant to make a few comments about porosity, which is a defect that is closely related to hot tearing. Typically, hot tears are expected to develop in the range $g_s = 90 - 95\%$, when permeability is low, strain rate is high and continuous liquid films still exist. On other hand, microporosity formation may start when $g_s \approx 80\%$ because the liquid pressure drop becomes significant. As a consequence, pores may exist before the conditions for hot tearing are met. Qualitatively, this pre-existing porosity may have two interactions with hot tearing. On the one hand, pores are basically voids and may thus serve as nuclei for tears. On the other hand, when porosity forms, the pressure in the liquid tends to drop less than in a pore free liquid. From that point of view, porosity may hinder tear growth by enhancing liquid flow at the tip of the crack. If the pore fraction $g_p$ becomes very high, pore coalescence may also become a tear growth mechanism. This means that the interaction between hot tearing and porosity may be important in some situations but is not simple to describe and predict.

### 2.4.2 Hot Tearing Tests

Qualitatively, the mechanisms that play a role in the hot tearing phenomenon have been described in the preceding section. However, these considerations do not give much quantitative information about hot cracking. The aim of the present section is thus to present the ongoing effort to characterize hot tearing from a quantitative point of view. This has been a research topic for more than fifty years and is not yet exhausted. It is indeed very complicated to design experimental tests in which hot tearing can be measured in a reliable manner. Moreover, it is desired that the results of these tests may be either directly applied to real castings or incorporated into theoretical models. Therefore, they must correspond to the casting conditions encountered in daily casthouse practices.

Hot tearing tests basically consists of monitoring the behavior of a mushy alloy in which significant stresses develop in the coherent region. Typically, a small region that is hotter (i.e. weaker) than the rest of the sample (hot spot) is generated so that tears are localized due to concentration of strains in the hot spot. Moreover, this hot spot is usually connected to a liquid region so that feeding may occur under favorable conditions. In general, a measure of the hot tearing susceptibility (often noted HCS[10]) is studied as a function of the materials or process parameters. The definition of the HCS is not unique and is one of the first difficulties that arise when trying to design a new hot tearing test. In the present section, we shall give a few examples of the most classical tests. A more complete review may be found in [78].

#### Ring Mold Tests

The principle of the ring mold test is to use a cylindrical mold with a cylindrical core to obtain a ring shaped casting [78]. Stresses arise upon solidification because the metal will shrink around the rigid core. The hindered contraction may cause hot tears. In this case, the HCS would typically be measured by the length of the observed tears. An example of such a test was performed by Drezet *et al* [79]. In this version, the core was water-cooled and both hoop and radial tears were observed.

The advantage of a ring mold test is that it is relatively easy to use as a model system in numerical calculations (due to its axisymmetry). On the other hand, it is not very easy to control the cooling conditions, and thus the applied strain.

#### Cold Finger Tests

The cold finger test [80, 81] is quite similar to ring mold tests. The liquid alloy is contained in a crucible. The test consists of inserting a water-cooled chill in the melt (see Figure 2.14a). This will cause the melt to solidify around this "finger". Moreover, thermal contraction around the conical and rigid chill will induce strains that may lead to hot tearing. These strains are concentrated in a hot spot extended along the finger and generated by reducing locally the cooling from the chill (a layer of graphite is painted on the finger). Tears will be found first at the top of the hot spot, were temperature and the radius of the finger are maximum. They will propagate down on some length. This length is used as a measure of the HCS.

As shown on Figure 2.14b, these authors could measure the $\lambda$-curve for Al-Cu [80]. This means that the hot tearing susceptibility of an alloy is dependent upon its concentration. In

[10]HCS stands for hot cracking susceptibility. This is the most widely used abbreviation to denote the tendency of a mushy alloy to get torn.

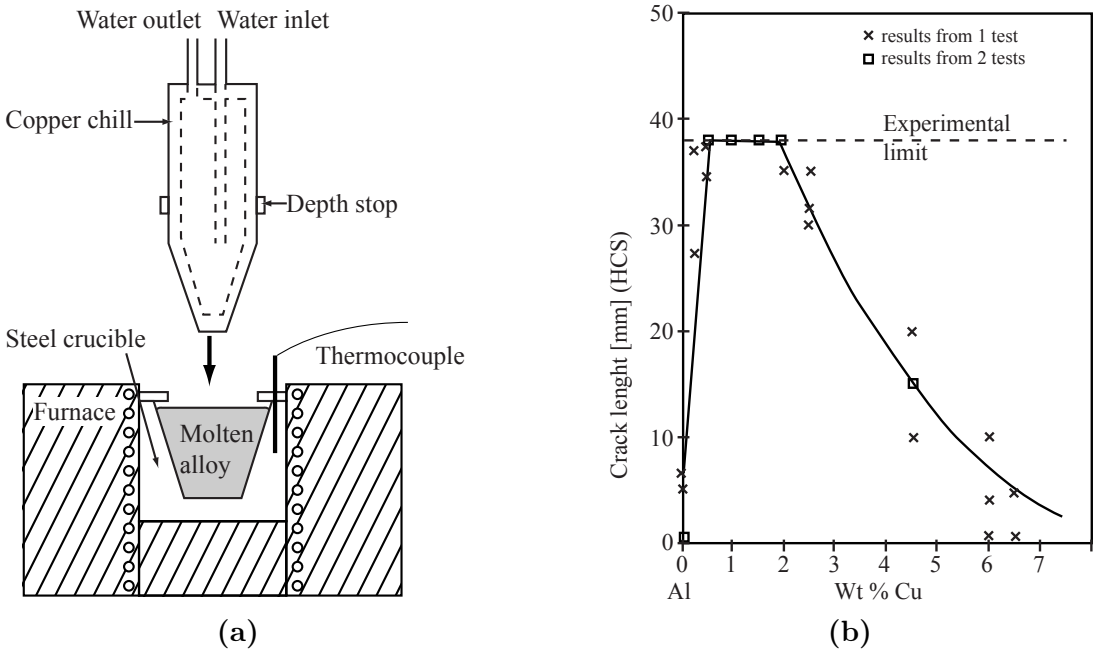


**Figure 2.14:** Redrawn from [80]. (a) Schematic of the cold finger test (b) HCS in the Al-Cu system, the $\lambda$-curve behavior is observed even though the maximum HCS occurs above the limit set by the experiment (tears cannot propagate on a distance longer than the finger).

general, there is an intermediate solute content (around 1%wt Cu in Al-Cu alloys) for which HCS is at a maximum (which is why a $\lambda$-shaped curve is obtained for HCS vs. $c_0$). In this specific case, the maximum in HCS cannot be located specifically, due to the limit imposed by the experimental device (cracking through the entire sample).

The $\lambda$-curve behavior can be understood considering two limiting cases. For a pure substance, there is no mushy zone ($g_s$ goes from 0 to 1 at the melting point) and hot tearing cannot occur. On the other hand, when the solute content is high, solidification will be terminated with a high proportion of eutectic. The range of solid fractions in which hot tearing may occur will thus not be found in the mushy zone because the intergranular liquid is solidified almost instantaneously at the eutectic temperature. Between these bounds, i.e. for low concentration alloys, hot tearing may occur.

Using this test, Warrington *et al* could also outline the effect of grain refinement [80]. The HCS is indeed rather high when no grain refiner is added (dendritic grains). In grain-refined samples, the HCS is lower but tends to increase as the amount of refiner increases (i.e. as the grain size decreases). Such a tendency was confirmed by the same authors using the same experimental setup for industrial alloys from the 7xxx series [81].

### Restrained Solidification Tests

Another widely used class of tests are based on restraining the solidification of a specimen in the longitudinal direction. One typical example is the Tatur test [82]. As suggested on Figure 2.15, the alloy is poured in a mold in which an external wheel is connected to the inner liquid inlet by several bars of different length. Due to restrained thermal contraction, these bars will be strained during solidification and some of them will break due to hot tearing. The maximum

length found among the bars that are not broken is used as a measure of HCS.

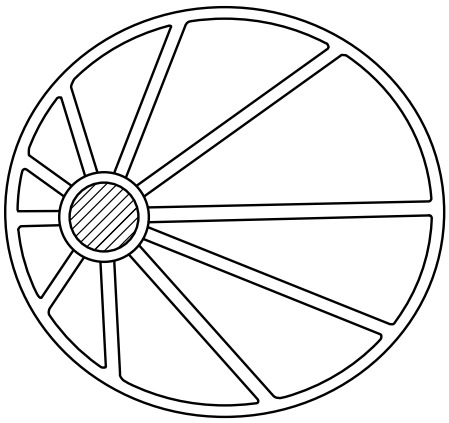

**Figure 2.15:** Redrawn schematically from [82]. Top view of the Tatur test mold. The liquid alloy is poured at the center of the mold (hatched area). The outside circle is solidified first and thermal contraction imposes strain to the radial bars. The maximum length of a bar without tear is used as a measure of the HCS.

Another type of widely used restrained solidification test is referred to as dogbone tests. Basically, the ends of the sample are solidified and fixed to a mold while the center is still mushy (thus acting as the hot spot) and in contact with liquid. An example of such a test was developed by Clyne and Davies [32]. These authors also developed a method to quantify the HCS. They measured the electrical resistivity of the solidified samples. From this, they were able to derive a crack fraction $X_{cr}$ that varies between 0 (sound sample) to 1 (completely cracked section). Using this method, they could outline the $\lambda$-curve behavior of Al-Mg Alloys.

A similar test was used by Spittle and Cushway (see Figure 2.16a) [83] and these authors also used $X_{cr}$ as a measure of the HCS. Their results on Al-Cu alloys are summarized on Figure 2.16b. The classical $\lambda$-curve behavior is found again. It also appears that grain refinement (to obtain globular solid grains) has a rather beneficial effect on hot tearing. The influence of superheat, which is related to the pouring temperature of the liquid alloy in the mold, is also shown. In general, the pouring temperature, together with the setup geometry and cooling condition, participate in the thermal field establishment. As a consequence, this parameter may influence the strain localization behavior as it is the case for this test.

More recently, Viano *et al* [84] used a more instrumented test based on the same principle. These authors quantified the HCS by measuring the brightness of X-ray images of the solidified samples. Their results regarding the effect of the solute concentration and grain refinement were in good agreement with [83].

### Tensile Tests

The last type of hot tearing test that shall be considered consists of standard tensile testing adapted to mushy alloys. Again, the center of the sample is mushy while the ends are solid. In this case, the ends are not fixed in a rigid mold but are attached to a tensile test apparatus. A controlled displacement can thus be applied to the sample and its force response can be recorded while solidification occurs. In general, such tests are more complicated to setup but they have the advantage of providing more information about the material since the thermal field and the

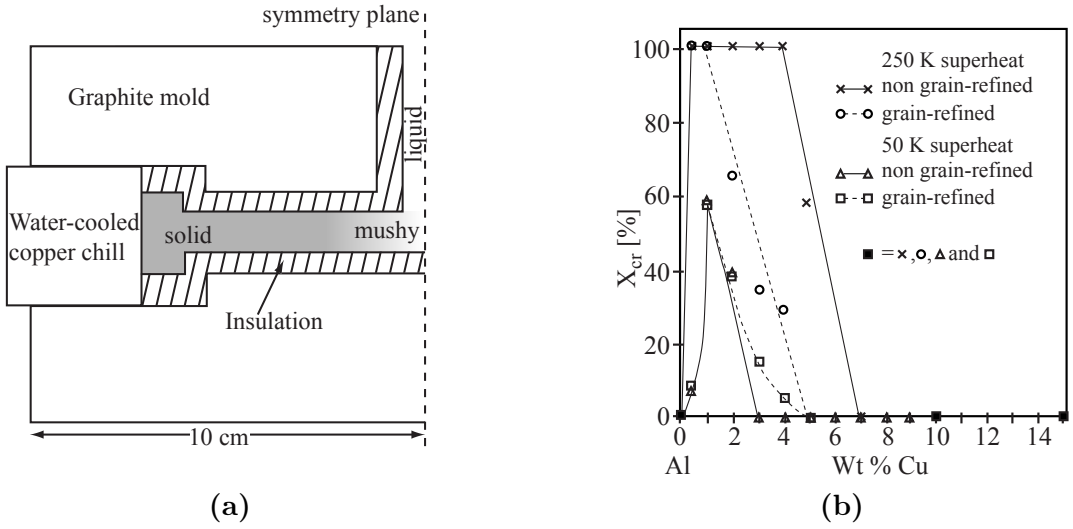


**Figure 2.16:** Adapted from [83]. (a) Schematic of the dogbone test (vertical section) (b) HCS in the Al-Cu system.

amount of strain imposed can be controlled separately. It is indeed only with this type of testing that rheological properties of both mushy and solid alloys may be measured.

Usually, a distinction is made between two testing modes : reheating and solidification. In reheating tests, a sample of the composition of interest is cast under the desired conditions. This is interesting because samples machined from full-scale DC cast ingots may be used. After complete solidification, the sample is mounted in the tensile machine. A limited region in the center of the specimen is then reheated up to the mushy state. The tensile test may then start. The main disadvantage of such tests is that the microstructure will evolve during reheating and may thus not represent well the as-cast state. It is also important to note that, in such tests, the hot spot is generally not in contact with a fully liquid region and that, as a consequence, feeding is not available[11]. In some cases, the hot spot is heated above the target temperature so that solidification is indeed occurring during the test, but there is still no large amount of liquid available. There are several examples of reheating tests in the literature [85–88]. One of them is of particular interest for the present work. Ludwig *et al* indeed used such a test to obtain the parameters and validate the constitutive behavior presented in Section 2.3.3 [2, 66].

Tensile tests under solidification are less interesting from a rheological point of view because the thermal field is much more difficult to control. However, they are more suitable for hot tearing assessment because the hot spot remains in contact with the melt. Moreover, the microstructure of the sample may be much closer to what is found during actual casting processes. These tests are exactly similar to the dogbone tests presented above except for the fact that it is possible to pull apart the end of the sample during solidification. There are less of these tests reported in the literature because they are even more difficult to design and setup. In spite of these difficulties, various research groups have obtained results with this method [89, 90].

One very good example is the test developed by Magnin *et al* [91]. In this test the solidified ends (with a hot spot at the center connected to a reservoir of liquid alloy) are pulled apart at a constant velocity until fracture occurs[12]. The force and displacement at the time of fracture

[11] this does not represent a drawback for materials properties measurements but it may lead to inaccurate results when reheating tests are used for hot tearing predictions.

[12] this test, known as the Alcan (Pechiney) rig test, will be described and studied in greater details later on.

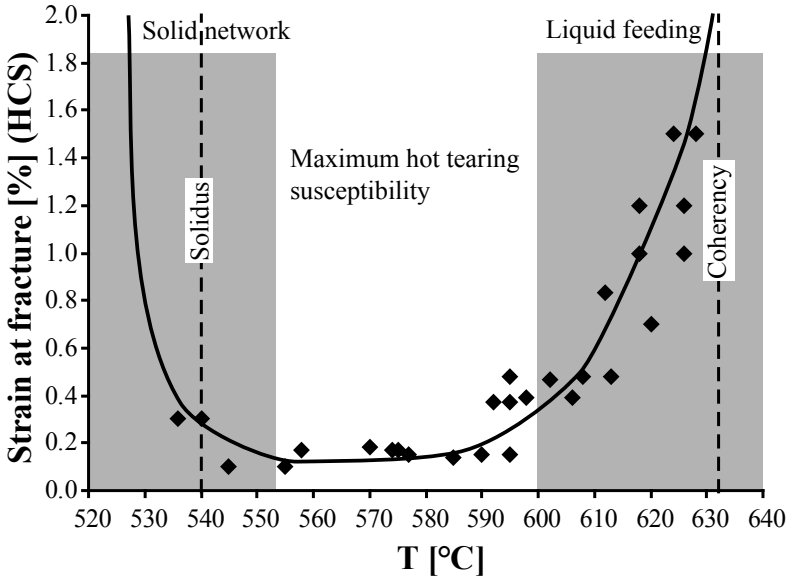


**Figure 2.17:** Ductility of Al-4.5wt%Cu dogbone samples loaded in tension during solidification, redrawn from [91].

can be thus recorded. The load at fracture increases when the temperature at which the test is started decreases, which is a well-known fact [2]. It is more interesting to study the strain at fracture (which can be estimated from the elongation) as a function of the temperature in the hot spot during tensile loading. Such a result is presented on Figure 2.17.

At rather high temperature, the solid grains are easily (i.e. under low stress) pulled apart by the applied strain. However, any void that forms will be healed by liquid feeding because the permeability is high enough in the hot spot. As a consequence, failure can only occur for very large strains, leading to a high ductility (i.e. low hot tearing tendency) even if the strength of the material is low. At low temperature, the solid skeleton is very well developed and coalescence is advanced. The alloy then behaves like a hot solid, exhibiting high ductility and significant strength. At an intermediate temperature, the hot tearing tendency is at a maximum because the solid skeleton is not coalesced yet and feeding mechanism cannot be active due to low permeability in the hot spot. The conjunction of these two factors lead to a minimum in the ductility of the alloy (U-shaped curve).

It should also be remarked that tensile tests are the most interesting ones when dealing with hot tearing. However, other stress states such as compression [2] or shear [2, 5] may be considered, especially when studying more closely the behavior of the mushy material rather than its failure.

### Industrial Tests

The tests presented above are useful because they are relatively well controlled. This allows investigating various phenomena as well as the effect of different parameters. As a consequence, these laboratory tests are important for the development of theoretical models of hot tearing. Once a model is established, it is however relevant to apply it to real cases in order to assess its ability to predict accurately the formation of defects. For such validation purposes, it is necessary to have access to well characterized full-scale castings produced under realistic industrial conditions. Such data is not very easy to obtain since their production is both costly and time

consuming and thus not very appealing to the industry.

Some data regarding full-scale billets are however available, either from DC casting installations setup at universities [31, 92] or from industrial partners [6]. An example of such data and their use in modeling will be presented later in this document.

### 2.4.3 Hot Tearing Models

In the preceding section, the classical experimental approaches to hot tearing have been summarized. The objective of this section is to describe the main aspects of theoretical descriptions of the hot tearing phenomenon. Models of hot tearing aim at providing a failure criterion applicable to mushy alloys under applied strain. This is a very complex problem to which a satisfactory solution has not yet been found [93]. The classical approach is to model the evolution of the hot tearing tendency as a function of various parameters without giving a criterion for whether or not cracking will occur in the system (the maximum HCS corresponds to the highest probability of finding a tear). It is thus relevant to recall how the various physical phenomena involved in hot tearing may be treated theoretically and to describe some of the existing hot tearing criteria. Please note that a more exhaustive review may be found in [78].

The most simple approach would be to assume the HCS to be proportional to the freezing range (equilibrium or non equilibrium) of the alloy (i.e. the range of temperature over which $g_s$ goes from 0 to 1) [29]. This is however too simplistic because hot tearing really occurs in a specific range of solid fractions, deep in the mushy zone [94].

An alternative approach was proposed by Clyne on Davies [95] based on the idea that hot tearing is likely to happen in the high solid fraction region of the alloy. They defined a vulnerable time $t_V$ during which hot tears may develop. They also considered the time $t_R$ during which stress relaxation processes are active. The hot tearing susceptibility is then expressed as :

$$\mathrm{HCS} = \frac{t_V}{t_R} \tag{2.57}$$

The authors proposed to use the local time spent in the range $90\% < g_s < 99\%$ as $t_V$ and the time such that $40\% < g_s < 99\%$ as $t_R$. Such a criterion has the advantage of being quite simple but the major drawback of not reproducing accurately the experimental data. Moreover, the process parameters such as the strain rate in the mushy zone cannot be accounted for in such a model. In general, a criterion like Equation (2.57) is clearly too simple to describe the problem at hand.

One aspect that is not clearly described by the above model is the fact that hot tearing will be prevented if liquid feeding is efficient enough to fill voids before they propagate catastrophically. One of the earliest models to take feeding into account was proposed by Feurer [96]. On one hand, this author considered the SPV, i.e. the volume of liquid that flows into a unit volume of material during a given time increment. The SPV has units of $[s^{-1}]$ and can be expressed using Darcy's law. On the other hand, the SRG is the shrinkage velocity, i.e. the rate of change in relative density. The SRG has units of $[s^{-1}]$ and can be expressed as a function of cooling rate and solidification shrinkage. In short, Feurer's hot tearing criterion states that the development of hot tears is possible only in the regions where SRG > SPV. This is a mathematical way of stating that hot tears will be healed when sufficient feeding is available. This model is interesting because it takes into account the liquid flow within the solid skeleton. However, the strains acting on the mushy zone cannot be taken into account in details using this approach. This criterion is therefore more relevant for predicting porosity formation.

From the above considerations, it appears that not only feeding but also strains are important to model hot tearing. It is thus important to focus on theories that include deformation of the solid skeleton to formulate hot tearing criteria. In general, there are three different quantities that can be used to characterize the mechanical constraint acting on the mushy zone : stress, strain and strain rate. One very interesting approach based on stress was given by Lahaie and Bouchard [97]. These authors considered that a mushy zone may be schematically represented in 2D as a population of hexagonal solid grains in a liquid as suggested on Figure 2.18.

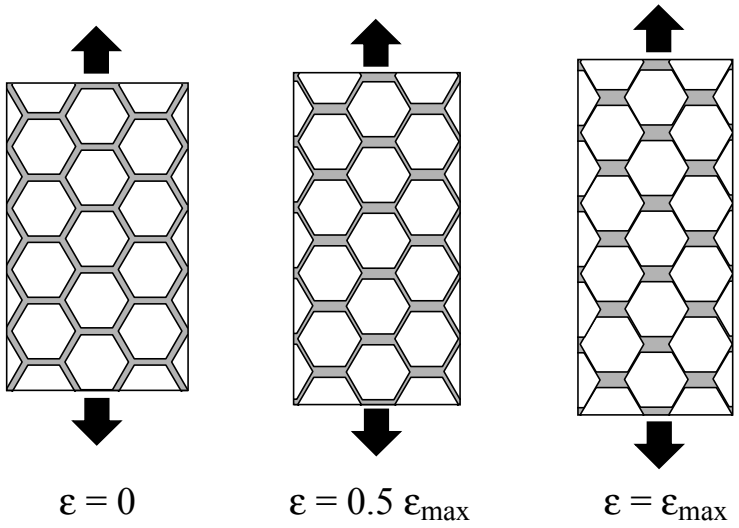


**Figure 2.18:** Simplified geometrical representation used in [97] for the derivation of a stress-based hot tearing criterion. Solid grains are white while the grey phase is the liquid. Please note that solid grains come in contact when sufficient deformation ($\epsilon_{max}$) is applied to the mushy zone.

When strain is applied to the mushy zone, the solid grains, which are assumed to be rigid, rearrange and liquid flows to accommodate their motion. If the liquid is assumed to be Newtonian and with a viscosity $\mu$, a relation between stress and strain is obtained for low strain :

$$\sigma = \frac{\mu\dot{\epsilon}}{9}\left(\frac{g_s^m}{1-g_s^m}\right)^3\left[\left(1-\frac{1}{2}\left(\frac{g_s^m}{1-g_s^m}\right)\epsilon\right)^{-3}+2\left(1+\left(\frac{g_s^m}{1-g_s^m}\right)\epsilon\right)^{-3}\right] \tag{2.58}$$

where the exponent $m$ is a microstructural parameter ($m = 1/2$ for columnar grains and $m = 1/3$ for equiaxed grains). At higher strain (above $\epsilon_{max}$ the solid grains start touching each other), further deformation can only be accommodated by liquid expansion since the grains are rigid. The viscoplastic deformation of the solid phase could also be introduced at this stage. In summary, the model from [97] gives access to the stress corresponding to a given strain. The criteria proposed for hot tearing is expressed in terms of the actual stress $\sigma(\epsilon)$ reaching a critical stress $\sigma_{crit}$. An expression for $\sigma_{crit}$ based on nucleating a void in the intergranular liquid is given by :

$$\sigma_{crit} = \frac{4\gamma_{l/v}}{3h}\left(1+\left(\frac{g_s^m}{1-g_s^m}\right)\epsilon\right)^{-1} \tag{2.59}$$

where $\gamma_{l/v}$ is the liquid-vapor interface energy and $h$ is the intergranular liquid film thickness at the beginning of loading.

This model is very interesting because it introduces the mechanical effects related to a population of solid grains moving in the liquid. Moreover, it has been generalized by Larouche *et al*

[90]. There are however disadvantages to this approach. First of all, the possibility of healing is not taken into account. Moreover, this hot tearing criterion is expressed based on a critical stress while experimental evidence tends to suggest that hot tearing is more of a strain (or even strain rate) induced phenomenon. Other stress-based models exist in the literature [86, 98]. They are based on a Griffith type approach associated with assumptions about how the geometry of the liquid and solid phases may be described at the micro scale level.

Another class of hot tearing criteria comes from strain-based models. The theoretical basis behind these models is usually not the most advanced. On the other hand, they are quite simple to apply in practice, which is why they are useful in industry. A typical example of a strain-based model is given by Magnin *et al* [91]. The idea is to define a relevant measure of the strain imposed by the process in the mushy zone $\epsilon_{process}$, e.g. the maximum principal strain. If this strain increases above the ductility of the material $\epsilon_{fracture}$, hot tearing may occur, as suggested on Figure 2.19.

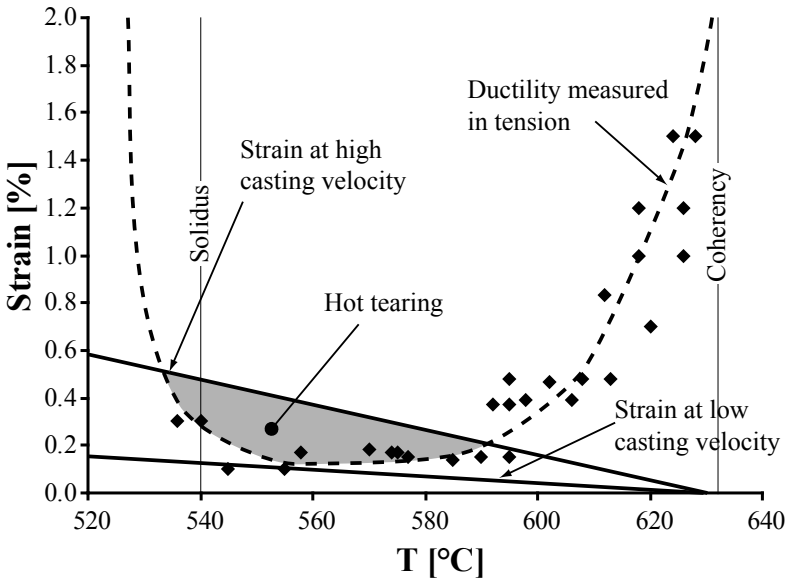


**Figure 2.19:** Strain-based hot tearing criterion proposed in [91]. Hot tearing is possible when the strain imposed by the process exceeds the ductility of the alloy measured in tension.

The value of $\epsilon_{fracture}$ is obtained from experimental measurements performed using a solidification tensile test setup (typically, the strain at fracture may be used). Those values thus include both the development of a coalesced solid network and the possibility of tear healing by flow of liquid. This is compared with $\epsilon_{process}$, which can be estimated from relatively simple mechanical modeling at the scale of the process. Typically, when the casting speed is increased, such strain will also increase. Other examples of similar criteria are found in the literature and applied to full-scale DC cast ingots [33, 99, 100].

At a more academic level, hot tearing models attempt to include more details of the physical phenomena that are involved. Quite often, these more advanced descriptions lead to strain rate-based models. These seem to be the most promising for accurate hot tearing predictions [93, 101]. The most widely used strain rate-based model was derived by Rappaz, Drezet and Gremaud (RDG) [37]. These authors used the approach developed by Niyama *et al* to model porosity [102] and included the effect of strains applied to the solid skeleton. To illustrate their derivation, these authors used pictures from direct observation experiments (see Figure 2.20).

Such results clearly show that there exists a solid fraction between 82% and 94% for which continuous liquid films exist around the dendrites and may thus break into a hot tear because their feeding by the melt will be very difficult. Please note that this result was found within a single grain (i.e. involves intragranular coalescence) and that intergranular coalescence, which is significant in the context of hot tearing, will occur at higher solid fraction.

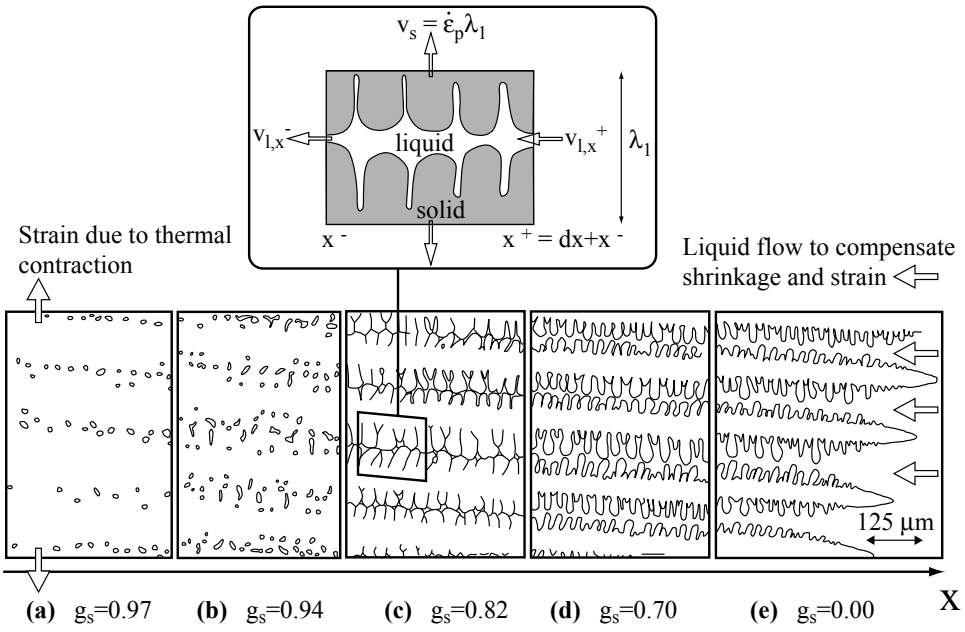


**Figure 2.20:** Adapted from [37]. A columnar mushy zone as observed in transparent alloys is used as a basis for the model and a small volume element is considered to compute the pressure drop across the mushy zone.

As suggested on Figure 2.20, these authors considered a columnar mushy zone in which the primary dendrite arm spacing is $\lambda_1$. Dendrites are assumed to grow along the $x$ direction in a thermal gradient $G$ and following isotherms, which move at velocity $v_T$. The mushy zone experiences a tensile strain rate $\dot{\epsilon}_p$ perpendicular to the growth direction. The liquid pressure $p_l$ will drop as the melt flows deeper into the mushy zone to compensate both strain and solidification shrinkage. The idea of the model is to compute $p_l$ and this is done by considering a small volume element, as represented on Figure 2.20.

At steady state, Equation (2.10) (p. 17) may be rewritten :

$$- v_T \frac{\partial}{\partial x} \left( g_s \rho_s + g_l \rho_l \right) + \nabla \cdot \left( g_s \rho_s \mathbf{v}_s + g_l \rho_l \mathbf{v}_l \right) = 0 \tag{2.60}$$

Introducing the solidification shrinkage $\beta = \frac{\rho_s}{\rho_l} - 1$, the authors obtained the following equation :

$$\frac{\mathrm{d}\left( g_l v_{l,x} \right)}{\mathrm{d}x} + \left( 1 + \beta \right) g_s \dot{\epsilon}_p - v_T \beta \frac{\mathrm{d}g_s}{\mathrm{d}x} = 0 \tag{2.61}$$

After integrating Equation (2.61) over a length $L$ in the mushy zone, applying the right boundary conditions and introducing Darcy's law (Equation (2.12) with permeability $K$ and viscosity $\mu$), the pressure drop $\Delta p_l = p_{atmospheric} - p_l$ can be expressed :

$$\Delta p_l = \left( 1 + \beta \right) \mu \int_0^L \frac{E}{K} \mathrm{d}x + v_T \beta \mu \int_0^L \frac{g_l}{K} \mathrm{d}x \tag{2.62}$$

where $E(x) = \int g_s \dot{\epsilon}_p \mathrm{d}x$. At this stage, the Carman-Kozeny relation can be introduced (Equation (2.13) with the secondary dendrite arm spacing $\lambda_2$ as characteristic length of the microstructure). The criterion for the nucleation of a void (i.e. hot tear nucleation) is simply given by $\Delta p_l \geq \Delta p_{crit}$. This means that a hot tear forms when the liquid pressure drop reaches a critical value (of the order of a few kPa [37]). Moreover, Equation (2.62) indicates that the pressure drops because of solidification shrinkage and strain. As $\dot{\epsilon}_p$ increases, so does $\Delta p_l$, which means that there exists a critical strain rate $\dot{\epsilon}_{p,max}$ above which a hot tear will nucleate. The value of $\dot{\epsilon}_{p,max}$ is the most important outcome of this model since the RDG criterion simply states that the HCS can be measured by $\dot{\epsilon}_{p,max}^{-1}$. A hot tear resistent alloy is thus able to withstand high strain rates without the formation of voids in the mushy zone. The model may thus be summarized under the following form :

$$F\left(\dot{\epsilon}_{p,max}\right) = \frac{\lambda_2^2}{180} \frac{G}{(1+\beta)\,\mu} \Delta p_{crit} - v_T \frac{\beta}{1+\beta} H \tag{2.63}$$

with :

$$\left.\begin{array}{rcl} F\left(\dot{\boldsymbol{\epsilon}}_{,max}\right) & = & \int_{T^{coal}}^{T^{coh}} \frac{E(T) g_s^2(T)}{(1-g_s(T))^3} \mathrm{d}T \\ E\left(T\right) & = & \frac{1}{G} \int g_s\left(T\right) \dot{\epsilon}_p\left(T\right) \mathrm{d}T \\ H & = & \int_{T^{coal}}^{T^{coh}} \frac{g_s^2(T)}{(1-g_s(T))^2} \mathrm{d}T \end{array}\right\} \tag{2.64}$$

The integrals in this model should be performed between the coherency temperature $T^{coh}$ (onset of strains) and $T^{coal}$ (the coalesced solid skeleton is no longer sensitive to tearing). If a significant amount of eutectic forms, integration should be performed up to the eutectic temperature $T_{eut}$. This is due to the fact that eutectic formation occurs before coalescence of the primary phase leading a decreased sensitivity of the alloy to hot tearing.

This model was successfully applied by its authors to reproduce the $\lambda$-curve measured for Al-Cu alloys [37]. Moreover, when compared to other classical criteria, it shows the best potential to reproduce tendencies well-known to the DC casting industry [93]. The model was also applied in numerical simulations of DC casting [103, 104]. It could also be adapted to equiaxed structures and used to predict that the HCS decreases if an equiaxed grain structure is promoted [36]. Braccini *et al* proposed an extension of the model [35]. These authors could indeed derive a critical strain rate for propagation of the voids (in order to differentiate between voids that remain as pores and voids that become hot tears).

The RDG model is quite widely used because it is able of reproducing the main tendencies of hot tearing. The fact that it is only a tear nucleation model may be a drawback even though there are many situations in which nucleation is the limiting step to hot tearing. Obviously, this criterion does not give a clear cut answer to whether or not tears are going to be formed. It only gives an indication to where in the casting the probability of finding the defect is highest. It should be remarked however that there exists no criteria that can predict accurately the formation and extent of hot tears in a real cast.

The models presented above are quite classical. Recently, there are a few aspects that have been further investigated by various research groups. First of all, the highest solid fraction at which hot tearing may occur has been studied by Rappaz and coworkers. The problem of coalescence indeed appears in the RDG criterion (in the integration bounds) and is experimentally known to have an effect on mechanical properties [68] and was studied theoretically [44]. By considering a population of grains [45, 46, 49] it appeared that a multiscale approach to hot tearing is very promising. The macroscopic approach is indeed able to describe accurately the process conditions down to a millimetric scale. Using this information, micro-scale models are

able of describing the localization of feeding and strain into the small remaining liquid films, possibly leading to a better understanding of how hot tears progress [105].

Another approach consists of developing fully coupled solvers for two-phase averaged equations, as will be described later. In such an approach, the complexity of the rheology of the mushy zone can be captured efficiently. In this context, M'Hamdi *et al* [1] proposed a criterion based on the local strain experienced by the alloy. A hot tear is assumed to nucleate when $p_l$ drops below a critical value $p_{crit}$, which is very similar to the RDG approach. This tear propagates due to further straining up to the point where the coalesced solid skeleton is formed. Please note that tear growth will only occur under tensile stress conditions. In this view, the HCS is expressed as [1]:

$$HCS = \begin{cases} 0 & \text{if} \quad p_l\left(g_s = g_s^{coal}\right) \geq p_{crit} \\ \theta \int_{t(p_l=p_{crit})}^{t\left(g_s=g_s^{coal}\right)} \left(w_v \dot{\epsilon}_{sw} + w_d \dot{\epsilon}_{cr}\right) \mathrm{d}t & \text{if} \quad p_l\left(g_s = g_s^{coal}\right) < p_{crit} \end{cases} \tag{2.65}$$

were $\dot{\epsilon}_{cr}$ and $\dot{\epsilon}_{sw}$ are defined by Equation (2.54), $\theta$ is equal to 1 if the average stress is positive (and to 0 in compression) and $w_v$ and $w_d$ are weighting factors. A very similar approach was proposed by Monroe *et al* for steel castings [106].

In conclusion, numerous hot tearing criteria have been proposed. Different phenomena have been included and comparison with experimental data show that the accuracy of the models varies strongly. However, there exists no quantitative criteria that is valid over a wide range of conditions. This is due to the complexity and number of phenomena that occur simultaneously in the mushy zone. Moreover, all of these different contributions usually depend on each other. As a consequence, even though the qualitative understanding of hot tearing is fairly advanced, accurate quantitative approach are not fully successful yet. The development of more and more advanced computer models, together with observation techniques of increasing precision is still potentially a way to reach this goal.

# Chapter 3

# Semi-Coupled Model

## 3.1 Problem

The objective of the present thesis is to describe quantitatively the constraints exerted on the mushy zone during a given solidification process. From this macroscale description of the problem, it is desired to gain further insight regarding the conditions for the formation of hot tears. In order to reach this goal, at least three different contributions have to be taken into account :

1. Thermal : the temperature field is of primary importance. On one hand, the solid fraction field, and thus the location of the coherent mushy zone, is directly related to temperature (an accurate description of $g_s(T)$ is a necessary input). On the other hand, it dictates how thermally induced strains develop during solidification and cooling of the alloy and are transmitted to this mushy zone. Simulating the thermal field evolution is based on the enthalpy conservation equation [56] :

$$\frac{\partial \overline{H}}{\partial t} + \nabla \cdot \left( \overline{H\mathbf{v}} \right) = \nabla \cdot (\overline{\kappa} \nabla T) \tag{3.1}$$

where $H$ is the enthalpy per unit volume, $\kappa$ is the thermal conductivity and $\overline{a}$ indicates the two-phase averaged value of $a$ (for example $\overline{\kappa} = g_s \kappa_s + g_l \kappa_l$). $\overline{H}$ is defined as a function of the latent heat $L$ and specific heat per volume $\overline{C_p}$ :

$$\overline{H}(T) = \int_0^T \overline{C_p}(\theta)\, \mathrm{d}\theta + (1 - g_s(T)) \cdot L \tag{3.2}$$

Most often, the boundary conditions are described by specifying the value of the heat flux at the surface (of normal $\mathbf{n}$) to be either zero (adiabatic) or related (by a heat transfer coefficient $h$) to the difference between the surface temperature $T_{surf}$ and outside temperature $T_{ext}$ :

$$\kappa \nabla T \cdot \mathbf{n} = -h (T_{surf} - T_{ext}) \tag{3.3}$$

Describing accurately the boundary conditions is often one of the main challenges encountered in modeling heat flow in real processes.

2. Mechanical : thermal strains together with the constraints imposed by the process (e.g. rigid mold preventing free contraction) lead to inhomogeneous stresses and strains in both the

solid shell and the mushy alloy. These strains (and their rate of variation $\dot{\boldsymbol{\epsilon}}^{vp}$) are the driving force for hot tearing and need to be characterized. The mechanical problem is expressed by the two-phase momentum conservation equation that was exposed in Section 2.3.2 :

$$\nabla \cdot \hat{\boldsymbol{\sigma}} + \overline{\rho}\mathbf{g} = \nabla p_l \tag{2.41}$$

This problem can be solved provided that the constitutive behavior of the material is described. For this purpose the rheological considerations from Section 2.3.3 are used.

3. Feeding : as already pointed out, hot tearing can be prevented if feeding of the mushy zone by the liquid alloy is efficient enough. In order to take this factor into account, the liquid pressure $p_l$ should also be predicted. At this stage, introducing a porosity formation model is expected to enhance the accuracy of the solution since liquid pressure drops will be smaller if gas precipitation is allowed. In order to model feeding, it is necessary to consider the two-phase mass conservation equation derived in Section 2.2 :

$$\frac{\partial}{\partial t}\overline{\rho} + \nabla \cdot (\overline{\rho}\mathbf{v}_s) - \nabla \cdot \left( \frac{\rho_l K}{\mu} (\nabla p_l - \rho_l \mathbf{g}) \right) = 0 \tag{2.14}$$

As far as porosity formation is concerned, the basic mechanism for pore nucleation has been exposed in Section 2.2.3 and further details about pore growth modeling may be found in [3, 53].

In order to study hot tearing, the coherent mushy zone, the location of which is predicted by the thermal model, is considered from the thermomechanical point of view. The problem is very complex due to the highly non-linear behavior of the solid-liquid mixture. The mechanical properties indeed depend strongly on the solid fraction (again, an accurate description of $g_s(T)$ is necessary). Moreover, liquid flow within the porous solid skeleton may be of importance. In this context, the problem is defined by Equations (2.14) and (2.41) :

$$\left.\begin{array}{rcl} \frac{\partial}{\partial t}\overline{\rho} + \nabla \cdot (\overline{\rho}\mathbf{v}_s) - \nabla \cdot \left( \frac{\rho_l K}{\mu} (\nabla p_l - \rho_l \mathbf{g}) \right) & = & 0 \\ \nabla \cdot \hat{\boldsymbol{\sigma}} + \overline{\rho}\mathbf{g} & = & \nabla p_l \end{array}\right\} \tag{3.4}$$

The unknowns are then the liquid pressure $p_l(\mathbf{x}, t)$ and the displacement field in the solid $\mathbf{u}_s(\mathbf{x}, t)$. It should be reminded that stresses are related to strains by the constitutive law for the mushy zone and that those strains are calculated by derivation of the displacement field. From this consideration, it is clear that Problem (3.4) is strongly coupled. Both unknowns indeed appear in both equations. In general, dealing with such a problem in finite elements requires solving both equations together for each time step.

Such a solver, known as TearSim$^{\text{TM}}$, has been developed by M'Hamdi and coworkers [1, 67, 71, 101, 107]. In short, these authors used Equations (2.50) to (2.53) to describe the rheology of the mushy zone. The solid alloy is described by (2.56). Moreover, the thermal contraction is introduced according to (2.42). Finally, these authors proposed the hot tearing criterion defined by Equation (2.65). This approach is very interesting because it includes comprehensively all the phenomena that can be captured at the scale of the casting. Moreover, it uses the most accurate description of the macro-scale phenomena, according to the best knowledge we have at present.

In practice however, some drawbacks to this approach are encountered. There is indeed neither a mushy zone refinement technique nor a porosity model that are included at this stage. Moreover, it is only available in 2D. In the present work, an alternative approach is proposed for the resolution of such problems. It is expected to allow for more flexibility in modeling various solidification problems.

## 3.2 Semi-Coupled Method

Let us start by recalling the definition of the effective stress :

$$\hat{\boldsymbol{\sigma}} = \boldsymbol{\sigma} + p_l \mathbf{I} \tag{2.40}$$

The present work is directed towards standard casting processes such as DC casting, gravity die casting or welding of aluminum alloys. In such cases, there is neither large pressure applied to the liquid phase nor strong metallostatic head. As a consequence, the liquid pressure is equal to the atmospheric pressure (101.3 kPa) minus the pressure drop established across the mushy zone for feeding $p_l = p_{atm} - \Delta p_l$. In aluminum alloys, typical values of the pressure drop $\Delta p_l$ are of the order of a few tens of kPa. On the other hand, coherent mushy zones are typically able of withstanding tensile stresses on the order of a few MPa. In this context, it is proposed that $p_l$ and its variation can be considered to be small when compared to the stresses [108]. In the semi-coupled method, the following assumption is thus made :

$$\hat{\boldsymbol{\sigma}} = \boldsymbol{\sigma} \tag{3.5}$$

This allows Problem (3.4) to be rewritten in a more classical form :

$$\left.\begin{array}{rcl} \nabla \cdot \boldsymbol{\sigma} + \overline{\rho}\mathbf{g} &=& 0 \\ \frac{\partial}{\partial t}\overline{\rho} + \nabla \cdot (\overline{\rho}\mathbf{v}_s) - \nabla \cdot \left( \frac{\rho_l K}{\mu} (\nabla p_l - \rho_l \mathbf{g}) \right) &=& 0 \end{array}\right\} \tag{3.6}$$

Problem (3.6) has become weakly coupled because $p_l$ no longer appears in the momentum conservation equation. The main drawback of this approach is that a decoupling assumption (Equation (3.5)) is introduced and that the resulting inaccuracy must be evaluated. On the other hand, in cases where this assumption is reasonable, it will be possible to solve the mechanical and liquid pressure problems with different, specifically dedicated solvers. A high level of accuracy and detail may thus be reached.

Having introduced a decoupling assumption, it is possible to solve the problem at hand in three steps, as suggested on Figure 3.1 [109] :

1. Thermal field determination.
2. Resolution of the thermomechanical problem.
3. Determination of the pressure in the liquid and fraction of porosity.

First of all, the thermal field $T(\mathbf{x}, t)$ is calculated using the finite element package Calcosoft$^{\text{TM}}$. Thermal calculations at the macroscopic scale can only be conducted if $g_s(T)$ is provided as input. Such data is available from microsegregation models linked to thermodynamic data or experimental measurements. In some cases, thermal calculations taking into account the strong coupling with the mechanical problem, or heat flow models introducing convection in the liquid phase may be required. These can be conducted relatively easily using well adapted solvers and thus potentially included in the present method.

Once the thermal field has been simulated in the entire casting, the mechanical problem can be addressed alone thanks to the decoupling assumption. This consists of solving the standard momentum conservation equation $\nabla \cdot \boldsymbol{\sigma} + \overline{\rho}\mathbf{g} = 0$ using the finite element package Abaqus$^{\text{TM}}$, which is specifically dedicated to mechanical problems. The temperature and solid fraction can

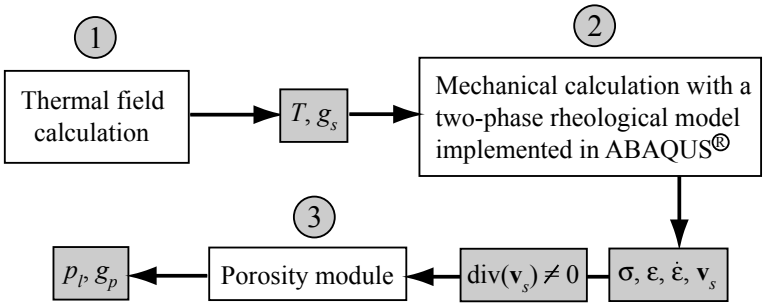


**Figure 3.1:** Flow chart for modeling casting processes using a semi-coupled approach [109].

be given as input to the solver. The challenge at this stage is to specify the behavior of the alloy for any temperature, as summarized in Table 3.1. First of all, let us consider the liquid and incoherent mush (i.e. below the coherency point : $g_s < g_s^{coh}$, with typically $g_s^{coh} = 0.65$). In this case, thermal contraction can be compensated by liquid feeding [60] and is thus neglected. Moreover, no inelastic deformation is considered. This material is thus described as linear elastic with a low value of Young's modulus $E$ (typically below 0.1 GPa). This description of the liquid is not perfect. However, it does not influence the mechanical problem in the mushy zone and proved to be the most efficient to achieve good numerical convergence of the mechanical solver.

At lower temperatures, the coherent mushy zone is formed. However, thermal contraction starts only when $g_s$ reaches a critical value $g_s^{th} \sim 0.8$ as shown in [60]. Please note that the typical value of $\alpha^{th}$ for aluminum alloys is $25 \cdot 10^{-6}$ K$^{-1}$. In this regime, elasticity is still described and $E$ is increasing strongly as the temperature drops. Moreover, inelastic strain is described by Equation (2.54) (p. 29) and the mushy alloy experiences some volumetric deformation (swelling in tension).

| | $\dot{\epsilon}_{th}$ | $\dot{\epsilon}_{cr}$ | $\dot{\epsilon}_{sw}$ |
|---|---|---|---|
| | | $\mathcal{B} \equiv \left(A_2 \hat{P}_s^2 + A_3 \hat{\sigma}_M^2\right)^{\frac{n-1}{2}}$ | |
| $g_s < 0.65$ | 0 | 0 | 0 |
| $0.65 < g_s < 0.8$ | 0 | $\hat{\sigma}_M A_3 \frac{\dot{\epsilon}_0}{(Cs_0)^n} \mathcal{B}$ | $-\frac{A_2 \hat{P}_s}{3} \frac{\dot{\epsilon}_0}{(Cs_0)^n} \mathcal{B}$ |
| $0.8 < g_s < 1.$ | $\alpha^{th}\dot{T}$ | $\hat{\sigma}_M A_3 \frac{\dot{\epsilon}_0}{(Cs_0)^n} \mathcal{B}$ | $-\frac{A_2 \hat{P}_s}{3} \frac{\dot{\epsilon}_0}{(Cs_0)^n} \mathcal{B}$ |
| $T_{merge} < T < T_{(g_s=1)}$ | $\alpha^{th}\dot{T}$ | $\frac{\dot{\epsilon}_0}{s_0^n} \sigma_M^n$ | 0 |
| $T < T_{merge}$ | $\alpha^{th}\dot{T}$ | $\sigma_M = \kappa(T)\, \epsilon_{cr}^{\eta(T)} \left(\frac{\dot{\epsilon}_{cr}}{\dot{\epsilon}_u}\right)^{\lambda(T)}$ | 0 |

**Table 3.1:** Summary of the mechanical behavior of the alloy.

For the fully solidified alloy at high temperature ($T > T_{merge}$ where $T_{merge}$ is around 400 °C), thermal contraction still occurs and the elastic modulus varies less rapidly with temperature (typically $E = 40$ GPa). Inelastic strains are still dominant and dictated by Equation (2.55). The specific volume of the alloy is however no longer affected by inelastic deformation (purely deviatoric strain).

Finally, the solid at moderate temperature (below $T_{merge}$) still deforms elastically and upon cooling. Its creep behavior is described by Equation (2.56) to account for work hardening. Please

note that the exact value of $T_{merge}$ is determined so that inelastic properties are continuous across the whole temperature range :

$$\left.\begin{array}{rcl} \lambda\left(T_{merge}\right) & = & \frac{1}{n} \\ \kappa\left(T_{merge}\right) & = & \frac{s_0}{\dot{\epsilon}_0^{\frac{1}{n}}} \\ \eta\left(T_{merge}\right) & = & 0 \end{array}\right\} \tag{3.7}$$

In practice, Equations (3.5) and (2.50) to (2.56) (pp. 26–29) have been implemented in Abaqus$^{\text{TM}}$, mainly through the CREEP user function. Mechanical calculations performed with this description of the material give access to all the quantities characterizing stresses and strains in the casting. In particular, the volumetric strain rate $\dot{\epsilon}_{sw} = \text{tr}\left(\dot{\boldsymbol{\epsilon}}^{vp}\right)$ can be extracted together with the solid velocity $\mathbf{v}_s$.

The last computation step of the semi-coupled method may then be performed. Mass conservation coupled with Darcy's law (Equation (2.14)) is solved for the liquid pressure with $T\left(\mathbf{x}, t\right)$ being provided as input. This is done using the ProCast$^{\text{TM}}$ porosity module developed by Péquet and coworkers [3, 53]. This solver is interesting because it introduces a mushy zone refinement technique. This means that the resolution of Equation (2.14), taking into account the variable permeability[1], is performed using a finite difference grid consisting of cubic cells, which are smaller than the finite elements used to solve the thermal problem (see Figure 3.2). This allows describing more precisely the liquid pressure drop across the mushy zone.

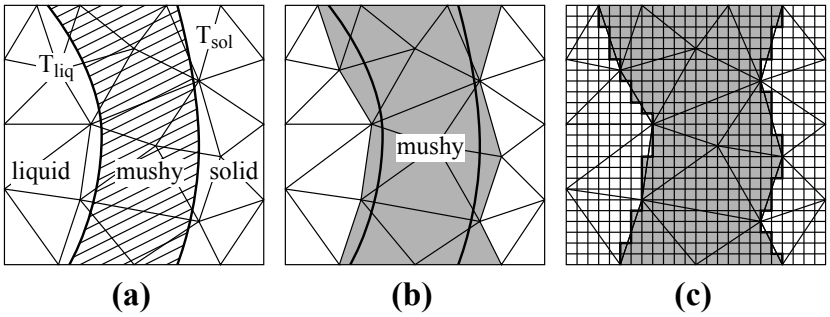


**Figure 3.2:** Adapted from [3]. (a) The thermal field determines the position of the mushy zone. (b) Finite elements with at least one node in the mushy zone are considered. (c) The mushy elements are divided in finer cubic cells. The mesh used in the porosity module consists only of the cells that are part of mushy elements (outlined in grey). This procedure leads to refined meshes in the mushy zone.

The porosity module was modified in order to take into account the strain term in the mass conservation equation. The following decomposition was applied :

$$\nabla \cdot \left(\overline{\rho}\mathbf{v}_s\right) = \overline{\rho}\nabla \cdot \mathbf{v}_s + \mathbf{v}_s \cdot \nabla\overline{\rho} \tag{3.8}$$

Often, the sponge-like behavior of the solid skeleton dominates the mechanically-induced variation of $\overline{\rho}$ . As a consequence, the following was used in some cases (neglecting $\nabla\overline{\rho}$) :

$$\nabla \cdot \left(\overline{\rho}\mathbf{v}_s\right) = \overline{\rho}\nabla \cdot \mathbf{v}_s = \overline{\rho}\text{tr}\left(\dot{\boldsymbol{\epsilon}}^{ie} + \dot{\boldsymbol{\epsilon}}^{el}\right) \tag{3.9}$$

[1] $K$ is expressed using Equation (2.13) with a constant value of $\lambda$ equal to the grain size of the alloy for grain-refined castings.

Please note that thermal strain rate is not included in this strain term because it is already taken into account by original porosity module through the relationship between $\bar{\rho}$ and $T$.

Strain in the mushy zone alters the amount of liquid necessary to compensate for the local volume change, as expressed in Equation (2.14). It also has an effect on the local solid fraction. The user indeed specifies the evolution of $g_s$ as a function of temperature. However, strain-induced volume change will also alter locally the value of $g_s$ which should indeed be expressed as :

$$g_s = g_s\left(T\right) + \Delta g_s^{mech} \tag{3.10}$$

where $g_s\left(T\right)$ is defined by the user using a microsegregation model and $\Delta g_s^{mech}$ is the mechanical solid fraction correction that is given by :

$$\Delta g_s^{mech} = \int -g_s tr\left(\dot{\boldsymbol{\epsilon}}^{ie}\right) \mathrm{d}t \tag{3.11}$$

This correction is often small. However, it may have an effect because it will be taken into account to compute the local permeability, which varies strongly with $g_s$ at the late stage of solidification. Please note that this correction may be activated or disabled by the user in both the mechanical (the strength of the material will also be strongly sensitive to $g_s$) and porosity calculations.

Another advantage of this method is that it gives access to results from a porosity module. When the amount of dissolved gas is set to zero, only $p_l$ is calculated (pores cannot nucleate). On the other hand, when the realistic value of $[H]_0$ is input, the fraction of porosity $g_p$ is calculated according to the method described shortly in Section 2.2.3 and in more details in [3]. This quantity is of interest in hot tearing studies since it characterizes voiding to some extent.

As a last remark concerning the porosity module, it should be said that it is only available in three dimensions and that the generation of the cellular mesh for finite difference calculations is based on a finite element mesh composed of tetrahedral elements only. This means that axisymmetric porosity calculations have to be conducted on a 3D mesh with the correct symmetry (usually, a quarter of the mesh obtained by rotation of the 2D axisymmetric mesh around the symmetry axis). Moreover, in 3D calculations, the hexahedral elements that are preferred for mechanical calculations have to be cut into tetrahedra before conducting the liquid pressure calculation. All these aspects are handled by the converter developed to follow the flow chart given on Figure 3.1.

## 3.3 Convergence Study

The semi-coupled method involves two different solvers to describe the mechanical and liquid flow aspects of the problem defined by a mushy zone under strain. In order to conduct such calculations, it is necessary to select numerical parameters such as mesh size $\Delta x$ and time step $\Delta t$. Their effects on the results together with selection guidelines are provided for each solver in the following sections.

### 3.3.1 Mechanical Solver

The mechanical solver (i.e. Abaqus$^{\mathrm{TM}}$) was benchmarked using a model tensile test, as suggested on Figure 3.3. A cylindrical specimen (1 cm in radius, 20 cm in length : $l_0 = 0.2$ m) is loaded in tension by applying a constant displacement rate (parallel to the sample axis) $\dot{u}_z$ to both its

ends. From this, an average strain rate $\dot{\epsilon}_{av}$ can be calculated: $\dot{\epsilon}_{av} = 2\frac{\dot{u}_z}{l_0}$. At mid-height, the specimen is hotter than at its extremities and temperature varies linearly between these bounds so that a constant thermal gradient along $z$ of magnitude $G$ is established. During the test, the sample is cooled at a constant rate $\dot{T}$ without altering the value of $G$. Moreover, $g_s(T)$ is assumed to vary linearly between 585 °C (which is the maximum temperature at the beginning of the test and corresponds to $g_s = 0.8$) and 505 °C ($g_s = 1$). All the parameters that have been used in this study are summarized in Table 3.2.

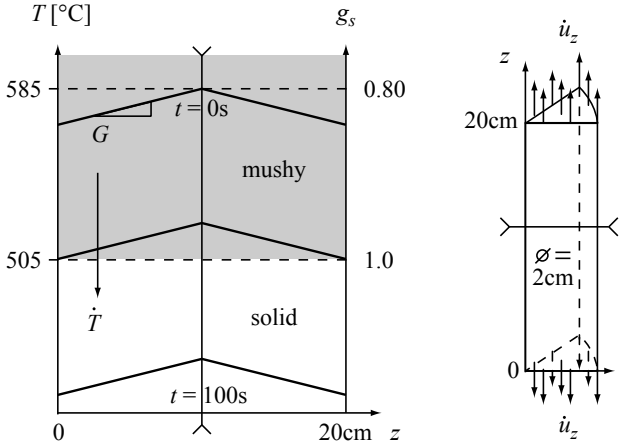


**Figure 3.3:** Thermal and mechanical conditions defined for the model tensile test.

The main result of this test is the reaction force $F$ recorded as a function of time. This is characteristic of the behavior of the alloy in tension. In order to focus more on what happens in the mushy zone, the final centerline profile (i.e. $r = 0$ and $0 < z < l_0$) of the cumulated volumetric strain[2] $\epsilon_{sw} = \int \dot{\epsilon}_{sw} \mathrm{d}t$ is considered. Both these quantities depend on the materials properties. Moreover, if they are calculated numerically, the values of $\Delta x$ and $\Delta t$ may influence the result. For the model alloy, the values of $F(t)$ and $\epsilon_{sw}(z)$ have thus been calculated under different test conditions ($\dot{T}$, $\dot{\epsilon}_{av}$ and $G$) for different values of $\Delta x$ and $\Delta t$.

| $\dot{u}_z$ $\left[\mathrm{m\ s^{-1}}\right]$ | $\dot{\epsilon}_{av}$ $\left[\mathrm{s^{-1}}\right]$ | $\dot{T}$ $\left[\mathrm{K\ s^{-1}}\right]$ | $G$ $\left[\mathrm{K\ m^{-1}}\right]$ | |
|---|---|---|---|---|
| $10^{-5}$ and $10^{-4}$ | $10^{-4}$ and $10^{-3}$ | -1 and -3 | 20, 200 and 800 | |
| $\frac{\mathrm{d}g_s}{\mathrm{d}T}$ $\left[\mathrm{K^{-1}}\right]$ | $T(g_s = 1)$ [°C] | $T_{max}$ [°C] | | |
| 0.025 | 505 | 585 | | |
| $A$ $\left[\mathrm{s^{-1}}\right]$ | $Q$ $\left[\mathrm{kJ\ mol^{-1}}\right]$ | $s_0$ [MPa] | $n$ | |
| $2.65{\cdot}10^7$ | 125 | 52 | 3.44 | |
| $p$ | $\alpha_0$ | $\alpha_1$ | $g_s^{coal}$ | $k$ |
| 0.315 | 10.54 | 0.0632 | 0.94 | 100 |

**Table 3.2:** Materials parameters used for the model tensile test.

The mesh was built with square (4-noded bilinear) axisymmetric elements of size $\Delta x$. The time incrementation procedure is a little bit more complex since an automatic scheme was selected [110]. The time step is controlled by the $\chi$ parameter, which is designed to keep the change in

[2] this quantity is referred to as CESW in Abaqus.

creep rate small within one time step. This parameter is given by :

$$\chi = \left(\dot{\epsilon}_{cr}|_{t+\Delta t} - \dot{\epsilon}_{cr}|_t\right) \Delta t \tag{3.12}$$

The user inputs the value of $\chi$ and the solver will determine the time step accordingly ($\Delta t$ will thus vary during the calculation and its average, $\Delta t_{av}$, can be calculated). For accurate solutions to be obtained it is relevant to use a value of $\chi$ given by the order of magnitude of the elastic strain in the problem [110]. Please note that, in Abaqus$^{\text{TM}}$, the $\chi$ parameter is known as CETOL.

Unfortunately, it is not possible to find an analytical solution to this model tensile test problem. To overcome this problem, several calculations were conducted for very fine meshes. It was found that the solution became independent of the numerical parameters when $\Delta x \leq 1$ mm and $\chi \leq 10^{-8}$. As a consequence, the exact solution of the problem, $\tilde{F}$ and $\tilde{\epsilon}_{sw}$ have been taken to be the calculated solution for $\Delta x = 1$ mm and $\chi = 10^{-8}$ ($\Delta t_{av} \approx 5 \cdot 10^{-3}$ s). The relative differences (noted $\Delta_{rel}$) between any solution and this reference were calculated according to :

$$\Delta_{rel} F = \frac{F\left(\chi, \Delta x\right) - \tilde{F}}{\tilde{F}} \quad \text{and} \quad \Delta_{rel} \epsilon_{sw} = \frac{\epsilon_{sw}\left(\chi, \Delta x\right) - \tilde{\epsilon}_{sw}}{\tilde{\epsilon}_{sw}} \tag{3.13}$$

These relative differences (which may be viewed as relative errors) indicate how the solution depends on the numerical parameters. They were studied as a function of $\Delta x$ and $\chi$.

First of all, the effect of the time step was studied. A typical example of the results obtained is given on Figure 3.4. It was found that $\Delta_{rel} F$ and $\Delta_{rel} \epsilon_{sw}$ depend only weakly on the test conditions ($G$, $\dot{\epsilon}_{av}$ and $\dot{T}$). This is not too surprising since $\chi$ is a dimensionless number and the time step is controlled based on the solution of the problem.

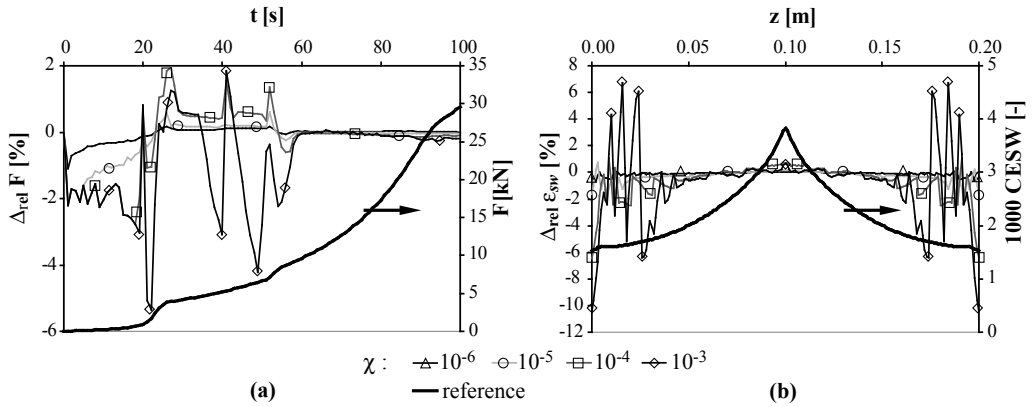


**Figure 3.4:** Solution of the problem (bold line) and relative differences for different values of $\chi$ : $10^{-6}$, $10^{-5}$, $10^{-4}$ and $10^{-3}$ for (a) $F\left(t\right)$ and (b) $\epsilon_{sw}\left(z\right)$. This result corresponds to $G = 200$ K m$^{-1}$, $\dot{T} = -3$ K s$^{-1}$, $\dot{\epsilon}_{av} = 10^{-3}$ s$^{-1}$ and $\Delta x = 0.1$ cm.

After considering all the different tests that were conducted, general tendencies could be outlined. First of all, the solution of the problem is much more sensitive to $\chi$ when the alloy is mushy (negligible errors are often found for solid alloys). Moreover, for $\chi \leq 10^{-5}$ (i.e. for typically $\Delta t_{av} \leq 0.1$ s) relative errors were found to be always below 5% for both $\epsilon_{sw}$ and $F$, which is considered to be very satisfactory. On the other hand when $\chi \geq 10^{-3}$ ($\Delta t_{av} \geq 0.25$ s), the relative errors may become larger than 10% and become non negligible in the solid phase.

Such results are not accurate enough. As a consequence, the following guideline was adopted when setting up the calculations :

$$10^{-6} \leq \chi \leq 10^{-4} \tag{3.14}$$

Above this range, the inaccuracy becomes significant while lower $\chi$ values increase the CPU time without enhancing the quality of the results. When such values are used for $\chi$, the relative error are always below 10%, which is acceptable considering the typical experimental uncertainty in this field. Moreover, this criterion is applicable over a wide range of process conditions and may thus be used in further calculations. In general, the exact value used for $\chi$ will be chosen considering both accuracy and CPU time.

Similarly, the effect of the mesh size was investigated (in the conditions where the time step has no significant effect, as described by Equation (3.14)). Again, a sample result is given on Figure 3.5. After studying the results of different calculations, it could be shown that satisfactory results (relative errors within 10%) were obtained if the increment of $g_s$ across one element was $5 \cdot 10^{-3}$ or less. In real problem, this condition should be satisfied at least in the principal loading direction and can thus be written :

$$\frac{\mathrm{d}g_s}{\mathrm{d}T} \left(\nabla T \cdot \mathbf{s}\right) \Delta x \leq 5 \cdot 10^{-3} \tag{3.15}$$

where $\mathbf{s}$ is a unit vector indicating the direction of the maximum principal stress. This condition can lead to very fine meshes. For large problems, this guideline can sometimes not be followed because of CPU time issues. In this case, the solution will loose accuracy, even though general tendencies are still described. For example, if the increment of solid fraction across the element is allowed to double (to $10^{-2}$), the relative error may typically peak up to 20% locally (but remains below 10% on average).

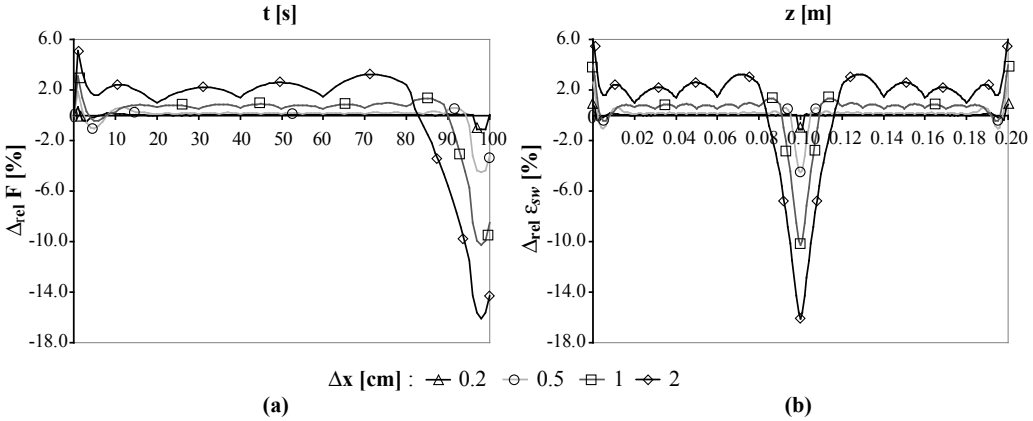


**Figure 3.5:** Relative differences for different values of $\Delta x$ : 0.2, 0.5, 1 and 2 cm for (a) $F(t)$ and (b) $\epsilon_{sw}(z)$. This result corresponds to $G = 200$ K m$^{-1}$, $\dot{T} = -3$ K s$^{-1}$, $\dot{\epsilon}_{av} = 10^{-3}$ s$^{-1}$ and $\chi = 10^{-8}$.

This benchmark problem leads to the establishment of guidelines for selecting both $\Delta t$ and $\Delta x$. These criteria are expressed as functions of dimensionless numbers and are thus applicable to the problems that shall be considered in further studies. Considering the high non linearity of the constitutive behavior of mushy alloys under strain, it is not surprising to find that these guidelines are quite restrictive and that the resulting CPU times may become large.

### 3.3.2 Liquid Pressure Solver

In order to study the behavior of the liquid pressure solver, a simple situation for which an analytical solution can be found [102] was studied. A one-dimensional mushy zone is traveling along the $x$ direction. The thermal gradient $G$ is constant across the mushy zone and isotherms move with velocity $v_T$. Moreover, steady state is assumed, thus giving : $\frac{\partial}{\partial t} = -v_T \frac{\partial}{\partial x}$. Furthermore, gravity is neglected in this approach.

It is known that the pressure drop in the mushy zone can be due to both solidification shrinkage and strains in the solid skeleton. Let us first focus on a problem without strains in the solid ($\mathbf{v}_s = 0$) and in which both phases have constant but different densities $\rho_s \neq \rho_l$. If $v_l$ is the component of $\mathbf{v}_l$ in the $x$ direction, Equation (2.10) for mass conservation may be rewritten :

$$\frac{\mathrm{d}}{\mathrm{d}x}\left(g_l v_l\right) - v_T \beta \frac{\mathrm{d}g_s}{\mathrm{d}x} = 0 \tag{3.16}$$

where $\beta = \frac{\rho_s}{\rho_l} - 1$ is the solidification shrinkage factor. Integration leads to :

$$g_l v_l - v_T \beta \left(1 - g_l\right) = \mathcal{C} \tag{3.17}$$

Since Equation (3.17) must also be true at the boundary with the fully liquid region (i.e. for $g_l = 1$), the integration constant can be found : $\mathcal{C} = v_l$. The following is thus obtained :

$$v_l = -v_T \beta \tag{3.18}$$

This expression can be introduced into Darcy's law (Equation (2.12), p. 17) :

$$g_l v_T \beta = \frac{K}{\mu} \frac{\mathrm{d}p_l}{\mathrm{d}x} \tag{3.19}$$

As a consequence, the analytical solution of the present problem, $\tilde{p}_l^{sh}$ is given by :

$$\tilde{p}_l^{sh}\left(g_l\right) = p_0 + \Delta\tilde{p}_l^{sh} \quad \text{with} \quad \Delta\tilde{p}_l^{sh} = \int_1^{g_l} g_l v_T \beta \frac{\mu}{K} \mathrm{d}x \tag{3.20}$$

where $p_0$ is the sum of the atmospheric pressure and the metallostatic head. At this point, the solidification path of the alloy has to be described. For the sake of simplicity, the alloy is assumed to solidify between $T_{liq}$ and $T_{liq} - \Delta T_{freeze}$ according to a power law (with an exponent $b > 1$) :

$$g_l = \left(\frac{\Delta T_{freeze} + T - T_{liq}}{\Delta T_{freeze}}\right)^b \Rightarrow \frac{\mathrm{d}g_l}{\mathrm{d}T} = \frac{b}{\Delta T_{freeze}} g_l^{1-\frac{1}{b}} \tag{3.21}$$

The Carman-Kozeny relation with a grain size $\phi$ can then be introduced and the following is obtained :

$$\Delta\tilde{p}_l^{sh} = v_T \beta \mu \frac{180}{\phi^2} \frac{\Delta T_{freeze}}{bG} \int_1^{g_l} \frac{\left(1 - g_l\right)^2}{g_l^2} g_l^{\frac{1}{b}-1} \mathrm{d}g_l \tag{3.22}$$

In general, the solution of the problem shall be written :

$$\tilde{p}_l = p_0 - \Omega^{sh}\mathcal{P}^{sh} \Longrightarrow \Delta\tilde{p}_l^{sh} = -\Omega^{sh}\mathcal{P}^{sh} \tag{3.23}$$

where

$$\Omega^{sh} = v_T \beta \mu \frac{180}{\phi^2} \frac{\Delta T_{freeze}}{G}$$

| | $b=1$ | $b=2$ | $b=3$ |
|---|---|---|---|
| $\mathcal{P}^{sh}$ | $\frac{1}{g_l}+2\ln g_l - g_l$ | $\frac{1}{3}g_l^{-\frac{3}{2}} - 2g_l^{-\frac{1}{2}} - g_l^{\frac{1}{2}} + \frac{8}{3}$ | $\frac{1}{5}g_l^{-\frac{5}{3}} - g_l^{-\frac{2}{3}} - g_l^{\frac{1}{3}} + \frac{9}{5}$ |

**Table 3.3:** Expressions of $\mathcal{P}^{sh}$ for different power law solidification paths.

is a characteristic pressure drop (expressed in [Pa]) and $\mathcal{P}^{sh}$ depends on the solidification path of the alloy. Analytical expressions can be obtained for different values of $b$, as given in Table 3.3.

It is also possible to use either the lever rule or Scheil's model to describe $g_s(T)$. In this case, the definition of $\Omega^{sh}$ is changed to take into account the equilibrium freezing range of the alloy: $\Omega^{sh} = v_T \beta \mu \frac{180}{\phi^2} \frac{\Delta T^{eq}_{freeze}}{G}$. The function $\mathcal{P}^{sh}$ is then expressed as a function of the partition coefficient $k$ (or $\theta = \frac{k}{1-k}$), assumed to be constant. These are given in Table 3.4.

| | $\mathcal{P}^{sh}$ |
|---|---|
| lever<br><br>$\theta = \frac{k}{1-k}$ | $\frac{1}{(1-k)\theta^3}\left\{\frac{\theta(\theta+1)^2}{\theta+g_l} + 2(\theta+1)\ln g_l - 2(\theta+1)\ln(\theta+g_l)\right.$<br><br>$\left. + \frac{\theta}{g_l} - \left(\theta^2 + 2\theta - 2(\theta+1)\ln(\theta+1)\right)\right\}$ |
| Scheil | $(k-1)\left\{\frac{1}{k-3}g_l^{k-3} - \frac{2}{k-2}g_l^{k-2} + \frac{1}{k-1}g_l^{k-1} - \frac{2}{(k-3)(k-2)(k-1)}\right\}$ |

**Table 3.4:** Expressions of $\mathcal{P}^{sh}$ for lever rule or Scheil solidification paths.

Let us now consider a problem in which the pressure drop is induced by strain in the solid network. For this case, the density of both phases are taken constant and equal, i.e. $\rho_s = \rho_l$ (no shrinkage). In such a case, Equation (2.10) can be rewritten:

$$\frac{\mathrm{d}}{\mathrm{d}x}\left(g_l\left(v_l - v_s\right)\right) = -\nabla \cdot \mathbf{v}_s \tag{3.24}$$

The volumetric strain rate $\nabla \cdot \mathbf{v}_s$ is assumed to be a constant noted $\dot{\epsilon}_{vol}$. If a power law solidification path (Equation (3.21)) is assumed, integration can be performed to obtain:

$$\frac{Gb}{\Delta T_{freeze}} g_l\left(v_l - v_s\right) = -\dot{\epsilon}_{vol} b g_l^{\frac{1}{b}} + \mathcal{C} \tag{3.25}$$

At the top of the mushy zone, where $g_l = 1$, there must be enough liquid flow to compensate for the increase in volume of the mushy alloy due to strains, which gives:

$$v_l\left(g_l = 1\right) = -\frac{\Delta T_{freeze}}{G}\dot{\epsilon}_{vol} \Rightarrow \mathcal{C} = 0 \tag{3.26}$$

Again, Darcy's law and Carman-Kozeny relation can be introduced and the mechanical pressure drop expressed as:

$$\Delta \tilde{p}_l^{mech} = \mu \dot{\epsilon}_{vol} \frac{180}{\phi^2}\left(\frac{\Delta T_{freeze}}{G}\right)^2 \frac{1}{b}\int_1^{g_l} \frac{\left(1-g_l\right)^2}{g_l^3} g_l^{\frac{2}{b}-1} \mathrm{d}g_l \tag{3.27}$$

This means that the solution to the mechanically-induced pressure drop problem has the form :

$$\tilde{p}_l^{mech} = p_0 - \Omega^{mech}\mathcal{P}^{mech} \tag{3.28}$$

where the values of $\mathcal{P}^{mech}$ are summarized in Table 3.5 and the characteristic pressure drop is now :

$$\Omega^{mech} = \mu\dot{\epsilon}_{vol}\frac{180}{\phi^2}\left(\frac{\Delta T_{freeze}}{G}\right)^2$$

| | $b=1$ | $b=2$ | $b=3$ |
|---|---|---|---|
| $\mathcal{P}^{mech}$ | $\frac{1}{g_l}+2\ln g_l - g_l$ | $\frac{1}{4}g_l^{-2}-\frac{1}{g_l}-\frac{1}{2}\ln g_l+\frac{3}{4}$ | $\frac{1}{7}g_l^{-\frac{7}{3}}-\frac{1}{2}g_l^{-\frac{4}{3}}+g_l^{-\frac{1}{3}}-\frac{9}{14}$ |

**Table 3.5:** Expressions of $\mathcal{P}^{mech}$ for different power law solidification paths.

The solutions become more complicated when the lever rule or Scheil's model are taken into account. The definition of the characteristic pressure drop is given by $\Omega^{mech} = \mu\dot{\epsilon}_{vol}\frac{180}{\phi^2}\left(\frac{\Delta T_{freeze}^{eq}}{G}\right)^2$. For the lever rule, Equation (3.25) has to be integrated numerically to obtain the values of $\mathcal{P}^{mech}$ while the expression obtained for Scheil's model involves $\zeta$, the ratio of the actual freezing range $(T_{liq}-T_{eut})$ to the equilibrium freezing range $(\zeta = \frac{\Delta T_{freeze}}{\Delta T_{freeze}^{eq}})$ :

$$\begin{aligned}\mathcal{P}^{mech}_{\text{Scheil}} = {} & \frac{k^2}{1-k}\left(\frac{g_l^{2k-3}}{2k-3}+\frac{g_l^{2k-4}}{2-k}+\frac{g_l^{2k-5}}{2k-5}+\frac{1}{(2k-3)(2-k)(2k-5)}\right)\\ & +\left(\frac{k^2}{k-1}-k\zeta\right)\left(\frac{g_l^{k-2}}{k-2}-2\frac{g_l^{k-3}}{k-3}+\frac{g_l^{k-4}}{k-4}-\frac{2}{(k-2)(k-3)(k-4)}\right)\end{aligned} \tag{3.29}$$

The analytical solutions for $\tilde{p}_l^{sh}$ and $\tilde{p}_l^{mech}$ show how a characteristic pressure drop $\Omega$ can be calculated. Figure 3.6 displays the multiplying factor $\mathcal{P}$ that relates the actual liquid pressure to this quantity. With this information, the relative importance of the strain and shrinkage contributions may be estimated.

Having obtained these analytical solutions, it is possible to assess the accuracy of the results given by the porosity module for a given cell size $\Delta x$ and time step $\Delta t$. For this purpose, the relative differences in $\mathcal{P}^{sh}$ and $\mathcal{P}^{mech}$ were studied under various conditions[3] :

$$\Delta_{rel}\mathcal{P}^{sh} = \frac{\tilde{p}_l^{sh} - p_l^{sh}(\Delta x, \Delta t)}{\tilde{p}_l^{sh}} \quad \text{and} \quad \Delta_{rel}\mathcal{P}^{mech} = \frac{\tilde{p}_l^{mech} - p_l^{mech}(\Delta x, \Delta t)}{\tilde{p}_l^{mech}} \tag{3.30}$$

First of all, it could be verified that the numerically calculated values of $\Delta_{rel}\mathcal{P}^{sh}$ were indeed independent of $\Omega^{sh}$. This means that the porosity module reproduces well the functional form of the solution. Moreover, the numerical solutions $p_l^{sh}$ and $p_l^{mech}$ were found to be identical for all values of $\Delta x$ and $\Delta t$ in the case $b=1$ as indicated by the analytical development.

The effect of the time step (which is constant and fixed by the user) was then assessed for all $g_s(T)$ relationships. Examples of the results that were obtained are given on Figure 3.7. Please note that only the region were $0.8 < g_s < 0.98$ is studied. This is because, on one hand,

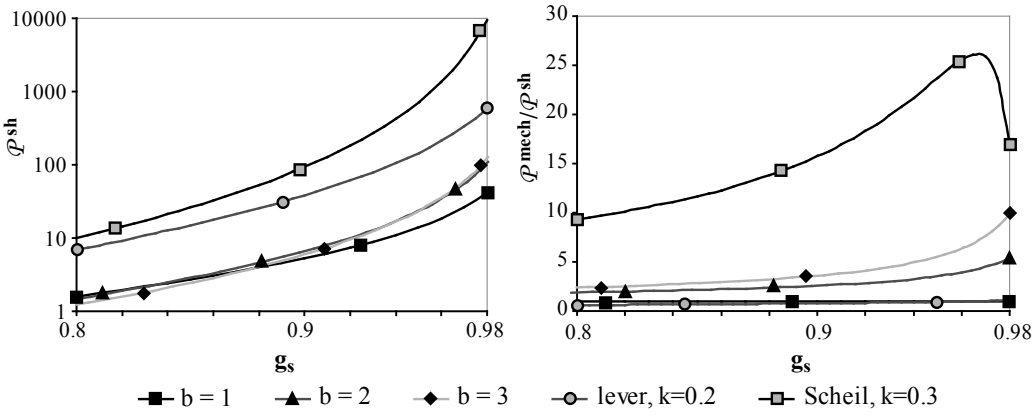


**Figure 3.6:** Values of $\mathcal{P}^{sh}$ and ratio $\frac{\mathcal{P}^{mech}}{\mathcal{P}^{sh}}$ for different solidification paths. Note that specific values were assigned to $k$ and that $\tilde{p}_l^{mech}$ for Scheil's model was calculated with $\zeta = 6.24$.

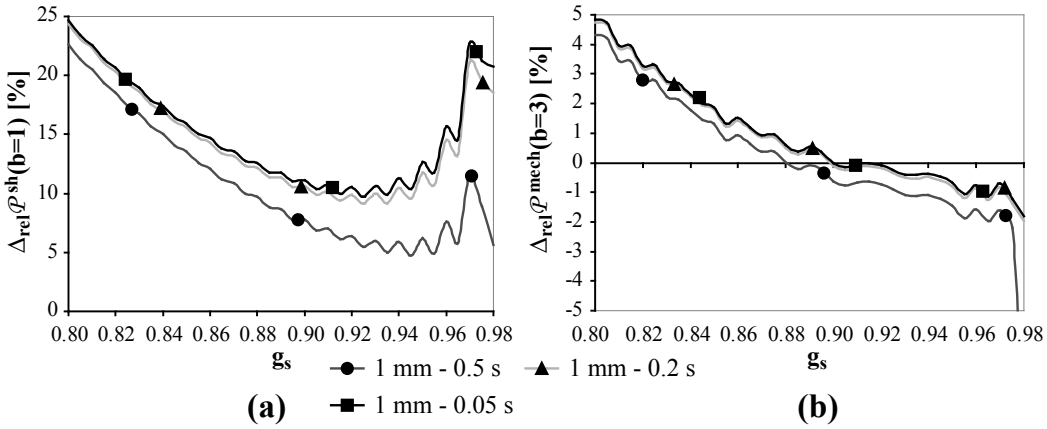


**Figure 3.7:** Values of (a) $\Delta_{rel}\mathcal{P}^{sh}$ for $b = 1$ and (b) $\Delta_{rel}\mathcal{P}^{mech}$ for $b = 3$. The mesh size was $\Delta x = 1$ mm and different values of $\Delta t$ (0.5 s, 0.2 s and 0.05 s) are used.

solidification is assumed to terminate with 2% of eutectic phase. On the other hand, below 80 % of solid, the pressure drops are negligible.

In all cases, it was found that, for a given value of $\Delta x$, there exists a critical value of $\Delta t$ below which the numerical solution becomes independent of $\Delta t$ ($\Delta_{rel}\mathcal{P}^{sh}$ and $\Delta_{rel}\mathcal{P}^{mech}$ no longer change upon a decrease in the time step). This means that the solution converges and it is thus desirable to use such a time step in further calculations. As suggested by Figure 3.7(a), the numerical solution may not converge towards an accurate solution if the mesh is too coarse. After compilation of all the results, it was found that a suitable time step to obtain a solution that had converged with respect to $\Delta t$ was given by the following guideline:

$$\frac{v_T \Delta t}{\Delta x} = 0.1 \tag{3.31}$$

In other words, this means that isotherms[4] should travel through one cell only in 10 time steps or more. This condition has the same form as the CFL (Courant, Friedrichs, Levy) condition for advection problems but is different in nature.

[3]different values of $G$, $v_T$, $\mu$, $\phi$ were applied as well as various microsegregation models.
[4]in general, the iso-$g_s$ for the relevant range of $g_s$ should be considered

The next step is to determine suitable values for the cell size $\Delta x$. For this purpose, several calculations were conducted using the different microsegregation models and using Equation (3.31) to select the time step. Again, the relative differences between the numerical and analytical solutions for the pressure profile were studied and two examples of the results that were obtained are given on Figure 3.8.

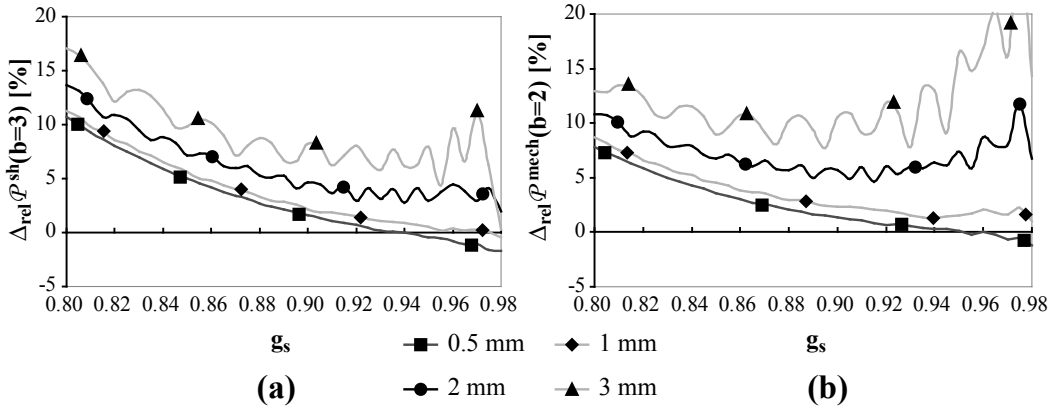


**Figure 3.8:** Values of (a) $\Delta_{rel}\mathcal{P}^{sh}$ for $b = 3$ and (b) $\Delta_{rel}\mathcal{P}^{mech}$ for $b = 2$. The time step was selected according to Equation (3.31) and different values of $\Delta x$ (0.5 mm, 1 mm, 2 mm and 3 mm) are used.

Again, the solution becomes independent of the mesh size if the value of $\Delta x$ is small enough. After examining all the results, it was found that results become independent[5] of the mesh size provided the variation of solid fraction across one cell is 0.5% or less. In other words, the mesh size should be selected according to :

$$\frac{\mathrm{d}g_s}{\mathrm{d}T} G \Delta x = 5 \cdot 10^{-3} \tag{3.32}$$

where the value of $\frac{\mathrm{d}g_s}{\mathrm{d}T}$ may be estimated only in the range $0.8 < g_s < 1$ since it is in this region that the pressure drops are significant.

The rules given by Equations (3.31) and (3.32) are again quite restrictive, especially as far as the mesh size is concerned. For some cases, CPU time considerations will not allow for such fine meshes to be used. In such conditions, it is useful to know that using a cell size three times larger than what is recommended (according to Equation (3.32)) leads to a an error of typically 10%.

At this stage, the conditions for the numerical solution to be independent of the numerical parameters are known. However, it is still important to know whether the converged numerical results agree with the analytical solutions. This can be done by considering Figure 3.9.

It turns out that there remains some differences between the analytical and numerical values of $\mathcal{P}^{sh}$ and $\mathcal{P}^{mech}$. In general, the error is mostly significant at relatively small values of $g_s$. This is not surprising because the numerical error is going to appear large where the analytical solution takes very low values. However, it is satisfactory to note that, for all of the realistic microsegregation models ($b = 1$ is not encountered in practice), this error remains below 10%. The pressure solver used in conjunction with the guidelines mentioned above can thus be considered suitable for the present purpose.

[5]meaning that the relative errors change by less than 2% when dividing $\Delta x$ by 2.

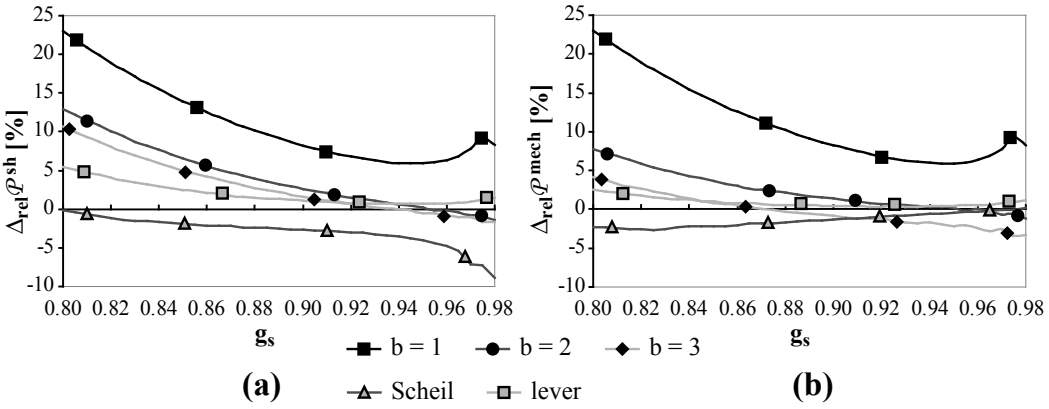


**Figure 3.9:** Values of (a) $\Delta_{rel}\mathcal{P}^{sh}$ and (b) $\Delta_{rel}\mathcal{P}^{mech}$ corresponding to the converged numerical solution for the different microsegregation models (lever rule was applied using $k = 0.2$ and Scheil's model with $k = 0.3$ and $\zeta = 6.24$).

## 3.4 Validity of the Decoupling Assumption

The semi-coupled method is based on the decoupling assumption expressed in Equation (3.5). In other words, the equation $\nabla \cdot \boldsymbol{\sigma} + \overline{\rho}\mathbf{g} = 0$ is solved instead of Equation (2.41) (p. 24). This means that there are in fact two contributions that are neglected, i.e. the liquid pressure itself $p_l$, which appears in the effective stress, and its gradient $\nabla p_l$.

Let us first consider the effect of the liquid pressure. The second invariant of the effective stress is equal to the second invariant of the total stress because they are related to deviatoric (shear) components of the stress state: $\hat{\sigma}_M = \sigma_M$. On the other hand, the first invariant of the effective and total stresses are related by:

$$\hat{P}_s = P_s - p_l \tag{3.33}$$

From the rheological point of view, the semi-coupled method consists of using $P_s$ instead of $\hat{P}_s$ in the constitutive relation between stress and strain rate (Equation (2.50)).

In order to study the effect of this approximation, a cylinder (20 cm diameter, 10 cm high) of mushy alloy under a constant thermal gradient $G = 600$ K m$^{-1}$ along the $z$ (axial) direction is considered. The properties of the AA5182 alloy are used (see Section 5.3) and an average strain rate of $\dot{\epsilon}_r = 10^{-3}$ s$^{-1}$ is applied in the radial direction. During this virtual experiment, solidification progresses. Initially the solid fraction is between 0 and 93.6% and is described by a power law solidification (Equation (3.21)) with $b = 3$. Under a constant cooling rate of $\dot{T} = -1$ K s$^{-1}$, the test is conducted up to complete solidification of the entire sample (100 s). These conditions are reasonably close to those encountered at the center of a DC cast billet.

The problem is solved using the semi-coupled approach ($p_l = 0$) to obtain the reaction force (to the applied strain rate) $\tilde{F}$ as a function of time and the final volumetric strain profile along the axial direction $\tilde{\epsilon}_{sw}(z)$. The same problem is then solved again assuming that the liquid pressure is a constant fraction of the solid pressure[6] and neglecting $\nabla p_l$. The relative differences[7] in force and volumetric strain:

$$\Delta_{rel}F = \frac{F\left(\frac{p_l}{P_s}\right) - \tilde{F}}{\tilde{F}} \quad \text{and} \quad \Delta_{rel}\epsilon_{sw} = \frac{\epsilon_{sw}\left(\frac{p_l}{P_s}\right) - \tilde{\epsilon}_{sw}}{\tilde{\epsilon}_{sw}}$$

[6] in this case, the value of the liquid pressure is known and can be used in the rheological expression.
[7] these differences may in fact be viewed as the relative error related to using the semi-coupled method.

can then be studied as a function of the $p_l$ to $P_s$ ratio. Sample results are found on Figure 3.10.

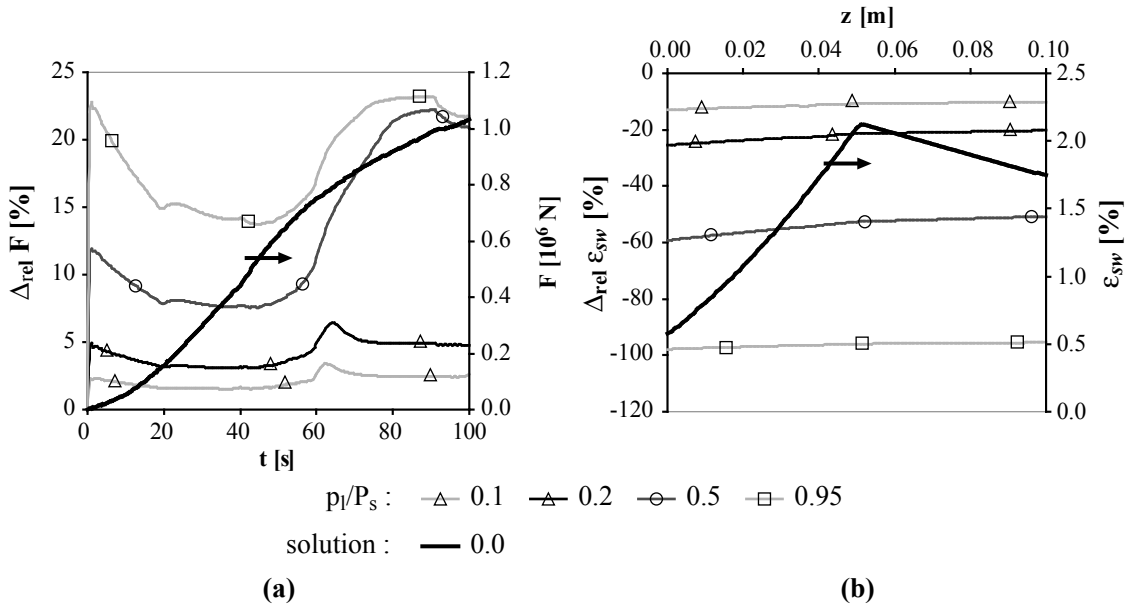


**Figure 3.10:** Reaction force vs. time and $\epsilon_{sw}$ vs. $z$. The solution of the problem for $p_l = 0$ (semi-coupled solution) and the relative differences obtained for various $\frac{p_l}{P_s}$ are displayed.

In tension, the reaction force increases when liquid pressure is taken into account because the negative $p_l$ pulls the grains together. In general, the reaction force is not strongly dependent upon the $\frac{p_l}{P_s}$ ratio (if the liquid pressure is 50% of $P_s$, the error introduced by the semi-coupled method is only of 10–20%). This is due to the fact that most of the strain rate is accommodated by the deviatoric component $\dot{\epsilon}_{cr}$. The latter depends on the effective pressure only through $\left(A_2\hat{P}_s^2 + A_3\hat{\sigma}_M^2\right)^{\frac{n-1}{2}}$. This quantity is not strongly sensitive to $\hat{P}_s$ (and thus to $p_l$) since the dominant contribution usually comes from $\sigma_M$.

Similarly, the values of $\epsilon_{sw}$ decrease due to the effect of $p_l$ because less swelling is possible when grains are pulled together. This quantity however is much more sensitive to the liquid pressure. In fact, the value of $\frac{p_l}{P_s}$ is roughly equal to the error introduced by the semi-coupled method. This is not surprising because $\epsilon_{sw}$ is controlled by the volumetric strain rate $\dot{\epsilon}_{sw}$. The latter is strongly dependent upon $p_l$ since it is directly proportional to $\hat{P}_s$ (see Equation (2.54)). In general , the error on the volumetric strain can be evaluated approximately by :

$$\Delta_{rel}\epsilon_{sw} \approx \frac{\int \frac{p_l}{P_s}\dot{\epsilon}_{sw}\mathrm{d}t}{\epsilon_{sw}} \tag{3.34}$$

In order to assess the effect of the $\nabla p_l$ term, a similar calculation was conducted. This time, $p_l$ is not assumed to be a function of the solid pressure. It is indeed more relevant to use the analytical solution $p_l = -\Omega^{sh}\mathcal{P}^{sh}$ (Equation (3.23)) for $b = 3$. In this case again, the liquid pressure is known a priori and exact calculations can be compared to the semi-coupled results. For these calculations, two corrections were taken into account. On one hand, $\hat{P}_s = P_s + \Omega^{sh}\mathcal{P}^{sh}$ is used in the rheological expression. Moreover, the term $\nabla p_l = -\Omega^{sh}\frac{\mathrm{d}\mathcal{P}^{sh}}{\mathrm{d}z}$ is included as a body force. It is possible to set $\Omega^{sh} = 0$ independently in both these corrections. As a result each one of them may be included or not in any calculation. The results are displayed on Figure 3.11.

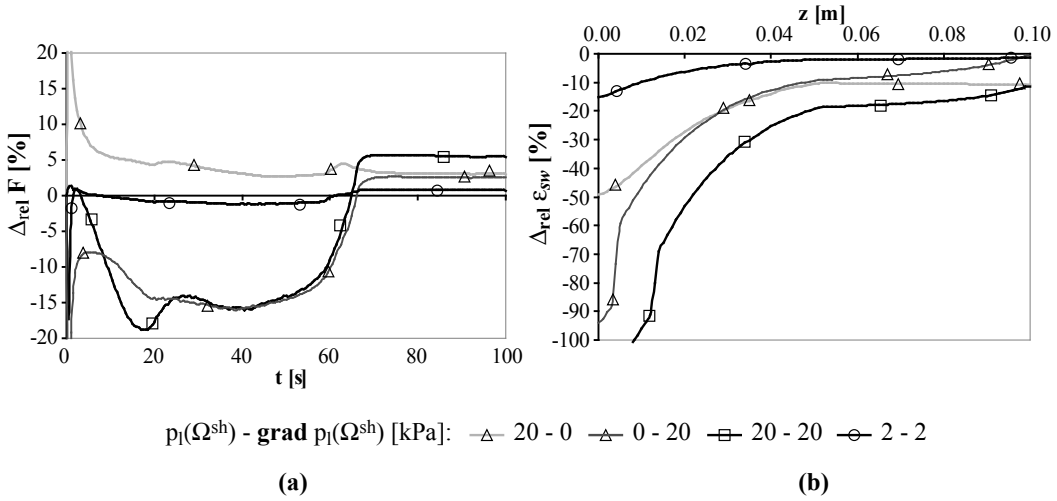


**Figure 3.11:** Reaction force vs. time and $\epsilon_{sw}$ vs. $z$. The relative differences obtained when including various terms are displayed. The values of $\Omega^{sh}$ expressed in kPa used to calculate $p_l$ and $\nabla p_l$ respectively are given for each curve. A zero value means that one of these contributions is neglected. The solution of this problem obtained by the semi-coupled method is the same as that displayed on Figure 3.10.

Using a very large value of $\Omega^{sh} = 20$ kPa shows that the effect of liquid pressure alone (pale grey curve with triangles) can be described as explained above. The effect on the reaction force is indeed relatively small while $\epsilon_{sw}$ is more sensitive to this correction. In both cases, the beginning of the test (when $P_s$ is still relatively small) is the most sensitive part.

As far as the $\nabla p_l$ term is concerned (dark grey line with triangles), it also has a greater effect at the beginning of the test. The correction of $\epsilon_{sw}$ is comparable to that obtained for the liquid pressure contribution while the effect on the reaction force is more marked in this case. When the exact problem is solved for $\Omega^{sh} = 20$ kPa (both contributions included, black line with squares), the relative difference with the semi-coupled solution (i.e. the error introduced by the semi-coupled method) is significant (up to 15% in $F$ and typically 30% in $\epsilon_{sw}$).

Having outlined the effect of both terms, a full calculation was performed with $\Omega^{sh} = 2$ kPa. This value is expected to be an upper bound to $\Omega$ values that are characteristic of the processes on which this work is focused. This means that the typical errors due to the semi-coupled approach are expected to be less or equal to those indicated by this limit (black line with circles). Typically, the force response in such a case will be accurate within 5% while the values of $\dot{\epsilon}_{sw}$ and $\epsilon_{sw}$ are within 10% of their fully coupled values.

Another test was conducted using a gradient $G = 400$ K m$^{-1}$ with an initial solid fraction in the range $0.78 < g_s < 0.99$ (power law solidification with $b = 3$). Similarly, a tensile test is conducted up to complete solidification ($\dot{T} = -1$ K s$^{-1}$ for 60 s). In this case however, the strain rate $\dot{\epsilon}_z = 10^{-3}$ s$^{-1}$ is applied in the axial direction, i.e. parallel to the thermal gradient. This was done to mimic the conditions encountered during a typical tensile test. The results are given on Figure 3.12.

Once again, calculations with a large value $\Omega^{sh} = 10$ kPa were conducted first. The effect of the liquid pressure (pale grey line with triangles) is significant and more marked on $\epsilon_{sw}$. In this case again, the $\nabla p_l$ term also has a significant effect (dark grey line with triangles), which is related to the ratio of $\frac{\mathrm{d}p_l}{\mathrm{d}z}$ to $\frac{\mathrm{d}\sigma_{zz}}{\mathrm{d}z}$. For a more realistic value of $\Omega^{sh} = 2$ kPa, the effect of $\nabla p_l$

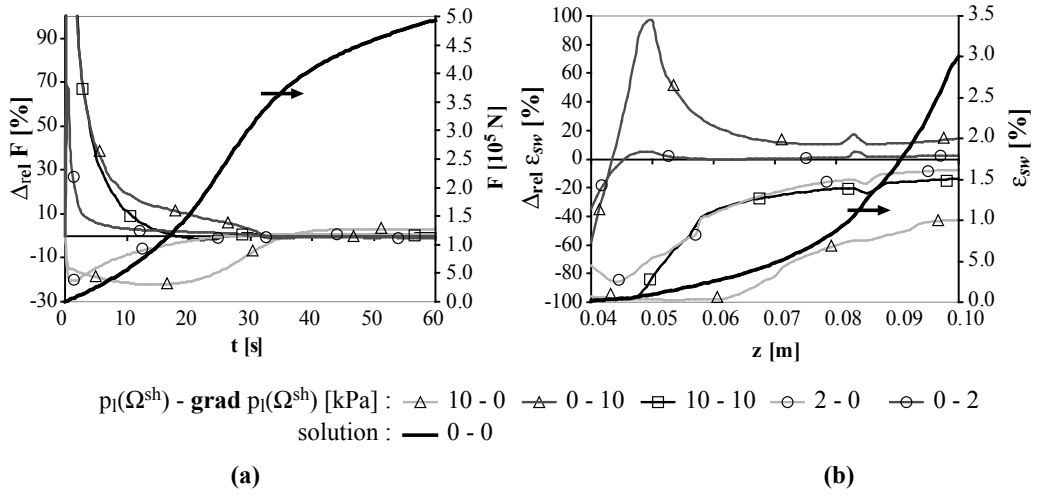


**Figure 3.12:** Reaction force vs. time and $\epsilon_{sw}$ vs. $z$. The solution of the problem for $p_l = 0$ and the relative differences obtained when including various terms are displayed. The values of $\Omega^{sh}$ expressed in kPa used to calculate $p_l$ and $\nabla p_l$ respectively are given for each curve. A zero value means that one of these contributions is neglected.

(dark grey line with circles) becomes negligible while $p_l$ (pale grey line with circles) still affects the value of $\epsilon_{sw}$ as predicted by Equation (3.34).

In general, the effect of the $p_l$[8] and $\nabla p_l$[9] terms will depend on the process conditions and may compensate each other or add up. The study presented in this section helped showing that the error related to the semi-coupled approach becomes significant for large pressure drops across the mushy zone. On the other hand, satisfactory accuracy (within 10%) is obtained provided two conditions are met :

1. The liquid pressure should be small when compared to the first stress invariant $P_s$. In general, it is desired that the following condition is met in the mushy zone :

$$\frac{p_l}{P_s} \leq 0.1 \tag{3.35}$$

2. The gradient of liquid pressure should be small when compared to the divergence of stress. Mathematically, this condition is expressed as :

$$\frac{|\nabla p_l|}{|\nabla \cdot \boldsymbol{\sigma}|} \leq 0.1 \tag{3.36}$$

Often in solidification processes, the above conditions are verified and the semi-coupled method may thus be applied, as had already been suggested in [111]. In the present work, all the cases studied met these requirements and the results presented later are thus accurate from this point of view. However, the validity of the conditions expressed by Equations (3.35) and (3.36) must be checked before the semi-coupled method is applied quantitatively to other cases. Significant inaccuracies are expected to arise in processes such as high pressure die casting for example or even continuous casting of steel (large metallostatic head).

[8] influences the volumetric strain evolution dictated by the rheological law.
[9] acts as a body force which can influence strain distribution and stress.

# Chapter 4

# Experimental Data

The present chapter is dedicated to the presentation of the experimental data that was available before the present work was conducted. Such data will be used for comparison with numerical results and it is thus relevant to review the experimental methods involved in obtaining such results. Two tensile tests performed in research laboratories, together with one series of full-scale billets casting were investigated.

## 4.1 Mushy Zone Tearing Test

In order to study coalescence, Grasso *et al* [5] designed a tensile test applicable to mushy alloys. For this purpose, a separable stainless steel mold (the top and bottom halves can be pulled apart) encloses a cylindrical dogbone-shaped cavity (with a reduced cross section of 1 cm in diameter at mid-height). This mold is also designed to be attached to a standard tensile test machine at the top and fixed to a copper chill at the bottom, as illustrated on Figure 4.1.

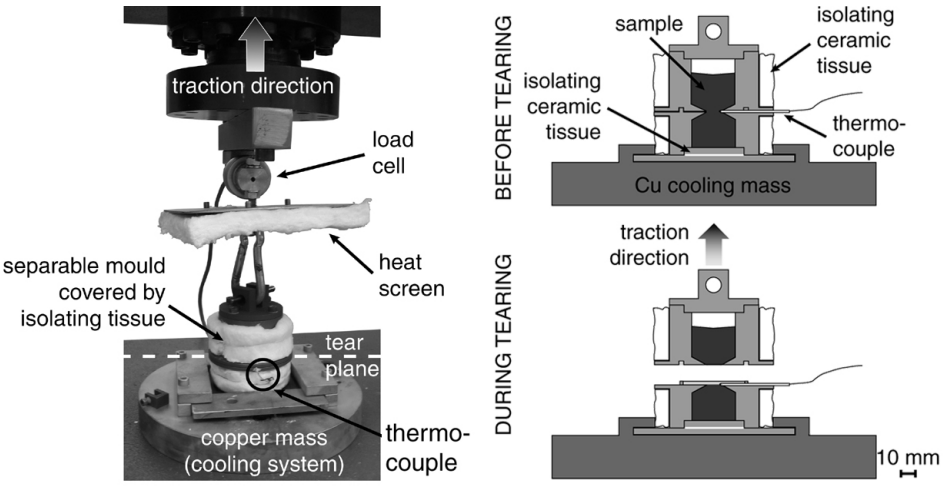


**Figure 4.1:** Picture of the setup and schematic representation of the mold used in the mushy zone tearing test [5].

The alloy selected for this study was Al-1wt%Cu because of its high hot tearing susceptibility. First of all, this alloy is melted and grain refiner is added (in a proportion of 1 kg of refiner per

ton of alloy). The melt is poured in the mold, which can then be closed. The filled mold is then put back into the furnace at about 800 °C until thermal equilibrium is reached (i.e. typically for 30 minutes). The mold is then taken out of the furnace and fixed into the tensile test setup. Since the lateral sides are covered with an efficient insulator, heat is mostly extracted at the bottom, due to contact with the copper chill. The temperature $T_{center}$ at mid height of the sample (in the reduced cross-section area, i.e. the neck) is monitored by a thermocouple inserted in the mold while solidification progresses from the bottom. When $T_{center}$ reaches a selected value $T_{tear}$ corresponding to a relevant value of $g_s$, the tensile test starts (both halves of the mold having been previously allowed to separate).

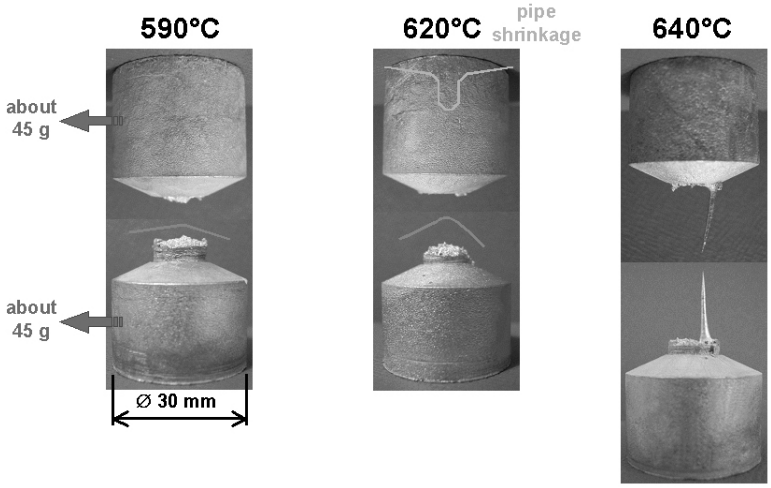


**Figure 4.2:** Samples torn at different temperatures [5].

In this test, a constant displacement rate $\dot{u} = 3.3$ mm s$^{-1}$ is imposed to the upper half of the mold while the bottom half remains fixed to the immobile copper chill. The force response of the sample is measured until fracture occurs. The thermal response is also available from the thermocouple placed at mid-height. Moreover, metallographic examination of the solidified samples revealed rather globular grains of about 300 $\mu$m in size.

Figure 4.2 shows pictures of three samples corresponding to different values of $T_{tear}$ after failure. It is important to remark that the crack front is not found in the middle of the reduced cross-section region. This is due to the fact that the thermal field is not symmetrical with respect to the tear plane (due to cooling from the bottom). Most often, tear propagate above the desired tear plane, where the mushy alloy is weaker. The magnitude of this deviation depends on the test temperature.

After failure, the samples were observed in an SEM. Both spikes and bridges were found on the fracture surface. This showed that the fracture modes evolves as $g_s$ increases. Around 90% of solid, evidence of intergranular failure along a liquid path is mostly observed. At higher solid content, some broken solid bridges appear. Below the solidus temperature, a more solid-like fracture mode is found. As an example, Figure 4.3 shows a fractography of a sample torn at $T_{tear} = 620$°C. The smooth features of the surface are indicators of an intergranular failure through a liquid path, which is typical of hot tearing.

During the tensile test, the maximum force is reached just before fracture occurs. This maximum force at fracture, $F_{fail}$, can be plotted as a function of $T_{tear}$ and such a result is shown on Figure 4.4. The rate of increase in tensile strength (measured by $F_{fail}$) is maximum between 620 °C and 630 °C. These temperatures correspond to solid fractions very close to $g_s = 0.95$, i.e.

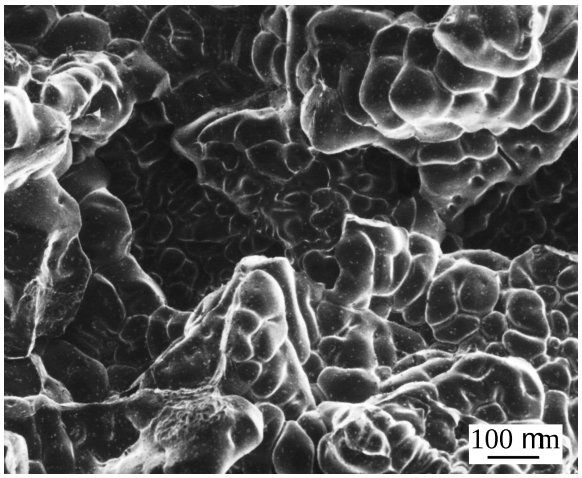


**Figure 4.3:** SEM image of a fracture surface for $T_{tear} = 620$ °C [5].

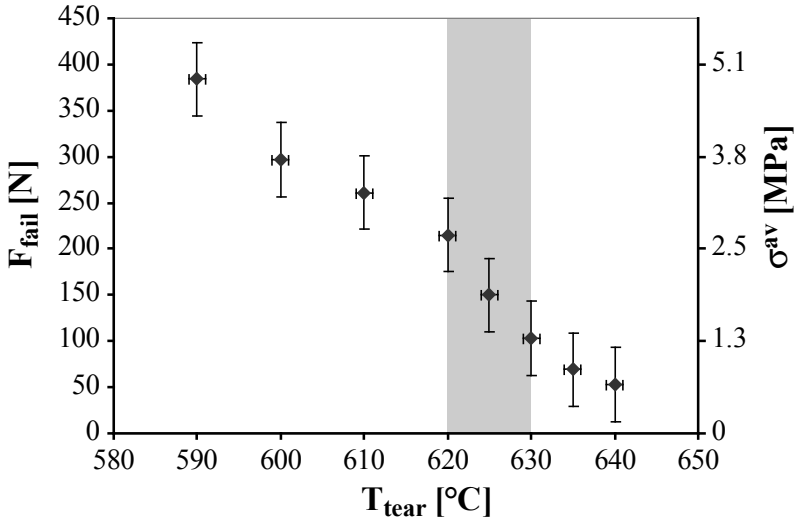


**Figure 4.4:** Force at fracture vs. tearing temperature from [5]. Please note that the grey shaded area indicates a sharp increase in tensile strength over a range of temperature corresponding to $0.95 < g_s < 0.96$. An indication of the average tensile stress $\sigma^{av}$ corresponding to the force at fracture is given and obtained by dividing $F$ with the section at the neck $S_0 = \pi \cdot \left(5 \cdot 10^{-3}\right) = 7.85 \cdot 10^{-5}$ m$^2$.

to the coalescence point. The increase in tensile strength may indeed be used as an indicator of when coalescence starts, as already outlined in [2]. Please note that $F_{fail}$ may be divided with the cross section of the sample at the neck to be converted into an average stress $\sigma^{av}$. However, this stress may not actually correspond to the intrinsic tensile strength of the material because it is inhomogeneous through the sample.

## 4.2 Alcan(-Pechiney)'s Rig Test

Another experiment that is going to be considered in this work is the dogbone test designed by Magnin *et al* [91]. This test was further developed and used by Commet and Vernède at the

Alcan (formerly Pechiney) research center in Voreppe, France [4].

In this test, a dogbone-shaped mold is positioned horizontally (the top of the mold is open) and its ends are connected to a tensile machine. An insulated U-shaped feeding system is designed so that the liquid alloy can fill the mold from the bottom, as shown schematically on Figure 4.5.

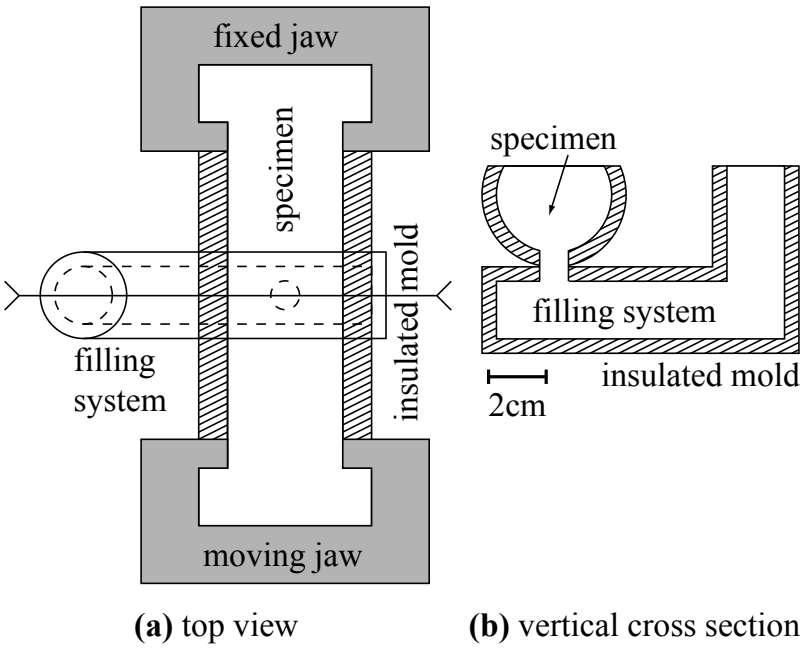


**Figure 4.5:** Schematic representation of the geometry of the rig test [4], both in (a) top view and (b) vertical cross-section.

At the beginning of the test, the mold is closed by a steel chill placed on top of it. The liquid alloy is then poured through the gating system and fills the mold from the bottom (Figure 4.6a). During the first seconds of the test, the alloy is thus in contact with the chill, which leads to the formation of a solid crust at the top of the specimen. After some time, the chill is removed and this crust is reheated by the underlying hot liquid. Moreover, the mold is insulated so that heat is mostly extracted through the jaws of the tensile machine, i.e. along the tensile direction (horizontal). After some time (typically 60 s), the isotherms are thus found to be roughly perpendicular to the direction in which strain will be applied. In the middle of the sample, a vertical symmetry plane is found. This location will act as a hot spot and corresponds to where failure is expected to occur (expected tear plane). Moreover, the feeding system is also insulated and remains filled during the test. As a consequence, the hot spot is always in contact with a reservoir of liquid alloy and healing may thus occur.

The temperature is monitored by thermocouples inserted at several locations in the mold and in the sample. When the temperature at the tearing plane[1] reaches a prescribed value $T_{tear}$, the tensile test starts. Tensile loading is conducted by applying a constant displacement rate to one end of the sample (the other one being fixed) along the longitudinal direction : $\dot{u} = 2.5,\ 10$ or $40$ mm min$^{-1}$. The reaction force from the sample can then be recorded. The evolution of the force and displacement at failure as a function of solid fraction in the tear plane

[1] more precisely, this temperature is measured by the thermocouple located in the tear plane, 8 mm below the sample surface and 3 mm away from the mold.

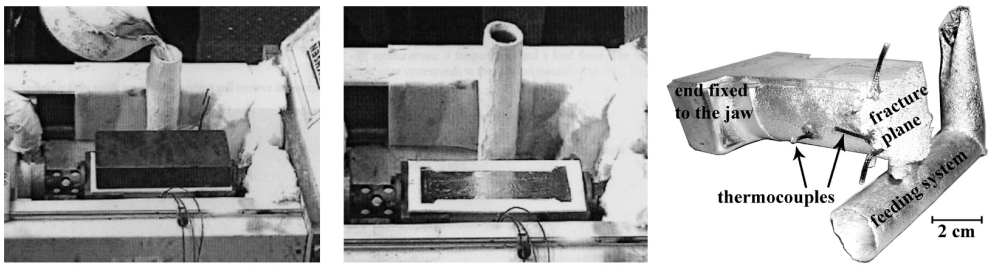


**Figure 4.6:** (a) at the beginning of the test, the mold is closed by the chill and liquid alloy is poured through the gating system (b) the chill was removed and solidification progresses along the sample in the longitudinal direction (c) fully solidified sample after the test.

can thus be studied. Please note that, before the tensile test is started, one end of the sample is allowed to move so that no stress due to thermal contraction arises.

Vernède *et al* [4] worked with various alloys (i.e. Al-2wt%Cu, Al-4wt%Cu and AA5182) and also studied fracture surfaces using SEM images. In the present study, we shall focus on the tensile results obtained for grain-refined (proportion 2 kg/ton) Al-2wt%Cu. For example, the force measured at fracture shows how most of the tensile strength develop around $g_s = 0.96$, as suggested on Figure 4.7. This experimental data was provided by B. Commet and S. Vernède from Alcan, research center in Voreppe (CRV), France.

## 4.3 Full-Scale Billet

In addition to the application of the semi-coupled approach to hot tearing tests performed at the laboratory scale, it is necessary to investigate the potential of the method for modeling full-scale industrial castings. Within the framework of the VIRCAST project, AA5182 billets were produced under industrial conditions, using a modified casting recipe in order to be able to study hot tearing more specifically. Several billets were cast as reported in [6].

In these tests, billets of 254 mm in diameter and 3.5 m in length were cast with the Wagstaff Hot Top AirSlip$^{TM}$ technology by Alcan (formerly Pechiney). The alloy selected for this hot tearing study is an AA5182 (typical composition : 4.50 wt%Mg, 0.37 wt%Mn, 0.28 wt%Fe, 0.11 wt%Si and 0.06 wt%Cu). The casting speed, $v_{cast}$, is prescribed as a function of the cast length according to the recipe shown on Figure 4.8. At start-up, the casting speed is kept low enough (80 mm min$^{-1}$) to ensure that no tears will form. Once a pseudo-steady state is reached, $v_{cast}$ is increased up to 140 mm min$^{-1}$ (with an increase of 60 mm min$^{-1}$ over 1 m). At some point during this ramp, a hot tear initiates at the center of the billet (along the centerline). After this maximum, the casting speed is ramped down and the hot tear heals. At the end of the casting, $v_{cast}$ may either remain constant or increase again (40 mm min$^{-1}$ in 200 mm) in order to initiate the tear again. The latter situation will be studied in this work.

The depth of the liquid pool was recorded by touching the sump with a rod during a typical experiment and may be used for validation of the thermal field model. Moreover, the amount of hydrogen dissolved in the melt was measured (using an Alscan$^{TM}$) for each of the billets, which is a very useful information when using the porosity module. After complete solidification, ultrasonic (US) measurements were conducted on the billets to locate hot tears. From this, it appeared that no defect is formed at start-up and that hot tears initiate for a casting speed

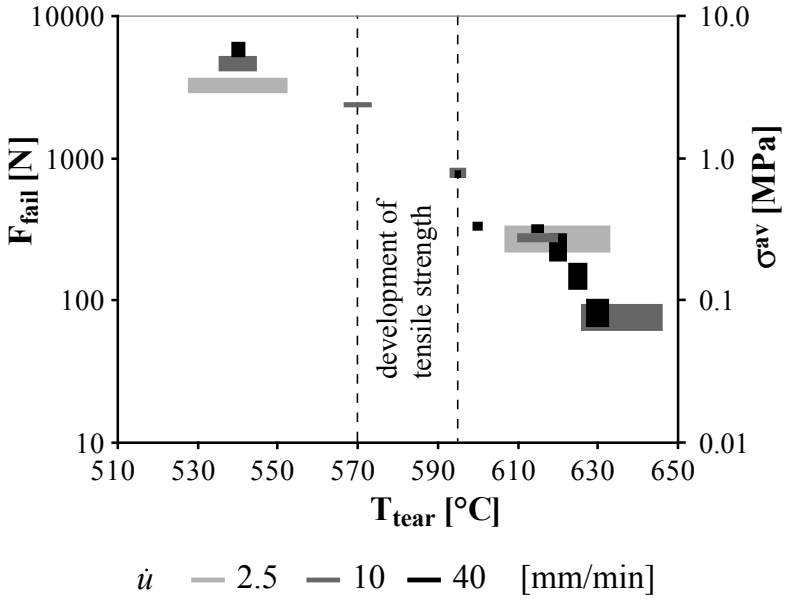


**Figure 4.7:** Force at fracture measured in the rig test [4] as a function of the test temperature for different traction speeds. The size of the spots indicates the experimental uncertainty and is related to the variation in temperature during the test and on the scatter in measured force for different tests under the same conditions. Please note that the force at failure is plotted on a logarithmic scale and that it increases sharply between 570 °C and 595 °C ($0.96 < g_s < 0.98$). The value of $F$ is proportional to a stress $\sigma^{av}$ (the proportionality constant is the cross-section of the sample $S_0 = 1010$ mm$^2$). Please note that $F_{fail}$ is rather insensitive to the strain rate, except at low temperature, where it is measured at yielding because tearing did not occur.

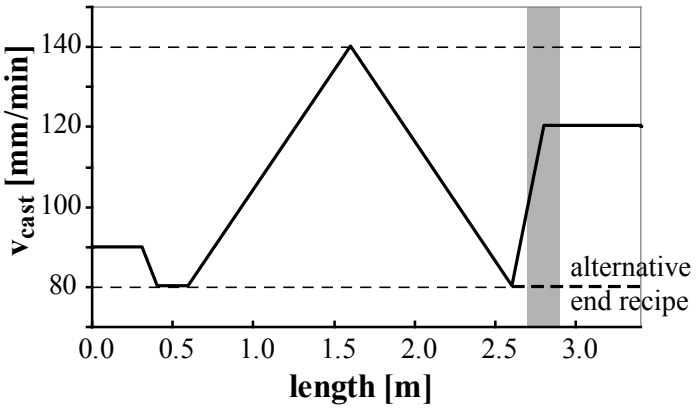


**Figure 4.8:** Casting recipe used for casting industrial size AA5182 billets for the purpose of studying hot tearing [6]. The grey-shaded region was observed in details by Grasso [5].

$v_{cast}^{start}$ and will only heal for a smaller casting speed: $v_{cast}^{heal} < v_{cast}^{start}$. This results is in agreement with the fact that initiation of a crack is often the critical step in hot tear formation. The same authors could also study the effect of grain refinement and alloy composition and show that the hydrogen content appeared to have no marked effect on hot tearing for these castings [6].

One of these billets was studied in more details by Grasso [5]. Using EBSD measurements,

this author showed that the tear propagated between highly misoriented grains, which is where the last remaining liquid films are found according to the theory of coalescence. Moreover, he could observe the hot tear directly in the part where the last increase in casting speed occurred (grey shaded area on Figure 4.8). Between 2.7 m and 2.95 m the billet was cut into 1 cm thick slices. The defects were then observed using a penetrant dye technique.

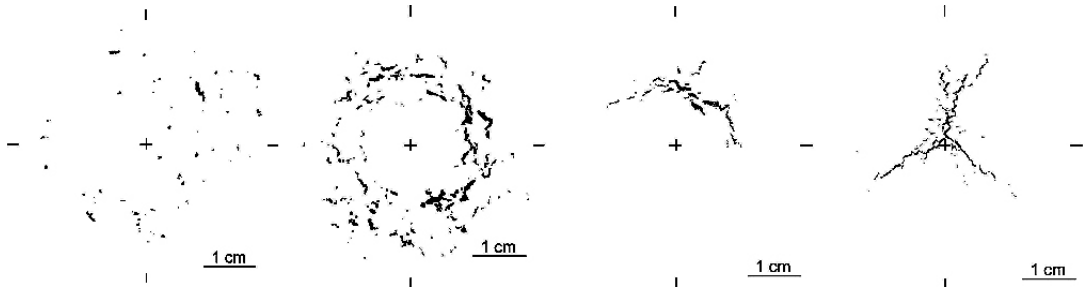


**Figure 4.9:** Evolution of the hot tear morphology during the increase in $v_{cast}$ at the end of the billet [5]. The cast height increases from left to right and the center of the billet is indicated by the cross.

Initially, no defect could be observed. Further up, porosity is found in an annular distribution around the center. As the casting speed is increased further, a rather linear macrocrack (hot tear) is observed. Finally, the tear develops into a star-shaped crack with three branches and becomes centered.

These industrial scale castings are very interesting because they are well documented and have been obtained using actual casthouse equipment, close to realistic processing conditions. On the other hand, they also involve all the complexity related to an industrial process. As a consequence, interpreting these results is quite complicated and quantitative analysis is only possible provided efficient numerical modeling is available.

# Chapter 5

# Simulation Parameters

In this chapter, all of the parameters that were used to model the experiments presented in the previous chapter are summarized. This includes meshing, time step, material properties and boundary conditions for the thermal, mechanical and liquid pressure (porosity) calculations.

## 5.1 Mushy Zone Tearing Test

### Thermal Model

The mushy zone tearing test developed by Grasso [5] was addressed first. The problem is axisymmetric and can thus be treated in 2D. For thermal modeling, both the sample and the mold are considered and included in the mesh, as shown on Figure 5.1. In the sample, the mesh is refined at the neck (reduced cross section), where strains will tend to concentrate. Due to this refinement, the quality of the mesh in the mold is rather poor locally (high aspect ratios). This is not expected to be a problem since those deformed elements will be used only for calculating the thermal field in the mold, which does not need to be calculated most accurately. The thermal boundary conditions were described as follows (see Figure 5.1) :

1. symmetry : the axis of cylindrical symmetry is treated with a zero flux condition.

$$\kappa \nabla T \cdot \mathbf{n} = 0$$

2. mold sample interface : the heat flux exchanged at the interface between the mold and the solidifying specimen is calculated as a function of the difference in the surface temperatures for each domain.

$$\kappa \nabla T \cdot \mathbf{n} = -h^{int} \left( T_{surf}^{sample} - T_{surf}^{mold} \right)$$

3. air gap : the mold is not completely filled with liquid alloy. As a consequence, some air is present between the top of the casting and the mold. This is described by a convective heat transfer.

$$\kappa \nabla T \cdot \mathbf{n} = -h^{air\ gap} \left( T_{surf} - T_{air\ gap} \right)$$

Due to previous temperature homogenization, this air is hot and does not exchange heat very efficiently.

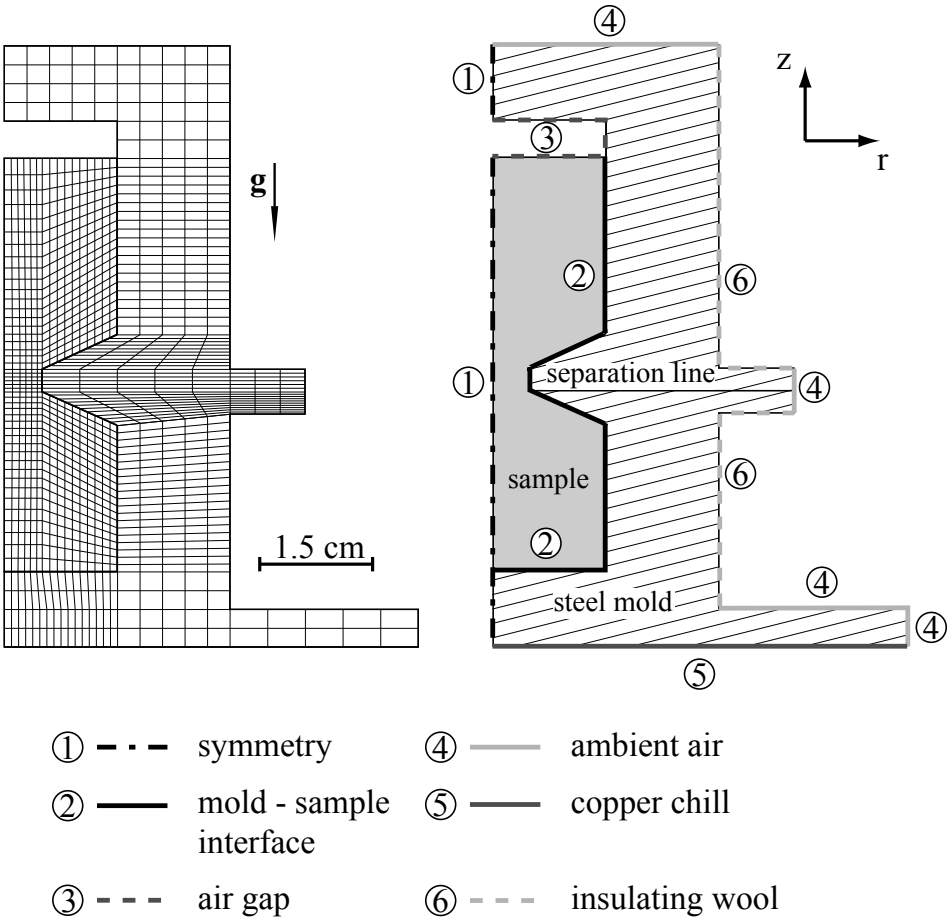


**Figure 5.1:** Mesh and thermal boundary conditions used for modeling the tensile tearing test of Grasso [5].

4. ambient air : part of the mold surface is exposed to the ambient air. The heat transfer at this boundary is modeled by :

$$\kappa \nabla T \cdot \mathbf{n} = -h^{ambient} \left( T_{surf} - T_{room} \right)$$

5. copper chill : the bottom of the mold is in contact with the copper block, so that :

$$\kappa \nabla T \cdot \mathbf{n} = -h^{chill} \left( T_{surf} - T_{copper} \right)$$

   At this boundary, the heat extraction is good but not extremely high because the thermal contact is not strongly enforced and the chill is not water-cooled.

6. insulating wool : parts of the mold are covered with an insulator that minimizes the heat exchange so as to promote unidirectional heat extraction through the bottom of the mold. This is modeled using :

$$\kappa \nabla T \cdot \mathbf{n} = -h^{insulator} \left( T_{surf} - T_{room} \right)$$

The values used for the different coefficients are given in Table 5.1. The efficiency of the various heat transfer phenomena is reflected by the corresponding values of $h$. Initially, the temperature

| $h^{int}$ | $h^{air\ gap}$ | $h^{ambient}$ | $h^{chill}$ | $h^{insulator}$ | $\left[\mathrm{W\ m^{-2}\ K^{-1}}\right]$ |
|---|---|---|---|---|---|
| 850 | 20 | 20 | 120 | 1 | |
| | $T_{air\ gap}$ | $T_{room}$ | $T_{copper}$ | | [°C] |
| | 700 | 25 | 25 | | |

**Table 5.1:** Coefficients used to describe the thermal boundary conditions in the mushy zone tearing test.

is assumed to be uniform with a value of 750 °C and the flow of the liquid alloy in the mold is not taken into account.

The materials parameters used in the thermal model are summarized in Table 5.2. The mold is made of stainless steel and is characterized by its volume specific heat $C_p^{steel}$ and its thermal conductibility $\kappa^{steel}$. The specimen is an Al-1wt%Cu with its own specific heat $C_p^{AlCu1}$ and thermal conductivity $\kappa^{AlCu1}$ taken as constants for the sake of simplicity. Moreover, upon solidification, the latent heat $L$ is released, proportionally to the increase in solid fraction. The solidification path $g_s\,(T)$ is such that solidification starts at $T_{liq}^{AlCu1} = 659.4$ °C and is terminated at 560 °C, i.e. above the eutectic temperature (of 548 °C in the Al-Cu system). This is shown on Figure 5.2 for the coherent mushy zone. The path used in the simulation was adapted from thermal measurements given in [5].

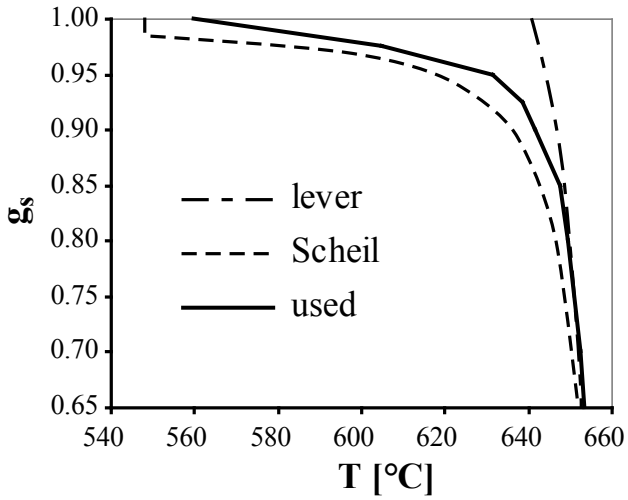


**Figure 5.2:** Solidification path for the Al-1wt%Cu alloy (used in the simulation and compared to the predictions of Scheil's model and the lever rule). Please note that the $g_s$ scale includes only the values that correspond to the coherent mushy zone.

The calculation was conducted for 700 s physical time using time steps of 2 s and lasted for 15 minutes on an Intel$^{\mathrm{TM}}$ Xeon @ 2GHz. Please note that the thermal calculation was in fact conducted in a quarter of a 3D cylindrical domain to ensure compatibility with the porosity module.

| | $C_p$ $\left[\mathrm{J\ m^{-3}\ K^{-1}}\right]$ | $\kappa$ $\left[\mathrm{W\ m^{-1}\ K^{-1}}\right]$ | $L$ $\left[\mathrm{J\ m^{-3}}\right]$ |
|---|---|---|---|
| steel | $5 \cdot 10^6$ | 40 | |
| Al-1wt%Cu | $3.2 \cdot 10^6$ | 170 | $9 \cdot 10^8$ |

**Table 5.2:** Thermal materials parameters used in the simulation of the mushy zone tearing test.

### Mechanical Model

The thermal model presented above provides the evolution of the temperature field $T(\mathbf{x}, t)$. This data is used as an input for the mechanical calculation. The latter is performed on the sample only (because the mold is assumed to be rigid) using the same mesh than for the thermal calculation[1]. As shown on Figure 5.3, the mesh is refined in the reduced cross-section area (neck) because the applied strain will be localized in that region.

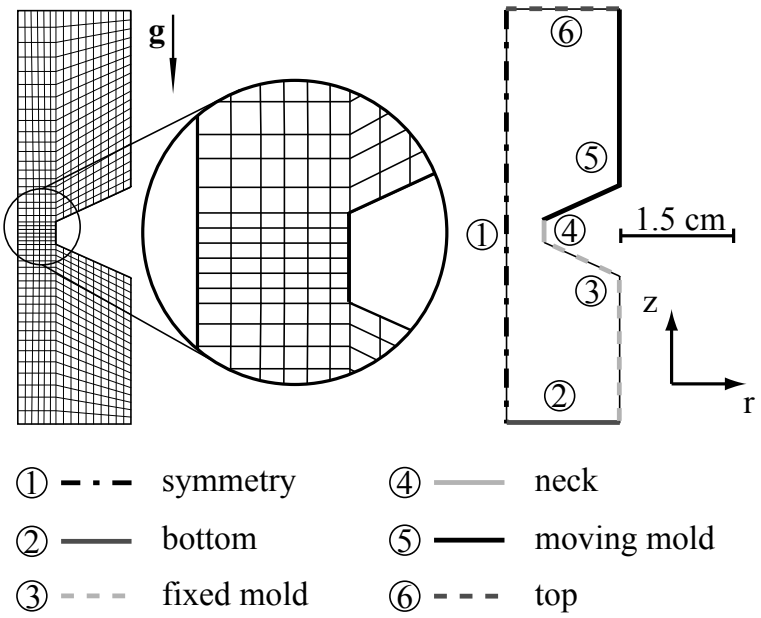


**Figure 5.3:** Mesh and mechanical boundary conditions used for modeling the tensile tearing test of Grasso [5].

Figure 5.3 also displays what conditions are applied to the boundaries of the sample :

1. symmetry : the axis of cylindrical symmetry corresponds to a zero displacement condition in the radial direction, $u_r = 0$. Free movement is allowed along the $z$ direction (zero tangential force $F_z = 0$).

2. bottom : even though the bottom of the cast is not really fixed to the mold, its vertical displacement is prescribed to zero because it is in contact with the immobile half of the mold and solidified at the time of the test, $u_z = 0$. In the radial direction, a zero force condition applies ($F_r = 0$).

[1] this time, a truly 2D domain with axisymmetric elements is used.

3. fixed mold : the sides of the casting in contact with the part of the mold that is fixed to the copper chill are not allowed to move in the axial direction $u_z = 0$. On the other hand, their motion is free in the radial direction $F_r = 0$.

4. neck : a zero force condition ($F_z = F_r = 0$) is applied at the surface of the cast in the neck area. Please note that applying different conditions to this region (stick to the mold, zero force or zero vertical displacement) did not have a significant influence on the results.

5. moving mold : the sides of the casting in contact with the mobile half of the mold move upwards at the applied tensile velocity $\dot{u}_z = 3.3$ mm s$^{-1}$ (and $F_r = 0$) as soon as the tensile test is started.

6. top : the top of the specimen experiences zero force $F_z = F_r = 0$.

Please note that gravity was neglected in these calculations.

Having specified the boundary conditions, it is necessary to describe the behavior of the material. First of all, the elastic modulus $E$ varies with temperature as shown on Figure 5.4 and Poisson's ratio is $\nu = 0.33$. Please note that Young's modulus has a constant very low value of $E = 0.04$ GPa in the mushy zone.

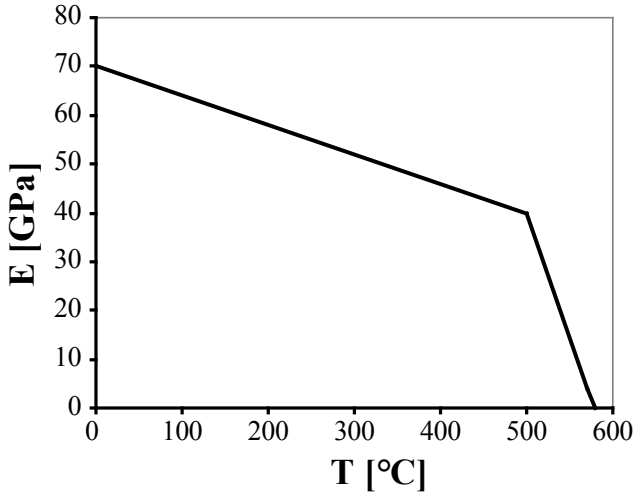


**Figure 5.4:** Young's modulus vs. temperature for the Al-1wt%Cu alloy.

The thermal contraction behavior ($g_s^{th} = 0.8$ and $\alpha^{th} = 25 \cdot 10^{-6}$ K$^{-1}$) could be neglected in these calculations because the strain rate imposed by the tensile machine is much larger than $\dot{\epsilon}_{th}$.

As far as the rheology of the material is concerned, the parameters determined for Al-4wt%Cu were used. It has already been shown that, for high temperature testing, this approximation is satisfactory, provided the correct (i.e. accurate for Al-1wt%Cu) $g_s(T)$ is used [2]. The mushy zone parameters are summarized in Table 5.3 and are those determined in [2], except for the coalescence point, $g_s^{coal}$, which is set to a slightly higher value.

The parameters for the hot solid rheology are also those from [2] and are summarized in Table 5.4. At lower temperatures, the parameters from [71] are used and are summarized in Table 5.5. Please note that the continuity of properties in temperature imposes that the generalized

| $p$ | $\alpha_0$ | $\alpha_1$ | $g_s^{coh}$ | $g_s^{coal}$ | $k$ |
|---|---|---|---|---|---|
| 0.11 | 4.45 | $1.07 \cdot 10^{-2}$ | 0.65 | 0.95 | 100 |

**Table 5.3:** Mushy zone rheology parameters, which appear in Equations (2.52) and (2.53) (p. 28) [2].

| $s_0$ [MPa] | $A$ $\left[\mathrm{s}^{-1}\right]$ | $Q$ $\left[\mathrm{kJ\ mol}^{-1}\right]$ | $n$ |
|---|---|---|---|
| 4.77 | $9 \cdot 10^5$ | 154 | 3.8 |

**Table 5.4:** Hot solid rheology parameters, which appear in Equation (2.45) (p. 26) [2].

| $\kappa = p_1^\kappa \left(1 - p_2^\kappa \tanh\left(\frac{T_{[\mathrm{K}]} - p_4^\kappa}{p_3^\kappa}\right)\right)$ | | | |
|---|---|---|---|
| $p_1^\kappa$ [MPa] | $p_2^\kappa$ | $p_3^\kappa$ [K] | $p_4^\kappa$ [K] |
| 210 | 0.75 | 132 | 540 |
| $\eta = p_1^\eta \left(1 - p_2^\eta \tanh\left(\frac{T_{[\mathrm{K}]} - p_4^\eta}{p_3^\eta}\right)\right)$ | | | |
| $p_1^\eta$ | $p_2^\eta$ | $p_3^\eta$ [K] | $p_4^\eta$ [K] |
| 0.155 | 1 | 135 | 500 |
| $\lambda = p_1^\lambda + p_2^\lambda T_{[\mathrm{K}]} + p_3^\lambda T_{[\mathrm{K}]}^2 + p_4^\lambda T_{[\mathrm{K}]}^3 + p_5^\lambda T_{[\mathrm{K}]}^4$ | | | |
| $p_1^\lambda$ | $p_2^\lambda$ $\left[\mathrm{K}^{-1}\right]$ | $p_3^\lambda$ $\left[\mathrm{K}^{-2}\right]$ | $p_4^\lambda$ $\left[\mathrm{K}^{-3}\right]$ | $p_5^\lambda$ $\left[\mathrm{K}^{-4}\right]$ |
| $-5.17 \cdot 10^{-5}$ | $2.69 \cdot 10^{-4}$ | $-2.56 \cdot 10^{-6}$ | $6.78 \cdot 10^{-9}$ | $-4.37 \cdot 10^{-12}$ |

**Table 5.5:** Intermediate temperatures rheology parameters, which appear in Equation (2.56) (p. 29) [71]. Please note that $T_{[\mathrm{K}]}$ is the temperature expressed in Kelvin.

Ludwik's model is used as soon as the temperature drops below $T_{merge} = 520$ °C. Moreover, work hardening becomes significant below $T_\epsilon = 423$ °C.

The parameters presented in these tables describe fully the mechanical behavior of the alloy as a function of temperature. Since the thermal field is available from a previous calculation and under the specified boundary conditions, it is possible to solve the problem numerically.

The mesh size (at the neck, the elements have a size $\Delta z = 0.5$ mm along the $z$ axis) and time step control parameter ($\chi = 10^{-6}$ for these calculations) are in agrement with the guidelines provided by Equations (3.14) and (3.15) (p. 53). Elements are axisymmetric, 4-noded and bilinear. Typical CPU times were 2 h on an Intel™ Itanium 2 @ 1.6 GHz.

### Liquid Pressure Model

The last modeling step is the porosity calculation. The results of both the thermal and mechanical simulations are used as input. In this case, the boundary conditions are quite simple. On the free surface at the top of the sample, the pressure is prescribed : $p_l = p_{atm} = 101.325$ kPa. The other boundaries of the sample are in contact with the mold, which means that the liquid cannot

escape (zero normal velocity).

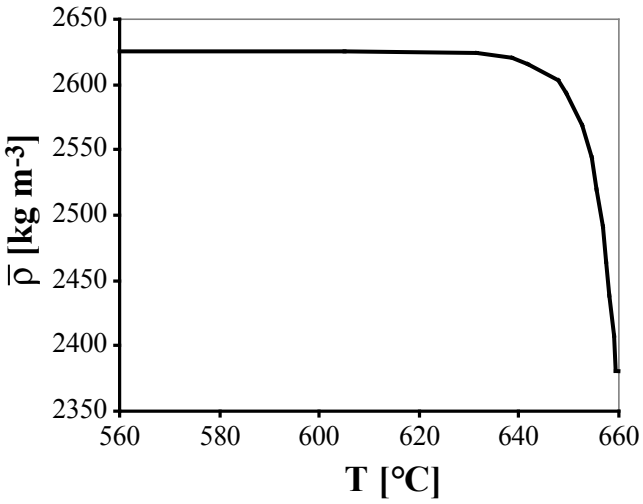


**Figure 5.5:** Average density vs. temperature for the Al-1wt%Cu alloy.

The liquid pressure calculation can be conducted based on the evolution of the average density $\overline{\rho}$ as a function of temperature. The values that were used are plotted on Figure 5.5 and take into account the influence of both temperature (change of phase fractions) and solute segregation (the liquid phase is enriched in copper, leading to a strong increaase of its density) upon $\overline{\rho}$ [3]. Since the term $\nabla \cdot (\overline{\rho}\mathbf{v}_s)$ is known from the mechanical solution, all the pump terms causing the liquid pressure drop are described (see Equation (2.14) on page 17). Moreover, the viscosity was set to a constant value $\mu = 10^{-3}$ Pa s while the permeability $K$ is given by Equation (2.13), where a constant grain size $\phi = 200$ $\mu$m was used.

Porosity formation was included in the model. Two different concentrations of hydrogen were tested (since no measurement on this quantity is available in this experiment) : $[H]_0 =$ 0.25 or 0.4 $\mathrm{cc_{STP}}/100\mathrm{g}$. Moreover, standard parameters were used, such as : hydrogen partition coefficient $k_H = 0.07$, $S = 0.69$ $\mathrm{cc_{STP}}/100\mathrm{g}$[2], $\gamma_{l/v} = 0.9$ J m$^{-2}$, nucleation radius of pores $r_{p,n} = 10$ $\mu$m and average density of nucleation sites for the pores $\rho_{nucl} = 10^9$ m$^{-3}$ [3].

The mesh used for the porosity calculation was based on the 3D axisymmetric model built for the thermal calculation (tetrahedral finite elements). It consists of finite difference cubic cells of $\Delta x = 0.5$ mm in size (see Figure 5.6). The time step was set to $\Delta t = 0.1$ s for most of the calculation and to $\Delta t = 0.01$ s during the tensile test. These values are in agreement with the guidelines given in Equations (3.31) and (3.32). The typical CPU time was of 2 h on an Intel$^{\mathrm{TM}}$ Xeon 2 @ 2 GHz.

## 5.2 Rig Test

### Thermal Model

The rig test presented in [4, 91] was treated in 3D. In the thermal model, both the sample and the metal present in the filling system are considered as shown on Figure 5.7. The mesh is fine

[2]this unit corresponds to cm$^3$ of gas under standard temperature and pressure dissolved per 100 g of alloy, i.e. 0.1 $\mathrm{cc_{STP}}/100\mathrm{g}$ correspond to $0.1\frac{2}{22\,400}\frac{27}{100} = 2.4$ ppm of dissolved hydrogen.

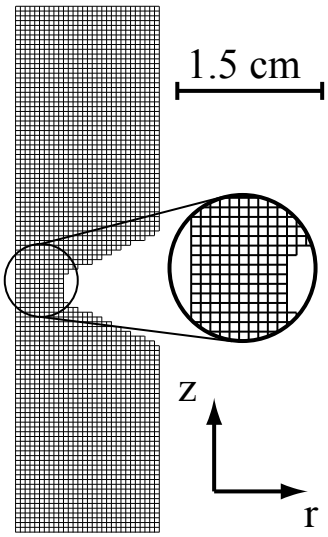


**Figure 5.6:** Cellular mesh used for liquid pressure and porosity modeling of the mushy zone tearing test.

in the longitudinal direction $z$ (tensile strain will be applied in that direction) and coarser in planes perpendicular to that direction (because the isotherms are mostly perpendicular to the main load direction). The sample is meshed using hexahedral elements while the feeding system is composed of tetrahedra.

The thermal boundary conditions are also summarized on Figure 5.7. They are described as follows :

1. symmetry plane perpendicular to $x$ : in the middle of the sample, there exists a vertical symmetry plane containing the tensile direction. On this plane, the heat flux is prescribed to be zero

   $$\kappa \nabla T \cdot \mathbf{n} = 0$$

   Please note that the filling system is not totally symmetrical with respect to that plane. This slight inaccuracy was however shown to have no significant effect on the thermal results.

2. symmetry plane perpendicular to $z$ : in the middle of the sample, there exists a vertical symmetry plane perpendicular to the applied load direction. A symmetry condition has thus to be applied to this plane.

   $$\kappa \nabla T \cdot \mathbf{n} = 0$$

3. feeding system : the feeding system is made of an insulating material and thus exchanges little heat with the outside. This is described with a convective heat transfer flux :

   $$\kappa \nabla T \cdot \mathbf{n} = -h^{fill} \left( T_{surf} - T_{room} \right)$$

   Please note that the geometry of the filling system is not very accurately represented by the mesh. However, due to the small heat exchanges in this region, this inaccuracy does not have a significant effect on the results.

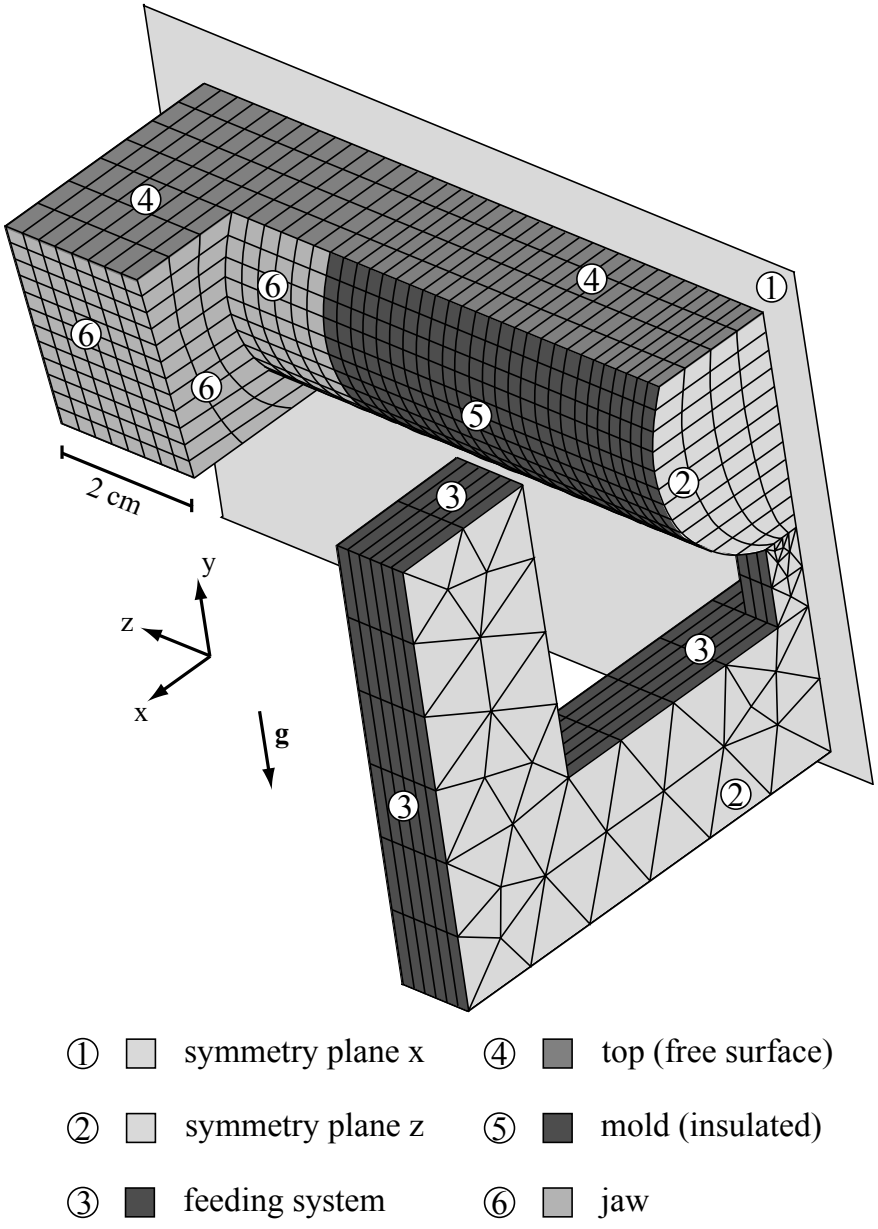


**Figure 5.7:** Mesh and thermal boundary conditions used for modeling the rig test [91].

4. top surface : for the first ten seconds, the top surface is in contact with the chill used to close the mold, leading to a very high heat extraction rate. After the removal of the chill, this surface is in contact with ambient air and much less heat can be exchanged :

$$\kappa \nabla T \cdot \mathbf{n} = -h^{top} \left( T_{surf} - T_{room} \right)$$

5. insulated mold : the gauge length of the sample is contained in a mold made of insulating material. The heat flux is thus small on this surface and described by :

$$\kappa \nabla T \cdot \mathbf{n} = -h^{mold} \left( T_{surf} - T_{room} \right)$$

6. jaw : the end of the sample solidifies in the jaw of the tensile test machine. At this location, no insulator is present so that most of the heat will be extracted through the machine. For

the sake of simplicity, the jaw is not included in the model and heat transfer is described using :

$$\kappa \nabla T \cdot \mathbf{n} = -h^{jaw} \left( T_{surf} - T_{room} \right)$$

The values used for the various coefficients are summarized in Table 5.6 and the value of $h^{jaw}$ is displayed on Figure 5.8. The latter coefficient depends on temperature. It indeed decreases upon solidification and this corresponds to the fact that the temperature in the jaw increases during the test (and an air gap may be formed), which slows down heat extraction. Please note that the initial temperature was uniform and set to 735 °C.

| $h^{top}$ | | $h^{fill}$ | $h^{mold}$ | $\left[\mathrm{W\ m^{-2}\ K^{-1}}\right]$ | $T_{room}$ [°C] |
|---|---|---|---|---|---|
| $0 < t < 10$ s | $t > 10$ s | | | | |
| 2000 | 10 | 5 | 5 | | 20 |

**Table 5.6:** Coefficients used to describe the thermal boundary conditions in the rig test.

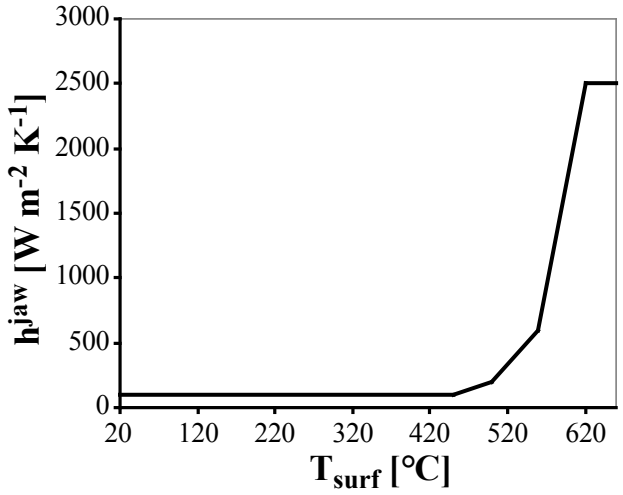


**Figure 5.8:** Heat transfer coefficient at the end of the sample (in contact with the jaws of the tensile test machine).

The materials parameters (Al-2wt%Cu in this case) for the thermal model were also specified. The latent heat was set to $L = 6.5 \cdot 10^8$ J m$^{-3}$ while the specific heat $C_p$ and thermal conductivity $k$ are temperature-dependent functions as plotted on Figure 5.9. Moreover, the solidification path is described by the $g_s(T)$ curve displayed on Figure 5.10. The liquidus of the alloy was $T_{liq}^{AlCu1} = 653$ °C and this data was adapted from [4]. The thermal calculation was conducted using time steps of 2 s (physical time : 400 s) and lasted for 1 minute on an Intel$^{\mathrm{TM}}$ Xeon @ 2GHz

### Mechanical Model

In the mechanical model, the filling system is not included because it does not have a significant effect on the strain field. In this region, the alloy indeed remains liquid during the test. In the sample, the mesh is identical to that used for solving the thermal problem. The boundary

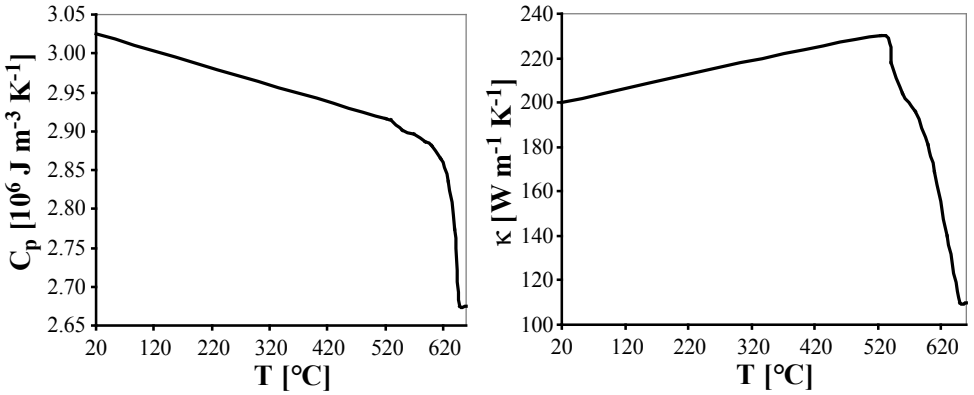


**Figure 5.9:** Specific heat and thermal conductivity as a function of temperature for the Al-2wt%Cu alloy.

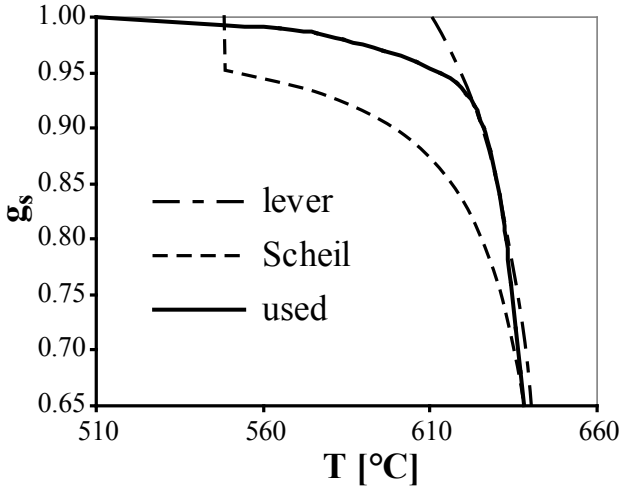


**Figure 5.10:** Solidification path for the Al-2wt%Cu alloy.

conditions that are applied to the sample are summarized on Figure 5.11. They are described as follows :

- symmetry plane perpendicular to x : on this plane the normal displacement must be zero : $u_x = 0$. Movement in all other directions is free (zero force $F_y = F_z = 0$).
- symmetry plane perpendicular to z : this plane corresponds to the expected tear plane and is not allowed to move in the tensile direction : $u_z = 0$. A zero force condition is applied in other directions ($F_x = F_y = 0$).
- jaw : the end of the sample is solidified in the jaw of the tensile test machine when the test is started. This region is free along the $x$ and $y$ axes ($F_x = F_y = 0$) and moves at a constant velocity in the axial direction : $\dot{u}_z$. The model is built using the symmetry of the sample while the actual tensile test is in fact performed with one fixed and one mobile jaw. The value applied for $\dot{u}_z$ must then be half the experimentally imposed displacement rate, as summarized in Table 5.7.
- top surface and mold : the top surface of the sample as well as the part in contact with the mold are free to move ($F_x = F_y = F_z = 0$)).

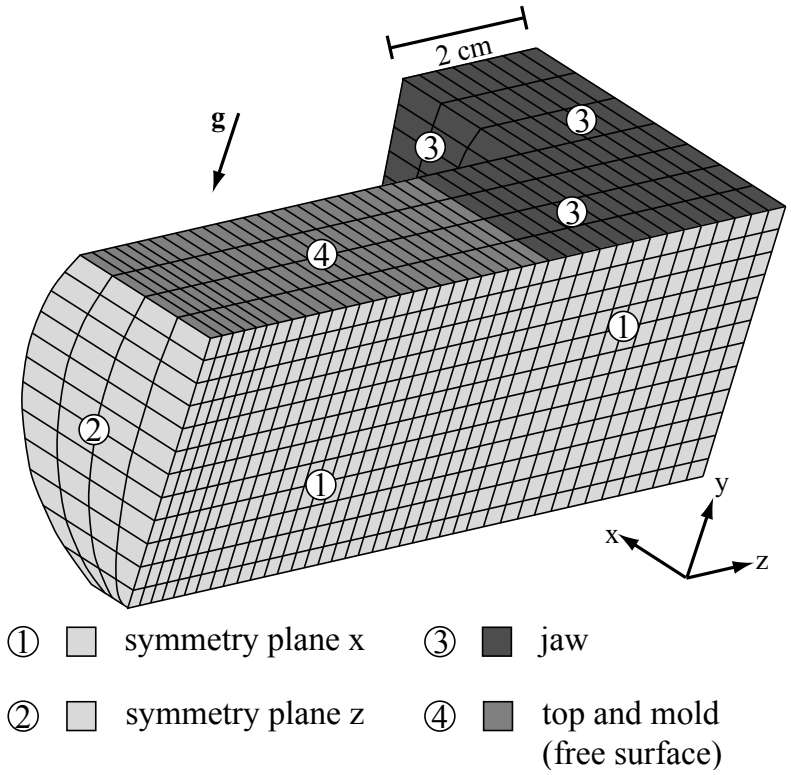


**Figure 5.11:** Mesh and mechanical boundary conditions used for modeling the rig test.

| | | | |
|---|---|---|---|
| Boundary condition $\dot{u}_z$ in $\left[\mathrm{m\ s^{-1}}\right]$ | $2.083 \cdot 10^{-5}$ | $8.333 \cdot 10^{-4}$ | $3.333 \cdot 10^{-4}$ |
| Corresponding experimental tensile speed in $\left[\mathrm{mm\ min^{-1}}\right]$ | 2.5 | 10 | 40 |

**Table 5.7:** Tensile speed, i.e. imposed displacement rate.

In the mechanical calculations, gravity as well as thermal contraction were neglected. This is reasonable because the applied tensile strain is by far the dominant contribution to the deformation of the sample (prior to the beginning of the tensile test, thermal stresses are prevented by allowing free contraction).

As far as the materials properties are concerned, Poisson's ratio was set to a constant value of $\nu = 0.33$ and Young's modulus depends on temperature as displayed on Figure 5.12. Please note that, even at low temperature, the elastic modulus is considerably lower than what is expected for aluminum alloys. This is due to the effect of the tensile test machine, whose compliance leads to a decrease in the apparent value of $E$. The value $E = 2.61$ GPa could be measured at room temperature by a test performed with a fully solidified sample.

Similarly to what was done for the Al-1wt%Cu, the rheological properties of Al-2wt%Cu are taken to be equal to those determined for Al-4wt%Cu, $g_s(T)$ excepted. This time, the actual value from [2] was used for $g_s^{coal}$. The mushy zone parameters are summarized in Table 5.8 and those for the hot solid in Table 5.9.

For lower temperatures, the data from [71] are used again and summarized in Table 5.10. Please note that the continuity of properties imposes that the generalized Ludwik's model is used as soon as temperature drops below $T_{merge} = 520$ °C. Moreover, work hardening becomes

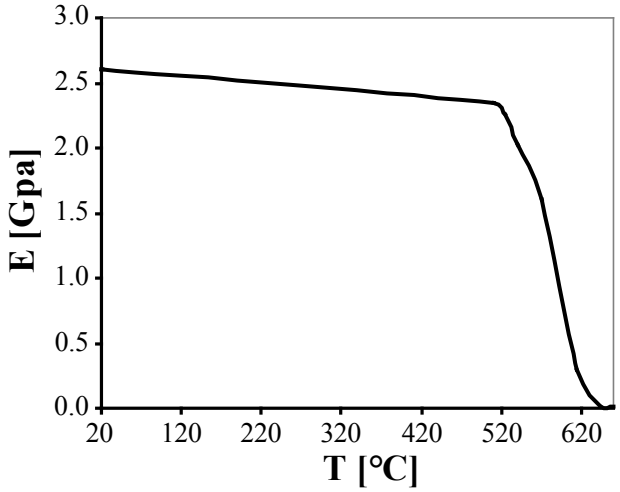


**Figure 5.12:** Effective Young's modulus (taking into account the compliance of the tensile test machine) for the Al-2wt%Cu alloy.

| $p$ | $\alpha_0$ | $\alpha_1$ | $g_s^{coh}$ | $g_s^{coal}$ | $k$ |
|---|---|---|---|---|---|
| 0.11 | 4.45 | $1.07 \cdot 10^{-2}$ | 0.65 | 0.94 | 100 |

**Table 5.8:** Mushy zone rheology parameters, which appear in Equations (2.52) and (2.53) (p. 28) [2].

| $s_0$ [MPa] | $A$ $\left[\mathrm{s}^{-1}\right]$ | $Q$ $\left[\mathrm{kJ\ mol}^{-1}\right]$ | $n$ |
|---|---|---|---|
| 4.77 | $9 \cdot 10^5$ | 154 | 3.8 |

**Table 5.9:** Hot solid rheology parameters, which appear in Equation (2.45) (p. 26) [2].

significant below $T_\epsilon = 423$ °C.

The mesh size (close to the tearing plane, elements have a size $\Delta z = 1.66$ mm along the $z$ direction) and time step control parameter ($\chi = 10^{-6}$ for these calculations) are in agrement with the guidelines provided by Equations (3.14) and (3.15) (p. 53). Elements are 8-noded linear. Typical CPU times were 6 h on an Intel$^{\mathrm{TM}}$ Itanium 2 @ 1.6 GHz to simulate 10 s of physical time.

### Liquid Pressure Model

In this step, the feeding system is included again (as on Figure 5.7). On the free surfaces, i.e. at the top the sample and at the top of the feeding system (please note that both these surfaces have the same height, i.e. $y$ coordinate), the pressure is prescribed : $p_l = p_{atm} = 101.325$ kPa. The other boundaries of the sample are in contact with the mold, and a zero liquid flow out of these boundaries is thus imposed.

The evolution of $\overline{\rho}$ with temperature is given on Figure 5.13. This curve was obtained taking into account both temperature and solute concentration effects. The copper segregated into the liquid indeed increases significantly the density of the latter phase at low temperature. The viscosity was set to a constant value $\mu = 1.35 \cdot 10^{-3}$ Pa s and the permeability $K$ is given by

| $\kappa = p_1^\kappa \left(1 - p_2^\kappa \tanh\left(\frac{T_{[\mathrm{K}]} - p_4^\kappa}{p_3^\kappa}\right)\right)$ | | | |
|---|---|---|---|
| $p_1^\kappa$ [MPa] | $p_2^\kappa$ | $p_3^\kappa$ [K] | $p_4^\kappa$ [K] |
| 210 | 0.75 | 132 | 540 |
| $\eta = p_1^\eta \left(1 - p_2^\eta \tanh\left(\frac{T_{[\mathrm{K}]} - p_4^\eta}{p_3^\eta}\right)\right)$ | | | |
| $p_1^\eta$ | $p_2^\eta$ | $p_3^\eta$ [K] | $p_4^\eta$ [K] |
| 0.155 | 1 | 135 | 500 |
| $\lambda = p_1^\lambda + p_2^\lambda T_{[\mathrm{K}]} + p_3^\lambda T_{[\mathrm{K}]}^2 + p_4^\lambda T_{[\mathrm{K}]}^3 + p_5^\lambda T_{[\mathrm{K}]}^4$ | | | |
| $p_1^\lambda$ | $p_2^\lambda$ $\left[\mathrm{K}^{-1}\right]$ | $p_3^\lambda$ $\left[\mathrm{K}^{-2}\right]$ | $p_4^\lambda$ $\left[\mathrm{K}^{-3}\right]$ | $p_5^\lambda$ $\left[\mathrm{K}^{-4}\right]$ |
| $-5.17 \cdot 10^{-5}$ | $2.69 \cdot 10^{-4}$ | $-2.56 \cdot 10^{-6}$ | $6.78 \cdot 10^{-9}$ | $-4.37 \cdot 10^{-12}$ |

**Table 5.10:** Intermediate temperatures rheology parameters, which appear in Equation (2.56) (p. 29) [71]. Please note that $T_{[\mathrm{K}]}$ is the temperature expressed in Kelvin.

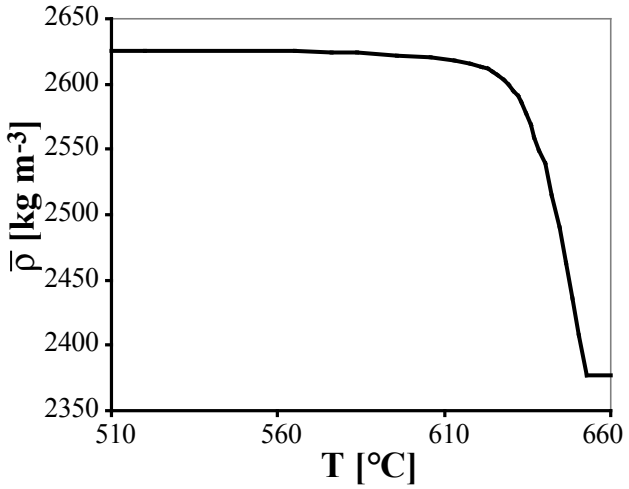


**Figure 5.13:** Average density vs. temperature for the Al-2wt%Cu alloy.

Equation (2.13) (p. 17), with a constant grain size $\phi = 100$ $\mu$m.

Porosity formation was included in the model. The amount of hydrogen dissolved in the melt was estimated as: $[H]_0 = 0.3$ $\mathrm{cc_{STP}}/100\mathrm{g}$. Moreover, standard parameters were used, such as: hydrogen partition coefficient $k_H = 0.07$, $S = 0.69$ $\mathrm{cc_{STP}}/100\mathrm{g}$, $\gamma_{l/v} = 0.9$ J m$^{-2}$, nucleation radius of pores $r_{p,n} = 10$ $\mu$m and average density of nucleation sites for the pores $\rho_{nucl} = 10^9$ m$^{-3}$ [3].

The finite difference mesh used for the porosity calculation was based on the tetrahedrized finite element mesh built for the thermal calculation. The cubic cells have a size $\Delta x = 1$ mm. The time step was set to $\Delta t = 0.1$ s. These values are in agreement with the guidelines given in Equations (3.31) and (3.32) (p. 57). The typical CPU time was 1.5 h on an Intel$^{\mathrm{TM}}$ Xeon 2 @ 2 GHz.

## 5.3 Full-Scale Billet

### Thermal Model

The billets cast within the framework of the VIRCAST project by Commet *et al* [6] have been used as an industrial scale case. This problem is axisymmetric and will thus be treated as such. Since the DC casting process is used, liquid is progressively added to the cast and this has to be taken into account when setting up the model.

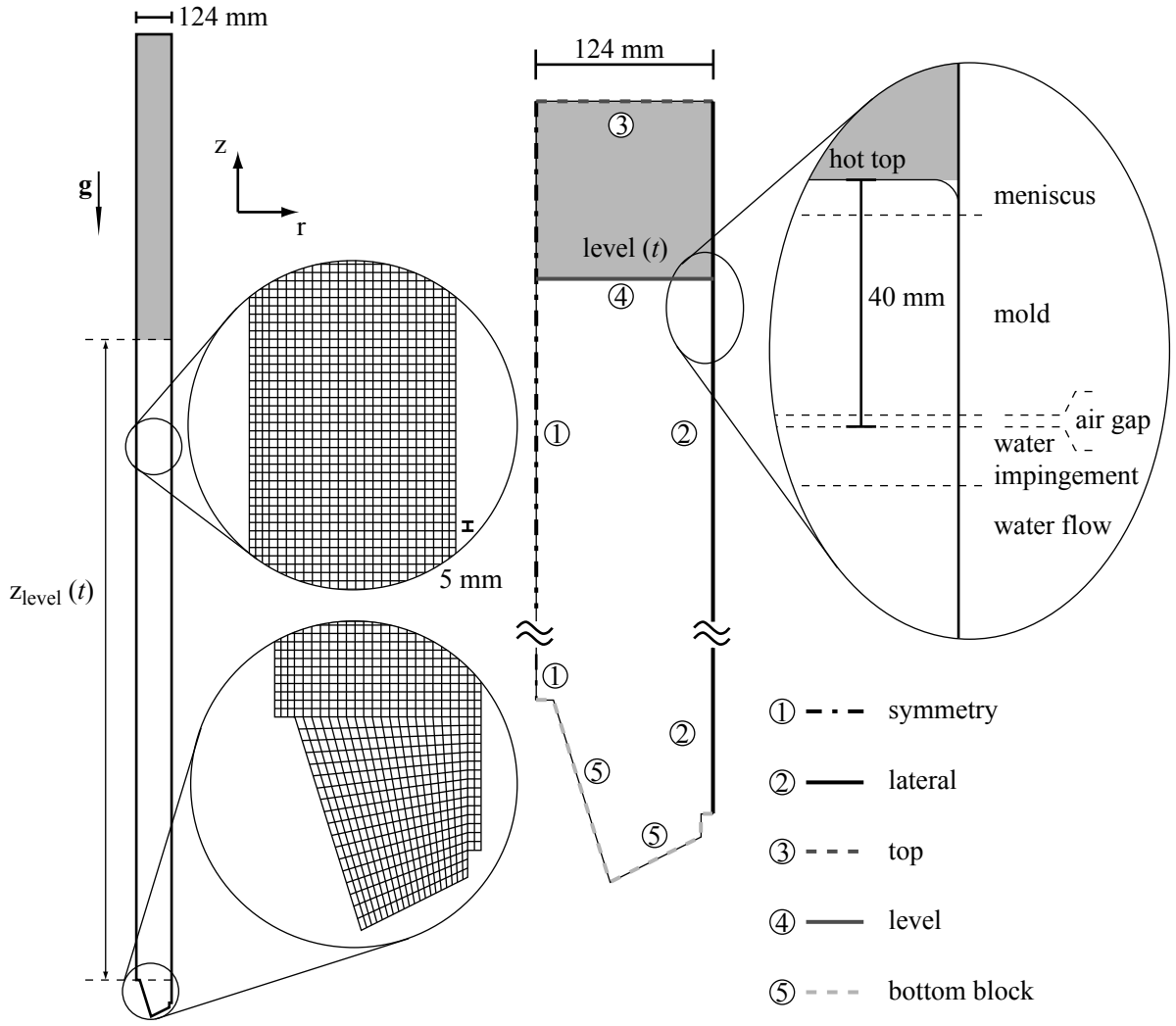


**Figure 5.14:** Mesh and thermal boundary conditions used for modeling the DC-cast billet.

The conditions and mesh used for the thermal calculations are illustrated on Figure 5.14. The entire billet is meshed and included in the calculation. However, at some time $t$ during the DC casting process, the height of the billet is only equal to $z_{level}$. This cast height is measured between the hot top and the bottom of the billet and goes from 0 to 3.4 m during the process. The value of $z_{level}$ depends on time and is related to the casting speed by :

$$\frac{\mathrm{d}z_{level}}{\mathrm{d}t} = v_{cast}\left(z_{level}\right) \tag{5.1}$$

Please remember that $v_{cast}$ is prescribed as a function of the cast height (i.e. $z_{level}$) as displayed on Figure 4.8 on page 68.

The boundary conditions are described as follows :

1. symmetry : along the cylindrical symmetry axis, the heat flux must be nil.
2. lateral : the external face of the billet is submitted to the complex boundary conditions already presented on Figure 1.2 on page 5. The following regimes must be distinguished :
   - above liquid level ($z > z_{level}$) : some material, outlined in grey, is already present in the mesh but was not actually cast. In this region an adiabatic condition is imposed (zero heat flux).
   - meniscus ($z_{level} - 6 \text{ mm} < z < z_{level}$) : the liquid alloy is surrounded by the mold and the hot top. Due to bad wettability, a meniscus will form and the liquid alloy will not be in contact with the mold. Cooling will not be efficient in this region and the heat flux is described by
     $$\kappa \nabla T \cdot \mathbf{n} = -h^{meniscus} \left( T_{surf} - T_{room} \right)$$
   - mold contact ($z_{level} - 38 \text{ mm} < z < z_{level} - 6 \text{ mm}$) : in the region where the cast is in close contact with the mold, the heat flux is described using
     $$\kappa \nabla T \cdot \mathbf{n} = -h^{mold} \left( T_{surf} - T_{room} \right)$$
     This is approximate as the mold is not at room temperature but this proved to be satisfactory in the present case.
   - air gap ($z_{level} - 40 \text{ mm} < z < z_{level} - 38 \text{ mm}$) : after solidification has progressed in the outer shell and before leaving the mold, an air gap is formed due to distortions. The cooling intensity is thus decreased locally :
     $$\kappa \nabla T \cdot \mathbf{n} = -h^{gap} \left( T_{surf} - T_{room} \right)$$
   - water impingement ($z_{level} - 50 \text{ mm} < z < z_{level} - 40 \text{ mm}$) : below the mold, the water jets used for secondary cooling impinge on the billet. This location is described with
     $$\kappa \nabla T \cdot \mathbf{n} = -h^{impinge} \left( T_{surf} - T_{room} \right)$$
     and its own boiling curve $h^{impinge}\left(T_{surf}\right)$ (Figure 5.15).
   - water flow ($z < z_{level} - 50 \text{ mm}$) : below the water impingement point, secondary cooling occurs, as already exposed on Figure 1.2. This is described by
     $$\kappa \nabla T \cdot \mathbf{n} = -h^{secondary} \left( T_{surf} - T_{room} \right)$$
     and corresponding boiling curve $h^{secondary}\left(T_{surf}\right)$ shown on Figure 5.15.
3. level : as already pointed out, the cast height $z_{level}$ indicates how much alloy has actually been cast at time $t$. The mesh however does not depend on time so that the top of the mesh corresponds to the final height of the billet. As a consequence, no real boundary condition can be applied at $z = z_{level}$. In order to approximate the effect of the hot top and describe reasonably well what is happening at $z_{level}$, all the material above $z_{level}$ (not actually cast yet and outlined in grey on Figure 5.14) is given a zero thermal conductivity $\kappa = 0$. Together with the adiabatic condition applied laterally for $z > z_{level}$, this leads to a constant temperature equal to the pouring (or initial) temperature being imposed at $z = z_{level}$.

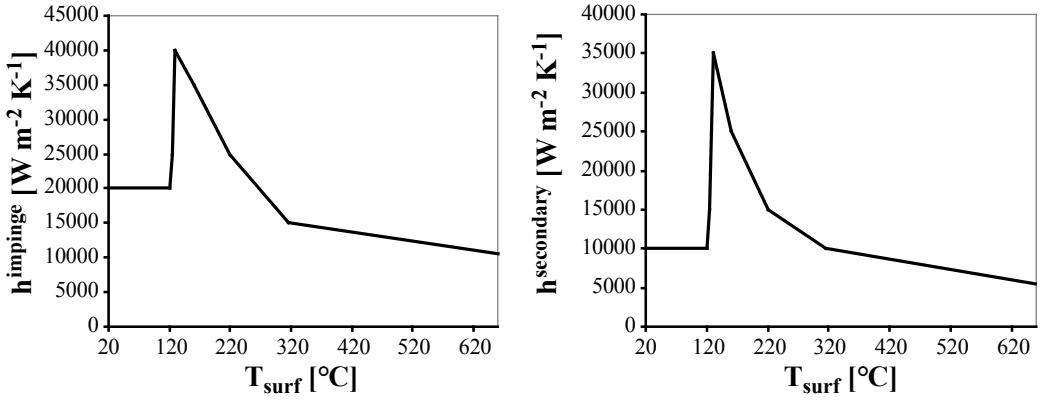


**Figure 5.15:** Boiling curves at and below the cooling water impingement point.

4. bottom block : the bottom block was not included in the mesh. The bottom of the cast is thus subjected to a heat flux given by

$$\kappa \nabla T \cdot \mathbf{n} = -h^{bottom} \left( T_{surf} - T_{room} \right)$$

where the transfer coefficient depends on the radial position as illustrated on Figure 5.16. This only accounts for the fact that the bottom block is thicker at the center and thus allows for less heat to be extracted at this location.

5. top : at the top of the mesh, a zero flux condition is applied. This does not have much effect because the top of the mesh is the actual top of the casting only at the very end of the process.

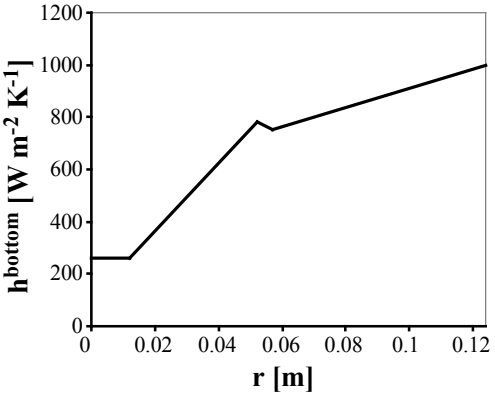


**Figure 5.16:** Heat transfer coefficient at the bottom of the billet.

The remaining details of these boundary conditions are given in Table 5.11. It should also be observed that most advanced phenomena such as water incursion or butt curl are not included in the model. This means that the description of the start-up phase may not be fully accurate. It is however not important in this case because hot tears are initiated during the quasi-steady state regime, quite far away from the start-up region.

As far as the material is concerned, the properties of the AA5182 alloy that was cast are used. First of all, the solidification path was obtained from [4] and is displayed on Figure 5.17 (liquidus : $T_{liq} = 631$ °C). The latent heat was set to $L = 9 \cdot 10^8$ J m$^{-3}$ and the values of

| $h^{meniscus}$ | $h^{mold}$ | $h^{gap}$ | $\left[\mathrm{W\ m^{-2}\ K^{-1}}\right]$ | $T_{room}$ [°C] |
|---|---|---|---|---|
| 0 | 500 | 100 | | 20 |

**Table 5.11:** Coefficients used to describe the thermal boundary conditions in the DC-cast billet.

$C_p$ and $\kappa$ are temperature dependent as shown on Figure 5.18. Please note that the value of thermal conductibility was set to $\kappa = 250$ W m$^{-1}$ K$^{-1}$ in the liquid phase to simulate the effect of convection (since flow in the liquid pool was not included in the thermal model).

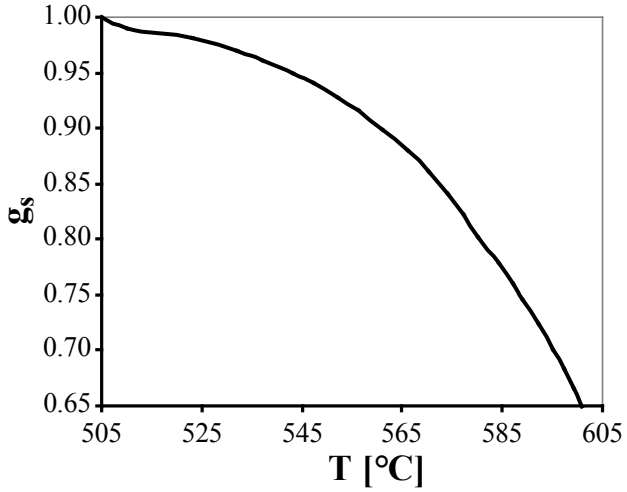


**Figure 5.17:** Solidification path for the AA5182 alloy.

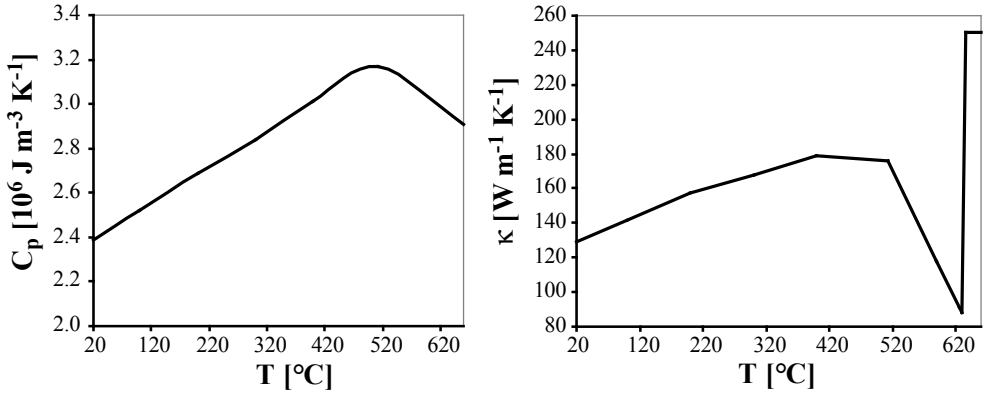


**Figure 5.18:** Specific heat and thermal conductivity as a function of temperature for the AA5182 alloy.

The initial temperature is equal to the pouring temperature and set to 670 °C according to the experimental data. The simulation was performed for a physical time of 2000 s with $\Delta t = 1$ s and the CPU time was of 4 hours on an Intel$^{TM}$ Xeon @ 2GHz.

### Mechanical Model

The mechanical model was built on the same mesh as the thermal model. In that case, the boundary conditions are very simple as shown on Figure 5.19 :

1. symmetry : along the cylindrical symmetry axis, the radial displacement is prescribed to zero : $u_r = 0$. Displacement along $z$ is free on this axis : $F_z = 0$.

2. free surfaces : all of the other boundaries experience a zero force condition ($F_r = F_z = 0$).

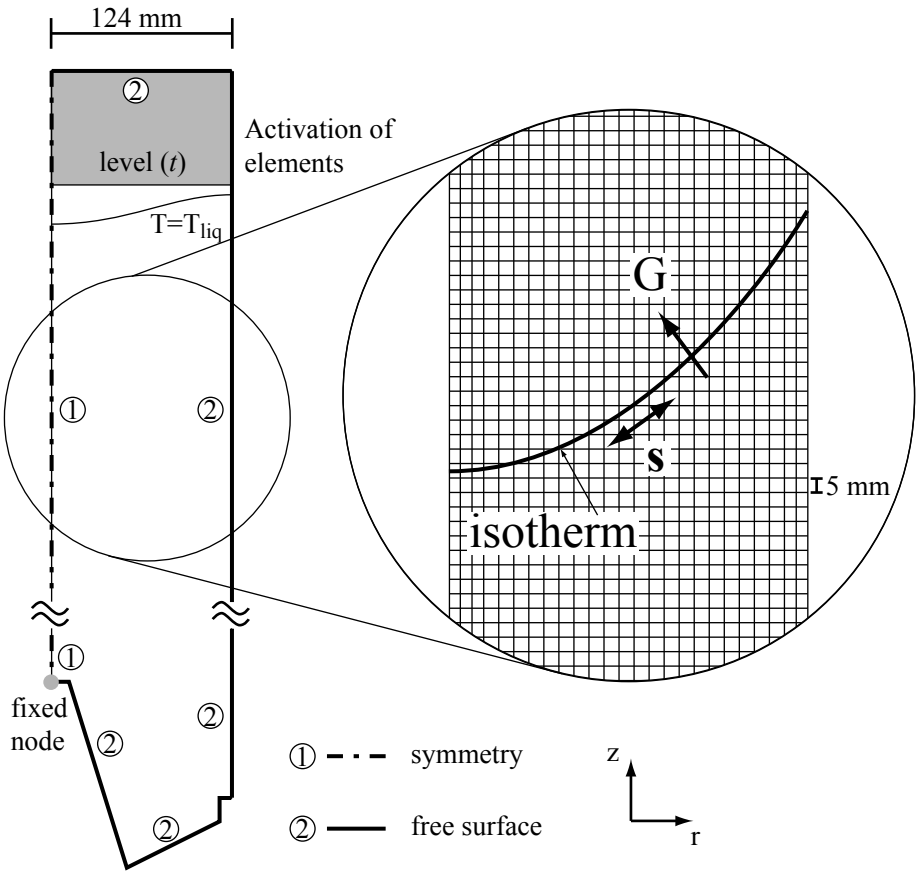


**Figure 5.19:** Mechanical boundary conditions used for modeling the DC-cast billet. A typical isotherm together with the direction of the thermal gradient $\mathbf{G} = \nabla \cdot T$ and the direction of maximal principal stress $\mathbf{s}$ are displayed locally together with the magnified mesh.

The node in contact with the center of the bottom block is not allowed to move vertically ($u_z = 0$) in order for the problem to be well conditioned. There is no advanced contact model between the cast and the bottom block. This means that, again, this model was not designed to reproduce accurately the start-up phase (which is tear-free anyway for this particular experiment).

In this case, the loading that applies to the cast is due to the inhomogeneous temperature field and resulting differential thermal strain. The latter is described by introducing the thermal expansion coefficient $\alpha^{th} = 25 \cdot 10^{-6}\ \mathrm{K}^{-1}$ as soon as the solid fraction drops below $g_s^{th} = 0.8$.

In the mechanical calculation again, the entire billet is meshed even though only a height $z_{level}(t)$ has actually been cast. The material that is meshed but not cast yet (outlined in grey on Figure 5.19) is treated as liquid and thus has a negligible influence on the solution of the problem.

However, including this material in the solution is a problem from the CPU time point of view. The mechanical solution can indeed be obtained much more rapidly (due to the decreased number of elements) if only the solid and mushy domain are considered. As a consequence, a procedure of element activation (only the elements of interest are used in the calculation) has been setup, similarly to the method of Drezet *et al* [23]. Regularly during the calculation, elements (that are present in the mesh but not yet used in the calculation) are activated based on a position ($z > z_{level}(t)$) or temperature criterion. In the present case, new elements are activated every 20 s so that all the elements with at least one node such that $T < 660$ °C are active at all time.

As far as material properties are concerned, Poisson's ratio is constant ($\nu = 0.3$) and the elastic modulus depends on temperature as shown on Figure 5.20. The properties of the mushy

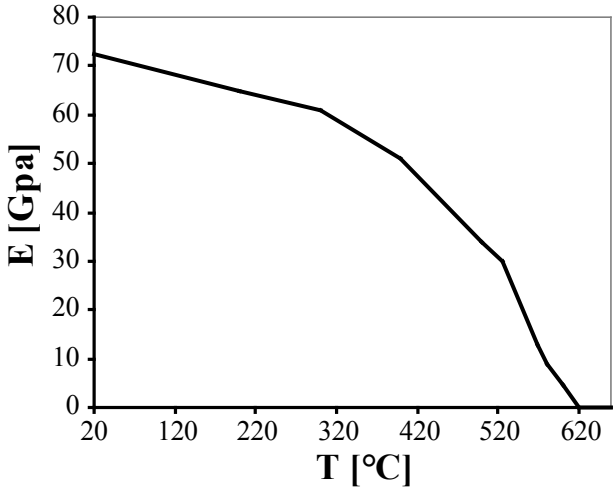


**Figure 5.20:** Elastic modulus for the AA5182 alloy.

alloy were also determined by Ludwig *et al* for AA5182 [66]. They could thus be used in this problem and the values are summarized in Table 5.12. For the hot solid, the properties are given in Table 5.13.

| $p$ | $\alpha_0$ | $\alpha_1$ | $g_s^{coh}$ | $g_s^{coal}$ | $k$ |
|---|---|---|---|---|---|
| 0.315 | 10.54 | $6.32 \cdot 10^{-2}$ | 0.65 | 0.94 | 100 |

**Table 5.12:** Mushy zone rheology parameters, which appear in Equations (2.52) and (2.53) (p. 28) [66].

| $s_0$ [MPa] | $A\ [\mathrm{s}^{-1}]$ | $Q\ [\mathrm{kJ\ mol}^{-1}]$ | $n$ |
|---|---|---|---|
| 52 | $2.67 \cdot 10^7$ | 125 | 3.44 |

**Table 5.13:** Hot solid rheology parameters, which appear in Equation (2.45) (p. 26) [66].

For lower temperatures, experimental data is available from [69]. For their numerical integration, these results were fitted with the parameters summarized in Table 5.14. Please note that the continuity of properties in temperature imposes that the generalized Ludwik's model is used as soon as temperature drops below $T_{merge} = 410$ °C. Moreover, work hardening becomes significant below $T_\epsilon = 400$ °C.

| $\kappa = p_1^\kappa + p_2^\kappa T_{[\mathrm{K}]} + p_3^\kappa T_{[\mathrm{K}]}^2 + p_4^\kappa T_{[\mathrm{K}]}^3 + p_5^\kappa T_{[\mathrm{K}]}^4$ | | | | |
|---|---|---|---|---|
| $p_1^\kappa$ [Pa] | $p_2^\kappa$ [Pa K$^{-1}$] | $p_3^\kappa$ [Pa K$^{-2}$] | $p_4^\kappa$ [Pa K$^{-3}$] | $p_5^\kappa$ [Pa K$^{-4}$] |
| $-2.555 \cdot 10^8$ | $5.805 \cdot 10^6$ | $-1.96 \cdot 10^4$ | $2.5934 \cdot 10^1$ | $-1.2 \cdot 10^{-2}$ |
| $\eta = p_1^\eta + p_2^\eta T_{[\mathrm{K}]} + p_3^\eta T_{[\mathrm{K}]}^2 + p_4^\eta T_{[\mathrm{K}]}^3 + p_5^\eta T_{[\mathrm{K}]}^4 > 0$ | | | | |
| $p_1^\eta$ | $p_2^\eta$ [K$^{-1}$] | $p_3^\eta$ [K$^{-2}$] | $p_4^\eta$ [K$^{-3}$] | $p_5^\eta$ [K$^{-4}$] |
| -8.932 | $9.11 \cdot 10^{-2}$ | $-3.339 \cdot 10^{-4}$ | $5.361 \cdot 10^{-7}$ | $-3.2 \cdot 10^{-10}$ |
| $\lambda = p_1^\lambda + p_2^\lambda T_{[\mathrm{K}]} + p_3^\lambda T_{[\mathrm{K}]}^2 + p_4^\lambda T_{[\mathrm{K}]}^3 + p_5^\lambda T_{[\mathrm{K}]}^4$ and $\lambda = 10^{-2}$ for $T < 200$ °C | | | | |
| $p_1^\lambda$ | $p_2^\lambda$ [K$^{-1}$] | $p_3^\lambda$ [K$^{-2}$] | $p_4^\lambda$ [K$^{-3}$] | $p_5^\lambda$ [K$^{-4}$] |
| $2.5820 \cdot 10^1$ | $1.6894 \cdot 10^{-1}$ | $4.065 \cdot 10^{-4}$ | $-4.27 \cdot 10^{-7}$ | $1.667 \cdot 10^{-10}$ |

**Table 5.14:** Intermediate temperatures rheology parameters, which appear in Equation (2.56) (p. 29), fitted on data from [69]. Please note that $T_{[\mathrm{K}]}$ is the temperature expressed in Kelvin.

The mesh (4-noded bilinear axisymmetric elements) size is close to constant $\Delta x \simeq 5$ mm. A typical value for the thermal gradient is $G \simeq 10^4$ K m$^{-1}$. As a consequence, the increment of solid fraction across one element in the direction of the thermal gradient is much larger than what is recommended by Equation (3.15) (p. 53). However, the maximum principal stress is typically found along the isotherms in the billet as suggested on Figure 5.19. The increment of $g_s$ across one element in that direction thus fulfills the mesh size selection guideline. The value of $\Delta x$ is thus considered to be acceptable for the present purpose even though full accuracy may not be reached. Please note that decreasing the mesh size is not really an option due to the already very long CPU time.

As far as time step is concerned, the control parameter was set to $\chi = 5 \cdot 10^{-5}$. This value was selected according to Equation (3.14). The complete simulation was conducted for 2000 s of physical time (time to cast the entire billet). Despite the gradual activation of elements, the corresponding CPU time was of 566 h (almost 24 days) on an Intel$^{\mathrm{TM}}$ Itanium 2 @ 1.6 GHz. This value is large because of the complexity of the problem and the degree of accuracy required.

### Liquid Pressure Model

As usual, a zero flow of liquid is prescribed normal to all boundaries except the top liquid surface, on which the atmospheric pressure $p_l = p_{atm} = 101.325$ kPa is imposed. Please note that the evaluation of the metallostatic pressure is correct since $p_{atm}$ is in fact imposed at $z = z_{level}$ and not at the top of the mesh.

The average density of the mushy alloy is displayed on Figure 5.21. The viscosity was set to

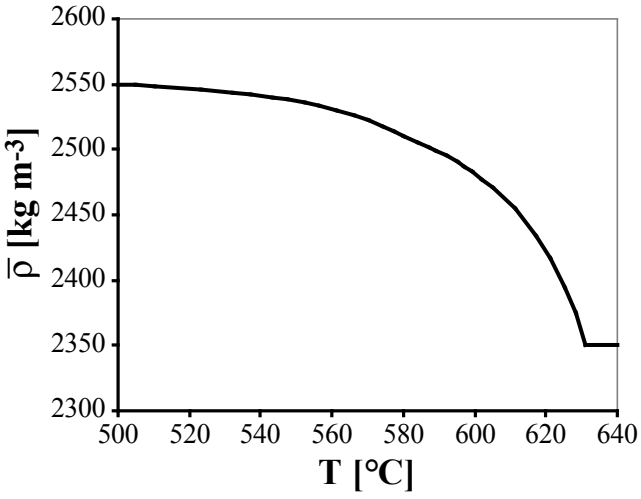


**Figure 5.21:** Average density vs. temperature for the AA5182 alloy.

a constant value $\mu = 1.35 \cdot 10^{-3}$ Pa s and the permeability $K$ is given by Equation (2.13), with a constant grain size $\phi = 100$ $\mu$m, which corresponds to experimental values.

Porosity formation was included in the model. The amount of hydrogen dissolved in the melt was set equal to the experimentally measured value : $[H]_0 = 0.3$ $\mathrm{cc_{STP}}/100\mathrm{g}$. Moreover, standard parameters were used, such as : hydrogen partition coefficient $k_H = 0.07$, $S = 0.69$ $\mathrm{cc_{STP}}/100\mathrm{g}$, $\gamma_{l/v} = 0.9$ J m$^{-2}$, nucleation radius of pores $r_{p,n} = 10$ $\mu$m and average density of nucleation sites for the pores $\rho_{nucl} = 10^9$ m$^{-3}$ [3].

The finite difference mesh used for the porosity calculation is composed of cubic cells with a size $\Delta x = 3$ mm. The time step was set to $\Delta t = 1$ s. These values are not in perfect agreement with the guidelines given in Equations (3.31) and (3.32) (p. 57). This is due to memory and time issues. However, a decent accuracy (within 15%) is expected for these results. When compared to the experimental uncertainty, this remains acceptable. To simulate the 2000 s necessary to cast the billet, the CPU time was of 48 h on an Intel$^{\mathrm{TM}}$ Xeon 2 @ 2 GHz.

# Chapter 6

# Results and Discussion

The aim on this chapter is to present, validate and analyze the results of the numerical model on the basis of experimental data. All the simulation parameters are given in Chapter 5. Moreover, the experimental methods and available measurements are summarized in Chapter 4.

## 6.1 Mushy Zone Tearing Test

### 6.1.1 Thermal Results

Let us begin with the mushy zone tearing test of Grasso [5] and start with the consideration of the thermal results. Figure 6.1 displays the thermal field in the mold and the sample (grain-refined Al-1wt%Cu alloy) at three times ($t_{simul}$ as measured during the simulation). At 300 s the sample is not significantly solidified. After 400 s, the neck is mushy and the tensile tests are conducted under such conditions. Finally, after 500 s, the sample is almost fully solidified.

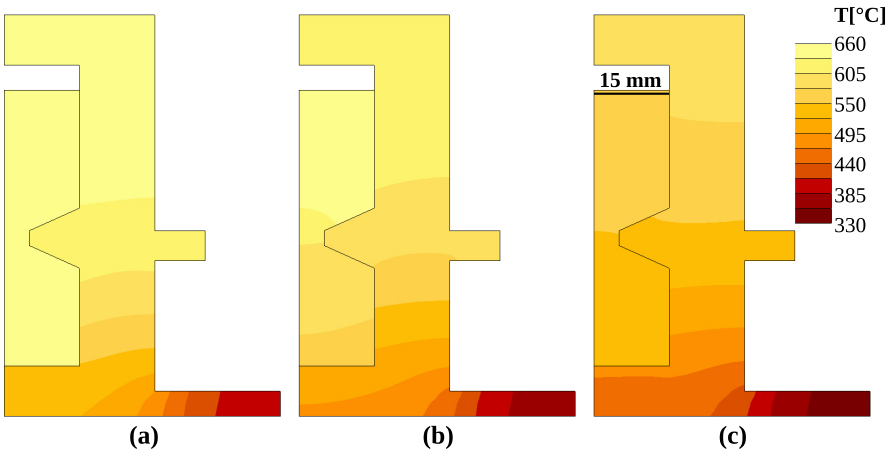


**Figure 6.1:** Thermal field in the steel mold and in the tearing test sample (grain-refined Al-1wt%Cu alloy) at three different times : (a) 300 s, (b) 400 s and (c) 500 s.

It is useful to study the thermal field in the sample in more detail. The tensile tests are conducted in the range 330 s $< t_{simul} <$ 430 s and the corresponding thermal conditions are

displayed on Figure 6.2. Please note that the temperature scale is focused on the range 590 °C < $T$ < 650 °C which corresponds to 0.78 < $g_s$ < 0.98. This shows that the isotherms in the neck are almost exactly perpendicular to the longitudinal $z$ direction (i.e. to the tensile axis). Moreover, due to the cooling conditions, the bottom half of the sample is colder than the top part. In addition, it is worth observing that, away from the neck, isotherms are curved (with their center of curvature located in the neck).

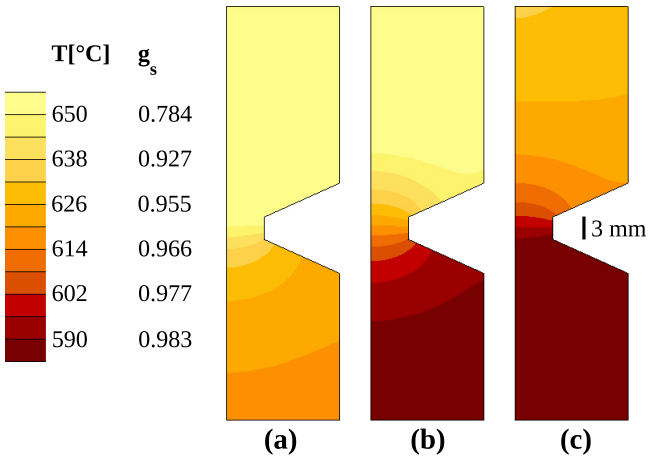


**Figure 6.2:** Thermal field in the sample at three different times : (a) 330 s (b) 380 s and (c) 430 s. The temperature range in which the tensile tests were conducted is displayed in detail. Please note that the corresponding solid fraction is also indicated on the temperature scale.

Having described the evolution of the temperature field in the sample, it is necessary to assess the quantitative validity of the thermal simulation. This can be done by considering Figure 6.3. The temperature measured by the thermocouple for several tests is displayed in thin grey lines. When this temperature reaches the critical value $T_{tear}$, the tensile test is started. From an experimental point of view, it appears that the thermal behavior is quite reproducible. The simulated temperature at the location of the thermocouple is also displayed (thick black line).

First of all, it should be noted that the temperature plateau due to latent heat release is much longer in the simulation than in experimental measurements (which is often observed [112]). Moreover, the initial condition in the model (homogeneous temperature) is not perfectly reproduced in the experiment (a significant amount of time is necessary to transfer the mold from the furnace to the tensile test machine). As a consequence, the time $t_{simul}$ is shifted so that time $t = 0$[1] corresponds to a temperature of 700 °C at the thermocouple in both the simulation and experiment.

With this time shift, the numerical model is in good agreement with the experimentally measured curve, especially below 630 °C where a constant cooling rate of $\dot{T} = -0.4$ K s$^{-1}$ is obtained. Finally, please note that the sharp decrease in the measured temperature (black cross on thin grey lines) corresponds to failure of the sample and is thus not reproduced by the simulation.

At this stage, it appears that the thermal model is well validated by the experiment. It may then be used to extract quantities that could not be measured directly and gain further information about the test. For example, the longitudinal thermal gradient averaged at the neck $\frac{\mathrm{d}T}{\mathrm{d}z}\big|_{neck}$ (referred to as $G_{neck}$ because $\frac{\mathrm{d}T}{\mathrm{d}r}$ is virtually nil in this region) can indeed be calculated

[1] this time is usually defined as the point when the model initial condition is satisfied.

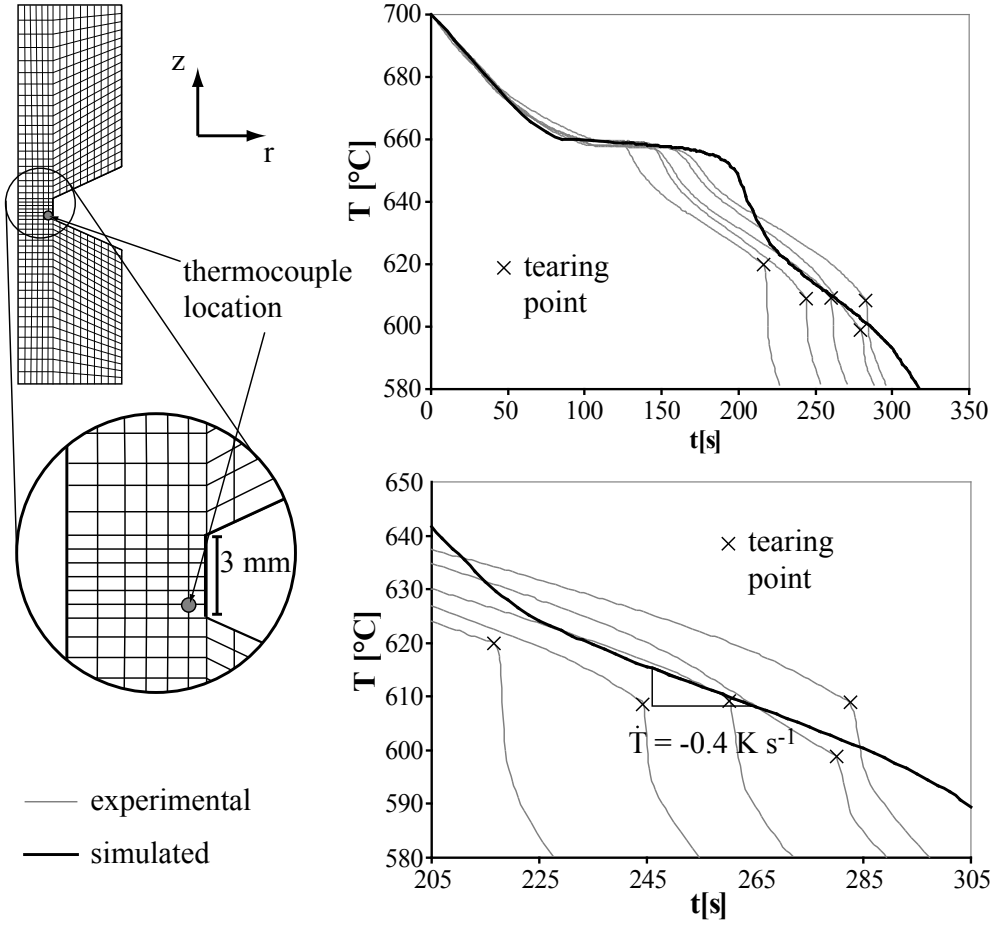


**Figure 6.3:** Position of the thermocouple and comparison between experimental temperature measurements (thin grey lines, corresponding to different tests) and the result given by the simulation (thick black line). Please note that the point at which tearing occurred is indicated by a cross on the experimental curves.

as shown on Figure 6.4. The gradient increases from the centerline of the sample to the periphery and has an average value around $G_{neck} = 5000$ K m$^{-1}$. At this stage, it is possible to verify that the mesh size is acceptable. The last 10% of solidification, i.e. the range $0.9 < g_s < 0.99$, corresponds to 80°C. As a consequence, the increment of solid fraction across one element along the principal loading direction can be estimated as :

$$G\frac{\Delta g_s}{\Delta T}\Delta x = 5000\frac{0.1}{80}5\cdot 10^{-4} \approx 3\cdot 10^{-3}$$

This shows that the mesh satisfies conditions (3.15) (p. 53) and (3.32) (p. 58).

Moreover, one of the problems associated with the mushy zone tearing test is that the fracture location is not exactly prescribed by the thermal field. There is indeed no strongly localized hot spot and tearing tends to occur above the separation plane of the mold (where the mushy material is weaker). The gradient is thus useful to estimate more accurately the temperature of the fracture surface.

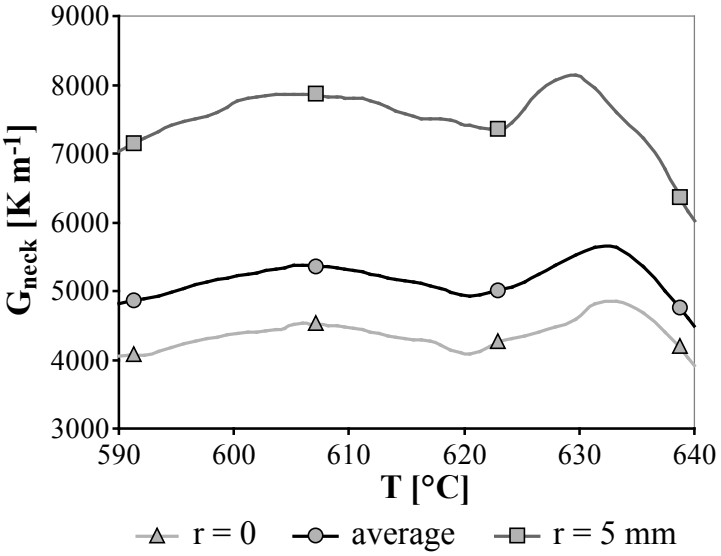


**Figure 6.4:** Thermal gradient along the $z$ direction in the neck (3 mm high region with reduced cross-section) plotted vs. the temperature at the thermocouple (i.e. at the bottom of the neck, in the periphery of the sample). The curves simulated at the centerline ($r = 0$), at the periphery ($r = 5$ mm) and averaged in the section are displayed.

### 6.1.2 Mechanical Results

The next step is to study the results of the mechanical calculations. First of all, let us consider how strains and stresses are distributed in the sample (see Figure 6.5). In the neck region, the mushy alloy experiences tensile conditions (positive strain and negative pressure) due to the applied strain. Please note that a compressive zone exists in the lower $g_s$ region above the neck.

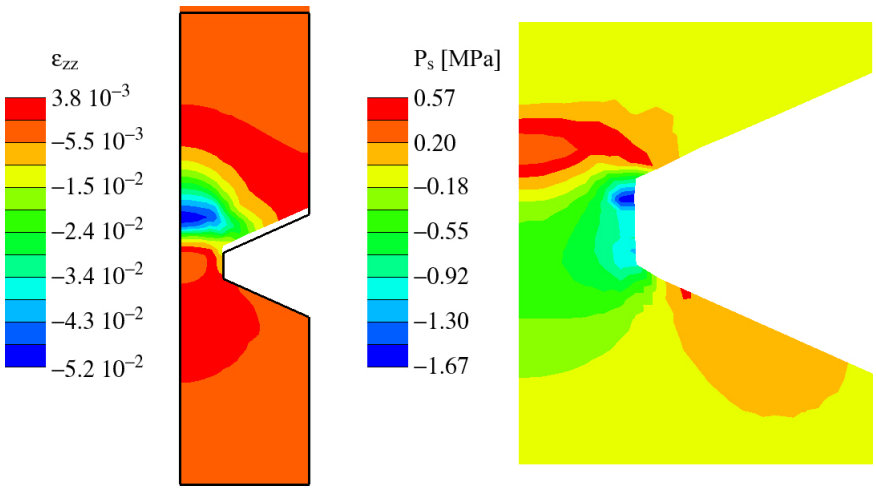


**Figure 6.5:** Axial strain field represented on the deformed shape (superimposed on the undeformed sample shape in thick black line) (left) and close-up of the solid pressure $P_s$ field in the neck region (right). This image corresponds to a displacement of the top of the mold of $u_z = 0.83$ mm ($t = 0.25$ s) and to a tearing temperature $T_{tear} = 630$ °C.

More specifically, it is important to remark that stress and strains get mostly concentrated at the top of the neck, in the region close to the mold (where the thermal gradient $G$ is maximum). This explains why fracture occurs at the top of the neck with a tendency to deviate upwards, following approximately the isotherms (or the iso-$g_s$ line).

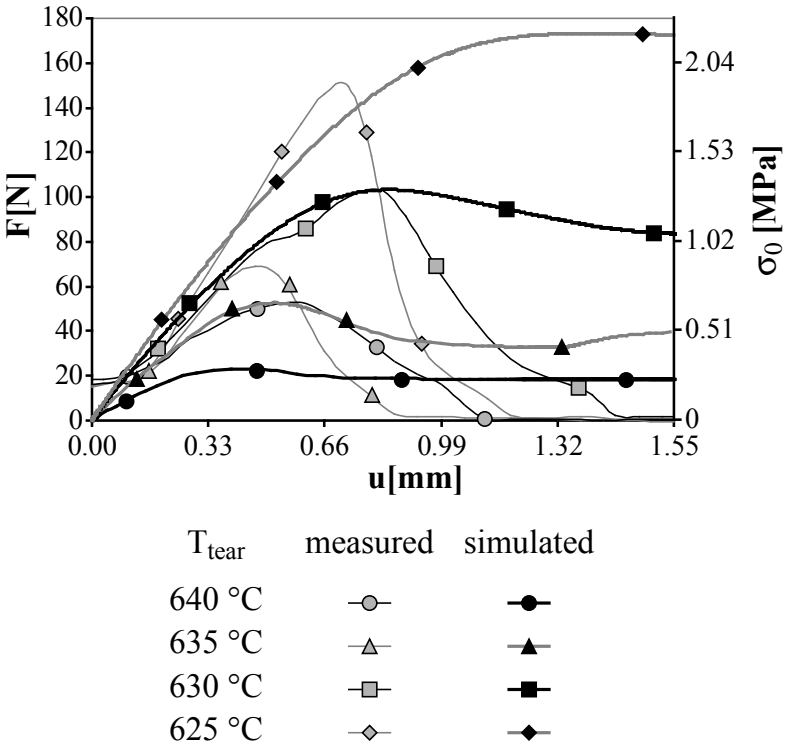


**Figure 6.6:** Comparison between the measured and simulated reaction forces for different values of $T_{tear}$. The nominal stress, $\sigma_0$, corresponding to $F$ was computed from the cross-section area at the neck and is shown on the alternative scale on the right. Curves with the same line color and symbol shape are to be compared.

Having outlined these general features, it is now necessary to assess the quantitative validity of the mechanical model. For this purpose, the simulated reaction force, $F$, is compared to the experimental measurements for various values of $T_{tear}$. Please note that the latter corresponds to the temperature at the location of the thermocouple (i.e. bottom of the neck) at the beginning of the tensile test. The results are displayed on Figures 6.6 and 6.7

The agreement between the experimental and simulated data is very good up to the point where hot tearing occurs. The reaction force $F$ is underestimated only for $T_{tear} = 640$ °C and $T_{tear} = 635$ °C. This slight inaccuracy is related to the fact that the thermal model predicts slightly too high temperatures above 630 °C. Overall, the mechanical model is thus very well validated by this experimental comparison.

This mechanical simulation may thus be trusted and used for further investigations. Figure 6.5 has already illustrated how it is possible to better understand and investigate the loading conditions that occur during this test. This helps understanding why tears tend to propagate from the top of the neck, which is a region of strain concentration.

Another purpose of this mechanical model is to provide the values of $\mathbf{v}_s$ and $\nabla \cdot \mathbf{v}_s$. This can indeed be used by the porosity module to calculate the liquid pressure. Moreover, this gives

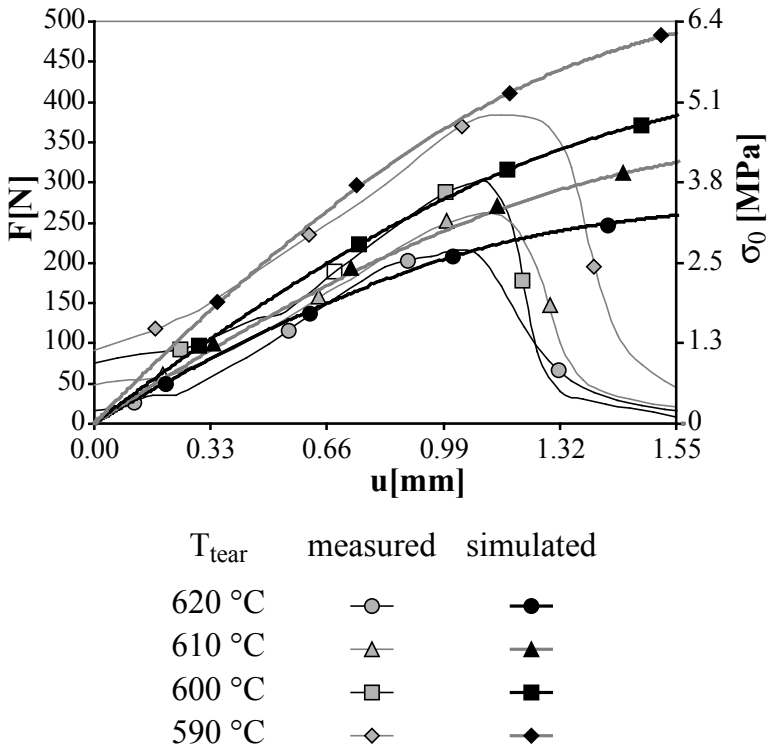


**Figure 6.7:** Comparison between the measured and simulated reaction forces for different values of $T_{tear}$. The nominal stress, $\sigma_0$, corresponding to $F$ was computed from the cross-section area at the neck and is shown on the alternative scale on the right. Curves with the same line color and symbol shape are to be compared.

access to the mechanical solid fraction correction as defined in Equation (3.11) (p. 50). In this test, it is important to note that this correction may locally be as large as a few percent. This high value is related to the fact that the swelling rate may become very high in this test (up to $\dot{\epsilon}_{sw} \sim 0.2\ \mathrm{s}^{-1}$) due to the fast displacement imposed to the top half of the mold.

Finally, this model can be used to understand the behavior of the mushy material. As already presented earlier, it is possible to plot the maximum force measured during the experiment, i.e. the force at failure $F_{fail}$ or tensile strength. On Figure 4.4 (p. 65), $F_{fail}$ was plotted against $T_{tear}$. However, the tearing temperature does not really indicate what is the value of $T$ at the tear front and at the time of fracture. Based on the thermal model, experimental time to failure and typical crack front positions measured in the experiment, it is possible to estimate the actual temperature at the tear front. This can be converted into the solid fraction of the tearing material.

As a consequence, using complementary information coming from both the experiment and the numerical model allows plotting the tensile strength as a function of the solid fraction at the tear (which could not be estimated accurately from $T_{tear}$). This result is shown on Figure 6.8. Please note that the error bars for the $F_{fail}$ values are estimated based on one of the test that had repeated several times. On the other hand, the error bar for the value of $g_s$ can be evaluated only using the numerical results. It takes into account both the deviation of the crack front in the thermal gradient and the correction from the mechanical solid fraction.

From this, it is possible to conclude that the tensile strength of the mushy Al-1wt%Cu alloy

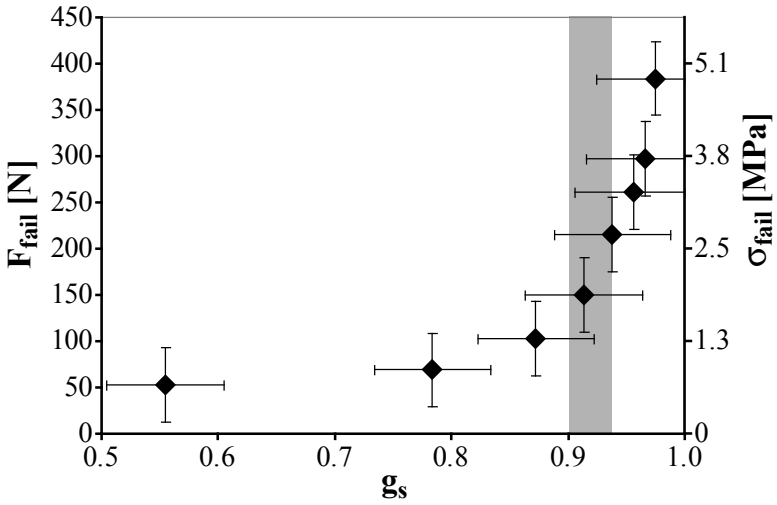


**Figure 6.8:** Maximum force (tensile strength) of the mushy alloy as a function of the solid fraction when and where tearing actually occurred.

starts developing rapidly for a solid fraction in the range $0.9 < g_s < 0.94$. Moreover, $F_{fail}$ will keep increasing sharply as coalescence progresses.

There is one other point that should be outlined at this stage considering Figures 6.6 and 6.7. In the experimental data, the maximum force $F_{fail}$ that is measured corresponds to the point where the material starts to fail (hot tearing). In the numerical model, a maximum force is also recorded as most clearly visible on Figure 6.6. This cannot be directly interpreted as tearing since no failure criterion was included in the numerical model. This maximum force is thus more similar to necking (tensile test related instability) than to failure.

It turns out that the stress concentration at the top of the neck near the mold initially contributes to the fact that the average stress (and thus the reaction force) increases with the applied displacement. At some point however, the stress in this region starts to decrease because the material loses cohesion due to the concentrated strain. We shall refer to this phenomenon as decohesion (of the mushy alloy) because it is not exactly similar to the usual room temperature necking instability. What should be remarked is that, for high tearing temperatures 625 °C $< T_{tear} <$ 640 °C, decohesion is observed in the simulation almost at the same time as failure is observed in the experiment. As solidification is more and more advanced, decohesion is delayed more than tearing and these two phenomena no longer seem to be related.

### 6.1.3 Porosity Results

At this stage, further information can be obtained using the porosity module. First of all, a calculation was conducted neglecting the strain contribution (solidification shrinkage alone). When a realistic amount of dissolved hydrogen is used ($[H]_0 = 0.25$ or 0.4 $cc_{STP}/100g$), the liquid pressure drops remains very small[2] and a roughly uniform amount of porosity is found in the sample. Under such circumstances, porosity in the casting is thus mainly induced by gas segregation. This situation may change when strains are applied to the neck region (i.e. during the tensile test). The amount of porosity may indeed increase locally due to tensile strains, as shown on Figure 6.9.

[2]reduced cross sections tend to enhance liquid flow as already mentioned in [109].

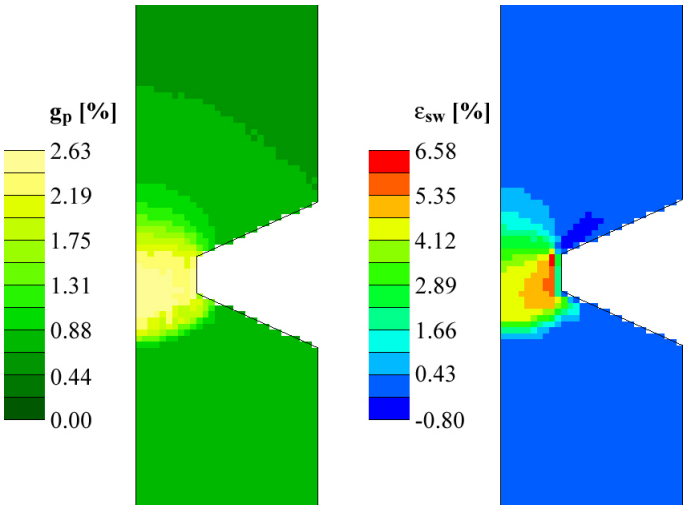


**Figure 6.9:** Porosity fraction and cumulated volumetric strain in the neck of the sample. This result corresponds to $T_{tear} = 590$ °C and to a displacement of $u_z = 1$ mm of the upper mold ($t = 0.3$ s). The amount of hydrogen dissolved in the melt is $[H]_0 = 0.25$ $cc_{STP}/100g$.

Figure 6.9 also displays the amount of volumetric strain $\epsilon_{sw}$ experienced by the mushy alloy. As expected, the maximum value of $\epsilon_{sw}$ is found at the top of the neck, close to the mold. This corresponds to the region of strain concentration indicated by the mechanical model. As far as the porosity fraction field $g_p(\mathbf{x}, t)$ is concerned, it seems to be less clearly localized. This is because a large strain rate applied to a relatively high permeability region may cause less voiding than a moderate strain rate applied to a low permeability region. As a consequence, porosity is not simply proportional to strain.

The amount of porosity in the sample is thus the sum of the two contributions associated with gas segregation and volumetric strain rate. The value of $g_p$, especially the fraction related to the applied strain, may be used to quantify voiding and thus damage in the material. Please note that the strain rate leads to an increase in $g_p$ by increasing the liquid pressure drop, up to $\Delta p_l = 140$ kPa for the lowest value of $T_{tear}$. In this test, the strain contribution to the amount of porosity clearly dominates the shrinkage term. Again, this is related to the very high displacement rate imposed to the top part of the sample and resulting high strain in the neck.

The fact that the strain contribution is dominant in the liquid pressure calculation could have been predicted by considering the ratio of the characteristic pressure drops introduced in Section 3.3.2 :

$$\frac{\Omega^{sh}}{\Omega^{mech}} = \frac{v_T \beta}{\dot{\epsilon}_{sw} \frac{\Delta T_{freeze}}{G}} \approx \frac{10^{-4} \cdot 8 \cdot 10^{-2}}{0.2 \frac{100}{5000}} \approx 2 \cdot 10^{-3}$$

This order calculation indeed indicates that $\Omega^{mech}$ is about three orders of magnitude larger than $\Omega^{sh}$, thus showing that the pressure drop is mainly due to the strain rate experienced by the solid skeleton.

Having noticed that the application of strain had a marked effect on the porosity field, a more quantitative approach was undertaken. The maximum amount of porosity in the sample at the time of fracture $g_{p,fail}^{max}$ was calculated : from the experimental data, it is indeed possible to determine when tearing occurred and, at this time, the value of $g_{p,fail}^{max}$ is predicted by the model. Please note that this maximum porosity fraction is always found in or slightly above the neck region. It may however not be exactly located at the tear front. It may thus be regarded as an

indicator of the damage present in the sample before its failure under tensile strain.

The results obtained for the two different gas contents are displayed on Figure 6.10. The value of $g_{p,fail}^{max}$ is plotted as a function of the solid fraction at the location of the tear. Please note that the error bars on $g_s$ should be the same as those plotted on Figure 6.8 but have been omitted for clarity of the graph. The correspondence between $T_{tear}$ and the actual solid fraction at fracture is also shown on this graph.

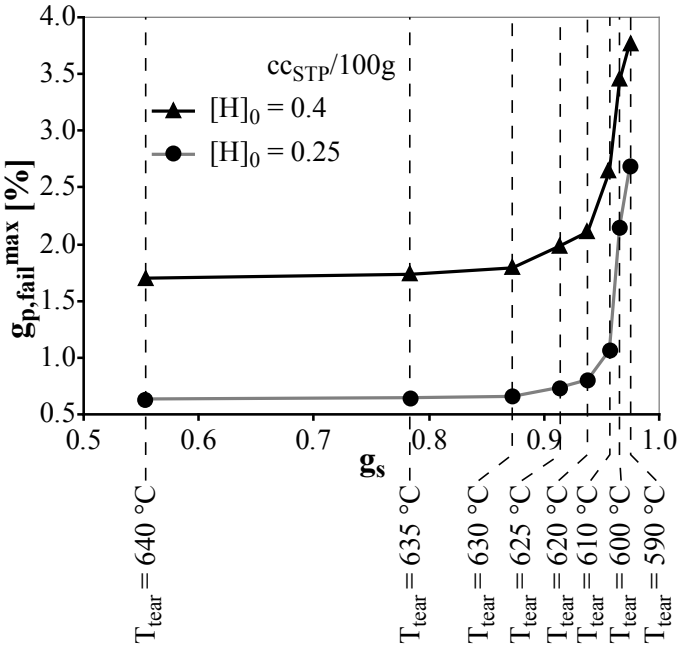


**Figure 6.10:** Maximum porosity fraction in the sample $g_{p,fail}^{max}$ as a function of the solid fraction at the location where tearing occurred. Please note that the error bars on $g_s$ are not displayed for clarity but are identical to those on Figure 6.8.

The results show that the amount of porosity related to hydrogen segregation in the melt (which is roughly equal to the value of $g_{p,fail}^{max}$ for $g_s = 0.6$) depends upon the amount of dissolved gas. This is not surprising because this contribution is mainly due to gas segregation. On the other hand, as $g_s$ increases, the damage increases sharply due to the applied strain and decreased permeability.

This is shown in more detail on Figure 6.11. On this graph, the same results for both values of $[H]_0$ are displayed. In lighter shades of grey, the results of the same calculations conducted without taking into account the mechanical solid fraction correction (no $g_s^{mech}$) are displayed. This illustrates that this correction has a significant effect on the results and that it is important to include it in the model.

Another piece of information that can be obtained from this results is that the damage prior to fracture starts increasing significantly for $0.89 < g_s < 0.93$. This appears to be in good correlation with conclusions drawn from the mechanical model with respect to a change in fracture mechanisms.

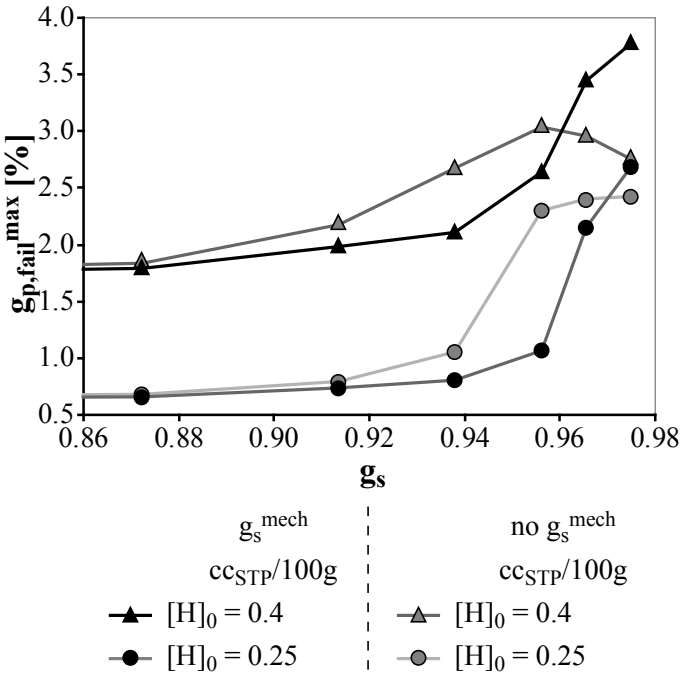


**Figure 6.11:** Maximum porosity fraction in the sample $g_{p,fail}^{max}$ as a function of the solid fraction at the location where tearing occurred. This graph shows only the solid fraction range over which $g_p$ deviates from the value dictated by shrinkage alone. Please note that the error bars on $g_s$ are not displayed for clarity.

### 6.1.4 Summary

We have shown that a large amount of information can be extracted from the numerical model, provided some experimental data is available. Such data was used for two distinct purposes. On one hand, the model needs to be quantitatively validated by comparison with actual measurements before it may be used to discuss further physical arguments.

On the other hand, the experimental results are used to determine where and when tearing occurred in the sample. This is very important because no failure model is available and fracture can thus not be predicted in the simulation. However, the numerical model may be used to determine accurately the conditions (thermal gradient, solid fraction, strain, damage, ...) experienced by the mushy alloy at the time and location of failure.

In the context of the mushy zone tearing test, this approach could be successfully applied to gain a deeper understanding of what is happening during the tensile test. It is indeed possible to distinguish between two failure modes that are active at different solid fractions.

At relatively high tearing temperatures, $T_{tear} > 625$ °C ($g_s < 0.92$), failure of the sample occurs when decohesion is predicted by the mechanical model. Moreover, under such conditions, the amount of damage found in the sample prior to failure remains small. It thus seems that tearing at high temperature is basically initiated by decohesion. This instability will depend on the sample geometry. As a consequence, the ductility measured in this system may not be really characteristic of the mushy material itself. This is one possible explanation for the fact that the measured ductility does not increase at high temperature, when healing is expected to come into play.

At lower temperature, i.e. for $T_{tear} < 625$ °C ($g_s > 0.92$), which corresponds to the range of solid fraction of interest for hot tearing, the situation is different. Tearing indeed occurs clearly before decohesion is predicted. Moreover, voiding (damaging) occurs in the sample before it breaks. It is thus both internal damage and applied strain that lead to tearing. This fracture mode seems more characteristic of the material properties under the applied strain rate.

In summary, this study shows two aspects of the use of a semi-coupled approach. After successful validation, it was indeed possible to characterize the test more precisely. For example, a good measure of the solid fraction at the tear front could be given. In addition to this, it is possible to distinguish different fracture modes. It was also possible to outline the fact that the behavior observed in this test is related to the relatively high strain rates induced by the fast motion of the top half of the mold during the test. On the other hand, the cooling rate $|\dot{T}|$ is smaller than what is often encountered in industrial practice. In that sense, the mushy zone tearing test does not reproduce very well typical DC casting conditions.

In conclusion, when tears propagate for $g_s < 0.92$, they are most likely initiated due to local decohesion and the results of this test should be interpreted carefully since the intrinsic ductility of the material is probably underestimated (failure is initiated by a test geometry dependent effect). On the other hand, if $g_s \geq 0.92$, tears are found after significant strain and damage has developed in the mushy alloy. As temperature decreases further, more and more damage is present when failure occurs and the apparent strength of the material increases. This is characteristic of the development of a coalesced solid network. This tensile test thus serves well the purpose for which it was designed (study of coalescence in a grain-refined alloy). On the other hand, it might be interesting to apply a smaller strain rate (and also a higher cooling rate) to obtain results under conditions more comparable to DC casting.

## 6.2 Rig Test

### 6.2.1 Thermal Results

Let us now consider the tensile test presented in Section 4.2. First of all, we shall describe what the thermal model indicates about the temperature field in the Al-2wt%Cu alloy when tensile tests are conducted. This discussion is based on Figure 6.12. On this figure, the temperature scale is focused on the range where the alloy is in a coherent mushy state ($g_s\,(640\,°\text{C}) = 0.61$ and $g_s\,(510\,°\text{C}) = 1$).

This result indicates that, when the tensile test occurs, the isotherms are perpendicular to the tensile axis ($z$ direction) in most of the sample. There are two regions where this is not exactly true. On one hand, in the jaw of the tensile test machine, the shape of the isotherms is distorted due to the geometry of the sample and significant heat extraction rate (cooling is mostly achieved from this side). Anyway, this region of the sample is mostly solidified prior to the test and does not really contribute to the reaction force since it moves with the jaw. On the other hand, in the middle of the specimen (i.e. at the expected tear plane), isotherms also tend to be curved. In that plane, the bottom of the sample experiences indeed a higher temperature, due to contact with the liquid alloy contained in the filling system. This should be kept in mind because it is specifically this region that will be strained up to failure during the tensile test.

The quantitative validity of the model was assessed using the actual temperature measurements performed in the sample during any tensile test. Four thermocouples are indeed introduced in the sample. Their locations is summarized in Table 6.1 and represented on Figure 6.13.

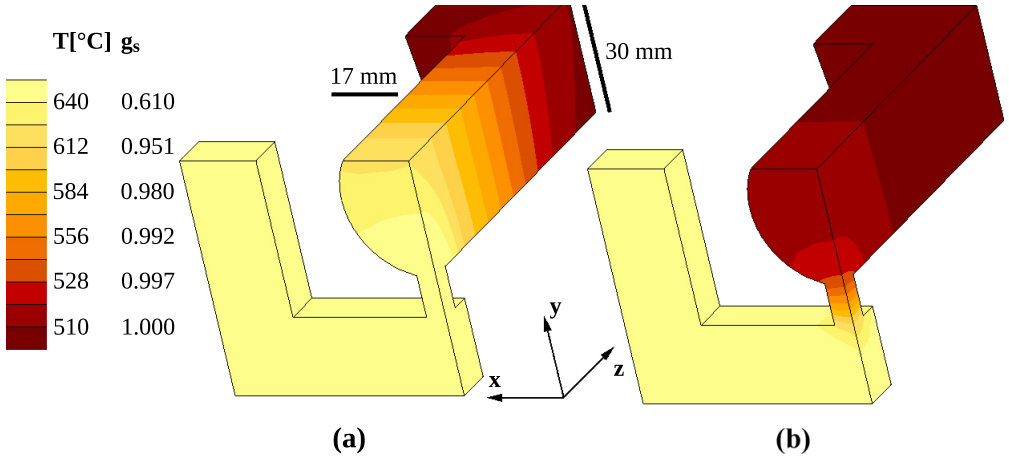


**Figure 6.12:** Thermal field in the Al-2wt%Cu sample at two different times : (a) 80 s, i.e. when the highest temperature tensile test is started (b) 132 s, i.e. when the lowest temperature tensile test is started. Please note that corresponding values of $g_s$ are indicated on the temperature scale.

For different tests, the recorded temperature is not exactly the same. Overall, the thermal field is however quite well reproduced in different experiments (with a typical cooling rate of $\dot{T} \approx -2$ K s$^{-1}$). On Figure 6.13, two measured curves that bound representatively the different experiments are shown (thin grey lines) for each thermocouple. On the same graphs, the simulated temperature at the same location is presented with a thick black line.

| | TC1 | TC2 | TC3 | TC4 |
|---|---|---|---|---|
| Distance from sample side ($-x$) [mm] | 3 | 3 | 3 | 3 |
| Distance from top surface ($-y$) [mm] | 8 | 18 | 25 | 18 |
| Distance from tearing plane ($z$) [mm] | 0 | 0 | 0 | 25 |

**Table 6.1:** Position of the thermocouples in the sample.

Taking into account the fact that the position of the thermocouple cannot be perfectly well controlled in the experiment, these results indicate that the thermal model setup to represent this test is satisfactory, at least in the temperature range where tensile tests are conducted. Please note that, in this case again, the simulation overestimates the duration of the temperature plateau due to latent heat release. As a consequence, the simulated and measured temperatures were synchronized (i.e. the initial condition from the thermal model does not correspond to $t = 0$) based on the end of this plateau.

With this correction, the validity of the simulated temperature field is verified and additional information can thus be obtained. It is indeed relevant to characterize the temperature gradients found in the sample. First of all, the variation of temperature in the direction of the tensile strain is fairly linear. As a consequence, the gradient may be evaluated between the center and the end of the sample :

$$G_z^{av} = 2\frac{T_{center} - T_{end}}{l_{sample}} \approx \left|\frac{\mathrm{d}T}{\mathrm{d}z}\right|$$

where $l_{sample} = 17$ cm is the length of the sample.

It turns out that the value of $G_z^{av}$ depends on the other coordinates $x$ and $y$. As a consequence,

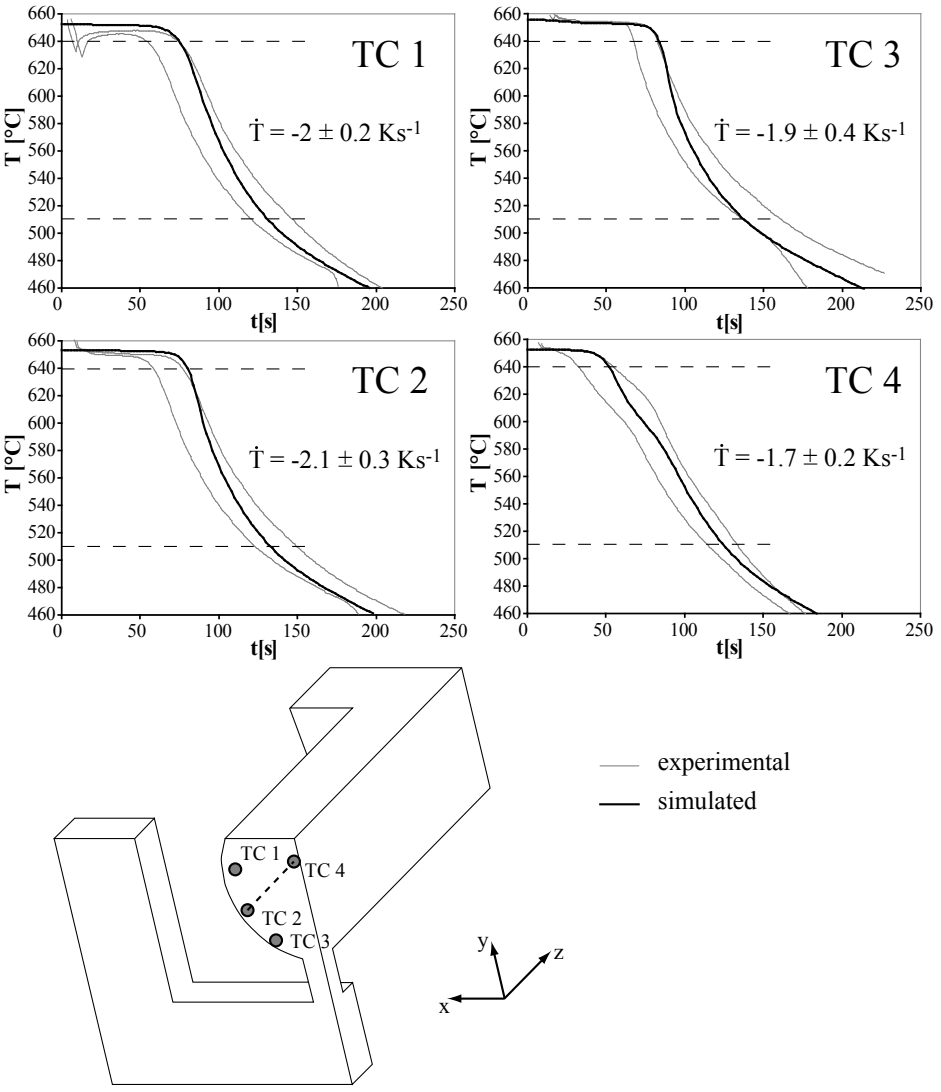


**Figure 6.13:** Position of the thermocouples and comparison between experimental temperature measurements and the result given by the simulation.

there exists a maximum, a minimum and an average for $G_z^{av}(x, y)$. These quantities are plotted as a function of the temperature at the location of thermocouple TC1 (when this temperature reaches the value $T_{tear}$, the tensile test is started) on Figure 6.14. It can be noted that $G_z^{av}$ decreases roughly linearly with temperature.

In addition to the gradient along the tensile axis, it is interesting to evaluate the temperature gradient $G_y^{av} = \left|\frac{\mathrm{d}T}{\mathrm{d}y}\right|$ along the vertical centerline of the specimen ($x = z = 0$). This quantity, which is related to the temperature difference between the top of the sample and the outlet of the filling system, is also plotted on Figure 6.14.

This information about the thermal gradient, which can only be obtained with this level of accuracy using simulated data, will be useful for further interpretation of the results. Moreover, it was used to verify that the selected mesh size is in good agreement with guideline (3.15) (p. 53).

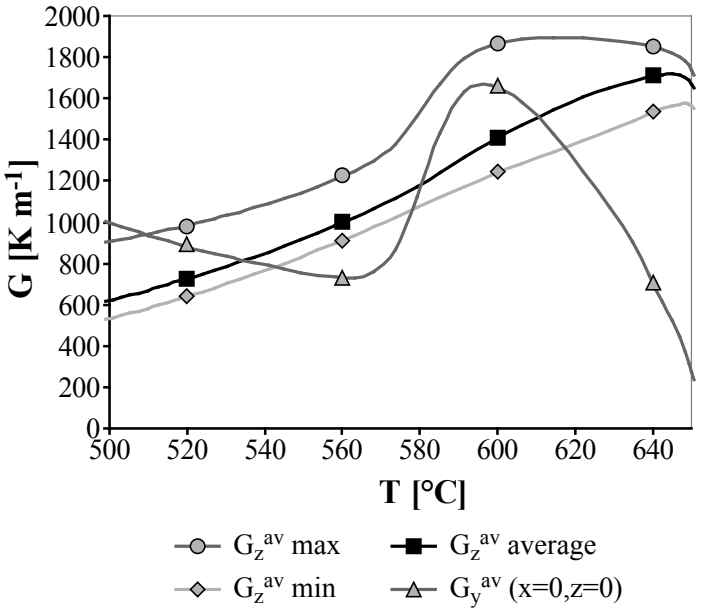


**Figure 6.14:** Thermal gradient along and perpendicular to the tensile axis as a function of $T$ at TC1 in the range where the tests were conducted.

### 6.2.2 Mechanical Results

One jaw of the tensile test machine moves at a constant velocity $\dot{u}_z$. As a consequence, an increasing strain is induced in the sample and will tend to be localized in the hot spot, i.e. at the center of the specimen. Let us first consider a typical result for the cumulated creep and swelling strains, $\epsilon_{cr}$ and $\epsilon_{sw}$, as shown on Figure 6.15.

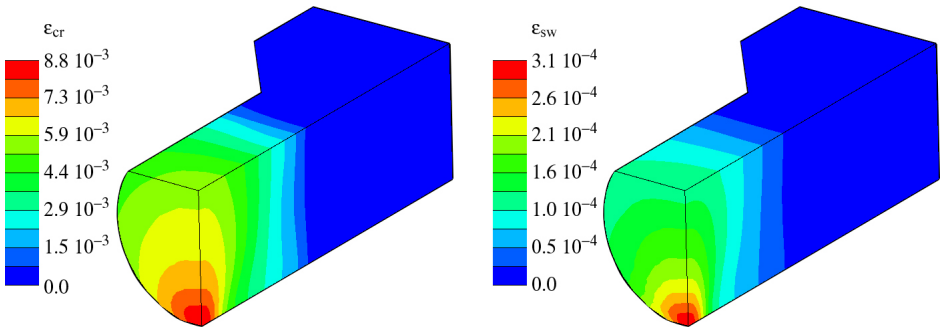


**Figure 6.15:** Effective creep and swelling strain for the test started at $T_{tear} = 570$ °C after 3 s with $\dot{u}_z = 10$ mm min$^{-1}$ (i.e. when $u_z = 0.5$ mm).

As expected, strain concentrates in the center of the specimen, i.e. around the center plane defined by $z = 0$. In this plane, there also exists a gradient of strain. The material near the outlet of the filling system is indeed the hottest and is thus even more deformed. For the interpretation of the results, the strain gradient in that plane is however not as important as the gradient obtained along $z$. In what follows, we shall thus consider quantities that are averaged at the tear plane, because they correspond to what is experienced by the mushy alloy where it fails. The center average of a given quantity $\Psi$ will be noted $\Psi^c$ and defined as:

$$\Psi^c = \frac{\int\int_{z=0} \Psi \mathrm{d}x\mathrm{d}y}{\int\int_{z=0} \mathrm{d}x\mathrm{d}y} \quad \text{with} \quad \int\int_{z=0} \mathrm{d}x\mathrm{d}y\,(t=0) = S_0 = 1010 \text{ mm}^2$$

When this quantity is evaluated at the time when failure occurred, it will be noted $\Psi^c_{fail}$. Please note that time at failure can only be evaluated based on the experimental data.

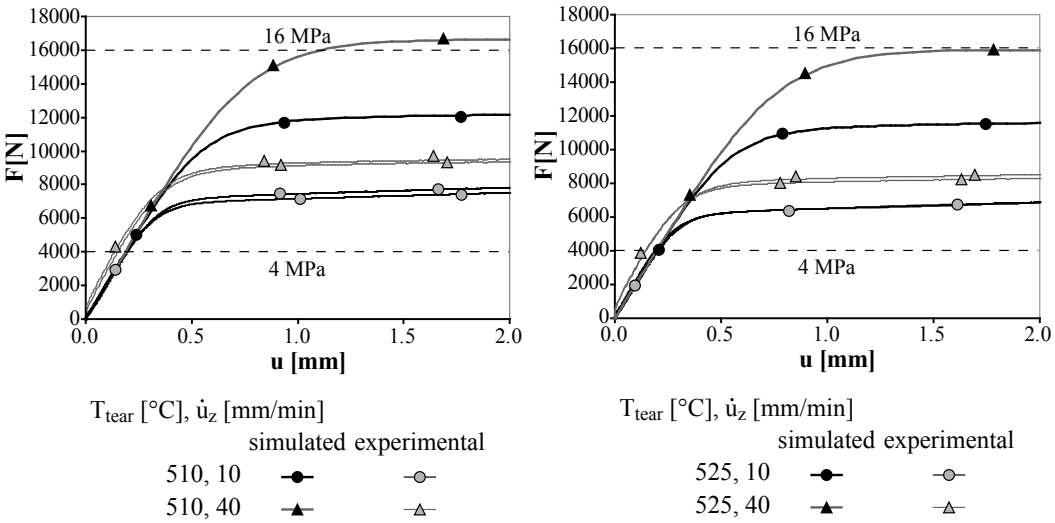


**Figure 6.16:** Comparison between the measured and simulated force recorded during various tests at low temperatures (510 °C and 525 °C). The values of nominal stress corresponding to $F$ are also suggested.

In order to validate the mechanical model, the force vs. displacement curve ($F(u)$) obtained from the simulation is compared with corresponding experimental measurements for different tearing temperatures $T_{tear}$ and applied displacement rates $\dot{u}_z$. The simulated curves are displayed with thick lines and black symbols. The experimental results are shown with thin lines and grey symbols (curves with the same symbol shape and line color correspond to identical conditions). Please note that, when available, two experimental curves are displayed for a given set of conditions in order to indicate the magnitude of the experimental uncertainty.

First of all, let us consider, the lowest temperature tests (Figure 6.16). When the tensile test is started at $T_{tear} = 510$ or 525 °C (at TC1), tearing does not occur. For these temperatures, the sample is almost entirely solidified and a classical viscoplastic behavior is thus observed. As expected, the experimental results are sensitive to the temperature and the applied displacement rate. The corresponding simulations tend to overestimate the reaction force during viscoplastic flow (in the initial region, when elastic deformation dominates the behavior of the sample, the agreement is good). However, the sensitivity to $T$ and $\dot{u}_z$ is reasonably well described.

These differences may be attributed to some inaccuracy in the thermal model or to small differences between the actual mechanical properties of the tested Al-2wt%Cu alloy and the model data. The agreement between the model and the experiments however remains fair. For $T_{tear} = 540$ °C (Figure 6.17 left), the center of the sample is mushy but the viscoplastic behavior is retained (due to the high solid fraction). $F$ is again somewhat overestimated during the viscoplastic plateau, which was expected since it was already the case in a fully solidified alloy but the strain rate sensitivity is well recovered. It is interesting to note that tearing occurred for all values of $\dot{u}_z$ except during one test at $\dot{u}_z = 2.5$ mm min$^{-1}$. At this velocity, solidification can in fact be completed before tearing occurs (in this test, a displacement of 0.2 mm is reached after about 5 s, which corresponds roughly to 10 °C of cooling).

As the tearing temperature is increased up to $T_{tear} = 595$ °C, the simulated values of $F$ rather tend to underestimate the experimental data (Figures 6.17 and 6.18). The most significant

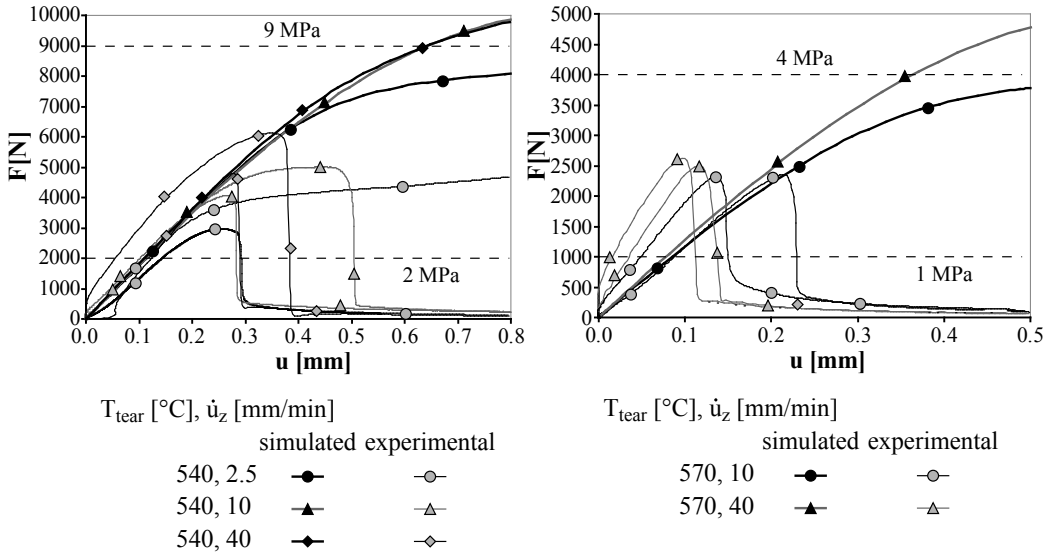


**Figure 6.17:** Comparison between the measured and simulated force recorded during various tests at relatively low temperature (540 °C and 570 °C). The values of nominal stress corresponding to $F$ are also suggested.

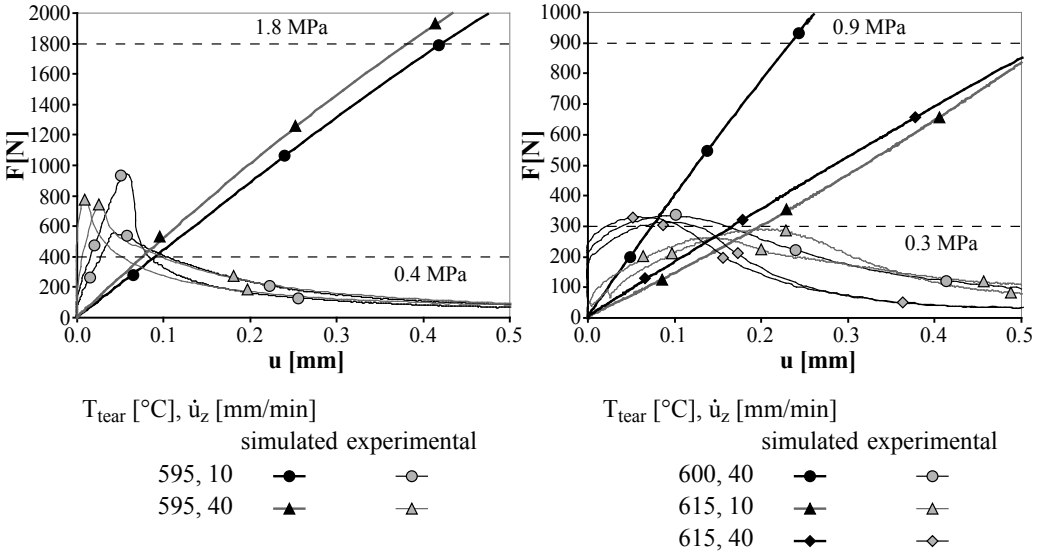


**Figure 6.18:** Comparison between the measured and simulated force recorded during various tests at moderate temperature (595 °C, 600 °C and 615 °C). The values of nominal stress corresponding to $F$ are also suggested.

differences between the model and actual measurements is found for the conditions where the material exhibits extremely limited ductility prior to failure (tearing). However, the sensitivity to temperature and applied strain rate remains reasonably well described by the model. At even higher temperatures (Figure 6.19), the ductility of the material increases and the force prediction recovers its fairly good accuracy.

In summary, the validity of the mechanical model is satisfactory. Due to some uncertainty in both the thermal model and materials properties, the reaction force (in other words, the stress) is not always perfectly well predicted by the simulation. However, it is important to note that the variation of $F$ with $T$ and $\dot{u}_z$ are well reproduced. As a consequence, the strain field is expected

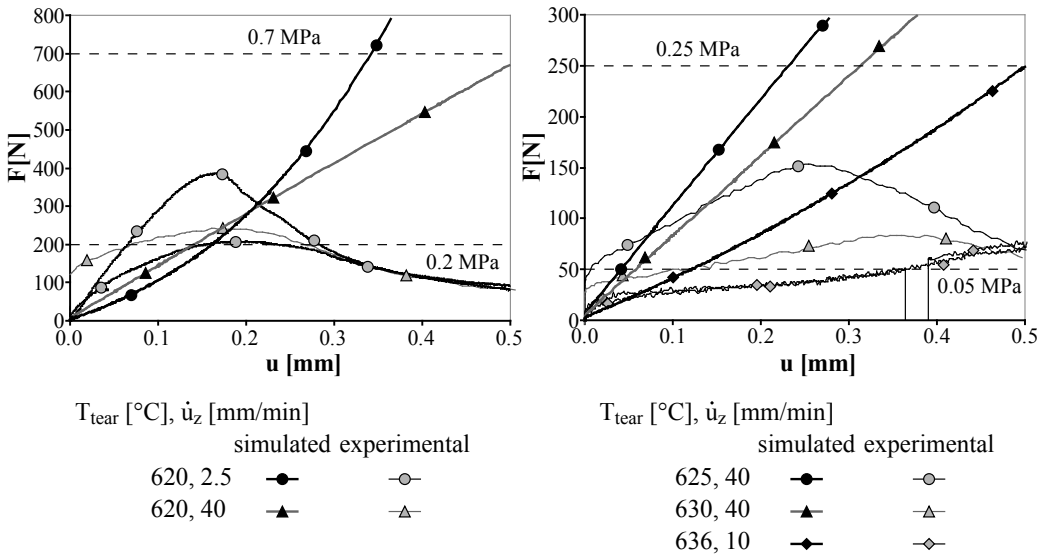


**Figure 6.19:** Comparison between the measured and simulated force recorded during various tests at high temperatures (620 °C to 636 °C).

to be calculated accurately and the model may be trusted from this point of view. In what follows, we shall thus focus on strain-related quantities, which are in general the most relevant to study in the context of hot tearing.

As a starting point, let us consider how the displacement at fracture $u_{fail}$ depends on the average temperature at the tear surface $T^c_{fail}$. Please note that in cases where tearing did not occur, the failure is measured by yielding (i.e. at the end of the elastic region). The result is shown on Figure 6.20.

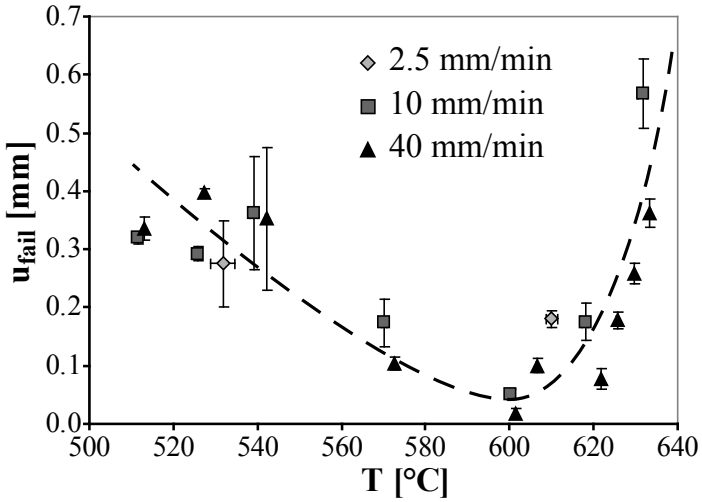


**Figure 6.20:** Measured displacement at fracture vs. average temperature in the tear plane.

What is obtained is a typical U-shaped curve where the apparent ductility of the alloy is high at both low (feeding) and high (solid-like behavior) solid fraction. This result is available experimentally [4]. The numerical model is very useful because is gives access to the strain at fracture (measured by the average value of $\epsilon_{zz}$ at the tear plane when tearing occurs and noted

$\epsilon^c_{fail}$), which is a more precise way to characterize the ductility of the alloy.

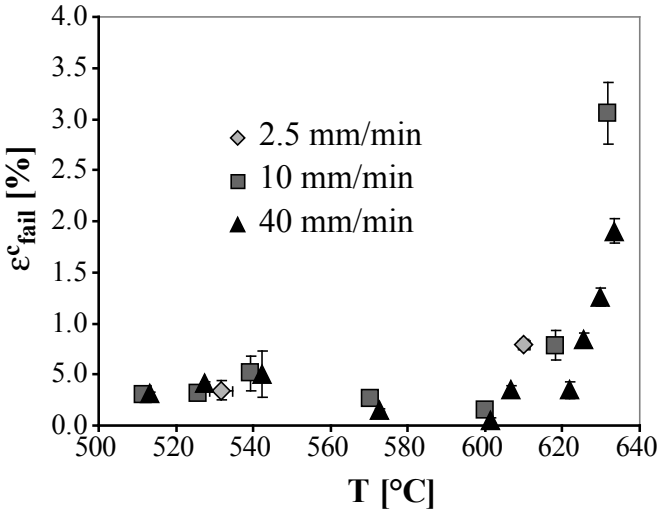


**Figure 6.21:** Strain at failure vs. average temperature in the tear plane.

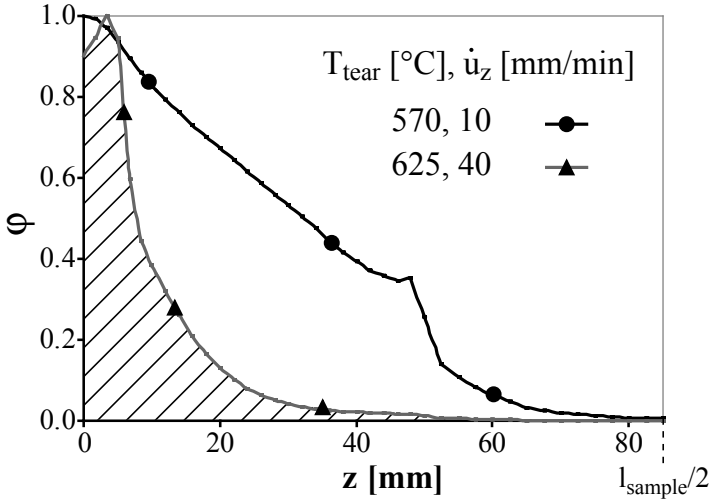


**Figure 6.22:** Profile of $\varphi$ across the length of the sample (this profile is symmetrical with respect to $z = 0$) for two different tests. The integral of $\varphi$ (hatched area, represents how the strain is distributed along the sample) is clearly higher at lower temperature and contributes significantly to the measured value of $u_{fail}$.

As shown on Figure 6.21, the plot of $\epsilon^c_{fail}$ against $T^c_{fail}$ has a less marked U shape. The displacement at failure is given by :

$$u_{fail} = \int_0^{l_{sample}} \epsilon^z_{zz,fail} \mathrm{d}z \quad \text{with} \quad \epsilon^z_{zz} = \frac{\int\int_z \epsilon_{zz} \mathrm{d}x\mathrm{d}y}{\int\int_z \mathrm{d}x\mathrm{d}y}$$

where $\epsilon^z_{zz}$ is the average strain in a section perpendicular to the $z$ axis ($\epsilon^{z=0}_{zz,fail} = \epsilon^c_{fail}$). Introducing the ratio of local strain at failure to the alloy ductility, $\varphi$, this can be rewritten :

$$u_{fail} = \epsilon^c_{fail} \int_0^{l_{sample}} \varphi \mathrm{d}z \quad \text{with} \quad \varphi = \frac{\epsilon^z_{zz,fail}}{\epsilon^c_{fail}}$$

This means that both strain repartition (characterized by $\varphi$) and the ductility of the alloy ($\epsilon^c_{fail}$) contribute to the value of the displacement at failure.

At low temperature, the ductility of the material increases rather slowly. However, the strain becomes much better distributed in the sample because of the higher strength of the material in the hot spot. As a result, high values of $u_{fail}$ are observed because a larger length of the sample is strained ($\int_0^{l_{sample}} \varphi \mathrm{d}z$ is high). On the other hand, at high temperature, the ductility $\epsilon^c_{fail}$ is high, inducing a large value of $u_{fail}$, while $\int_0^{l_{sample}} \varphi \mathrm{d}z$ is rather low. This is illustrated on Figure 6.22

When compared to the experimental data, the model has the advantage of being able to distinguish between two contributions, namely variation of the intrinsic properties of the material and inhomogeneous strain repartition (the latter being also related to the test geometry and cooling conditions).

In hot tearing studies, it is also very relevant to consider the ductility of the mushy alloy as a function of the solid fraction. Figure 6.23 displays the ductility $\epsilon^c_{fail}$ plotted against $g^c_{s,fail}$. It appears that the ductility (i.e. resistance to strain) is minimum around $g_s = 96$ %. Please note that this value also corresponds to the transition between two different stress states. At higher $g_s$ the alloy experiences conditions close to uniaxial tension ($X = -\frac{1}{3}$). At lower solid fractions, the value of $X$ decreases (towards -0.5), which means that the stress state becomes triaxial with small tensile components normal to the principal loading direction.

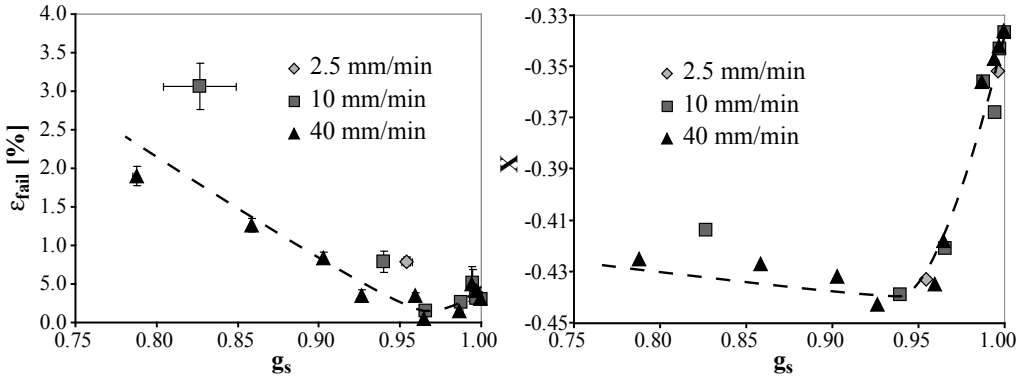


**Figure 6.23:** Strain and stress triaxiality at failure vs. average solid fraction in the tear plane.

Another quantity that is relevant to study is the strain rate, which will be measured here by $\dot{\epsilon}^c_{zz}$. This quantity, which can be extracted from the numerical results, depends on the applied displacement rate. We shall thus consider a normalized strain rate $\frac{1}{\tau}$ including $\dot{u}_z$ and the length of the sample $l_{sample}$. This quantity can be evaluated at the beginning of the test ($\tau_i$) or at failure ($\tau_{fail}$). These are defined as follows :

$$\tau_i = \frac{\dot{u}_z}{\dot{\epsilon}^c_{zz,initial} \cdot l_{sample}} \quad \text{and} \quad \tau_{fail} = \frac{\dot{u}_z}{\dot{\epsilon}^c_{zz,fail} \cdot l_{sample}} \tag{6.1}$$

Please note that $\tau$ may be interpreted as a measure of the length (expressed as a fraction of $l_{sample}$) on which the strain rate is effectively applied (as suggested on Figure 6.24). In an homogeneous material under uniaxial tensile conditions, $\tau = 1$.

Both these quantities are plotted as a function of temperature on Figure 6.25. At the very beginning of the test, the normalized strain rate $\tau_i$ depends almost linearly upon $T^c$ (left). A

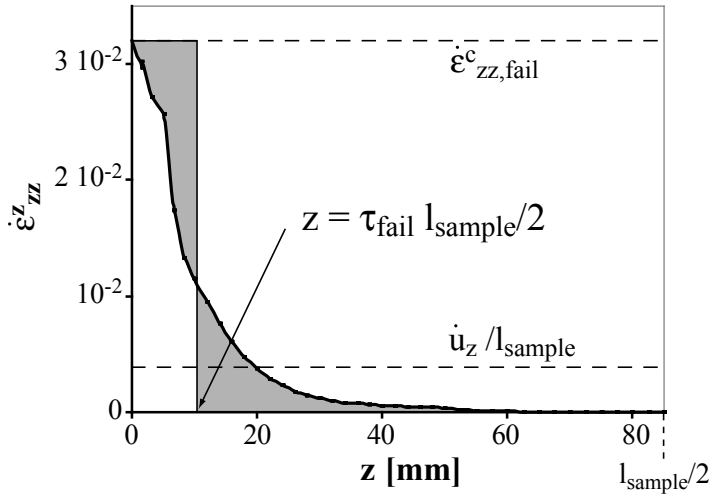


**Figure 6.24:** Interpretation of $\tau_{fail}$ from the consideration of the strain rate profile $\dot{\epsilon}^z_{zz}$ at the time of tearing. The grey shaded regions have the same area. This example corresponds to a temperature $T_{tear} = 640°C$ and a velocity of 40 mm min$^{-1}$.

significant deviation from this behavior is observed at the point when the mushy alloy is torn (right).

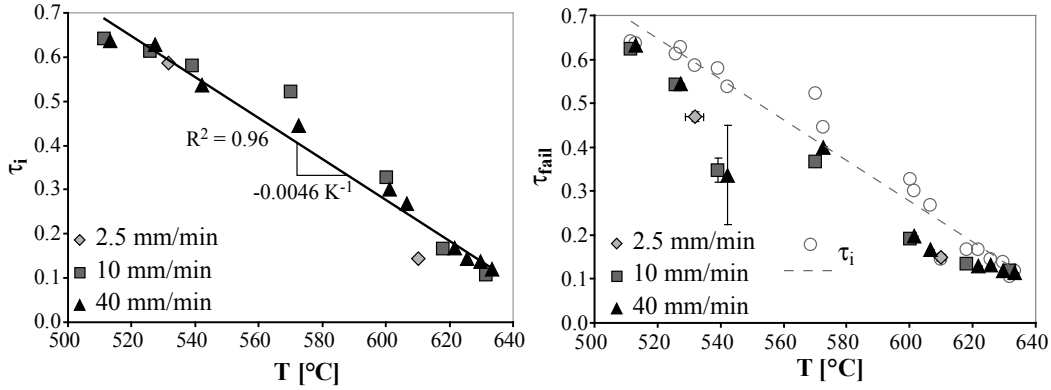


**Figure 6.25:** Normalized strain rate $\tau$ initially and at failure. Initially, the data is well fitted by a linear relationship. The initial points together with this linear fit are recalled in light grey on the plot of $\tau_{fail}$ vs. $T^c$.

In order to characterize hot tearing in this test, it appears to be more relevant to study the variation of $\tau_{fail}$ as a function of the average solid fraction in the tear plane at failure, $g^c_{s,fail}$. This result is shown on Figure 6.26. It is interesting to note that the value of $\tau_{fail}$ remains roughly constant up to $g_s = 0.95$. When the solid fraction is higher, $\tau_{fail}$ increases indicating a transition to a coalesced solid network. This increase indeed means that the strain rate is getting less and less localized at the center of the specimen. This is only possible when the mushy material at $T^c$ has a strength that becomes comparable to that of the neighboring solid.

At lower solid fractions $\tau_{fail}$ remains approximately constant. However, it should be kept in mind that $\tau$ does not vary much in time and that its average value during the tensile test is close to $\tau_{fail}$. This means that the absolute value of the strain rate does not correlate with tearing. This is in contradiction with the prediction of models such as the RDG criterion. These results

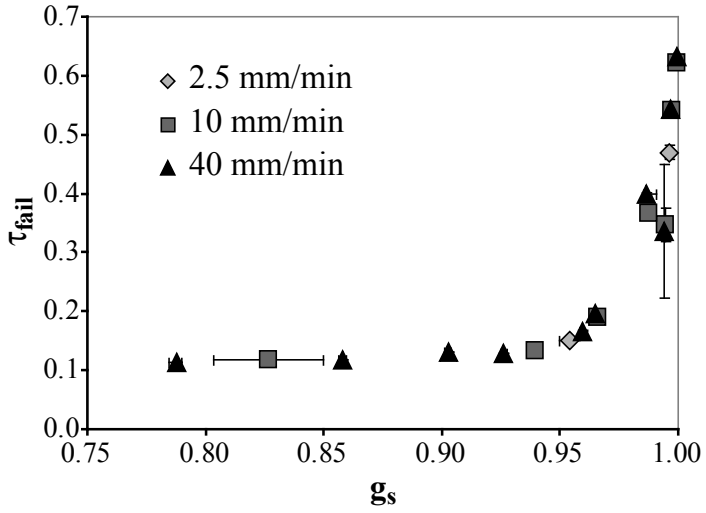


**Figure 6.26:** Normalized strain rate at failure vs. average solid fraction in the tear plane.

in fact indicates that, when $T^c > T^{coal}$, the concentration of strain at the center of the specimen is constant (independent of temperature and applied displacement rate). Moreover, tearing is found to occur at some critical strain that depends weakly upon the strain rate.

### 6.2.3 Porosity Results

First of all, it is worth considering how the value of the liquid pressure just before solidification is completed varies across the sample. This is displayed on Figure 6.27. It appears that $p_l$ varies significantly within the tear plane. A minimum pressure is found away from both the top surface and the outlet of the filling system (which remains fully liquid during the test). From the feeding point of view, the minimum value of the liquid pressure, $p_l^{min}$, indicates the most critical region for hot tearing.

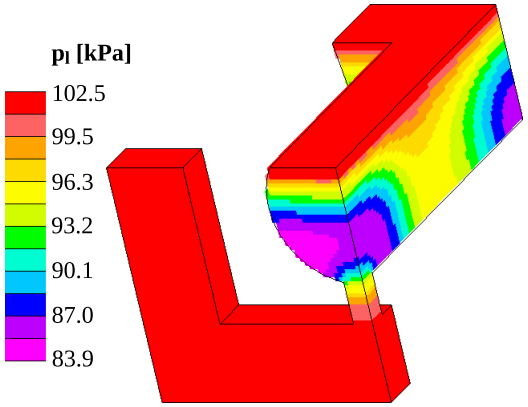


**Figure 6.27:** Liquid pressure in the last remaining liquid.

In the same region, a maximum porosity fraction $g_p^{max}$ is found. However, the values of $g_p$ in the tear plane tend to be more homogeneous than those of $p_l$. In order to characterize the availability of liquid feeding, the value of $p_{l,fail}^{min}$ and $g_{p,fail}^{max}$ were extracted from the simulation and plotted against $T_{fail}^c$. This result is displayed on Figure 6.28. On the same graphs, the result

that was obtained without taking into account strains ($\nabla \cdot \mathbf{v}_s$) in the pressure calculation is also shown.

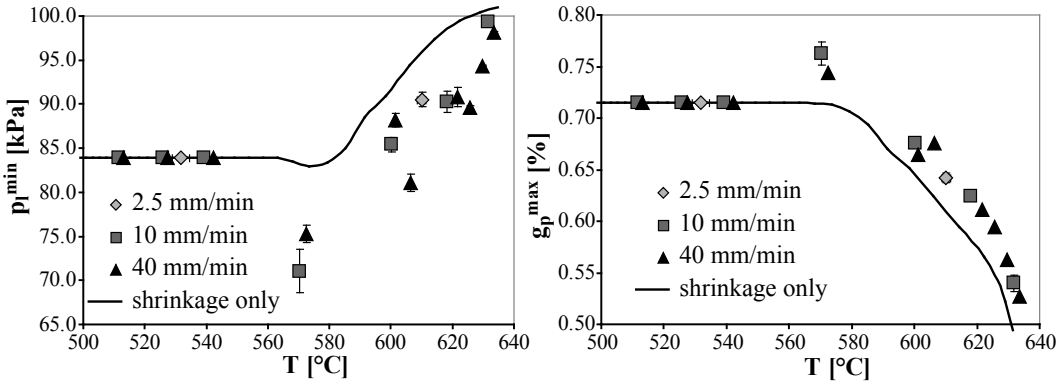


**Figure 6.28:** Minimum liquid pressure and maximum porosity fraction at failure as a function of $T^c_{fail}$. The result obtained for a calculation taking into account solidification shrinkage only (no strain term taken into account) is also shown (black line).

The pressure drops are rather small (within 30 kPa), which indicates that using the semi-coupled method is indeed relevant. Moreover, the dominant contribution to the variation of $p_l$ comes from the solidification shrinkage. As it can clearly be observed on the values of $g^{c,max}_{p,fail}$, the strain rate contribution remains small even though it is not completely negligible. This was expected as the ratio:

$$\frac{\Omega^{sh}}{\Omega^{mech}} = \frac{v_T \beta}{\dot{\epsilon}_{sw} \frac{\Delta T_{freeze}}{G}} \approx \frac{2 \cdot 10^{-3} \cdot 8 \cdot 10^{-2}}{10^{-4} \frac{100}{1500}} \approx 25$$

indicates that $\Omega^{sh}$ is indeed dominant. Please note that $\dot{\epsilon}_{sw}$ is much smaller than $\dot{\epsilon}_{zz}$ because the latter is partially compensated by $\dot{\epsilon}_{xx}$ and $\dot{\epsilon}_{yy}$. From that point of view, the rig test is different from the mushy zone tearing test. In the latter case, the amount of porosity as well as the liquid pressure drop were strongly influenced by the relatively large strain rate imposed to the sample.

Another consequence of this is that the amount of porosity increases steadily with $g^c_{s,fail}$. This is shown on Figure 6.29. This quantity is indeed determined by solidification dynamics. As a consequence, the transition observed in the straining behavior of the mushy alloy around $g_s = 0.95 - 0.96$, does not disturb the porosity formation pattern in the sample.

### 6.2.4 Summary

The semi-coupled method was successfully applied to the rig test (from Alcan-Pechiney). Both the thermal and mechanical models proved to be accurate to a satisfactory extent. Moreover, simulated data could be combined with the experimentally measured time to failure in order to investigate what is happening when the sample is torn apart by the imposed displacement.

First of all, the ductility measured by $\epsilon^c_{zz,fail}$ could be studied. The simulation indicated neither excessive strain concentration nor instabilities such as necking or decohesion during the test. As a consequence, this strain at failure appears to be characteristic of the behavior of the material.

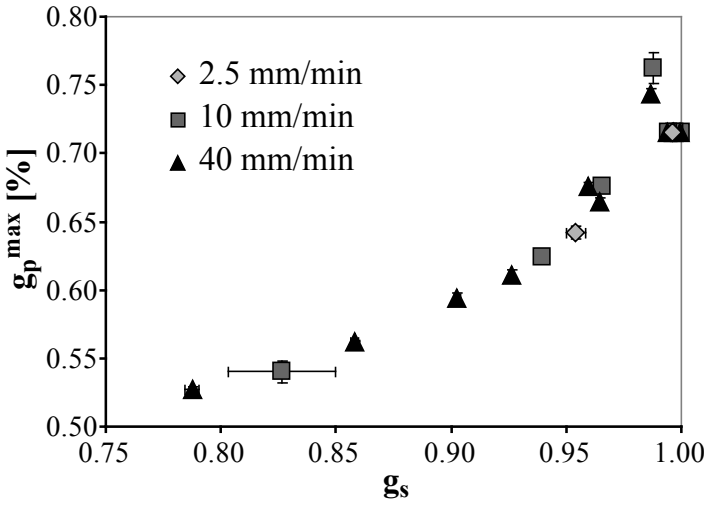


**Figure 6.29:** Maximum porosity fraction at failure as a function of solid fraction in the tear plane.

At low solid fraction, it was found that the ductility is high because liquid feeding allows for grain rearrangement without void creation. At very high solid fractions, the ductility of the material increases with $g_s$ but remains smaller than what is obtained for $0.75 < g_s < 0.9$. On the other hand, at high $g_s$, strain is distributed much more evenly in the $z$ direction, leading to very high values of the displacement at fracture $u_{fail}$ and to the typical U-shaped curve. The difference between intrinsic materials properties and strain repartition is thus available from the numerical model.

Around $g_s = 0.96$ the ductility is minimum, indicating that neither grain rearrangement (and liquid feeding) nor solid-like deformation of a coalesced solid network are strongly active deformation mechanisms. In fact, this solid fraction corresponds to the transition between these two deformation regimes and to a high risk of failure (hot tearing) due to the low ductility of the mushy alloy.

This transition also appeared from the consideration of the normalized value of the strain rate at fracture $\tau_{fail}$ which increases rapidly above $g_s = 0.96$. This increase can be related to the more homogeneous repartition of strain obtained under such conditions. When the hottest material indeed becomes coalesced, the properties of the alloy vary much less in space (as opposed to the case where two solid regions are connected by a non-coalesced mushy region in the center).

In summary, above $g_s = 0.96$, deformation gets more and more evenly distributed in the sample because the gradient of strength decreases. In addition, the ductility of the material increases slowly because it basically behaves like a solid. Tearing can only occur when sufficient strain is applied and healing is impossible. Below this limit, the strain concentration remains roughly constant and the strain rate is thus imposed by the boundary condition. In this regime, the ductility of the material increases strongly as $g_s$ decreases because grains can rearrange and voiding is prevented by feeding. At a given strain, the grain structure becomes too entangled to rearrange and tearing occurs. In this test, hot tearing appears to be induced at some critical strain and the influence of strain rate is not dominant.

On the other hand, the amount of porosity expected in the sample is mostly determined by solidification shrinkage. The rather limited effect of strain on this quantity indicates that no significant deformation-induced damage is accumulated in the sample before its failure. This condition is quite similar to what is known in DC casting.

In conclusion, the rig test appears to be quite effective to characterize the behavior of mushy alloys in tension. The experimental data have the advantage of representing well the typical strain rates encountered in DC casting. The numerical model helps showing how the intrinsic ductility of the material varies as well as the concentration of strain in the expected tear plane.

What is difficult to establish however is how to apply these results to a more complex situation such as what happens during hot tearing in a DC-cast billet. The conditions of the rig test are indeed quite specific : e.g. tensile stress state with the maximum principal stress perpendicular to the isotherms, independence of cooling conditions and applied load.

## 6.3 Full-Scale Billet

Up to this point, we have studied tensile tests conducted on mushy samples at the laboratory scale. They have several specific features that should be outlined :

- The applied load is mainly uniaxial.
- The isotherms are mostly perpendicular to the principal loading direction and parallel to the observed hot tears.
- Strains can be applied to the material independently from the cooling conditions.
- Due to nucleation and growth of tears, the sample is entirely broken.

We will now examine how the semi-coupled method may be applied to an industrial scale case, i.e. the casting of an entire billet. In various aspects, this is quite different from the cases studied previously :

- The isotherms are perpendicular to the observed tears.
- The strains applied to the mushy zone are dictated by the temperature field and thus depend upon the cooling conditions.
- The tears nucleate in the mushy zone and are propagated to some extent by the fact that the mushy zone travels through the casting. The billet is not entirely broken by hot tearing.

As illustrated on Figure 6.30, numerical modeling gives access to a large amount of quantitative information about this casting. As far as experimental data is concerned, it mainly indicates where hot tears are found. However, there is no indication of when these tears have formed at some given location, i.e. the solid fraction at the time of failure is not known. This situation is different from what was known for the tensile tests and makes the interpretation of the results even more difficult.

Before looking at the simulation results, let us summarize what we know about cracking in the billet (for the particular casting that we decided to study). After casting, it was examined by ultrasonic (US) testing to detect the presence of a hot tear. This tear was found to be located along the centerline ($r = 0$). It is not present at the bottom of the billet (i.e. the region cast during the start-up phase). It is initiated during the first increase in $v_{cast}$. It disappears during the ramping down of the casting speed (healing). When $v_{cast}$ increased again at the end of the casting, a new tear appeared and was retained up to the top of the billet.

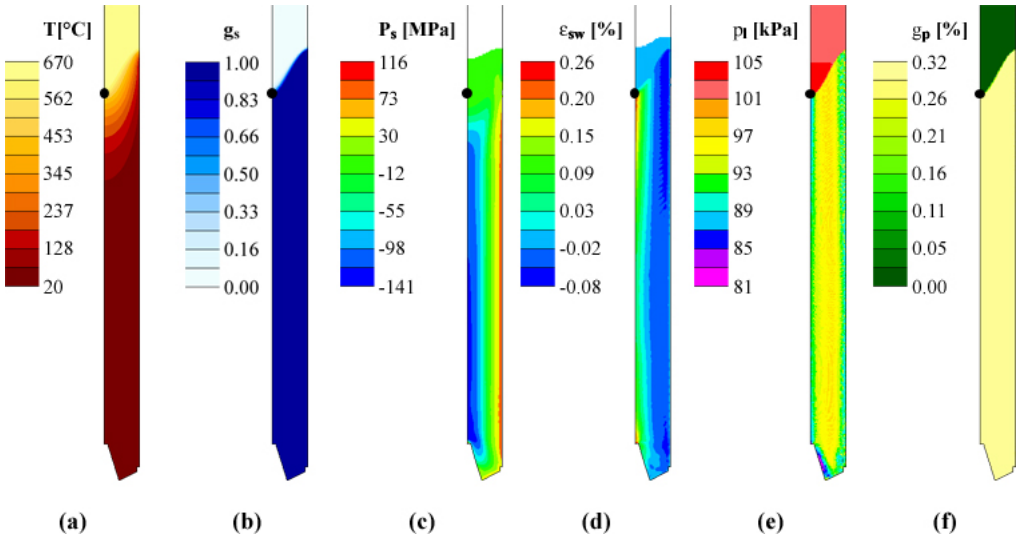


**Figure 6.30:** Different quantities that can be calculated by the semi-coupled method in a billet. These pictures are extracted at 880 s, when $z\left(g_s = 0.95\right) = z^{0.95} =$ 1065 mm. This position, indicated by the black dot, corresponds to where the first hot tear was detected by ultrasonic (US) measurements at the centerline of the billet. (a) temperature $T$ (b) solid fraction $g_s$ (c) pressure in the solid $P_s$ (d) cumulated volumetric strain $\epsilon_{sw}$ (e) liquid pressure $p_l$ (f) fraction of porosity $g_p$. Please note that on (c) and (d), the top part of the billet appears in white, meaning that the corresponding elements are not activated yet (mechanical results).

The second region of tearing was studied by Grasso [5]. It was cut into 14 mm thick slices and the tear was observed with the naked eye. This study confirmed that the tear was indeed located along the centerline. Just after nucleation, the shape of the crack is rather linear. After some length (i.e. after the advancing tear has had some time to develop), a characteristic three-branched star shape is established and retained for the rest of the casting (see Figure 4.9 on page 69). These observations are summarized in Table 6.2 and represented graphically on Figure 6.31. Please note that the hot tear can be observed by the naked eye only if it is open enough, which explains why the US measurement indicates tear nucleation earlier (i.e. at lower $z$).

| event | nucleation | healing | nucleation | linear | star-shaped |
|---|---|---|---|---|---|
| detection | US | US | US | eye | eye |
| z [mm] | 1065 | 2230 | 2740 | 2836 | 2906 |

**Table 6.2:** Evolution of the hot tear found at the centerline of the billet : event, detection method and corresponding position in the billet.

At this stage, it is useful to introduce the notation we shall use to indicate the position and velocity of an isotherm. As an example, the position of the isotherm of $T = 550$ °C will be noted $z^{550}$ and its velocity $v_T^{550}$. Similarly, in terms of solid fraction, the isosurface of $g_s = 0.9$ is located at $z^{0.9}$ and has a velocity $v_T^{0.9} = \frac{\mathrm{d}z^{0.9}}{\mathrm{d}t}$. As a consequence $v_{cast}\left(z_{level}\right)$ can also be written $v_T^{670}\left(z^{670}\right)$. Please note that, otherwise stated, these velocities and positions will be evaluated at the centerline ($r = 0$) because it is where tears are found. Similarly, the thermal gradient $G^{0.6}$ will refer to $\frac{\mathrm{d}T}{\mathrm{d}z}\big|_{r=0,z^{0.6}}$ and the cooling rate $\dot{T}^{0.6}$ is evaluated under the same conditions. Other

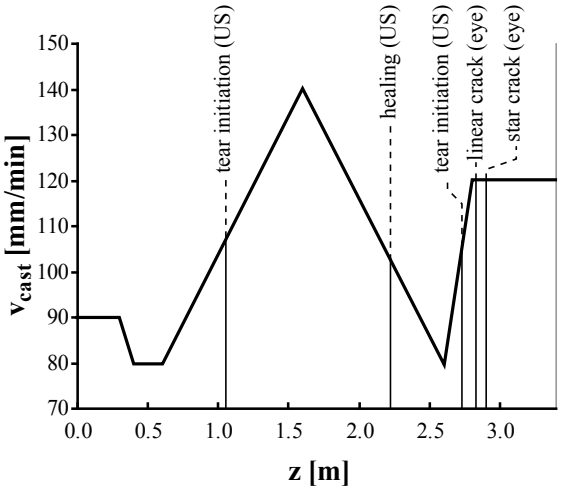


**Figure 6.31:** Summary on the hot tearing events. Please note that $z$ stands for $z_{level}$ when plotting $v_{cast}$.

quantities such as $\epsilon^{sw,0.9}$, $p_l^{0.95}$ should always be understood in the same way, i.e. they represent the value of the corresponding field, evaluated at $r = 0$ and at the $z$ position of the isotherm corresponding to the solid fraction indicated as a superscript. For the sake of clarity, Figure 6.32 represents schematically how the $z$ position is measured.

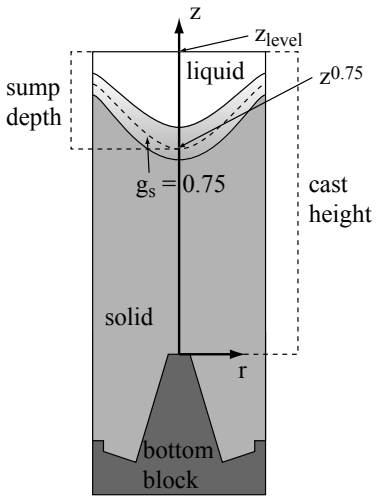


**Figure 6.32:** Schematic representation of the reference frame for the $z$ coordinate. The position of the isotherms along the centerline, the cast height and the sump depth are measured along this axis.

### 6.3.1 Thermal Results

In order to validate the thermal model, experimental measurements of the sump depth obtained for a similar cast are considered [6]. They are compared with the simulated sump depth as measured by $z_{level} - z^{0.4}$, $z_{level} - z^{0.7}$ and $z_{level} - z^{0.95}$ (it is indeed difficult to know exactly to which solid fraction corresponds the penetration of the measurement rod). This comparison is displayed on Figure 6.33.

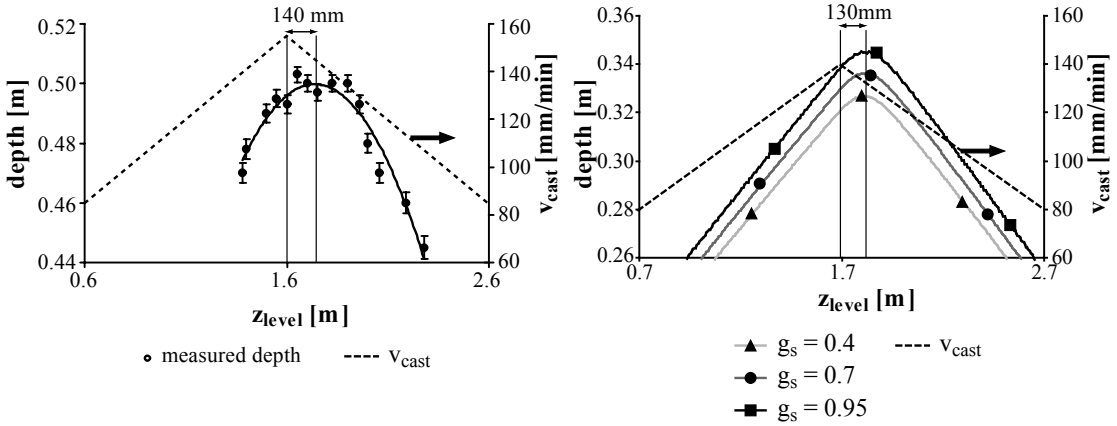


**Figure 6.33:** Experimental measurements of the sump depth from [6] compared with simulated values (difference between $z_{level}$ and the vertical position along the centerline of the iso-$g_s$ line for 0.4, 0.7 or 0.95). Due to the experimental method, the measured depth is not expressed with respect to the liquid level and can thus not be compared directly with the simulated data.

Due to small differences in the experimental conditions and the fact the experiment cannot be performed with the liquid level as a reference position, the absolute values of the sump depth should not be compared. What is important however is that the experiment indicates that there exists a time delay between the observed maximum sump depth and the maximum imposed casting speed. This delay is due to thermal inertia of the casting and can be converted in term of a difference in $z_{level}$ : $\Delta z_{level} = \int_{(t \leftrightarrow v_{cast}^{max})}^{(t \leftrightarrow depth^{max})} v_{cast} \mathrm{d}t$. According to the parabolic fit of the experimental measurements, this shift corresponds to $\Delta z_{level} = 140$ mm. The shift predicted by the numerical simulation was found to be around[3] $\Delta z_{level} = 130$ mm thus indicating that the thermal model is fairly accurate, at least once the start-up phase is over.

As summarized above, the position at which the hot tear appears ($z_{tear}$) and heals ($z_{heal}$) is known. Instead of this position, it would be more interesting to determine what is the velocity of the isotherms when and where the tear is initiated ($v_{T,tear}$) or healed ($v_{T,heal}$). Commet proposed that $v_{T,tear}$ could be estimated as $v_{cast}\,(z_{tear})$ [6]. In general, this can only be an estimation since the hot tear does not form at $z_{level}$ (in fact, hot tearing can only occur some distance below $z_{level}$, where $0.8 < g_s < 0.99$). Moreover, the thermal inertia of the system will depend on many parameters and affect the local isotherm velocity.

In this context, the numerical model can be used to know how fast a given isotherm (corresponding to e.g. $g_s = 0.95$) moves as a function of its position in the sample (lagrangian evolution of $v_T$). Such a result is shown on Figure 6.34. If one considers a given position in the billet (eulerian view of the problem), it turns out that all the isotherms in the coherent mushy zone will pass that position with approximately the same velocity. This velocity is moreover close to the casting speed, which corresponds to the imposed value of $v_T$ at the liquid level (i.e. for the 670 °C isotherm). In fact, the isotherms are some distance below $z_{level}$ and thermal diffusivity ($\alpha = \frac{\kappa}{C_p} \approx 7 \cdot 10^{-5}$) is such that it takes some time before these isotherms increase their speed (if $v_{cast}$ is increasing). These two effects compensate so that it is acceptable to approximate e.g. $v_T^{0.9}\left(z^{0.9}\right)$ with $v_{cast}\,(z_{level})$ as suggested in [6].

From this result, it is possible to measure accurately what was the velocity at which various isotherms were traveling at the points where the hot tear was started and healed. During the first

[3] it depends weakly on what solid fraction is assumed to be touched by the rod measuring this depth.

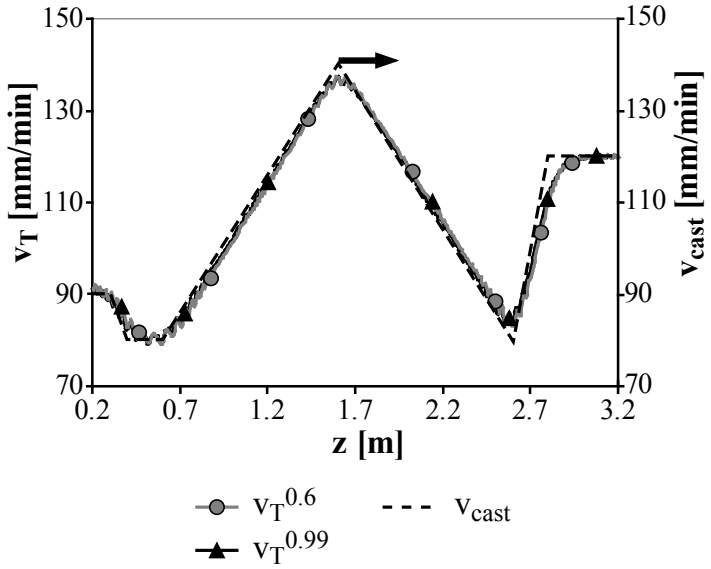


**Figure 6.34:** Velocity of the isotherms as a function of their position: $v_T^{0.6}\left(z^{0.6}\right)$ and $v_T^{0.99}\left(z^{0.99}\right)$.

increase in $v_{cast}$, the tear appeared at a location corresponding to $v_T = 105.9 \pm 0.5$ mm min$^{-1}$. For healing of the tear, it was necessary to ramp the isotherm velocity down to $v_T = 104.2 \pm 0.5$ mm min$^{-1}$. For the second increase in $v_{cast}$, tearing appeared for $v_T = 100.8 \pm 1.1$ mm min$^{-1}$. As was expected, hot tearing happens at lower velocity when the casting speed is varying rapidly (second increase of $v_{cast}$). Moreover, once a tear exists in the billet, it will only heal if the casting speed is dropped below the value at which it was initiated.

Further information is available from the thermal model as it is possible to extract, along the centerline, the thermal gradient around a given isotherm, e.g. $G^{0.8}\left(z^{0.8}\right)$. This quantity will depend strongly upon which isotherm is considered, as shown on Figure 6.35. As the time (or local solid fraction) at which the tear was started or healed is not known, it is not possible to extract one value of $G$ that corresponds to the conditions of tearing. However, it is possible to observe that the thermal gradient increases with $g_s$ and seems to exhibit a maximum value between $g_s = 0.9$ and $g_s = 0.99$, which is typically the range that is critical for hot tearing. The typical order of magnitude of the thermal gradient in that significant range is of 7000 K m$^{-1}$.

Similarly, the cooling rate experienced by the material at the location of a given isotherm can be extracted from the simulated thermal field. The local cooling rate is negative and its absolute value (displayed on Figure 6.36) increases as solidification proceeds. Again, it is difficult to extract the exact value of $\dot{T}$ at which the tear nucleates or heals (because the corresponding solid fraction is not known). However, is seems that $\dot{T} \approx -10$ K s$^{-1}$ is the reasonable order of magnitude to be used to characterize this casting.

In summary, the thermal model provides detailed information about the conditions under which hot tearing is expected to occur. However, characteristic quantities such as thermal gradient or cooling rate cannot be accurately evaluated at the onset/end of hot tearing because the time at which this defect is formed/healed is not known exactly.

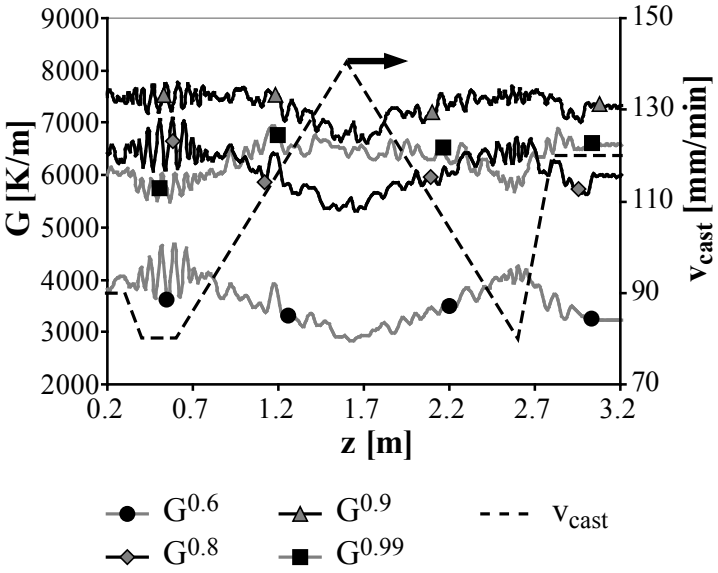


**Figure 6.35:** Thermal gradient at the position of several isotherms corresponding to $g_s = 0.6$, 0.8, 0.9 and 0.99.

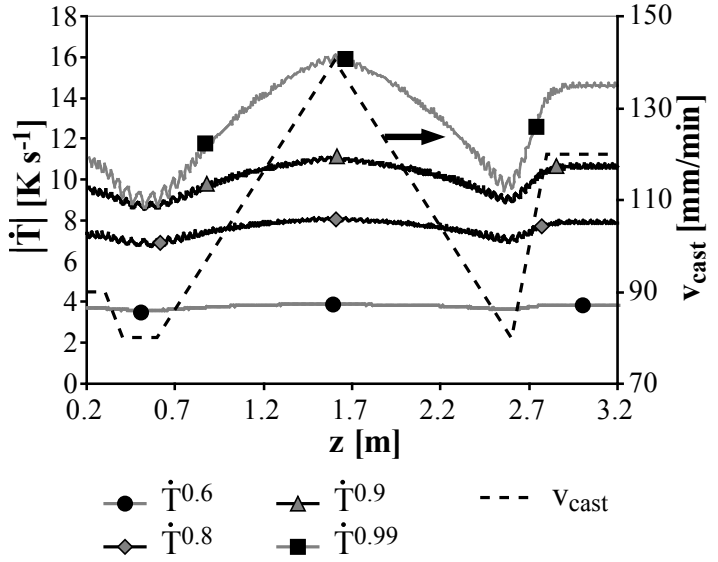


**Figure 6.36:** Absolute value of the cooling rate at the position of several isotherms corresponding to $g_s = 0.6$, 0.8, 0.9 and 0.99.

### 6.3.2 Mechanical Results

Before considering strains in the mushy zone, it is worth making a few comments about the stresses predicted in the billet by the model. Along the centerline, the dominant stress contribution (i.e. the maximum principal stress) is tensile and oriented in the radial direction. As a consequence, it is interesting to study the value of $\sigma_{rr}$ evaluated on a given isotherm (corresponding to some value of $g_s$) as a function of the position of this iso-$g_s$. This result is shown on Figure 6.37. It is important to note that the order of magnitude of the tensile stress experienced by the mushy alloy in the range of solid fractions where it is expected to fail is typically 1–2 MPa.

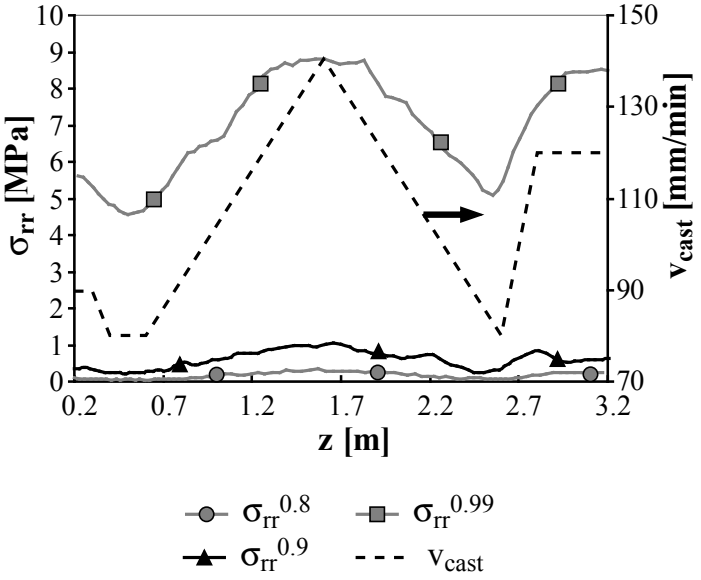


**Figure 6.37:** Radial stress at the centerline of the billet as a function of the position of the iso-$g_s$ on which this stress is evaluated.

Along the centerline of the billet, it is also interesting to study the volumetric strain cumulated up to a given solid fraction :

$$\epsilon_{sw}^{g_s} = \int_{g_s=g_s^{coh}}^{g_s} \dot{\epsilon}_{sw} \mathrm{d}t$$

This quantity was indeed used more or less directly in recently formulated hot tearing criteria [1, 106]. It is plotted as a function of the position of the corresponding iso-$g_s$ for three different solid fractions on Figure 6.38. Again, it is difficult to evaluate accurately $\epsilon_{sw}^{g_s}$ when tearing occurs because $g_{s,tear}$ is unknown. However, it is interesting to note that, for $g_s = 0.99$, the positions of tear initiation (two occurrences) correspond to $\epsilon_{sw}^{0.99} = 0.165 \pm 0.005$ % while healing occurs for $\epsilon_{sw}^{0.99} = 0.145 \pm 0.005$ %. This indicates that $\epsilon_{sw}$ appears to be a quite good indicator of the hot tearing tendency in that problem in the sense that hot tearing seems to arise when $\epsilon_{sw}$ exceeds a given value.

As suggested by the RDG criterion [37], which seems to be well suited to the present situation [93], it is also relevant to study the variation of the strain rate (measured by the rate of swelling $\dot{\epsilon}_{sw}$) evaluated at some given solid fraction along the billet. This is displayed on Figure 6.39. Below $g_s^{coh}$, $\dot{\epsilon}_{sw}$ is zero according to the rheology of the material. Above $g_s^{coal}$ the mushy alloy behaves very much like a solid and the swelling rate thus tends to decrease as indicated by $\dot{\epsilon}_{sw}^{0.99}$ (the dense solid deforms with $\dot{\epsilon}_{sw} = 0$). Moreover, the numerical results indicate that the volumetric strain rate remains fairly constant in the range $0.8 < g_s < 0.94$, at least in the region where hot tearing is initiated and healed.

Since $\dot{\epsilon}_{sw}$ varies only slightly with $g_s$ in the range of solid fraction in which hot tears may form, it is possible to study the value of this parameter when the hot tear is initiated (2 locations) :

$$\dot{\epsilon}_{sw}^{initiation} = 1.67 \pm 0.07 \cdot 10^{-4} \text{ s}^{-1}$$

On the other hand, healing is found at a location such that :

$$\dot{\epsilon}_{sw}^{healing} = 1.55 \pm 0.07 \cdot 10^{-4} \text{ s}^{-1}$$

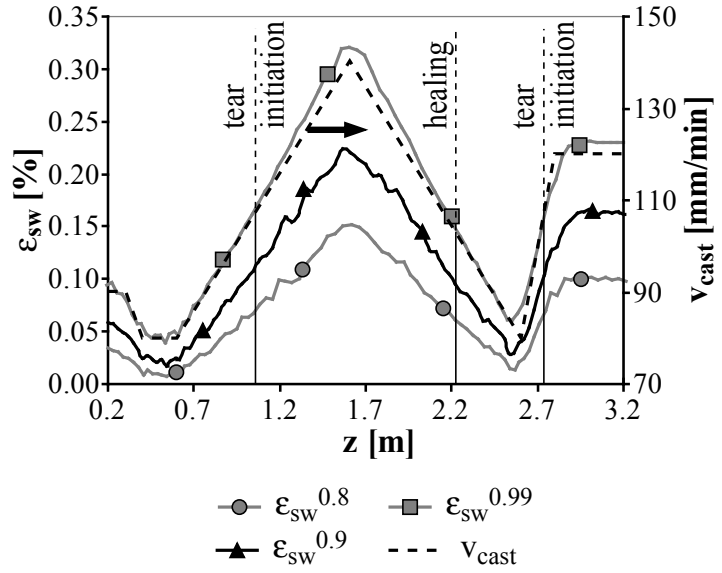


**Figure 6.38:** Cumulated volumetric strain up to a given solid fraction plotted against the corresponding $z^{g_s}$.

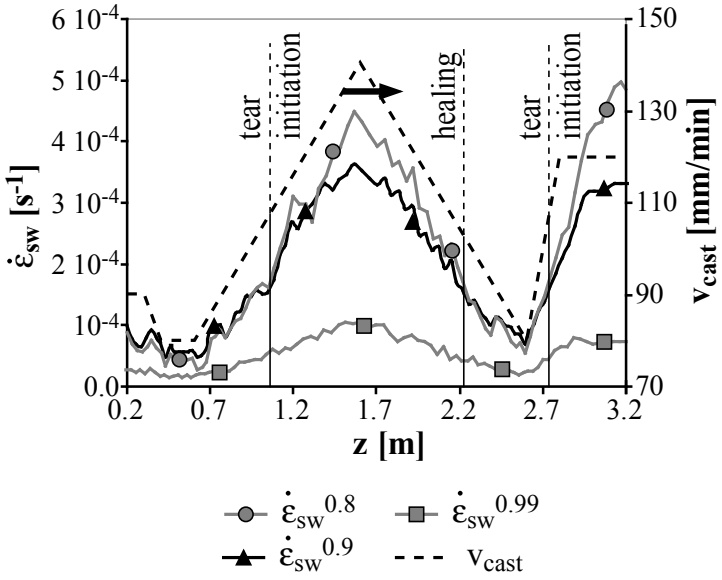


**Figure 6.39:** Volumetric strain rate $\dot{\epsilon}_{sw}$ evaluated at a given solid fraction and plotted against the corresponding $z^{g_s}$.

In summary, the presence of a hot tear in the billet would have been well predicted by saying that there exists a critical volumetric strain rate (coherent with [101]) $\dot{\epsilon}^c_{sw} = 1.6 \cdot 10^{-4}$ s$^{-1}$ such that hot tearing occurs wherever $\dot{\epsilon}_{sw}$ exceeds $\dot{\epsilon}^c_{sw}$ in the range $0.85 < g_s < 0.95$. The existence of a critical value $\dot{\epsilon}^c_{sw}$ is also what is predicted by the RDG criterion, which shows that such a critical strain rate corresponds to a critical liquid pressure drop in the liquid [37]. Knowing the $g_s\,(T)$ relationship for the AA5182 alloy and introducing reasonable orders of magnitude for the various parameters ($G = 7000$ K m$^{-1}$, $\phi = 100$ $\mu$m, $\beta = 8.5$ %, $v_T = 2$ mm s$^{-1}$, $g_s^{coal} = 0.98$ and $\mu = 1.3$ Pa s), the RDG criterion indicates that the critical strain rate $\dot{\epsilon}^c_{sw} = 1.6 \cdot 10^{-4}$ s$^{-1}$ corresponds to a critical pressure drop $\Delta p_{crit} = 14.2$ kPa. This value is close to the actual liquid

pressure drop predicted by the model when hot tears are initiated, as presented in the next section. In the present case, the RDG criterion appears to be able to predict fairly accurately the relation between $\dot{\epsilon}_{sw}$ and $\Delta p_l$.

Even though the volumetric strain rate correlates well with the hot tearing pattern, it is not possible to conclude that a hot tearing criterion that would take this quantity alone into account is suitable for all situations. As outlined above, the cumulated volumetric strain also appears to be a reasonable indicator (i.e. a critical value of $\epsilon_{sw}$ above which hot tearing is found could also be defined). It is in fact likely that both strain and strain rate (at least) play a role in hot tearing formation.

### 6.3.3 Porosity Results

Let us now examine the results obtained from the porosity module. First of all, it is possible to evaluate the relative importance of the shrinkage and strain contribution to the liquid pressure drop. For this purpose, let us consider the following:

$$\frac{\Omega^{sh}}{\Omega^{mech}} = \frac{v_T \beta}{\dot{\epsilon}_{sw} \frac{\Delta T_{freeze}}{G}} \approx \frac{2 \cdot 10^{-3} \cdot 8.5 \cdot 10^{-2}}{2 \cdot 10^{-4} \frac{125}{7000}} \approx 50$$

This calculation indicates that the characteristic pressure drop associated with shrinkage is much larger than that induced by the strain rate. As a consequence, the calculated pressure will be mainly dictated by the thermal model and the value of $\overline{\rho}(T)$. The calculated profile of the liquid pressure in the last interdendritic liquid, $p_l^{0.99}$, as a function of $z^{0.99}$ is displayed on Figure 6.40. On the same figure, this data is also plotted as a liquid pressure drop, $\Delta p_l = p_0 - p_l$, where $p_0$ is the sum of the atmospheric and metallostatic pressures. When compared to the typical stresses encountered in the mushy zone ($\sim 2$ MPa), this indicates that the semi-coupled method is indeed very well suited to describing the casting of such a billet (since $\frac{\sigma}{\Delta p_l} \sim 10^2$).

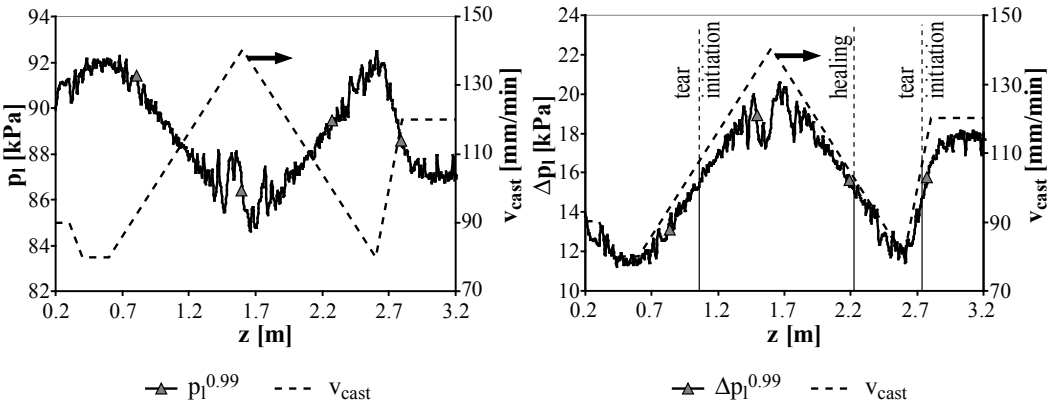


**Figure 6.40:** Pressure in the liquid, absolute value and pressure drop, just before solidification is completed as a function of position along the centerline of the billet.

This result indicates that the pressure drop increases with $v_{cast}$. Physically, this means that feeding is more difficult when the casting speed is high, which was expected. This aspect of hot tearing modeling is thus captured in the present simulation.

The pore fraction predicted along the centerline of the billet is shown on Figure 6.41. This quantity follows the same trend as the liquid pressure drop and thus varies very similarly to the

casting speed. What is very important to remark is that $g_p$ is small (typically 0.3%) and hardly varies throughout the billet (amplitude of variation of about 0.01%). This prediction appears to

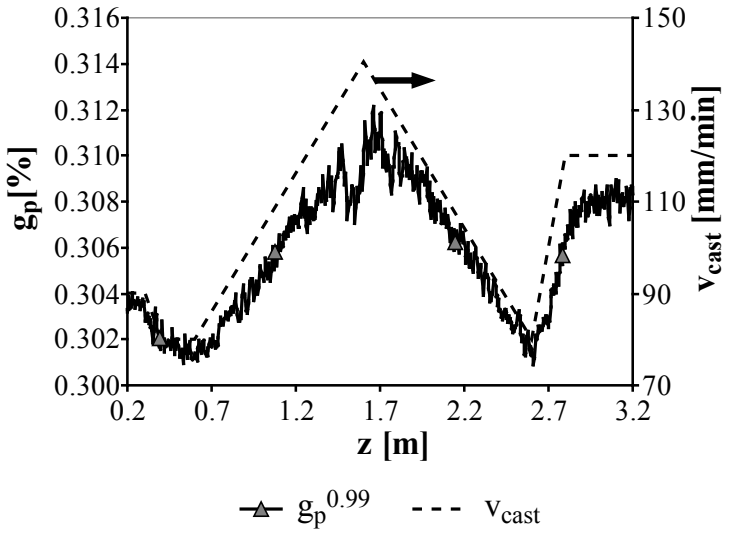


**Figure 6.41:** Porosity fraction predicted along the centerline of the billet.

be in good agreement with experimental observations. The amount of hydrogen, and thus the amount of porosity in the casting, is indeed known to have no marked effect on the hot tearing tendency in DC casting [6].

### 6.3.4 Summary

We have shown that the semi-coupled method is relevant in this case since the liquid pressure drop is small when compared to stresses in the solid. Moreover, this approach is able of providing a lot of information about DC casting of an AA5182 billet.

However, using this information to describe and predict the hot tearing phenomenon is more difficult. When compared to laboratory scale tensile tests, the billet is indeed more complex for two reasons. On one hand, the strain applied to the mushy zone is controlled by the cooling conditions. As a consequence, faster cooling will also lead to more straining and higher liquid pressure drop, which means that all the classical hot tearing indicators increase simultaneously and it is thus difficult to distinguish the effect of each one of them on the observed hot tearing tendency.

On the other hand, it is difficult to know what are the exact conditions that correspond to hot tearing. The only experimental information is indeed where the hot tear is found but there is no evidence of when (i.e. at which solid fraction) tearing occurred. As a consequence, it is difficult to make accurate correlations between simulated values and experimentally observed hot tears. As a comparison, information about both of these aspects was available in the tensile tests studied previously.

Considering reasonable solid fractions for hot tearing and using the fact that some quantities are roughly constant over a range of $g_s$, it is possible to deal with the second difficulty to some extent and to estimate the conditions experienced by the mushy material at failure.

To study the hot tearing susceptibility, four indicators can be considered based on existing theoretical models: $v_T$, $\epsilon_{sw}$, $\dot{\epsilon}_{sw}$ and $\Delta p_l$. They are normalized by the maximum value they

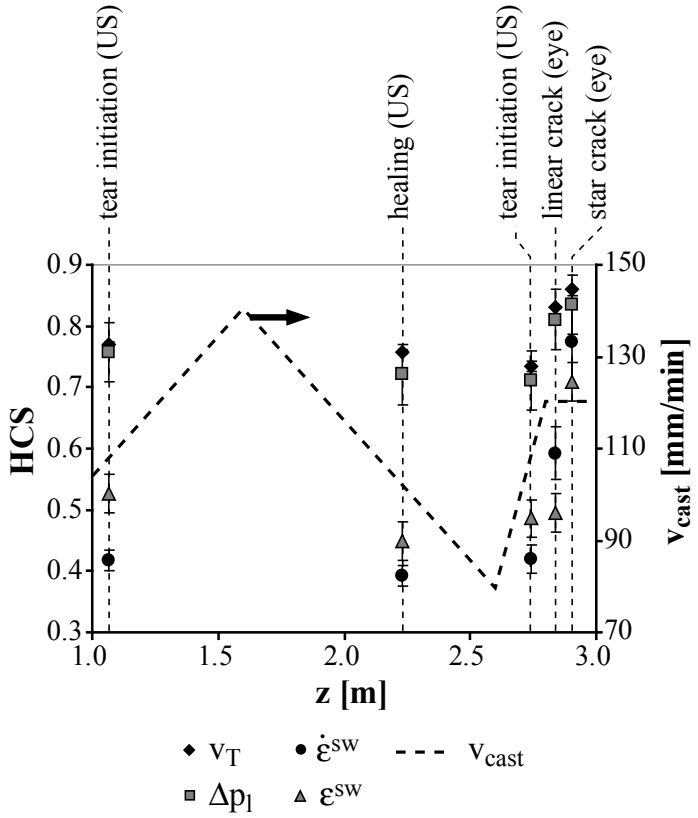


**Figure 6.42:** Value of different possible indicators of the hot tearing tendency at the locations where the tear morphology changed.

reached during the cast to define corresponding measures of HCS (e.g. HCS = $\frac{v_T}{v_T^{max}}$). These four different HCS were measured at the locations where changes were observed in the hot tear pattern (see Table 6.2). The result of this study is shown on Figure 6.42.

All these indicators follow a similar trend. They all increase with $v_{cast}$ and are larger in torn regions. For $\epsilon_{sw}$, $\dot{\epsilon}_{sw}$ and $\Delta p_l$, a roughly constant value appears as the limit between tear nucleation and healing. When HCS is above this limit, tearing is found. Moreover, during the last increase in $v_{cast}$, these indicators keep increasing, which seems coherent with the establishment of a star-shaped tear.

As already pointed out, it seems to be difficult to pick one of these indicators as being more relevant since they all indicate the same trend. This is due to the fact that all the relevant phenomena depend upon the thermal field and a higher casting speed make the material more prone to hot tearing from all points of view (more strain and less healing possibility). It is in fact likely that several aspects (cooling rate, strain state and liquid feeding) are significant but their relative importance is difficult to assess at this stage.

In conclusion, the study of hot tearing in DC cast billets using continuum modeling does not clearly bring a new insight in what is happening during hot tearing. This is a consequence of the features of the process itself. Hot tearing theories may thus be validated in such a case but it seems difficult to establish new criteria, which would be more advanced than those already existing, without further information (theoretical or experimental).

# Chapter 7

# Conclusion and Perspectives

## 7.1 Conclusion

The objective of this work was to study the formation of hot tearing at the scale of an entire casting and using continuum modeling approaches. Hot tearing is known to occur in mushy alloys under strain, when the network of solid grains is not fully percolated and feeding by the intergranular liquid is difficult. Even though the general context for the formation of this defect is known, quantitative theories are difficult to formulate and their predictive capability remains limited.

The problem of hot tearing is very complex because numerous physical phenomena come into play and interact with each other. Moreover, the properties of the mushy alloys are difficult to measure and model accurately. In addition to this, the geometry of the casting and boundary conditions that it experiences may become quite complicated to describe. For all of these reasons, assessing the problem at hand is only possible provided efficient numerical modeling tools are available.

Theoretical considerations have shown that the problems of heat flow, solid deformation and liquid feeding have to be solved in the coherent mushy zone in order to characterize hot tearing. A two-phase approach was presented, in which the equations for mass and momentum conservation in a mushy alloy were coupled and should be solved together to obtain the pressure in the liquid, $p_l$, and the displacement in the solid, $\mathbf{u}_s$. The solution of such a coupled problem can only be obtained provided a suitable numerical solver is developed, as was done by M'Hamdi *et al* [1].

In the present work, another solution scheme was proposed by introducing a decoupling assumption that appears to be reasonable in various processes, such as DC casting. Assuming that the liquid pressure (and its gradient) is small compared to the stresses in the solid, the momentum conservation problem can be written in a simplified form, which can then be solved using commercially available software.

The main drawback of this method is that an inaccurate version of the problem at hand is solved. However, it was possible to show that this inaccuracy remains small in a significant variety of cases, which are relevant to the study of hot tearing in aluminum alloys. On the other hand, the semi-coupled approach offers several advantages : its is easier to implement in existing softwares, it is more flexible and it allows using well adapted solving methods for each problem. This is due to the fact that, in this approach, three different softwares were used for the calculation of the quantities of interest in hot tearing formation.

The semi-coupled method was indeed implemented using Calcosoft$^{TM}$ (thermal model), Abaqus$^{TM}$ (mechanical solver) and the porosity module from ProCast$^{TM}$ (liquid pressure and pore fraction model). The thermal problem was solved first and the temperature field was then used as an input for the mechanical calculation. The result of the latter, namely the divergence of the solid velocity field, was then used in the computation of the evolution of the pressure in the liquid, $p_l$. In addition to the set of input/output tools that were developed to allow these three softwares to communicate, most of the implementation effort was put into the porosity module (strain term in the mass conservation equation and mechanical solid fraction correction) and the description of the mechanical behavior of the alloy. The results of the work conducted by Ludwig *et al* [2] were indeed implemented into Abaqus$^{TM}$ together with the rheology of the solid alloy at moderate temperature.

The accuracy of this numerical tool could be assessed and guidelines for the selection of mesh size and time steps were proposed. Having obtained this information, the semi-coupled method was applied to three cases for which experimental measurements were available. In general, it was found that the validity of the thermal model was well verified when compared to experimental data, provided the boundary conditions were described accurately enough. Moreover, the mechanical model also provided results that were in good agreement with actual measurements performed during various tests, on a fairly broad range of temperature and strain rate.

The first test to which the semi-coupled approach was applied is the mushy zone tearing test of Grasso [5]. The model could first be used to outline two failure modes occurring in the torn samples. At high temperature, failure appeared to be related to local decohesion. As a consequence, tearing under such conditions is more related to the test itself than to the intrinsic properties of the material. At lower temperature however, this artifact is not observed and failure in the alloy occurs after some damage has formed. It was important to note that relatively high strain rates were experienced by the mushy alloy during the test. As a result, the observed failure modes do not represent well the conditions of hot tear formation in a DC-cast ingot.

In addition to the information obtained about the test itself, the semi-coupled method also provided useful information when discussing the results. The increase in tensile strength could indeed be characterized in terms of an accurate solid fraction at which tearing actually occurred. Such information showed that percolation due to coalescence started around $g_s = 0.92$. This tearing test was thus found to be efficient for the study of this phenomenon, which is one important aspect of hot tearing.

The next case that was considered was a tensile test developed by Magnin *et al* [91] and referred to as the (Alcan-Pechiney) rig test. Vernède and Commet [4] used this setup to characterize the ductility of mushy alloys. This test was conducted with strain rates that are similar to those encountered in DC casting. The experimental data was used to validate the numerical model and the latter gave further interesting results. It was indeed possible to identify strain concentration effects and to extract intrinsic material properties, such as the ductility as a function of $g_s$. One of the most important conclusions of this work was that, under these conditions, hot tearing seems to occur when a solid fraction dependent critical strain (i.e. ductility, which depends on $g_s$) is reached. The strain rate effects were found to be less significant.

These tensile tests have some particular features that are important. They are well instrumented, isotherms are roughly parallel to the observed tears and the applied strain is controlled independently from the cooling conditions. The last case that was studied in the present work is that of a full-scale DC-cast billet. In this industrial test, there is less experimental information available, hot tears are perpendicular to the advancing isotherms and the strain experienced by the mushy zone is directly controlled by the cooling conditions. It is thus not obvious to

extrapolate results from the study of the tensile tests to this case.

The semi-coupled method could be applied to the DC casting of an entire billet. The numerical model was used to obtain information about local isotherm velocity, strain, strain rate and liquid pressure. These quantities are classical indicators of the hot tearing tendency. Their values could be correlated to experimentally observed hot tears. However, these correlations are not fully accurate since the solid fraction at which hot tears form and heal could not be measured experimentally.

Another difficulty that arises when interpreting the result of such calculations comes from the fact that all the hot tearing indicators follow a similar trend. When the casting speed is increased, both the strain and the strain rate increase in the mushy alloy and feeding also becomes more difficult. As a consequence, several possible criteria could be used to explain qualitatively when and where the hot tear appears. However, a more advanced criterion that would be able to predict whether or not hot tearing actually occurs is not available at this stage.

## 7.2 Perspectives

The semi-coupled method implemented in the present work has proven to be an efficient tool to study solidification processes at the scale of an entire casting. A good flexibility is obtained because different problems are solved using dedicated solvers. The main drawback of this method is that the effect of liquid pressure is neglected in the mechanical calculation. When this assumption is not acceptable, the present approach may thus not be applied.

If necessary, another approach with an increased level of accuracy could be setup without altering too much the general flow chart proposed in this work. It is indeed interesting to remark that the liquid pressure is often determined mostly by solidification shrinkage ($\Omega^{sh} >> \Omega^{mech}$). It is then reasonable to neglect the strain term in the liquid pressure calculation. The values of $p_l$ could then be obtained immediately after the thermal calculation. Using $p_l$ and $\nabla p_l$ as input, the mechanical problem expressed in its complete form (in terms of the effective stress, see Equation (2.41) on page 24) could be solved. This approach would be relevant in processes where $p_l$ or $\Delta p_l$ become very high (e.g. high pressure die casting or continuous casting of steel) provided rheological models are also available under such conditions.

The work that was conducted during the present thesis also leads to more general conclusions regarding modeling of hot tearing at the continuum scale. It appears that not all the phenomena relevant to hot tearing are captured efficiently using a two-phase averaged approach. Hot tearing involves indeed mechanisms with very different characteristic length scales (e.g. strain field at the scale of the casting and strain localization in intergranular liquid films) as outlined by Vernède [7]. A multiscale modeling approach is thus necessary to obtain a clear theoretical picture of hot tearing.

In this context, there are two ways in which continuum scale modeling can be used. The first approach is suited for industrial applications. After a reasonably accurate thermal model has been setup to represent the process, the mechanical calculation may be conducted using relatively simple rheological models, e.g. as expressed in Equation (2.56) (p. 29). Compressibility and partial cohesion of the mushy zone do not need to be taken into account explicitly at this stage because any measure of $\dot{\epsilon}$ will indicate the correct trends ($\dot{\epsilon}_{sw}$ is roughly proportional to e.g. $\dot{\epsilon}_{cr}$). Moreover, the liquid pressure drop is often controlled mainly by solidification shrinkage so that volumetric strain rate does not need to be accounted for in porosity calculations. Such calculations are less CPU time intensive.

In this approach, the variation of various hot tearing indicators will be reproduced even though their actual values may not be correct. This information is sufficient because it is not possible to find a definition of HCS that actually predicts whether or not hot tears will form. Various criteria indeed indicate where the highest probability of failure is found. Actually casting some billets and optimizing the process using a trial and error approach can in this case be limited by using numerical modeling but not avoided.

A model such as that developed in the present work is best suited for more fundamental research purposes and that is the other perspective in which such an approach is relevant. One very important drawback is that calculations become very long when applied to real processes. However, a great level of complexity and detail is included. In particular, the rheological behavior as expressed by Ludwig *et al* [2] is an important contribution to a thorough description of what is happening when hot tears form.

In fact, the semi-coupled method has proven its ability to describe accurately the temperature, strain, strain rate, liquid pressure and porosity fraction in an entire casting. The variation of these quantities down to a scale of a few mm can be captured using this approach. The possibility of obtaining such detailed information at this scale is important because this data may be used as input to granular models, which capture the phenomena occurring on length scales of a few tens of $\mu$m to a few cm (e.g. feeding and strain localization) [7]. The local temperature, cooling rate, strain and strain rate could indeed be used as boundary conditions for granular calculations. On the other hand, the granular model could be used to describe in more details how the cohesion of the mushy alloy evolves as a function of various parameters.

Multiscale modeling involving both a two-phase approach similar to what was developed in the present work and granular models appears as the most promising way to improve quantitative descriptions of hot tearing. This may even give access to numerical tools able of predicting hot tear formation efficiently enough to bring the trial and error process in the casthouse down to a very limited level.

# Bibliography


[1] M. M'Hamdi, A. Mo, and H. G. Fjaer. TearSim: a two-phase model addressing hot tearing formation during aluminum direct chill casting. *Metall. Mater. Trans. A*, **37A**, pp. 3069–3083, 2006.

[2] O. Ludwig, J.-M. Drezet, C. L. Martin, and M. Suéry. Rheological behavior of Al-Cu alloys during solidification : constitutive modeling, experimental identification, and numerical study. *Metall. Mater. Trans. A*, **36A**, pp. 1525–1535, 2005.

[3] C. Péquet, M. Gremaud, and M. Rappaz. Modeling of microporosity, macroporosity and pipe-shrinkage formation during the solidification of alloys using a mushy-zone refinement method : applications to aluminum alloys. *Metall. Mater. Trans. A*, **33A**, pp. 2095–2106, 2002.

[4] S. Vernède. *Traction à l'état pâteux : Etude des propriétés mécaniques d'alliages d'aluminium à l'état semi solide.* Master's thesis, Ecole Centrale Paris, 2003.

[5] P.-D. Grasso. *Coalescence and mechanical behaviour of semi-solid aluminium alloys in relation to hot tearing.* Ph.D. thesis, EPFL, Lausanne, 2004.

[6] B. Commet, P. Delaire, J. Rabenberg, and J. Storm. Measurement of the onset of hot cracking in DC cast billets. In N. Crepeau (editor), *Light Metals 2003*, pp. 711–717. TMS, 2003.

[7] S. Vernède. *A granular model of solidification as applied to hot tearing.* Ph.D. thesis, EPFL, 2007.

[8] J. Barralis and G. Maeder. *Métallurgie : élaboration, structures-propriétés, normalisation.* Nathan, 1997.

[9] European Aluminum Association. Market report, 2005.

[10] E. Emley. Continuous casting of aluminium. *Int. Metal Rev.*, **June 1976**, pp. 75–115, 1976.

[11] D. Stefanescu. *The new metals handbook: Volume 15, Casting.* ASM International, 1988.

[12] A. Larouche, Y. Caron, and D. Kocaefe. Impact of water heat extraction and casting conditions on ingot thermal response during DC casting. In B. J. Welch (editor), *Light Metals 1998*, pp. 1059–1064. TMS, 1998.

[13] J. Sengupta, S. Cockcroft, D. Maijer, M. Wells, and A. Larouche. On the development of a three-dimensional transient thermal model to predict ingot cooling behavior during the start-up phase of the direct chill-casting process for an AA5182 aluminum alloy ingot. *Metall. Mater. Trans. B*, **35B**, pp. 523–539, 2004.

[14] J. G. Collier and J. R. Thome. *Convective boiling and condensation, $3^{rd}$ edition.* Oxford University Press, Walton Street, Oxford OX2 6DP, England, 1994.

[15] E. Caron and M. Wells. Effect of advanced cooling front (ACF) phenomena on film boiling and transition boiling regimes in the secondary cooling zone during the direct-chill casting of aluminum alloys. *Mater. Sci. Forum*, **519-521**, pp. 1687–1692, 2006.

[16] J. Sengupta, D. Maijer, M. Wells, S. Cockcroft, and A. Larouche. Mathematical modelling of the thermomechanical behavior of a 5182 aluminum ingot during the start-up phase of the DC casting process : the role of bottom block. In J.-L. Anjier (editor), *Light Metals 2001*, pp. 879–885, 2001.

[17] J. Sengupta, S. Cockcroft, D. Maijer, M. Wells, and A. Larouche. The effect of water ejection and water incursion on the evolution of thermal field during the start-up phase of the direct chill casting process. *J. Light Metals*, **2**, pp. 137–148, 2002.

[18] W. Droste, J.-M. Drezet, G.-E. Grün, and W. Schneider. 3D-modeling of ingot geometry development of DC-cast aluminum ingots during the start-up phase. In K. Schneider and W. Ehrke (editors), *Continuous Casting*, pp. 175–183. Wiley, 2000.

[19] B. Hannart, O. Bonnet, and A. Noraz. Open mold without distortion for DC casting of aluminum slabs : modeling and testing the optimum shape and material. In *Light Metals 1997*, pp. 1065–1070. TMS, 1997.

[20] J. E. Chu, M. G. Jacoby. Macrosegregation characteristics of commercial size aluminum alloy ingot cast by the direct chill casting method. In C. M. Bickert (editor), *Light Metals 1990*. TMS, 1990.

[21] E. Haug, A. Mo, and H. J. M. Thevik. Macrosegregation near a cast surface caused by exudation and solidification shrinkage. *Int. J. Heat Mass Trans.*, **38**, pp. 1553–1563, 1995.

[22] H. Thevik, A. Mo, and T. Rusten. A mathematical model for surface segregation in aluminum direct chill casting. *Metall. Mater. Trans. B*, **30B**, pp. 135–142, 1999.

[23] J.-M. Drezet and M. Rappaz. Modeling of ingot distortions during direct chill casting of aluminum alloys. *Metall. Mater. Trans. A*, **27A**, pp. 3214–3225, 1996.

[24] H. G. Fjaer and A. Hakonsen. The mechanism of pull-in during DC-casting of aluminum sheet ingots. In *Light Metals 1997*, pp. 683–690. TMS, 1997.

[25] W. Droste, G.-E. Grün, W. Schneider, and J.-M. Drezet. Thermo-mechanical modeling to predict shrinkage, shape and mold openings for DC-cast rolling ingots. In W. Schneider (editor), *Light Metals 2002*, pp. 703–708. TMS, 2002.

[26] A. J. Williams, T. N. Croft, and M. Cross. Modeling of ingot development during the start-up phase of direct chill casting. *Metall. Mater. Trans. B*, **34B**, pp. 727–734, 2003.

[27] O. Ludwig, J.-M. Drezet, B. Commet, and B. Heinrich. Modelling of internal stresses in DC casting and sawing of high strength aluminum alloys slabs. In C.-A. Gandin and M. Bellet (editors), *MCWASP XI*. TMS, 2006.

[28] B. Zhang, S. Cockroft, D. Maijer, J. Zhu, and P. A.B. Casting defects in low-pressure die cast aluminum alloy wheels. *JOM*, **57**, pp. 35–43, 2005.

[29] J. Campbell. *Castings, $2^{nd}$ edition.* Butterworth-Heinemann, 1991.

[30] A. H. Amundsen. Fractographic studies : WP5.1 – 2nd series of 5182-01 ht castings. Technical report, VIRCAST – Elkem Aluminum Research, 2003.

[31] D. Eskin, V. Savran, and L. Katgerman. Effects of melt temperature and casting speed on the structure and defect formation during direct-chill casting of an Al-Cu alloy. *Metall. Mater. Trans. A*, **26A**, pp. 1965–1976, 2005.

[32] T. Clyne and G. Davies. A quantitative solidification cracking test for castings and an evaluation of cracking in aluminium-magnesium alloys. *J. Brit. Foundry*, **68**, pp. 238–244, 1975.

[33] B. Commet and A. Larouche. An integrated approach to control hot tearing in sheet ingot casting. In T. Galloway (editor), *Light Metals 2006*, pp. 833–838, 2006.

[34] M. Braccini, C. L. Martin, M. Suéry, and Y. Bréchet. Hot tearing phenomena in Al-Cu alloys : grain refinement effect. *Matériaux et Techniques*, **5-6**, pp. 19–24, 2000.

[35] M. Braccini, M. Suéry, C. Laguerre, and M. Stucky. Influence de l'affinage sur la fissuration à chaud des alliages d'aluminium-cuivre utilisés en fonderie. *La Revue de Métallurgie-CIT/Science et Génie des Matériaux*, **Février 2003**, pp. 157–164, 2003.

[36] M. Easton, J. Grandfield, D. H. StJohn, and B. Rinderer. The effect of grain refinement and cooling rate on the hot tearing of wrought aluminium alloys. *Mater. Sci. Forum*, **519-521**, pp. 1675–1680, 2006.

[37] M. Rappaz, J.-M. Drezet, and M. Gremaud. A new hot tearing criterion. *Metall. Mater. Trans. A*, **30A**, pp. 449–455, 1999.

[38] W. Kurz and D. J. Fisher. *Fundamentals of solidification, fourth revised edition.* Trans Tech Publications, 1998.

[39] H. Brody and M. C. Flemings. Solute redistribution in dendritic solidification. *T. Metall. Soc. AIME*, **236**, pp. 615–624, 1966.

[40] T. Clyne and W. Kurz. Solute redistribution during solidification with rapid solid state diffusion. *Metall. Mater. Trans. A*, **12A**, pp. 965–971, 1981.

[41] C. Wang and C. Beckermann. A unified solute diffusion model for columnar and equiaxed dendritic alloy solidification. *Mat. Sci. Eng. A - Struct.*, **A171**, pp. 199–211, 1993.

[42] C. Wang and C. Beckermann. A multiphase solute diffusion model for dendritic alloy solidification. *Metall. Mater. Trans. A*, **24A**, pp. 2787–2802, 1993.

[43] H. Combeau, J.-M. Drezet, A. Mo, and M. Rappaz. Modeling of microsegregation in macrosegregation computations. *Metall. Mater. Trans. A*, **27A**, pp. 2314–2327, 1996.

[44] M. Rappaz, A. Jacot, and W. J. Boettinger. Last-stage solidification of alloys : theoretical model of dendrite-arm and grain coalescence. *Metall. Mater. Trans. A*, **34A**, pp. 467–479, 2003.

[45] V. Mathier, A. Jacot, and M. Rappaz. Coalescence of equiaxed grains during solidification. *Modelling Simul. Mater. Sci. Eng.*, **12**, pp. 479–490, 2004.

[46] S. Vernède and M. Rappaz. Transition of the mushy zone from continuous liquid films to a coherent solid. *Philos. Mag.*, **86**, pp. 3779–3794, 2006.

[47] A. Dahle and D. StJohn. Rheological behavior of the mushy zone and its effect on the formation of casting defects during solidification. *Acta Mater.*, **47**, pp. 31–41, 1999.

[48] A. Dahle and L. Arnberg. Development of strength in solidifying aluminium alloys. *Acta Mater.*, **45**, pp. 547–559, 1997.

[49] S. Vernède, P. Jarry, and M. Rappaz. A granular model of equiaxed mushy zones : formation of a coherent solid and localization of feeding. *Acta Mater.*, **54**, pp. 4023–4034, 2006.

[50] J. Ni and C. Beckermann. A volume-averaged two-phase model for transport phenomena during solidification. *Metall. Mater. Trans. B*, **22B**, pp. 349–361, 1991.

[51] H. Darcy. *Les fontaines publiques de la ville de Dijon*, chapter Appendice - Note D : Détermination des lois d'écoulement de l'eau à travers le sable, pp. 591–595. Dalmont, 1856.

[52] Ø. Nielsen, L. Arnberg, A. Mo, and H. Thevik. Experimental determination of mushy zone permeability in aluminum-copper alloys with equiaxed microstructures. *Metall. Mater. Trans. A*, **30A**, pp. 2455–2462, 1999.

[53] G. Couturier and M. Rappaz. Effect of volatile elements on porosity formation in solidifying alloys. *Modelling Simul. Mater. Sci. Eng.*, **14**, pp. 253–271, 2006.

[54] D. Poirier, K. Yeum, and A. Maples. A thermodynamic prediction for microporosity formation in aluminum-rich Al-Cu alloys. *Metall. Mater. Trans. A*, **18A**, pp. 1979–1987, 1987.

[55] K. Carlson, Z. Lin, C. Beckermann, G. Mazurkevich, and M. Schneider. Modeling of porosity formation in alumimum alloys. *Mater. Sci. Forum*, **519-251**, pp. 1699–1706, 2006.

[56] M. Rappaz, M. Bellet, and M. Deville. *Modélisation numérique en science et génie des matériaux*. Number 10 in Traité des matériaux. PPUR, 1998.

[57] O. Coussy. *Mechanics of porous continua*. Wiley, 1995.

[58] T. H. Courtney. *Mechanical behavior of materials*. McGraw-Hill, 2000.

[59] A. Stangeland, A. Mo, Ø. Nielsen, D. Eskin, and M. M'Hamdi. Development of thermal strain in the coherent mushy zone during solidification of aluminum alloys. *Metall. Mater. Trans. A*, **35A**, pp. 2903–2915, 2004.

[60] A. Stangeland, A. Mo, and D. Eskin. Thermal strain in the mushy zone for aluminum alloys. *Metall. Mater. Trans. A*, **37A**, pp. 2219–2229, 2006.

[61] D. Eskin, Suyitno, J. Mooney, and L. Katgerman. Contraction of aluminum alloys during and after solidification. *Metall. Mater. Trans. A*, **35A**, pp. 1325–1335, 2004.

[62] C. Martin, M. Braccini, and M. Suéry. Rheological behavior of the mushy zone at small strains. *Mat. Sci. Eng. A - Struct.*, **A325**, pp. 292–301, 2002.

[63] S. McElwain, A. Roberts, and A. Wilkins. Yield functions for porous materials with cubic symmetry using different definitions of yield. *Adv. Eng. Mater.*, **8**, pp. 870–876, 2006.

[64] D. Wood. *Soil behaviour and critical state soil mechanics*, chapter 5, pp. 112–137. Cambridge University Press, 1990.

[65] O. Ludwig. *Etude expérimentale et modélisation du comportement rhéologique d'alliages Al-Cu en cours de solidification dans le cadre de la fissuration à chaud en coulée continue.* Ph.D. thesis, Institut National Polytechnique de Grenoble (INPG), 2004.

[66] O. Ludwig, J.-M. Drezet, P. Ménès, C. L. Martin, and M. Suéry. Rheological behavior of a commercial AA5182 aluminum alloy during solidification. *Mat. Sci. Eng. A - Struct.*, **413-414**, pp. 174–179, 2005.

[67] M. M'Hamdi, A. Mo, and C. Martin. Two-phase modeling directed towards hot tearing formation in aluminium direct chill casting. *Metall. Mater. Trans. A*, **33A**, pp. 2081–2093, 2002.

[68] A. Fallet, G. Chichignoud, C. Martin, M. Suéry, and P. Jarry. Influence of barium addition on the microstructure and the rheological behaviour of partially solidified Al-Cu alloys. *Mat. Sci. Eng. A - Struct.*, **426**, pp. 187–193, 2006.

[69] W. Van Haaften, B. Magnin, W. H. Kool, and L. Katgerman. Constitutive behavior of as-cast AA1050, AA3104 and AA5182. *Metall. Mater. Trans. A*, **33A**, pp. 1971–1980, 2002.

[70] H. G. Fjaer and A. Mo. ALSPEN - a mathematical model for thermal stresses in direct chill casting of aluminum billets. *Metall. Mater. Trans. B*, **21B**, pp. 1049–1061, 1990.

[71] L. Nicolli, A. Mo, and M. M'Hamdi. Modeling of macrosegregation caused by volumetric deformation in a coherent mushy zone. *Metall. Mater. Trans. A*, **36A**, pp. 433–442, 2005.

[72] I. Farup, J.-M. Drezet, and M. Rappaz. In situ observation of hot tearing formation in succinonitrile-acetone. *Acta Mater.*, **49**, pp. 1261–1269, 2001.

[73] P.-D. Grasso, J.-M. Drezet, and M. Rappaz. Hot tear formation and coalescence observations in organic alloys. *Journal of Metals - electronic edition*, 2002.

[74] C. Davidson, D. Viano, L. Lu, and D. H. StJohn. Observation of crack initiation during hot tearing. *Int. J. Cast Metal Res.*, **19**, pp. 59–65, 2006.

[75] O. Ludwig, M. Dimichiel, L. Salvo, M. Suéry, and P. Falus. In-situ three-dimensional microstructural investigation of solidification of an Al-Cu alloy by ultrafast X-ray microtomography. *Metall. Mater. Trans. A*, **36A**, pp. 1515–1523, 2005.

[76] A. Phillion, S. Cockcroft, and P. Lee. X-ray micro-tomographic observations of hot tear damage in an Al- Mg commercial alloy. *Scripta Mater.*, **55**, pp. 489–492, 2006.

[77] W. Pellini. Strain theory of hot tearing. *Foundry*, **80**, pp. 125–133, 1952.

[78] D. Eskin, Suyitno, and L. Katgerman. Mechanical properties in the semi-solid state and hot tearing of aluminum alloys. *Prog. Mat. Sci.*, **49**, pp. 629–711, 2004.

[79] J.-M. Drezet and M. Rappaz. Study of hot tearing in aluminum alloys using the ring mold test. In B. Thomas and C. Beckermann (editors), *MCWASP VIII*. TMS, San Diego, 1998.

[80] D. Warrington and D. McCartney. Development of a new hot-cracking test for aluminium allloys. *Cast metals*, **2**, pp. 134–143, 1989.

[81] D. Warrington and D. McCartney. Hot-cracking in aluminium alloys 7050 and 7010 - a comparative study. *Cast metals*, **3**, pp. 202–208, 1991.

[82] M. Braccini. *Optimisation des pièces moulées : étude des phénomènes de fissuration à chaud dans les alliages Al-Cu*. Ph.D. thesis, Institut National Polytechnique de Grenoble (INPG), 2000.

[83] J. Spittle and A. Cushway. Influences of superheat and grain structure on hot-tearing susceptibilities of Al-Cu alloy castings. *Met. Technol.*, **10**, pp. 6–13, 1983.

[84] D. Viano, D. StJohn, J. Grandfield, and C. Cáceres. Hot tearing in aluminium - copper alloys. In H. Kvande (editor), *Light Metals 2005*, pp. 1069–1073. TMS, 2005.

[85] I. Novikov and V. Portnoi. Method of testing alloys in tension in the solidus-liquidus range. *Russ. Castings Prod.*, **4**, pp. 163–166, 1966.

[86] A. J. Williams and A. Singer. Deformation, strength, and fracture above the solidus temperature. *Journal of the Institute of Metals*, **96**, pp. 5–12, 1968.

[87] H. Nagaumi and T. Umeda. Study of the crack sensitivity of 6xxx and 7xxx aluminum alloys. *Mater. Sci. Forum*, **426-432**, pp. 465–470, 2003.

[88] L. Colley, M. Wells, and D. Maijer. Tensile properties of as-cast aluminum alloy AA5182 close to the solidus temperature. *Mat. Sci. Eng. A - Struct.*, **A 386**, pp. 140–148, 2004.

[89] P. Ackermann, W. Kurz, and W. Heinemann. In situ testing of solidifying aluminum and Al-Mg shells. *Mater. Sci. Eng.*, **75**, pp. 79–86, 1985.

[90] D. Larouche, J. Langlais, W. Wu, and M. Bouchard. A constitutive model for the tensile deformation of a binary aluminum alloy at high fractions of solid. *Metall. Mater. Trans. B*, **37B**, pp. 431–443, 2006.

[91] B. Magnin, L. Maenner, L. Katgerman, and S. Engler. Ductility and rheology of an Al-4.5%Cu alloy from room temperature to coherency temperature. *Mater. Sci. Forum*, **217-222**, pp. 1209–1214, 1996.

[92] Suyitno, D. Eskin, V. Savran, and L. Katgerman. Effects of alloy composition and casting speed on structure formation and hot tearind during direct-chill casting of Al-Cu alloys. *Metall. Mater. Trans. A*, **35A**, pp. 3551–3561, 2004.

[93] Suyitno, W. H. Kool, and L. Katgerman. Hot tearing criteria evaluation for direct-chill casting of an Al-4.5 pct Cu alloy. *Metall. Mater. Trans. A*, **36A**, pp. 1537–1546, 2005.

[94] M. Flemings. *Solidification processing*. McGraw-Hill, 1974.

[95] T. Clyne and G. Davies. The influence of composition on solidification cracking susceptibility in binary alloy systems. *J. Brit. Foundry*, **74**, pp. 65–73, 1981.

[96] U. Feurer. Mathematisches modell des warmrissneigung von binaeren aluminiumlegierungen. *Giessereiforschung*, **28**, pp. 75–80, 1976.

[97] D. Lahaie and M. Bouchard. Physical modeling of the deformation mechanisms of semisolid bodies and a mechanical criterion for hot tearing. *Metall. Mater. Trans. B*, **32B**, pp. 697–705, 2001.

[98] Suyitno, W. H. Kool, and L. Katgerman. Micro-mechanical model of hot tearing at triple junctions in DC casting. *Mater. Sci. Forum*, **369-402**, pp. 179–184, 2002.

[99] H. Nagaumi and T. Umeda. Prediction of internal cracking in a direct-chill cast, high strength, Al-Mg-Si alloy. *J. Light Metals*, **2**, pp. 161–167, 2002.

[100] A. Phillion, S. Cockcroft, J. Sengupta, and D. Maijer. Implementation of a strain-based hot tearing criterion in direct chill cast aluminum ingots. In H. Kvande (editor), *Light Metals 2005*, pp. 1063–1068, 2005.

[101] M. M'Hamdi, S. Benum, D. Mortensen, H. G. Fjaer, and J.-M. Drezet. The importance of viscoplastic strain rate in the formation of center cracks during the start-up phase of direct-chill cast aluminum extrusion ingots. *Metall. Mater. Trans. A*, **34A**, pp. 1941–1952, 2003.

[102] E. Niyama, T. Uchida, M. Morikawa, and S. Saito. A method of shrinkage prediction and its application to steel casting practice. *Int. Cast Met. J.*, pp. 52–63, 1982.

[103] J.-M. Drezet and M. Rappaz. Prediction of hot tears in DC-cast aluminum billets. In J.-L. Anjier (editor), *Light Metals 2001*, 2001.

[104] A. Phillion and S. Cockcroft. Prediction of hot tears in DC-cast aluminium ingots. In A. Tabereaux (editor), *Light Metals 2004*, 2004.

[105] M. Rappaz, J.-M. Drezet, V. Mathier, and S. Vernède. Towards a micro-macro model of hot tearing. *Mater. Sci. Forum*, **519-521**, pp. 1665–1674, 2006.

[106] C. Monroe and C. Beckermann. Development of a hot tear indicator for steel castings. *Mat. Sci. Eng. A - Struct.*, **413-414**, pp. 30–36, 2005.

[107] I. Farup and A. Mo. Two-phase modeling of mushy zone parameters associated with hot tearing. *Metall. Mater. Trans. A*, **31A**, pp. 1461–1472, 2000.

[108] V. Mathier, J.-M. Drezet, and M. Rappaz. Two-phase modeling of hot tearing in aluminum alloys using a semi-coupled method. In C.-A. Gandin and M. Bellet (editors), *MCWASP XI*. TMS, 2006.

[109] V. Mathier, J.-M. Drezet, and M. Rappaz. Two-phase modelling of hot tearing in aluminium alloys using a semi-coupled approach. *Modelling Simul. Mater. Sci. Eng.*, **15**, pp. 121–134, 2007.

[110] Abaqus Inc. *Abaqus user's manual*, chapter Inelastic mechanical properties, pp. 18.2.4–8 – 18.2.4–9. Hibbit, Karlsson and Sorensen, 2006.

[111] J.-M. Drezet, O. Ludwig, M. M'Hamdi, H. G. Fjaer, and C. L. Martin. FEM modeling of the compressibility of partially solidified Al-Cu alloys: comparison with a drained compression test. In A. Tabereaux (editor), *Light Metals 2004*, 2004.

[112] G. Bell. On the performance of the enthalpy method. *Int. J. Heat Mass Trans.*, **25**, pp. 587–589, 1982.

# List of Symbols

| Symbol | Meaning | Units |
|---|---|---|
| **Misc. symbols and operators** | | |
| $\tilde{}$ | indicates exact solution to a problem | |
| $\|\mathbf{v}\|$ | norm of the $\mathbf{v}$ vector | [v] |
| $\|a\|$ | absolute value of $a$ | [a] |
| $\dot{a}$ | time derivative of some quantity $a$ | [a] $\mathrm{s}^{-1}$ |
| $^T$ | indicates a vector's transpose | |
| $\nabla$ | operator nabla defined by $\nabla = \left(\frac{\partial}{\partial x}, \frac{\partial}{\partial y}, \frac{\partial}{\partial z}\right)$ and used to note the gradient of $a$, $\nabla a$, or the divergence of $\mathbf{v}$, $\nabla \cdot \mathbf{v}$ | [a] $\mathrm{m}^{-1}$ |
| **Greek letters** | | |
| $\alpha'$ | modified Fourier number introduced in the Clyne-Kurz microsegregation model | |
| $\alpha^{th}$ | linear thermal expansion coefficient | $\mathrm{K}^{-1}$ |
| $\alpha$ | rate of evolution of cohesion at small strain | |
| $\alpha_0,\ \alpha_1$ | constants determining the saturation value of $\alpha$ | |
| $\beta$ | solidification shrinkage | |
| $\delta$ | interface thickness | m |
| $\Delta x$ | mesh size | m |
| $\Delta t$ | time step | s |
| $\Delta t_{av}$ | average time step | s |
| $\Delta_{ref}$ | relative difference between a given solution and the exact solution | |
| $\Delta T_b$ | coalescence undercooling | K |
| $\Delta T_{freeze}$ | freezing range of the alloy | K |
| $\Delta T^{eq}_{freeze}$ | equilibrium freezing range of the alloy | K |
| $\Delta s_f$ | entropy of fusion per unit volume | $\mathrm{J\ m^{-3}\ K^{-1}}$ |
| $\Delta g^{mech}_s$ | mechanical solid fraction | |
| $\Delta p^{sh}_l$ | shrinkage-induced pressure drop | Pa |
| $\Delta p^{mech}_l$ | strain rate-induced pressure drop | Pa |
| $\epsilon_{sw}$ | cumulated volumetric strain | |
| $\epsilon_{cr}$ | cumulated creep strain | |
| $\dot{\epsilon}_e$ | equivalent viscoplastic strain rate | $\mathrm{s}^{-1}$ |

| Symbol | Meaning | Units |
|---|---|---|
| $\dot{\epsilon}_0$ | thermally activated factor describing the hot solid rheology | $s^{-1}$ |
| $\dot{\epsilon}_{cr}$ | equivalent creep strain rate | $s^{-1}$ |
| $\dot{\epsilon}_{sw}$ | equivalent volumetric strain rate | $s^{-1}$ |
| $\boldsymbol{\epsilon}$ | strain tensor | |
| $\dot{\boldsymbol{\epsilon}}$ | strain rate tensor | $s^{-1}$ |
| $\boldsymbol{\epsilon}^{el}$ $\dot{\boldsymbol{\epsilon}}^{el}$ | elastic strain and strain rate tensors | – $s^{-1}$ |
| $\boldsymbol{\epsilon}^{th}$ $\dot{\boldsymbol{\epsilon}}^{th}$ | thermal strain and strain rate tensors | – $s^{-1}$ |
| $\boldsymbol{\epsilon}^{ie}$ $\dot{\boldsymbol{\epsilon}}^{ie}$ | inelastic strain and strain rate tensors | – $s^{-1}$ |
| $\boldsymbol{\epsilon}^{pl}$ $\dot{\boldsymbol{\epsilon}}^{pl}$ | plastic strain and strain rate tensors | – $s^{-1}$ |
| $\boldsymbol{\epsilon}^{vp}$ $\dot{\boldsymbol{\epsilon}}^{vp}$ | viscoplastic strain and strain rate tensors | – $s^{-1}$ |
| $\phi$ | grain size | m |
| $\gamma_{gb}$ | grain boundary energy | J $m^{-2}$ |
| $\gamma_{s/l}$ | solid-liquid interface energy | J $m^{-2}$ |
| $\gamma_{l/v}$ | liquid-vapor interface energy | J $m^{-2}$ |
| $\Gamma$ | interface transfer term in two-phase averages | |
| $\eta$ | strain sensitivity of the solid alloy | |
| $\kappa$ | characteristic stress in Ludwik's rheological model | Pa |
| $\kappa$ | curvature of a pore | $m^{-1}$ |
| $\kappa$ | thermal conductivity | W $m^{-1}$ $K^{-1}$ |
| $\lambda$ | strain rate sensitivity of the solid alloy | |
| $\lambda_2$ | secondary dendrite arm spacing | m |
| $\mu$ | viscosity of the liquid alloy | Pa s |
| $\mu$ | strain rate sensitivity of the solid alloy | |
| $\nu$ | Poisson's ratio | |
| $\rho$ | density of a single phase material | kg $m^{-3}$ |
| $\overline{\rho}$ | average density of a solid-liquid mixture | kg $m^{-3}$ |
| $\sigma_M$ | Mises stress | Pa |
| $\hat{\sigma}_M$ | effective Mises stress | Pa |
| $\sigma_y$ | Yield stress in uniaxial tension | Pa |
| $\boldsymbol{\sigma}$ | stress tensor | Pa |
| $\hat{\boldsymbol{\sigma}}$ | effective stress tensor | Pa |
| $\tau$ | strain rate normalized by displacement rate and length of the sample | |
| $\Omega_0$ | averaging volume | $m^3$ |
| $\Omega^{sh}$ | characteristic shrinkage-induced liquid pressure drop | Pa |
| $\Omega^{mech}$ | characteristic strain-induced liquid pressure drop | Pa |
| $\chi$ | control parameter in automatic time incrementation procedure | |

| **Roman letters** | | |
|---|---|---|
| $A$ | Arrhenius pre-factor | $s^{-1}$ |
| $A_2,\ A_3$ | rheological softening functions | |
| $c_0$ | nominal concentration of an alloy | wt% |
| $C$ | cohesion of the mushy alloy | |

| Symbol | Meaning | Units |
|---|---|---|
| $C^*$ | saturation value of cohesion | |
| $C_p$ | heat capacity per unit volume | J m$^{-3}$ K$^{-1}$ |
| $\mathbf{C}$ | elastic stiffness tensor | Pa |
| $E$ | Young's modulus | Pa |
| $\mathcal{F}$ | yield function | |
| $F$ | force | N |
| $\mathbf{g}$ | gravity vector | m$^2$ s$^{-1}$ |
| $g_l$ | volume liquid fraction $g_l = 1 - g_s$ | |
| $g_s$ | volume solid fraction | |
| $g_s^{coh}$ | coherency point | |
| $g_s^{coal}$ | coalescence point | |
| $g_s^{th}$ | critical solid fraction below which thermal contraction causes stress | |
| $g_p$ | volume pore fraction | |
| $\mathcal{G}$ | (visco)plastic potential | |
| $G$ | thermal gradient | m K$^{-1}$ |
| $h$ | heat transfer coefficient | W m$^{-2}$ K$^{-1}$ |
| $H$ | enthalpy per unit volume | J m$^{-3}$ |
| $[H]_0$ | nominal concentration of hydrogen in the melt | cc$_{\mathrm{STP}}$/100g |
| $[H]_l$ | hydrogen concentration in the liquid phase | cc$_{\mathrm{STP}}$/100g |
| $[H]_l^*$ | solubility limit of hydrogen in the liquid | cc$_{\mathrm{STP}}$/100g |
| HCS | hot tearing susceptibility | various |
| $\mathbf{I}$ | unit tensor | |
| $k$ | partition coefficient | |
| $k$ | constant accounting for coalescence in the mushy zone rheological model | |
| $K$ | permeability | m$^2$ |
| $L$ | latent heat per unit volume | J m$^{-3}$ |
| $m$ | slope of the liquidus line | K wt%$^{-1}$ |
| $n$ | exponent of the power-law creep | |
| $p$ | exponent for the determination of the saturation value for cohesion | |
| $p_l$ | pressure in the liquid | Pa |
| $P_s$ | pressure in the solid | Pa |
| $\hat{P}_s$ | effective pressure in the solid | Pa |
| $Q$ | activation energy | J mol$^{-1}$ |
| $r_p$ | pore radius | m |
| $r_{p,n}$ | pore radius at nucleation | m |
| $R$ | ideal gas constant | J K$^{-1}$ mol$^{-1}$ |
| $s_0$ | characteristic resistance to stress | Pa |
| $S$ | Sieverts coefficient | cc$_{\mathrm{STP}}$/100g |
| $\mathbf{S}$ | deviatoric stress tensor | Pa |
| $\hat{\mathbf{S}}$ | deviatoric effective stress | Pa |
| $t$ | time | s |
| $T$ | temperature | K |
| $\dot{T}$ | cooling rate | K s$^{-1}$ |
| $T^{coh}$ | coherency temperature | K |
| $T^{coal}$ | coalescence temperature | K |

| Symbol | Meaning | Units |
|---|---|---|
| $T_f$ | melting point of pure aluminum | K |
| $T_{liq}$ | liquidus of the alloy | K |
| $T_{eut}$ | eutectic temperature | K |
| $T_{sol}$ | solidus of the alloy | K |
| $T_{surf}$ | temperature at the surface of the cast | K |
| $T_{tear}$ | tearing temperature : temperature at which the load is applied during a tensile test | K |
| $T_\epsilon$ | temperature below which strain hardening becomes significant | K |
| $\mathbf{u}$ | displacement field | m |
| $\mathbf{v}$ | velocity field | m $s^{-1}$ |
| $v_T$ | velocity of the isotherms | m $s^{-1}$ |
| $v_{cast}$ | casting speed | m $s^{-1}$ |
| $\mathbf{x}$ | position in space | m |
| $X$ | stress triaxiality | |
| $z_{level}$ | cast height in a billet | m |

# List of Figures

# List of Tables

Vincent Mathier
Petites-Buttes 20B 1180 Rolle
vincent.mathier@a3.epfl.ch
04.04.1980
Swiss

# Ph.D. in Materials Science and Engineering

## Education

**2003-2007** **PhD Thesis** (EPFL, LSMX) : Materials Science and Engineering
Modelling of continuous casting processes of aluminum alloys
*Collaboration with Alcan, General Motors, Hydro, Umicore and Calcom-ESI*

2003 **Master of Science** : Materials science and engineering
**Awards** : *Best master grades amongst engineering faculties*
*Best average grade in materials science and engineering*

1998-2003 Ecole Polytechnique Fédérale de Lausanne (**EPFL**)

- Diploma work — 4 months
  Computational Materials Laboratory (**LSMX**), Pr. M. Rappaz
  *Experimental Study and Numerical Modelling of Coalescence in Heavily Inoculated Aluminum Alloys*
- **Exchange program** — 1 year
  Carnegie Mellon University, Pittsburgh PA, USA
- Internship — 3 months
  **Alcan**, Casting Technology Center, Chippis, Switzerland
  *Water Modelling of Grain Motion in DC Casting*
- Internship — 6 weeks
  **EPFL**, Laboratory of Construction Materials
  *Numerical Modelling of Crack Growth in Concrete*

1998 English course, Vancouver BC, **Canada** — 10 weeks

1995-1998 Maturité Fédérale Scientifique, Yverdon-les-Bains, Switzerland
**Awards** : *Mathematics, French dissertation, History*

## Language

- French : Mother tongue
- English : Fluent
- German : Good understanding

## Software

- System : UNIX, Linux, Windows
- Modelling tools : Abaqus, Calcosoft, ProCAST
- Programming : C, C++, FORTRAN, Visual C++
- Misc. : MSoffice, Illustrator, Photoshop, LaTeX

## Interests

- Table tennis club, Domdidier : accounting, team captain, juniors' coach
- Theater, classic literature

## Publications list

### Refereed Journals

V. Mathier, M. Rappaz, and A. Jacot. Coalescence of equiaxed grains during solidification. *Modelling Simul. Mater. Sci. Eng.*, **12**, pp. 479–490, 2004.

V. Mathier, J.-M. Drezet, and M. Rappaz. Two-phase modelling of hot tearing in aluminium alloys using a semi-coupled method. *Modelling Simul. Mater. Sci. Eng.*, **15**, pp. 121–134, 2007.

### Refereed Proceedings

M. Rappaz, P.-D. Grasso, V. Mathier, J.-M. Drezet, and A. Jacot. How does coalescence of dendrite arms or grains influence hot tearing ?. In M.G. Chu, D.A. Granger and Q. Han (editors), *Solidification of Aluminum Alloys*. TMS, 2004.

M. Rappaz, J.-M. Drezet, V. Mathier, and S. Vernède. Towards a micro-macro model of hot tearing. *Mater. Sci. Forum*, **519–521**, pp. 1665–1674, 2006.

V. Mathier, J.-M. Drezet, and M. Rappaz. Two-phase modeling of hot tearing in aluminum alloys using a semi-coupled method. In C.-A. Gandin and M. Bellet (editors), *MCWASP XI*. TMS, 2006.

J.-M. Drezet, V. Mathier, and D. Allehaux. FE Modelling of laser beam welding of aluminium alloys with special attention to hot cracking in transient regimes. To appear in M. Kocak (editor), *Mathematical modelling of weld phenomena 8*.